

UC Irvine

UC Irvine Electronic Theses and Dissertations

Title

Giant anisotropic magnetoresistance in a collinear antiferromagnet

Permalink

<https://escholarship.org/uc/item/7xp4c1mc>

Author

Mishner, Mara

Publication Date

2023

Peer reviewed|Thesis/dissertation

UNIVERSITY OF CALIFORNIA,
IRVINE

Giant anisotropic magnetoresistance in a collinear antiferromagnet

DISSERTATION

submitted in partial satisfaction of the requirements
for the degree of

DOCTOR OF PHILOSOPHY

in Physics

by

Mara Mishner

Dissertation Committee:
Professor Ilya Krivorotov, Chair
Professor Zuzanna Siwy
Assistant Professor Judit Romhányi

2023

DEDICATION

For my parents,
MaryEllen and Scott

TABLE OF CONTENTS

	Page
LIST OF FIGURES	v
LIST OF TABLES	xi
ACKNOWLEDGMENTS	xii
VITA	xiii
ABSTRACT OF THE DISSERTATION	xiv
1 Introduction	1
2 Background	3
2.1 Magnetic Free Energy	3
2.1.1 Zeeman Energy	4
2.1.2 Exchange Interaction	4
2.1.3 Magnetic Anisotropy Energy (MAE)	5
2.1.4 Perpendicular Magnetic Anisotropy (PMA)	7
2.2 Magnetization Dynamics	8
2.3 Antiferromagnetism	9
2.4 FM/AFM Exchange Coupling	12
2.5 Anisotropic Magnetoresistance (AMR)	16
3 Experimental Methods	21
3.1 Fabrication Tools	21
3.1.1 Sputter Deposition	21
3.1.2 Ion Mill Etching	28
3.1.3 Electron Beam Evaporation	30
3.2 Structural Characterization Tools	31
3.2.1 Atomic Force Microscopy	31
3.2.2 X-Ray Diffraction (XRD)	38
3.3 Lithography Techniques	47
3.3.1 Electron Beam Lithography (EBL)	47
3.3.2 Photolithography	60
3.4 Magnetic Characterization	63

3.4.1	Anomalous Hall Effect	63
3.4.2	Ferromagnetic Resonance (FMR)	66
3.4.3	AC Magnetoresistance	70
4	Quantitative measurements of AMR in PtMn antiferromagnet	84
4.1	Introduction	84
4.2	PtMn Thin Films	86
4.2.1	Physical Properties	86
4.2.2	Epitaxial Growth	86
4.2.3	Film Characterization	88
4.3	Experimental Results	91
4.3.1	AMR in CoFeMnSi	91
4.3.2	AMR in PtMn/CoFeMnSi	93
4.4	Data Analysis and Modeling	97
4.5	Discussion	101
4.6	Conclusions	106
5	Development and characterization of nanopillar arrays	110
5.1	Introduction	110
5.2	Fabrication of Nanopillars	112
5.2.1	Overview	112
5.2.2	Preliminary Steps	113
5.2.3	Sample Preparation	118
5.2.4	Pillar Definition	119
5.2.5	Hall Cross Definition	126
5.2.6	Ion Mill Etch to Define Hall Cross	129
5.3	Nanopillar Characterization by AHE	130
5.4	Discussion and Future Work	134
6	Epitaxial magnesium aluminum ferrite films grown by reactive sputtering	137
6.1	Motivation	137
6.2	Film Composition and Growth	138
6.3	Structural Characterization	139
6.4	Magnetic Characterization	142
6.5	Discussion and Conclusions	144
7	Conclusion	146
	Appendix A Sputtering System Standard Operating Procedure	148
	Appendix B Residual Gas Analyzer (RGA)	230
	Appendix C Co-sputtering Mathematica Notebook	234
	Appendix D AMR Analysis with Wheatstone Bridge	238

LIST OF FIGURES

	Page
2.1 Paramagnetic (a), ferromagnetic (b), antiferromagnetic (c), and ferrimagnetic (d) ordering.	5
2.2 Shape anisotropy in a FM film. In AFMs with $\vec{M}=0$, shape anisotropy does not exist.	7
2.3 Precession of the magnetization vector without (left) and with (right) Gilbert damping.	9
2.4 AFM magnetic susceptibility χ as a function of temperature. Susceptibility for $T < T_N$ is dependent on the direction of the applied field relative to the AFM easy axis. Image taken from [7].	11
2.5 Exchange bias under Meiklejohn and Bean model when AFM anisotropy is small (a) or large (b).	13
2.6 The sign difference in the exchange constant J for individual FM and AFM layers leads to frustration of AFM spins at the FM/AFM interface. Interfacial AFM spins cant slightly away from their easy axis and into the direction of the applied field, yielding a small net AFM moment. This effect is limited to the interface and the AFM spins in the bulk remain uncanted.	15
2.7 Resistance extrema in AMR are related to the orientation between magnetization and current.	17
2.8 In a ferromagnet, spin-up or -down d bands are shifted, leading to an availability of s and d states at E_{Fermi} . In materials with strong spin-orbit coupling, spin \uparrow and \downarrow d electrons mix. s electrons can now scatter into available $d \uparrow$	18
2.9 The scattering of conduction electrons is greatest when current flow I is parallel to the magnetic order parameter and smallest when it is perpendicular.	18
3.1 AJA International ATC-2000F sputter deposition system.	22
3.2 Seven sputtering guns on the ATC-2000F deposition system are shown housed in chimneys. Chimney shutters are swung open when making a deposition. As targets reach the end of their lifetime, deep circular rings become prominent on their surface.	23
3.3 The atoms of a single-crystal (epitaxial) film are periodically arranged, whereas a polycrystalline film consists of smaller "crystallites" and long-range atomic order is fully absent in an amorphous film.	25
3.4 When there is an in-plane lattice mismatch an epitaxial film must strain to accommodate to the substrate. Strain relaxes at a certain film thickness.	26

3.5	Difference in pattern transfer when etching at low versus high angles. Re-deposition of milled material often builds up at the edge of a mask.	28
3.6	Hall bars were defined by etching away all exposed metal until the substrate (clear) becomes visible.	29
3.7	Electron beam evaporation under high-vacuum.	31
3.8	AFM tip loading procedure using Anton Paar insertion tool.	33
3.9	The AFM actuator (left) holds the probe tip and is slid into or out of the AFM during a tip exchange. The ideal frequency choice of the tip is slightly off-resonance (right).	34
3.10	Layout of the Ted Pella HS-100MG calibration stub (left)–kept in the AFM tool box– and an actual portion of it as seen under the AFM (center). All features on the stub have a step height of 114 +/- 3% nm as specified on the backside of the stub box.	34
3.11	Silhouette of the AFM tip while being lowered to the sample surface using the Head Stage controls. Lower the tip to within one notch mark of the sample surface.	35
3.12	AFM image of a step height used for calibration.	36
3.13	A raw AFM image (grey) must be leveled in order to acquire accurate height information. This is done in the Tosca Analysis software by defining a 3-point plane on the image which encompasses an area known to be of equal height. The leveled image is shown in color.	37
3.14	A line drawn across a leveled AFM height image (inset) yields a step profile from which feature height can be deduced.	38
3.15	X-ray radiation of wavelength λ is scattered by two different atoms of a crystalline solid. The lower incident beam must travel an extra length of $2d \sin(\theta)$ compared to the top beam. When this length is equal to an integer multiple of λ , the two scattered waves constructively interfere.	39
3.16	Rigaku Smartlab goniometer. Optical alignment for any measurement is automated through the Rigaku software.	40
3.17	Common XRD measurements and their geometries. In 2θ - ω , the diffraction vector \vec{S} is fixed and only crystal planes parallel to the sample surface are probed. In GIXRD, \vec{S} continually changes direction and planes that are tilted with respect to the sample surface are probed. In rocking curves, \vec{S} is finely rocked about a fixed position to study diffraction from a single plane.	41
3.18	Measurement packages available in the Rigaku software.	42
3.19	Dialogue box for setting 2θ - ω measurement conditions. If using a scintillation detector, select data acquisition mode 1D.	43
3.20	To align the goniometer to the known 2θ value of a crystalline substrate, follow the rocking curve measurement workflow in the Rigaku software from steps 1 through 3.	44
3.21	Behavior of an incident X-ray for various incident angles (left) and an example of an XRR profile (right). In (a), an incident X-ray (blue) is completely reflected (red) from the sample surface and does not penetrate into the film; in (b), the incident X-ray propagates along the sample surface at a critical incident angle θ_C ; in (c), incident X-rays refract into the sample when $\theta > \theta_C$	46

3.22	GlobalFit software (left) and an example XRR fit with best fit parameters (right).	47
3.23	A resist mask fabricated with negative tone electron-beam resist.	48
3.24	The spin coater has clearly seen a long life. It is critical to follow the cleaning protocol to avoid further degradation.	49
3.25	Black valves for controlling vacuum level (left) and keypad controls (right).	50
3.26	SEM image of a global alignment mark made with PMMA resist. Large features such as these should be written with a large beam current (6.4 nA) which reduces write time.	53
3.27	Modify the parameters under Highlighted Entry Data according to Table 3.3.	57
3.28	Entity type can be set to Pattern (singular) or Array.	58
3.29	Full layout of MA6.	61
3.30	Because MA6 is intended for 4 inch wafers, smaller samples should be mounted to a dummy wafer with vacuum grease.	62
3.31	MA6 control panel.	63
3.32	"Ready for Load" message on MA6 screen.	63
3.33	A nanopillar oriented at the center of a Hall cross to be probed by the anomalous Hall effect.	65
3.34	A sample is mounted onto the CPW (with backside similarly sliced) using epoxy and then suspended vertically between the pole pieces.	66
3.35	A thin film sample is placed film-side down on the coplanar waveguide.	67
3.36	Schematic of connections for FMR with field-modulation.	68
3.37	Typical FMR resonance peak of Lorentzian form.	69
3.38	Wheatstone bridge circuit diagram.	70
3.39	LayoutEditor designs of the conventional Hall bar photomask (left) and the caterpillar Hall bar photomask (right). The caterpillar segments 1 through 7 wind in 15° increments.	72
3.40	Dimensions of the conventional Hall bar photomask (left) and caterpillar variety (right). Both photomasks are intended for 10 x 10 mm samples.	72
3.41	Resistance versus field angle (AMR) is measured by rotating the dewar between the pole pieces. Similarly, resistance versus field data collected at a particular field angle may be used to determine sample saturation. Measurements can be taken at 77 K by funneling in liquid nitrogen through a small opening on the top of the dewar lid. The HDMI-compatible dewar lid with carrier socket is shown right.	73
3.42	Numerical labeling of the Hall bar contacts. The bar is of thickness t , length L , and width w , with contact separation $a = b$ (figure taken from Appendix A of Lake Shore 7500/9500 Series Hall System User's Manual).	74
3.43	Numbered red circles are the chip carrier pins to which Hall bar contacts 1 through 6 should be wirebonded to as detailed in the text. A real example is shown right.	75
3.44	Samples are mounted to the chip carrier with vacuum grease and must be inserted into the carrier socket in the exact orientation shown left. When using the 3D-printed insertion tool (right), its thicker leg must face the crown-shaped feature that appears on only a single corner of the socket.	75

3.45	Full schematic of connections for the low-noise AMR measurement using a Wheatstone bridge.	76
3.46	A-B splitter (left) and lock-in measurement settings (right). User beware that this Signal Recovery lock-in has problems above 30 dB gain– replace with SRS 380 or use with caution.	77
3.47	A 1:1 audio transformer is soldered to the back of the Wheatstone bridge. This is a crucial component which seems to be removed from the several spare bridges currently in lab storage!	80
3.48	Components of the AMR setup: grounded Wheatstone bridge (left), switchbox (middle), and adapter (right).	80
4.1	Crystal structure of tetragonal PtMn with nominal lattice constants [31]. . .	87
4.2	RBS spectra (2.3 MeV $^4\text{He}^{++}$) of 16 nm films of Pt _{53.6} Mn _{46.4} at.% (top) and Pt _{43.8} Mn _{56.2} at.% (bottom) were used to calibrate films to equiatomic composition. Measurements are courtesy of Rutgers University.	88
4.3	(a) XRD 2θ scan of an MgAl ₂ O ₄ /PtMn(16 nm)/Ta(2 nm) film shows a preferred (001) texture. Epitaxy is also corroborated by a flat grazing incidence spectrum. (b) In-plane ϕ measurement on the film of (a) taken from 0° to 360°.	89
4.4	AFM images of a 16 nm PtMn film (a) with a 2 nm Ta cap and (b) without a cap, where S_q is RMS roughness. (c) SEM image of a PtMn(20 nm)/Ta(2 nm) film. (d) 3D surface of the un-capped PtMn film shown in (b) as measured by AFM.	91
4.5	(a) Measurement schematics for an arbitrary segment of the Hall bar shown fully in Figure 1.5b. The longitudinal component of sample resistance R was measured under an AC current I_{AC} applied along specific crystallographic directions of PtMn in a saturating field H , where θ is the angle between H and I_{AC} . (b) All films in our work, including the bare CoFeMnSi films, were patterned into the extended Hall bar geometry shown which turns in 15° intervals. The angle α (magnified inset for clarity) represents the angle of applied current with respect to the [010] direction of PtMn. AMR measurements conducted at each α allows AMR to be probed along the various crystallographic directions of PtMn.	93
4.6	Resistance versus angle of CoFeMnSi(3 nm)/Ta(2 nm) films grown on MgAl ₂ O ₄ at 400°C for I_{AC} along (a) $\alpha = 0^\circ$ and (b) $\alpha = 45^\circ$. Equal AMR percentages confirm that CoFeMnSi AMR does not depend on α	94
4.7	AMR percentage versus growth temperature in 3 nm films of CoFeMnSi. . .	94
4.8	Angular-dependent resistance for t_{PtMn} bilayer when (a) $\alpha = 0^\circ$ (b) $\alpha = 15^\circ$ (c) $\alpha = 30^\circ$ (d) $\alpha = 45^\circ$ (e) $\alpha = 60^\circ$ (f) $\alpha = 75^\circ$ and (g) $\alpha = 90^\circ$. (h) Angle between between resistance minimum and $\theta = 0^\circ$ versus α	95
4.9	(a) Dependence of AMR magnitude on α in a PtMn/CoFeMnSi bilayer with $t_{\text{PtMn}} = 4$ nm. (b) AMR magnitude as a function of t_{PtMn} when $\alpha = 0, 45,$ and 90° . The corresponding PtMn crystal directions are: [110] ($\alpha = 45^\circ$), [010] ($\alpha = 0^\circ$), and [100] ($\alpha = 90^\circ$).	96
4.10	Resistance versus applied field angle when $\alpha = 45^\circ$ in bilayers with (a) $t_{\text{PtMn}} = 20$ nm and (b) $t_{\text{PtMn}} = 3$ nm.	97

4.11	(a) Bilayer resistance versus t_{PtMn} (blue) fit under a combined parallel resistance and FS model (red). (b) Thickness dependence of bilayer magnetoresistance ΔR (blue) modeled with Equation 4.5 (red).	99
4.12	(a) Isolated AMR percentage from the PtMn layer in PtMn/CoFeMnSi bilayers as a function of t_{PtMn} when $\alpha = 45^\circ$. (b) Bilayer ΔR for t_{PtMn} (points) with fit line (blue) predicted by 3D atomistic model.	100
4.13	Interactions within and between atomic layers of PtMn.	101
4.14	The sensitivity of the magnetoresistance measurement setup is highlighted by our ability to detect AMR as small as 4.8E-5% in a 16 nm film of PtMn. . .	103
4.15	Cartoon illustration depicting the influence of FM magnetization direction (blue) on two in-plane AFM domains (green) when $\alpha = 45^\circ$	104
5.1	Step-by-step nanopillar fabrication process.	113
5.2	Three 10" wafers with the multilayer stack depicted were deposited by Ever-spin with a CoFeB layer of 20, 40, or 50 nm.	114
5.3	LayoutEditor designs for the crosshatch pattern. Vertical HSQ stripes of 5 micron widths are patterned by EBL onto the sample. Lines of MAN-2401 are then patterned horizontally overtop the vertical lines in a separate EBL step. To avoid headaches, it is useful to make one set of lines slightly wider than the other.	115
5.4	AFM image of the crosshatch with a step height measurement.	117
5.5	Crosshatch pattern on bare SiO ₂ substrate (left) used to determine HSQ etching rate. After milling the crosshatch then removing the MAN-2401 (right), the numbered areas represent the resulting regions: etched HSQ (1), etched SiO ₂ substrate (2), un-etched HSQ (3), and un-etched SiO ₂ (4). The 3-4 step height yields the height of un-etched HSQ while the 1-3 step height yields the the amount of HSQ that has been etched.	118
5.6	Crosshatch as seen under an optical microscope (left). A square patterned by EBL out of an HSQ/PMMA bilayer (right).	119
5.7	Full design of the Hall cross with dot array at its center (left). The first EBL step is to write the array and alignment marks (right).	120
5.8	The array size should exceed the dimensions of the active region at the center of the cross.	121
5.9	High-aspect ratio dot masks developed in the standard aqueous mixture of 1 wt % NaOH and 4 wt % NaCl which have fallen over.	122
5.10	HSQ dot array developed in diluted salty developer.	123
5.11	SEM image of a single pillar observed using the stage tilt.	124
5.12	Sacrificial nanopillars as seen under the SEM during fabrication development. Without passivation after milling, nanopillars will oxidize upon breaking vacuum.	125
5.13	NPGS will scan for the L-shaped alignment marks on the sample within the area enclosed by the four square windows. Ensure that all features in the alignment file are written in solid lines (accessible by highlighting the feature and choosing the Information tab). Only dashed lines will be written in NPGS.	128
5.14	NPGS Run File settings with two alignment steps.	129

5.15	Final Hall cross with central array. Some bloating related to dosage is seen near the cross edges.	130
5.16	R vs H for a blanket film with $t_{\text{CoFeB}} = 20$ nm (left). Estimated dipolar field of 30 nm diameter nanopillars as a function of array pitch (right).	131
5.17	R vs H sweeps after linear background subtraction of $10 \times 10 \mu\text{m}$ arrays as a function of nanopillar diameter for $t_{\text{CoFeB}} = 40$ nm and pitch 200 nm (left) or 150 nm (right).	131
5.18	V_{AHE} in a 30 nm nanopillar.	132
5.19	FORC curves of a 30 nm nanopillar array with 200 nm pitch. The outer envelope of the FORC defines the major hysteresis loop.	133
5.20	PMMA dot masks ($I = 25$ pA, dose = $40,000 \mu\text{m}/\text{cm}^2$) with attempted diameters of 50, 40, 30, 25 nm (descending) developed in MIBK(1):IPA(3). . .	135
6.1	XRD $2\text{-}\theta$ scan of an 18 nm MAFO film (left) with the associated MAFO(004) rocking curve (right).	139
6.2	In Pt-capped MAFO films, the (004) diffraction peak suppresses as a function of ArO_2 flow rate into the sputtering chamber during deposition.	140
6.3	Interfacial roughness between MAFO and 2 nm of Pt as a function of ArO_2 flow (left). Roughness values were taken from X-ray reflectivity profiles (right).	141
6.4	FMR resonant field and linewidth data for a 16 nm MAFO film taken along the easy(110) and hard(100) directions.	142
6.5	Resonance signal and angular dependent FMR (in-plane) measured at $f = 15$ GHz.	143

LIST OF TABLES

	Page
3.1 Standard ion milling parameters.	29
3.2 Electron beam resist options (MAN-2401 doubles as a photoresist).	48
3.3 Run File Entity settings.	56
3.4 Center-to-center distance and line spacing dictate the space between points in the electron beam. Smaller spacing improves resolution but increases write time. The configuration parameter, in parentheses, specifies the beam current: 1.6 pA(-9), 3.2 pA(-8), 6.4 pA(-7), 13 pA(-6), 25 pA(-5), 50 pA(-4), 100 pA(-3), 200 pA(-2), 400 pA(-1), 800 pA(0), 1600 pA(1), 3200 pA(2), 6400 pA(3).	59
4.1 CoFeMnSi physical properties.	92
5.1 Coercive field of the arrays for a given pillar diameter.	132

ACKNOWLEDGMENTS

It took a village to complete my PhD. Let us now meet the villagers.

To my research advisor, Professor Ilya Krivorotov, I express my sincerest gratitude for his guidance and patience throughout this process. In the face of challenges, Ilya's perspectives were indispensable to me and I was always afforded generous time and space to learn, however clumsily. I am equally grateful to him for fostering a lab that values shared knowledge among its members. I will forever be indebted to my lab mates throughout the years who taught me the practicalities of experimental science and whose company I have cherished keeping along the way: Alejandro Jara, Chris Safranski, Jen-Ru Chen, Eric Montoya, Amanatullah (Mishu) Khan, Joshua Yang, Xinyao (Ada) Pei, David Nelson, Mark Hayward, Emma Frantz, Matthew Abramson, and Thomas Gredig.

I also wish to thank my advancement and dissertation committee members— Professors Zuzanna Siwy, Javier Sanchez-Yamagishi, Judit Romhanyi and Matt Law— for taking time out of their busy schedules to provide feedback on my research, as well as the staff at IMRI and INRF for overseeing the instruments that made many aspects of this work possible.

To my parents, MaryEllen and Scott, and my brother, Evan, there is no sufficient repayment I can make for their unconditional support in every endeavor I have ever chosen to pursue. Their encouragement kept me going in the moments I strongly considered giving up. There is also no telling where I would be without my best friend Caroline, who has been my biggest cheerleader from the moment I received my acceptance letter to the day of my graduation six years later. Amidst my diatribes, monologues, and general complaining, she has always been the voice of reason. Last, but certainly not least, I cannot exclude Morris who makes me a happier, more selfless person.

Common knowledge would have it that getting a PhD is strictly an academic pursuit but it is also something intensely personal. Repeated failure has at times been a brutal teacher but an effective one undoubtedly. (There is no faster way to learn about the resilience of the human spirit than by manually threading the needle of a wirebinder with tweezers and a dental mirror). I have stumbled many times in my graduate school career. But if I am proud of anything at all, it is for having always continued.

Inquisitive, stubborn, and a bit nosy, I will in some ways forever be a graduate student by nature. So to the Krivorotov group students to come I humbly offer my parting wisdom: the juice is worth the squeeze.

VITA

Mara Mishner

EDUCATION

Doctor of Philosophy in Physics University of California	2023 <i>Irvine, California</i>
Master of Science in Physics University of California	2022 <i>Irvine, California</i>
Bachelor of Science in Physics University of Maryland	2017 <i>College Park, Maryland</i>

RESEARCH EXPERIENCE

Graduate Research Assistant University of California	2018–2023 <i>Irvine, California</i>
--	---

TEACHING EXPERIENCE

Graduate Teaching Assistant University of California	2017–2018 <i>Irvine, California</i>
Undergraduate Teaching Assistant University of Maryland	2015–2017 <i>College Park, Maryland</i>

ABSTRACT OF THE DISSERTATION

Giant anisotropic magnetoresistance in a collinear antiferromagnet

By

Mara Mishner

Doctor of Philosophy in Physics

University of California, Irvine, 2023

Professor Ilya Krivorotov, Chair

Manipulation of the spin degree of freedom in magnetic materials is a path towards a new generation of electronics known as spintronics. In traditional spintronic devices, ferromagnets are the active spin-dependent element and anisotropic magnetoresistance (AMR) is commonly used as an electrical readout method of magnetic order. Recently, research interest has shifted towards antiferromagnetic (AFM) materials as alternatives to ferromagnets: AFMs produce no stray magnetic fields, have ultrafast dynamics, and are capable of generating large magneto-transport effects.

This dissertation presents the first quantitative measurements of AMR in a compensated, high-temperature antiferromagnet PtMn. The magnitude of AMR in PtMn is revealed to be giant which is useful for potential device applications such as ultrafast non-volatile magnetic memory. In the process of reaching this goal, several preliminary developments are chronicled. These include the epitaxial growth of PtMn, AMR studies of the ferromagnet CoFeMnSi, and the development of an AC magnetoresistance measurement setup with $1\text{ m}\Omega$ sensitivity. Moreover, a novel detection scheme is detailed, wherein the AMR of an AFM material can be measured with low noise by exchange-coupling the AFM to a ferromagnet with zero AMR. This AMR detection method could plausibly extend to other exchange-coupled FM/AFM systems beyond the one studied in this work.

In a separate aspect of this dissertation, single-crystal films of the insulating, ferrimagnetic oxide $\text{MgAlFe}_2\text{O}_4$ are grown by reactive magnetron sputtering. Epitaxial magnetic insulators with high saturation magnetization and low Gilbert damping are highly desirable alternatives to the iron garnets typically found in spin caloritronics. The crystallographic quality of $\text{MgAlFe}_2\text{O}_4$ films is investigated by X-ray diffraction as a function of oxygen concentration during film deposition. The magnetic properties of $\text{MgAlFe}_2\text{O}_4$, including Gilbert damping and magnetic anisotropy, are also characterized by ferromagnetic resonance.

In yet another aspect of this dissertation, a nanofabrication recipe for micron-scale arrays of tall nanopillars is described. High aspect ratio nanopillars are useful in the creation of magnetic tunnel junctions (MTJs) with perpendicular magnetization, which have gained popularity due to scaling limitations associated with in-plane varieties. Arrays of pillars with 30 nm diameters are fabricated from an MTJ-like film stack using electron beam lithography and ion mill etching. Magnetization dynamics within the $10 \times 10 \mu\text{m}$ arrays are probed via the anomalous Hall effect as a function of pillar diameter and array pitch.

Chapter 1

Introduction

Spin transport electronics, or simply *spintronics*, is an area of study concerned with manipulating the spin of the electron to produce novel electrical devices. Whereas conventional semiconductor electronics utilize only the charge of the electron, spintronics uses the spin degree of freedom alone, or the combination of spin *and* charge, to create tinier, faster, and more energy efficient technologies. Because the spin of the electron carries a small magnetic moment, the natural language for controlling the behavior of spins on large scales is magnetism.

It is well-established that the global arrangement of spins within a material gives rise to various types of magnetism. Ferromagnets have traditionally played the leading role in most spin-based applications, but the discovery of magnetotransport effects in antiferromagnets has thrust them into the spotlight as candidates for the next generation of spintronic devices potentially operable at THz frequencies.

Ways to manipulate the antiferromagnetic order parameter are essential towards the realization of antiferromagnetic spintronics. However their weak magnetic susceptibility makes control by applied magnetic fields quite challenging. In this dissertation, manipulation of

the order parameter in single-crystal films of the metallic antiferromagnet PtMn was accomplished at room temperature by exchange coupling PtMn to the ferromagnet CoFeMnSi. This coupling enables the manipulation of magnetic order in PtMn and allows us to report the first quantitative measurements of anisotropic magnetoresistance (AMR) in a compensated, high-temperature antiferromagnet. The magnitude of AMR in PtMn is demonstrated to be large—on the order of several percent— which suggests it may be utilized as an electrical readout method in future antiferromagnetic spintronic devices.

Chapter 2

Background

2.1 Magnetic Free Energy

All electrons carry an intrinsic form of angular momentum called spin which has an associated magnetic dipole moment $\vec{\mu}$. The sum of the magnetic moments $\vec{\mu}$ per unit volume V within a material is defined as its magnetization $\vec{M} = (\sum \vec{\mu}_i)/V$. The orientation of \vec{M} typically lies along one or more preferred axes governed by lattice symmetry and sample shape. This preference is called magnetic anisotropy. In an applied magnetic field, the equilibrium direction of magnetization is determined by the minimum of the total free energy density F_{tot} ,

$$F_{tot} = F_{Zeeman} + F_{ex} + F_{MCA} + F_{demag} \quad (2.1)$$

where F_{Zeeman} is the energy associated with the Zeeman interaction, F_{ex} is the energy associated with the exchange interaction, F_{MCA} is the energy associated with the magnetocrystalline anisotropy, and F_{demag} is the demagnetization energy associated with dipole-dipole interactions. Only the energy contributions pertinent to this thesis are included in Equation 2.1 and discussed below.

2.1.1 Zeeman Energy

The effect of an applied magnetic field \vec{H}_{ext} on a magnetic moment is called the Zeeman interaction and its associated energy

$$F_{\text{Zeeman}} = -\vec{M} \cdot \vec{H}_{\text{ext}} \quad (2.2)$$

can be expressed in terms of magnetization \vec{M} . This energy term seeks to align \vec{M} along the direction of \vec{H}_{ext} . By nature of the dot product, an energy minimum occurs for $\vec{M} \parallel \vec{H}_{\text{ext}}$.

2.1.2 Exchange Interaction

The exchange interaction is the main cause of ordering inside magnetic materials and originates from wavefunction symmetry considerations between indistinguishable, neighboring electrons i and j . Namely, it reconciles the Coulomb repulsion of two negatively charged electrons in an atomic solid, usually on adjacent lattice sites, with the Pauli exclusion principle forbidding them from occupying the same quantum state.

The Hamiltonian for the Heisenberg exchange interaction takes the form

$$\hat{H}_{\text{ex}} = -2J_{ij}\langle \hat{s}_i \cdot \hat{s}_j \rangle \quad (2.3)$$

with \hat{s}_i and \hat{s}_j being the spin operators for each atomic site and J_{ij} the exchange constant whose sign determines the type of magnetic ordering. When $J_{ij} > 0$, the exchange interaction favors electrons with parallel spins and leads to ferromagnetism. When $J_{ij} < 0$, the interaction favors electrons with anti-parallel spins and leads to antiferromagnetism (Fig. 2.1). Exchange energy is largely responsible for the formation of magnetic domains—or local regions of uniform magnetization—within magnetic specimens.

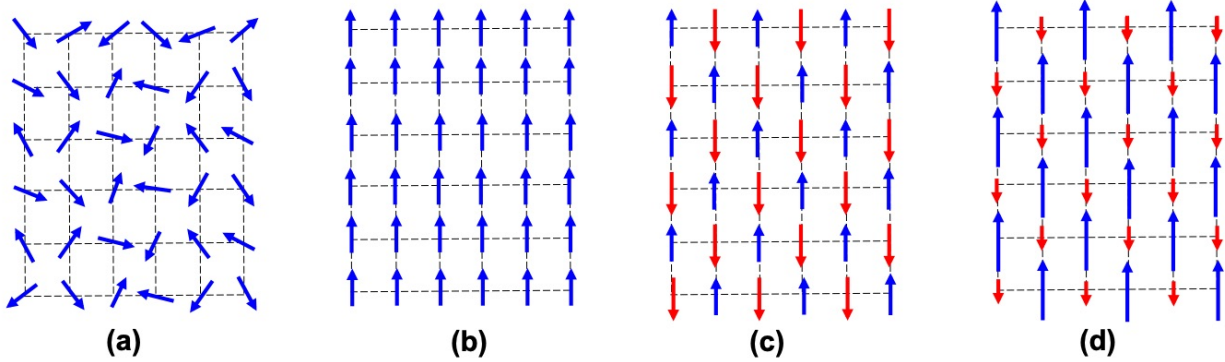


Figure 2.1: Paramagnetic (a), ferromagnetic (b), antiferromagnetic (c), and ferrimagnetic (d) ordering.

Though strong, exchange interactions decay exponentially with distance making them short-ranged and confined to near neighbors (longer range interactions are occasionally possible through "superexchange" [1]). In comparison, dipolar interactions are weaker but extend to longer distances within the lattice. The magnetostatic exchange length δ_{ex} below which exchange energy dominates over dipolar energy is given by [2]:

$$\delta_{\text{ex}} = \sqrt{\frac{J_{ij}}{2\pi M_S^2}}. \quad (2.4)$$

2.1.3 Magnetic Anisotropy Energy (MAE)

The magnetization of magnetic materials can have energetically preferential directions that are dictated by the symmetry of the crystal lattice and shape of the sample. The tendency for \vec{M} to align along one of these directions is determined by the magnetic anisotropy energy (MAE) present in the system. The direction that minimizes this energy defines a magnetic easy axis while the direction that maximizes it is a hard axis. Similarly, MAE can be defined as the work W_{MAE} required to rotate the magnetization away from an easy axis to any arbitrary direction:

$$F_2 - F_1 = \int_1^2 dW_{\text{MAE}} = MAE \quad (2.5)$$

where 1 and 2 denote the initial and final directions of magnetization and free energy [3].

Magnetocrystalline Anisotropy (MCA)

Magnetocrystalline anisotropy (MCA) is a type of MAE where the direction of \vec{M} depends on the crystal axes inside the sample. This kind of anisotropy arises from the coupling of the electron's magnetic moment to the crystal lattice due to the spin-orbit interaction. The free energy contribution F_{MCA} is usually defined phenomenologically as a power series expansion of the directional cosines $(\alpha_x, \alpha_y, \alpha_z)$ of the magnetization \vec{M} with respect to the crystallographic axes. Consequently, F_{MCA} takes on distinct forms for specific crystal symmetries [3].

Demagnetization Energy (Shape Anisotropy)

Shape anisotropy in thin films is a result of long-range magnetic dipolar interactions at the bounds of the sample. A finite volume of ferromagnetic material will produce magnetic surface charges at its boundaries, giving rise to a demagnetizing field \vec{H}_{demag} that tends to misalign the magnetic moments inside the volume itself. Generally speaking, the demagnetization energy tries to align the magnetization along the sample surface in order to minimize these surface charges, which usually results in the formation of an easy axis along the longest axis of the sample (in-plane for a thin film, z-axis for a cylinder, etc.). As a result, \vec{H}_{demag} reduces the effective field felt by the sample when exposed to an applied field (i.e., $\vec{H}_{\text{eff}} = \vec{H}_{\text{app}} - \vec{H}_{\text{demag}}$). Since \vec{H}_{demag} directly depends upon the shape of the volume it gives rise to demagnetization, or shape, anisotropy.

The demagnetizing field is expressed as

$$\vec{H}_{\text{demag}} = \overleftarrow{N} \cdot \vec{M} \quad (2.6)$$

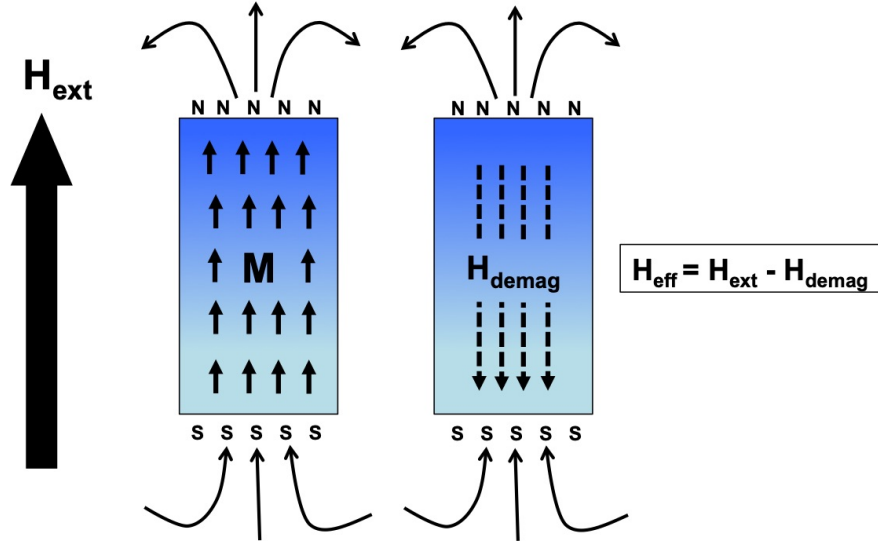


Figure 2.2: Shape anisotropy in a FM film. In AFMs with $\vec{M}=0$, shape anisotropy does not exist.

where \overleftrightarrow{N} is the demagnetization tensor. In samples of high symmetry (e.g. sphere, cylinders, ellipsoids) \overleftrightarrow{N} reduces to a simple form but can require numerical calculation in more complex cases. Ultimately, the free energy term due to demagnetization is given by a volume integral over the dot product between \vec{M} and \vec{H}_{demag} [4]:

$$F_{\text{demag}} = \frac{-\mu_0}{2} \int_V dV \vec{M} \cdot \vec{H}_{\text{demag}}. \quad (2.7)$$

2.1.4 Perpendicular Magnetic Anisotropy (PMA)

When the thickness of a thin film reaches the ultra-thin limit, the role of the surface becomes increasingly important and the preferred direction of magnetization, which typically lies in the film plane due to shape anisotropy, can become out of plane. Perpendicular magnetic anisotropy (PMA), or a preference for out of plane magnetization, is a reflection of the large difference in anisotropy between the film surface (or interface) and the bulk [5]. PMA has an intrinsic dependence on material parameters which makes it sensitive to properties like sample roughness, thickness, microstructure, and mechanical stress.

To separate bulk K_b from interfacial K_i anisotropy contributions to the PMA of a ferromagnetic thin film, the thickness t_{FM} dependence of the effective magnetic anisotropy energy

$$K_{\text{eff}} = K_b - \frac{M_s^2}{2\mu_0} + \frac{K_i}{t_{\text{FM}}} \quad (2.8)$$

is typically measured (using $M(H)$ or FMR techniques to deduce K_{eff}), and $(-\frac{M_s^2}{2\mu_0})$ is included as a demagnetization term [6]. The vertical intercept of a linear extrapolation to $K_{\text{eff}}t_{\text{FM}}$ vs. t_{FM} returns the value of K_i while K_b can be determined from the slope. Similarly, the transition point between a preferred in-plane to out-of-plane magnetization direction is demarcated by the intercept at $K_{\text{eff}}t_{\text{FM}} = 0$.

2.2 Magnetization Dynamics

In its equilibrium state, a stationary magnetic moment in an applied magnetic field will align along the direction of the field. If an external stimulus then drives the moment out of equilibrium, it begins to oscillate around its equilibrium position according to the Landau-Lifshitz-Gilbert (LLG) equation of motion:

$$\frac{\partial \vec{M}}{\partial t} = -\gamma \left[\vec{M} \times \vec{H}_{\text{eff}} \right] + \frac{\alpha}{M_S} \left[\vec{M} \times \frac{\partial \vec{M}}{\partial t} \right]. \quad (2.9)$$

In real systems with some magnetization \vec{M} and saturation magnetization M_S , \vec{M} does not align simply to the applied field \vec{H}_{ext} but rather to an effective, time-independent field \vec{H}_{eff} which is the sum of \vec{H}_{ext} and all internal fields due to anisotropies. The two terms in Equation 2.9 represent the two distinct torques that \vec{M} experiences due to \vec{H}_{eff} : the first describing the precessional motion of \vec{M} around \vec{H}_{eff} , and the second describing energy dissipation due to magnetic damping which is quantified by the dimensionless Gilbert damping parameter α . In the absence of Gilbert damping, \vec{M} precesses indefinitely about \vec{H}_{eff} at some fixed

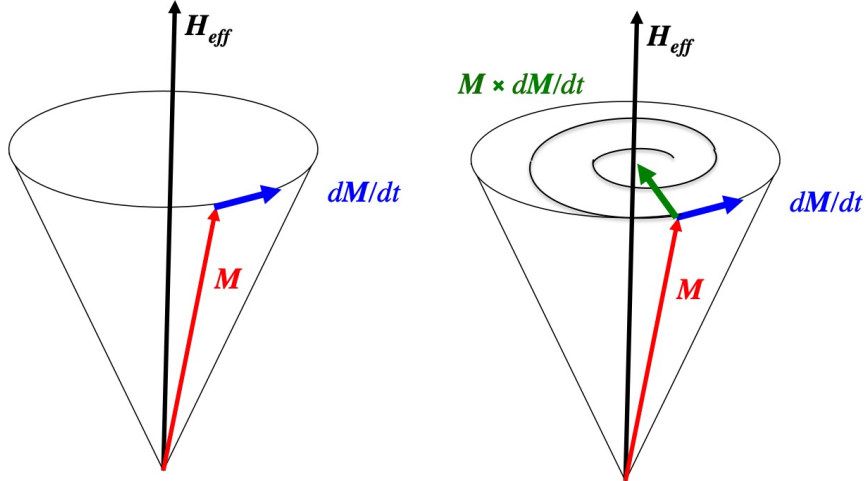


Figure 2.3: Precession of the magnetization vector without (left) and with (right) Gilbert damping.

precession angle. With Gilbert damping, the precession angle reduces until \vec{M} is eventually pulled in the direction of \vec{H}_{eff} (Fig. 2.3).

2.3 Antiferromagnetism

Antiferromagnetism is a type of magnetic ordering in which neighboring magnetic moments inside of a material are anti-aligned with respect to one another resulting in zero net magnetization. This type of magnetic lattice is best imagined as the sum of two sub-lattices whose magnetizations \vec{M}_1 and \vec{M}_2 are equal but opposite in direction (Fig. 2.1). All antiferromagnets (AFMs) have a Néel temperature T_N above which they lose their anti-parallel ordering and become paramagnetic, marking a transition point between an ordered and disordered state. To differentiate between the two warrants the introduction of an *order parameter* which, in the case of an AFM, is defined as the difference in magnetization between its sub-lattices, $\vec{L} = \vec{M}_1 - \vec{M}_2$ (also called the Néel vector). Order parameters are not exclusive to AFMs however. In a ferromagnet, where the Curie temperature T_C marks the transition between ferro- and paramagnetism, the order parameter is simply defined as its

magnetization.

The difference between the antiferro- and paramagnetic phases can be seen from the magnetic susceptibility, χ , which relates the magnetization of a material to the strength of an applied magnetic field \vec{H} (Fig. 2.4). For $T > T_N$, the magnetic moments on the sub-lattices orient randomly and χ obeys the standard Curie-Weiss law for a paramagnet

$$\chi = \frac{C}{T + \theta}, \quad T > T_N, \quad \theta > 0 \quad (2.10)$$

where C and θ are two constants. In the low temperature limit or $T < T_N$, the magnetic sub-lattices arrange themselves in opposite directions characteristic of antiferromagnetism, but the susceptibility is strongly dependent on the direction of \vec{H} with respect to the orientations of \vec{M}_1 and \vec{M}_2 . The axis along which the sub-lattices lie is determined by magnetocrystalline anisotropy. If a weak \vec{H} is applied parallel to this axis, it can be shown that the *parallel* susceptibility $\chi_{\parallel} \rightarrow 0$ as $T \rightarrow 0$ K and \vec{H} has little effect. If a weak \vec{H} is applied perpendicular to the axis, the *perpendicular* susceptibility χ_{\perp} is a constant, independent of temperature up to T_N . Compared to ferromagnetic substances where χ can be in excess of 1000, χ values for AFMs are extremely small, on the order of 10^{-2} at room temperature [7].

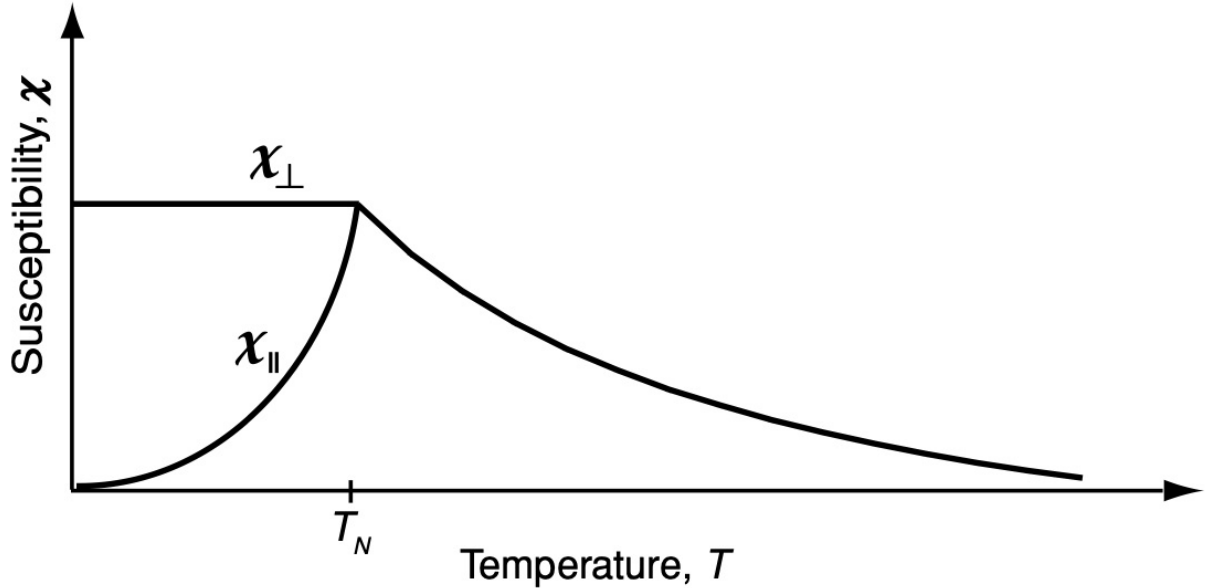


Figure 2.4: AFM magnetic susceptibility χ as a function of temperature. Susceptibility for $T < T_N$ is dependent on the direction of the applied field relative to the AFM easy axis. Image taken from [7].

Although the low magnetic susceptibility of AFMs makes them macroscopically unresponsive to applied fields, it was predicted and later experimentally confirmed that the manipulation of the AFM order parameter can yield many of the spin- and magneto-transport phenomena seen in ferromagnets [8–11]. In addition, the staggered AFM moments can have preferred axes of orientation that can be altered through exchange bias, strain, electric fields, or optical methods, indicating that AFMs may be richly dynamic [12, 13]. Control of the AFM order parameter paves a path towards nanoscale technologies based on AFMs which would have several advantages: AFMs are unperturbed by magnetic fields, can have dynamics in the THz regime, produce zero stray fields, and may be insulating, semiconducting, or metallic in nature. These qualities make them ideal candidates for non-volatile memory elements with fast response times. Ways in which the AFM order parameter can be efficiently detected and controlled is an ongoing area of research.

2.4 FM/AFM Exchange Coupling

In FM/AFM bilayers, a FM may experience a shift in its hysteresis loop due to the interfacial coupling of its spins to those in the adjacent AFM layer. This discovery, first observed in 1956 by Meiklejohn and Bean, became known as *exchange bias* and has become an integral part of reading and writing in modern magnetic media [14].

A phenomenological description of exchange bias under the Meiklejohn and Bean model can be presented with the help of Figure 2.5(a). A saturating field is initially applied to a FM/AFM bilayer at a temperature $T_N < T < T_C$ such that the spins of the AFM are randomly oriented while the the FM spins align along the direction of an applied field. In step one, the temperature is lowered to $T < T_N$, while the saturating field is still applied, such that the AFM spins begin to order antiferromagnetically in a process known as field-cooling. Note that the FM/AFM spins across the interface align ferromagnetically with a coupling strength J_{int} . In step two, the direction of the applied field is reversed causing the FM spins to begin to rotate. However, if the AFM has sufficient magnetic anisotropy (i.e. $> J_{\text{int}}$), the AFM spins will exert a torque on the FM spins to keep them pinned in their current direction. The AFM is said to induce a unidirectional anisotropy in the FM. In step three, the FM spins fully reverse when the applied field is sufficient to overcome the torque from the AFM. When the field direction is reversed yet again, as in step four, the antiferromagnetic coupling at the FM/AFM interface makes it energetically preferable for the FM spins to reverse direction and thus they do so for a smaller value of applied field.

The added energy cost to reverse the FM magnetization manifests itself as a shift in the hysteresis loop away from the origin by the size of the exchange field H_{eb} . The exchange bias energy of the bilayer system (normalized to the coupling area) can be expressed as $E_{\text{eb}} = H_{\text{eb}} M_S t_{\text{FM}}$ where the loop shift H_{eb} is generally inversely proportional to FM thickness, $H_{\text{eb}} \propto 1/t_{\text{FM}}$. Above a certain blocking temperature T_B , however, the exchange bias

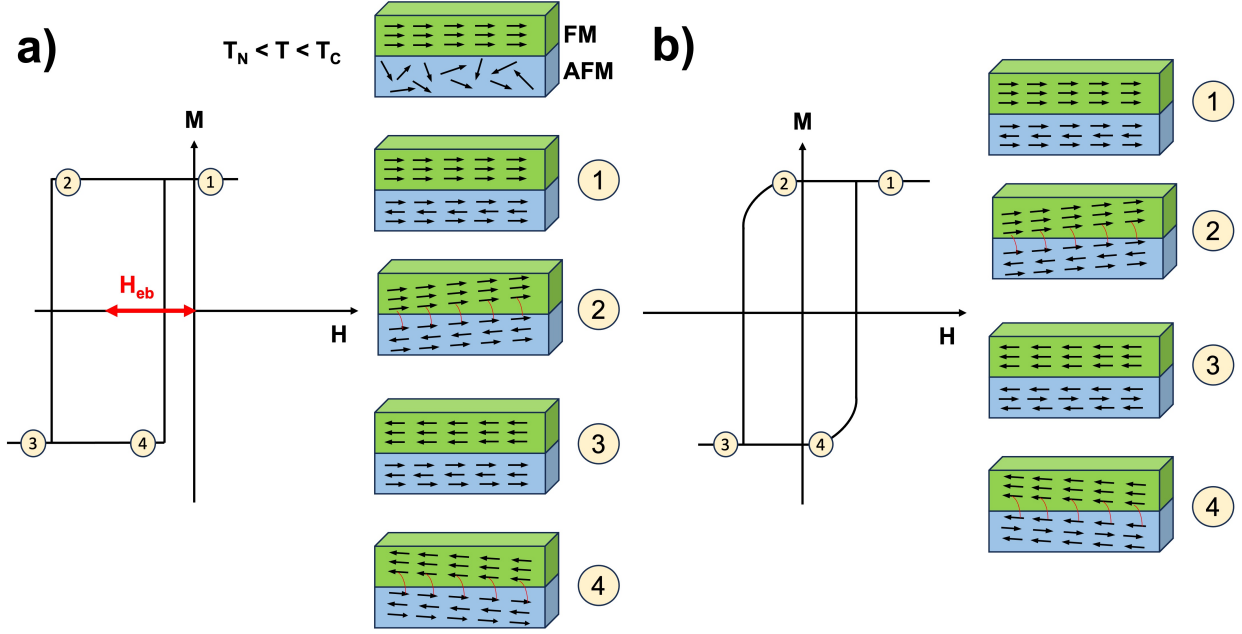


Figure 2.5: Exchange bias under Meiklejohn and Bean model when AFM anisotropy is small (a) or large (b).

phenomenon disappears completely. This temperature typically depends upon finite size effects in the AFM layer but can be quite complex for thin films. For highly crystalline structures with thick AFM layers $T_B \approx T_N$ is often observed, while polycrystalline systems with thin AFMs generally have $T_N \gg T_B$ [15].

While Figure 2.5(a) captures the conventional picture of exchange bias when the magnetic anisotropy of the AFM is assumed to be large, it requires modification if the AFM anisotropy is small (i.e. $< J_{\text{int}}$). In such a system, the initial configuration after field-cooling has taken place is shown in step one of Figure 2.5(b). When the applied field is reversed in step two, the FM spins begin to rotate but drag the spins in the AFM layer along with them if the AFM has extremely low anisotropy. In this situation, it becomes favorable for the FM and AFM layers to rotate coherently in response to the applied field. The behavior is analogous for negative saturation in steps three through four. The additional motion of the AFM order results in an enhanced coercivity of the hysteresis loop, meaning the field required to reverse the FM magnetization actually becomes larger.

The two main assumptions in both descriptions of exchange bias outlined with Figure 2.5 are that: (1) the magnetization rotation is coherent and (2) the FM and AFM easy axes are parallel. The energy E per unit surface area S of the FM/AFM structure within this model is given as [16]

$$E/S = -HM_{\text{FM}}t_{\text{FM}}\cos(\theta - \beta) + K_{\text{FM}}t_{\text{FM}}\sin^2(\beta) + K_{\text{AFM}}t_{\text{AFM}}\sin^2(\alpha) - J_{\text{int}}\cos(\beta - \alpha) \quad (2.11)$$

where H is the external field, M_{FM} is the saturation magnetization of the FM, t_{FM} and t_{AFM} are the FM and AFM layer thicknesses, K_{FM} and K_{AFM} are the FM and AFM anisotropies, α is the angle between AFM spins and the AFM easy axis, β is the angle between FM spins and the FM easy axis, and θ is the angle between H and the FM easy axis. The first term in Equation 2.11 represents the Zeeman interaction due to the applied magnetic field. The second and third terms are the respective FM and AFM anisotropies, and the fourth term is an FM/AFM interface coupling term. With no applied field and no coupling J_{int} , Equation 2.11 reduces to just terms two and three. When the AFM has large anisotropy ($J_{\text{int}} < K_{\text{AFM}}t_{\text{AFM}}$) such that its spins are fixed along the AFM easy axis and $\alpha \sim 0$, term three drops out. For this case, it has been shown that the hysteresis loop shifts laterally by an amount $H_{\text{eb}} = J_{\text{int}}/M_{\text{FM}}t_{\text{FM}}$. Furthermore, if the AFM anisotropy is low ($J_{\text{int}} > K_{\text{AFM}}t_{\text{AFM}}$), and AFM and FM spins rotate together under an applied field, then $\alpha - \beta \sim 0$.

Deeper investigation into the micromagnetic origins of FM/AFM exchange coupling was prompted by the fact that the Meiklejohn and Bean model failed to predict H_{eb} values commensurate with those observed experimentally. A more realistic model was eventually put forth by Koon [17], and later Schulthess and Butler [18], that attributed FM/AFM exchange coupling to the canting of AFM spins at the interface of the two materials (Fig. 2.6). In this model, the difference in sign of the exchange coupling constant between the FM ($J > 0$) and AFM ($J < 0$) layers leads to the frustration of magnetic moments at the FM/AFM interface. The result of such competing exchange interactions is the canting, or slight bending,

of interfacial AFM spins. With AFM magnetic sub-lattices no longer perfectly cancelling, a small net moment is produced in the AFM layer that interacts with the much larger magnetization of the neighboring FM. To minimize overall energy, the magnetization of the FM aligns perpendicular to the direction of Néel order. This perpendicular coupling between FM magnetization and AFM order parameter gives rise to an exchange field which can be as large as 10^3 T [1, 19].

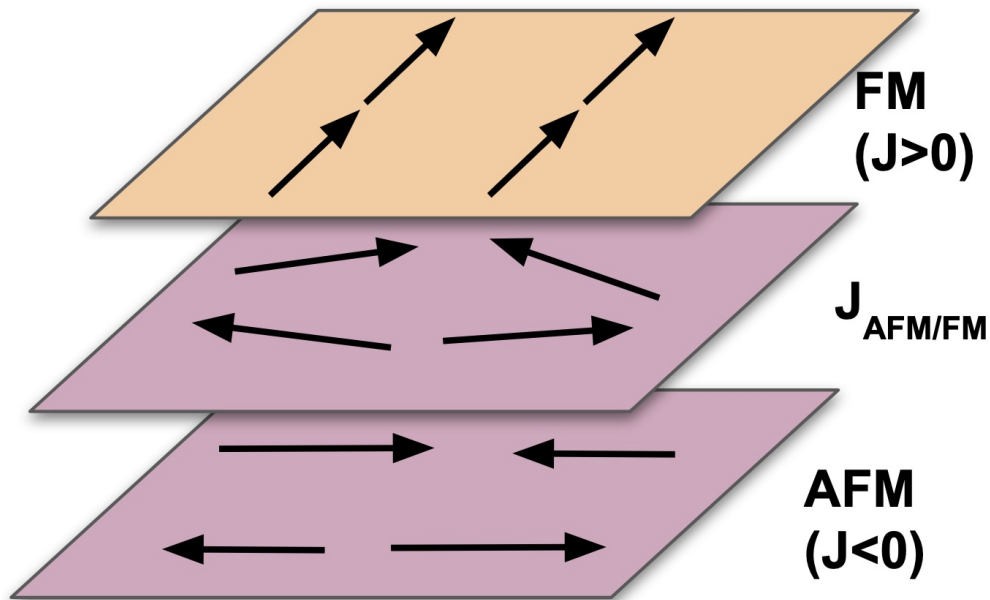


Figure 2.6: The sign difference in the exchange constant J for individual FM and AFM layers leads to frustration of AFM spins at the FM/AFM interface. Interfacial AFM spins cant slightly away from their easy axis and into the direction of the applied field, yielding a small net AFM moment. This effect is limited to the interface and the AFM spins in the bulk remain uncanted.

Important to remember is that FM/AFM exchange coupling is an interfacial effect: the size of the FM/AFM exchange field decays with distance from the interface and AFM spins far from it experience only minimal torque from the FM [16]. Thus the rotation of AFM order through a full 360° via exchange coupling, is only possible when the AFM layer is sufficiently thin such that this interaction is maximal. This effect can be further complicated by surface roughnesses and the compensated or uncompensated nature of AFM spins at the interface,

both of which will influence the strength of the resulting FM/AFM exchange field [16].

2.5 Anisotropic Magnetoresistance (AMR)

The ability of a magnetic material to change its electrical resistance in response to an applied magnetic field is known as magnetoresistance and exists in several forms (ordinary, giant, tunneling, spin Hall, etc.). Anisotropic magnetoresistance (AMR) is a specific type of magnetoresistance in which the relative angle between the applied current direction and the magnetic order parameter causes electrical resistance to vary as

$$R = R_0 + R_{\text{AMR}} \cos^2(\theta) \quad (2.12)$$

in polycrystalline materials, where R_0 is the background resistance and R_{AMR} is defined as the difference ($R_{\parallel} - R_{\perp}$) between field applied parallel or perpendicular to the order parameter (Fig. 2.7). In single crystal films, higher order resistance terms are sometimes observed on top of the usual $R \sim \cos^2 \theta$ dependence, suggesting that the direction of the order parameter and current with respect to the crystal axes of a sample can have an additional impact on AMR [20–26].

The origin of AMR can be attributed to modified s - d scattering due to spin-orbit coupling (the interaction between spin magnetic moment and orbital angular momentum). When atoms are brought together into a solid their electronic orbitals overlap which leads to the formation of electron energy bands by the discrete nature of electron energy levels (Fig. 2.8). In ferromagnetic materials these energy bands exist for both spin \uparrow and \downarrow electrons but the d -bands are shifted relative to one another due to exchange interactions. This splitting leads to an availability of both s and d states at E_{Fermi} for $s\downarrow$ electrons, which is not possible for $s\uparrow$ electrons since all $d\uparrow$ states are full. In materials with strong spin-orbit coupling, $d\uparrow$ and

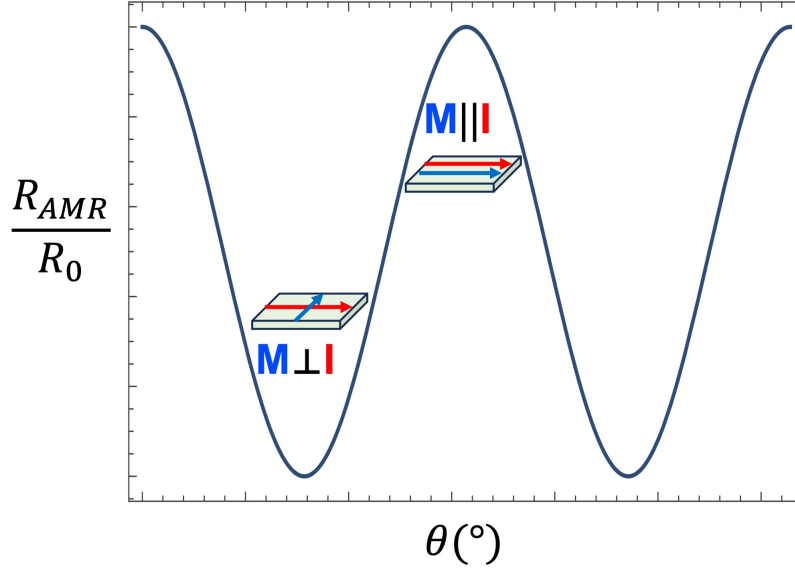


Figure 2.7: Resistance extrema in AMR are related to the orientation between magnetization and current.

$d\downarrow$ wavefunctions are mixed and $s\uparrow$ electrons are now able to scatter into $d\uparrow$ states. It can be shown that the degree to which this s - d mixing occurs— and the s - d scattering rate by extension— is related to the magnetization of the material, or more generally, its magnetic order parameter. Specifically, when electrical current is passed through such a magnetic material in an applied magnetic field, s electrons (primarily responsible for conduction due to the low mobility of d electrons) experience a higher or lower probability of scattering based on whether current flow is parallel or perpendicular to the direction of magnetic order. A change in resistance based on the relative angle between electric current and magnetic order parameter is thus observed [7, 27].

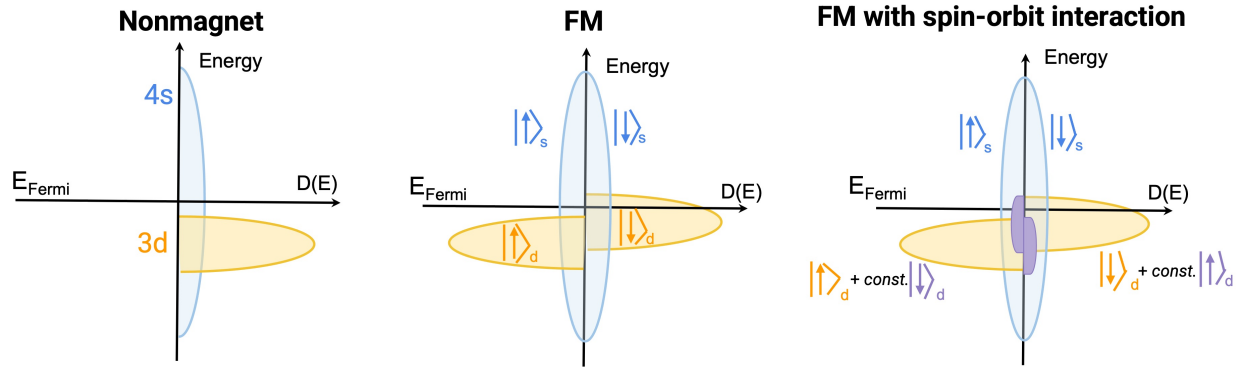


Figure 2.8: In a ferromagnet, spin-up or -down d bands are shifted, leading to an availability of s and d states at E_{Fermi} . In materials with strong spin-orbit coupling, spin \uparrow and \downarrow d electrons mix. s electrons can now scatter into available $d \uparrow$.

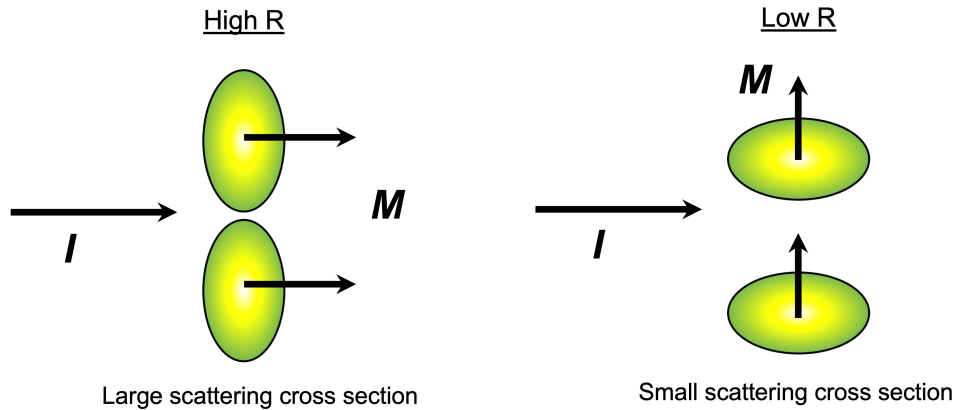


Figure 2.9: The scattering of conduction electrons is greatest when current flow I is parallel to the magnetic order parameter and smallest when it is perpendicular.

AMR may exist in antiferromagnets and ferromagnets alike, with typical values for the latter falling between 1-10% at room temperature [20, 28, 29]. Unlike ferromagnets, whose net magnetic moment means they can be readily manipulated by applied fields (provided they exceed the coercive and anisotropy fields of the FM itself, which rarely exceed 1 T [19]), AFMs have no net magnetization and possess only weak magnetic susceptibility. The manipulation of their order parameter is inherently more difficult and typically requires exchange-coupling the material to a FM. Given this added challenge, the number of AFM materials for which AMR data exists is limited but recent evidence suggests it may be similar in magnitude to FMs [23, 30].

References

- [1] Marder, M. P. *Condensed matter physics* (John Wiley & Sons, 2010).
- [2] Abo, G. S. *et al.* Definition of magnetic exchange length. *IEEE Transactions on Magnetics* **49**, 4937–4939 (2013).
- [3] Lindner, J. & Farle, M. in *Magnetic Heterostructures* 45–96 (Springer, 2008).
- [4] Exl, L., Suess, D. & Schrefl, T. Micromagnetism. *Handbook of Magnetism and Magnetic Materials*, 1–44 (2020).
- [5] Johnson, M., Bloemen, P., Den Broeder, F. & De Vries, J. Magnetic anisotropy in metallic multilayers. *Reports on Progress in Physics* **59**, 1409 (1996).
- [6] Ikeda, S. *et al.* A perpendicular-anisotropy CoFeB–MgO magnetic tunnel junction. *Nature materials* **9**, 721–724 (2010).
- [7] Coey, J. M. *Magnetism and magnetic materials* (Cambridge university press, 2010).
- [8] Zhang, W. *et al.* Spin Hall effects in metallic antiferromagnets. *Physical review letters* **113**, 196602 (2014).
- [9] Zhang, W. *et al.* All-electrical manipulation of magnetization dynamics in a ferromagnet by antiferromagnets with anisotropic spin Hall effects. *Physical Review B* **92**, 144405 (2015).
- [10] Fukami, S., Zhang, C., DuttaGupta, S., Kurenkov, A. & Ohno, H. Magnetization switching by spin-orbit torque in an antiferromagnet–ferromagnet bilayer system. *Nature materials* **15**, 535–541 (2016).
- [11] Zhang, W. *et al.* Giant facet-dependent spin-orbit torque and spin Hall conductivity in the triangular antiferromagnet IrMn₃. *Science advances* **2**, e1600759 (2016).
- [12] Shi, J. *et al.* Electrical manipulation of the magnetic order in antiferromagnetic PtMn pillars. *Nature Electronics* **3**, 92–98 (2020).
- [13] Scholl, A., Liberati, M., Arenholz, E., Ohldag, H. & Stöhr, J. Creation of an antiferromagnetic exchange spring. *Physical review letters* **92**, 247201 (2004).
- [14] Meiklejohn, W. H. & Bean, C. P. New magnetic anisotropy. *Physical review* **102**, 1413 (1956).
- [15] Nogués, J. *et al.* Exchange bias in nanostructures. *Physics reports* **422**, 65–117 (2005).
- [16] Öhandley, R. *Modern Magnetic Materials Principles and Application* 2000.
- [17] Koon, N. Calculations of exchange bias in thin films with ferromagnetic/antiferromagnetic interfaces. *Physical review letters* **78**, 4865 (1997).

- [18] Schulthess, T. & Butler, W. Consequences of spin-flop coupling in exchange biased films. *Physical review letters* **81**, 4516 (1998).
- [19] Marti, X. *et al.* Room-temperature antiferromagnetic memory resistor. *Nature materials* **13**, 367–374 (2014).
- [20] Van Gorkom, R., Caro, J., Klapwijk, T. & Radelaar, S. Temperature and angular dependence of the anisotropic magnetoresistance in epitaxial Fe films. *Physical Review B* **63**, 134432 (2001).
- [21] Ramos, R., Arora, S. & Shvets, I. Anomalous anisotropic magnetoresistance in epitaxial Fe₃O₄ thin films on MgO (001). *Physical Review B* **78**, 214402 (2008).
- [22] Tondra, M. *et al.* Thickness dependence of the anisotropic magnetoresistance in epitaxial iron films. *Journal of applied physics* **73**, 6393–6395 (1993).
- [23] Wang, C. *et al.* Anisotropic magnetoresistance in antiferromagnetic Sr₂IrO₄. *Physical Review X* **4**, 041034 (2014).
- [24] Ahadi, K. *et al.* Anisotropic magnetoresistance in the itinerant antiferromagnetic EuTiO₃. *Physical Review B* **99**, 041106 (2019).
- [25] Fina, I. *et al.* Anisotropic magnetoresistance in an antiferromagnetic semiconductor. *Nature communications* **5**, 1–7 (2014).
- [26] Ziese, M. in *Handbook of Magnetism and Magnetic Materials* 435–475 (Springer, 2021).
- [27] Campbell, I. Hall effect and resistivity anisotropy in Ni alloys. *Physical Review Letters* **24**, 269 (1970).
- [28] McGuire, T. & Potter, R. Anisotropic magnetoresistance in ferromagnetic 3d alloys. *IEEE Transactions on Magnetics* **11**, 1018–1038 (1975).
- [29] Campbell, I., Fert, A. & Jaoul, O. The spontaneous resistivity anisotropy in Ni-based alloys. *Journal of Physics C: Solid State Physics* **3**, S95 (1970).
- [30] Bodnar, S. Y. *et al.* Magnetoresistance effects in the metallic antiferromagnet Mn₂Au. *Physical Review Applied* **14**, 014004 (2020).

Chapter 3

Experimental Methods

3.1 Fabrication Tools

3.1.1 Sputter Deposition

Sputtering is a method of thin film deposition whereby argon plasma is used to eject material from a target source and coat a substrate placed in the path of the ejected atoms. Compared to more limited and time-consuming growth techniques like pulsed-laser deposition or molecular beam epitaxy, sputtering has the advantage of versatility: two targets can be ignited simultaneously to create alloy films (*co-sputtering*), heated growths and magnetic annealing can be performed in situ, and reactive gases like oxygen can be introduced inside of the sputtering chamber to drive chemical reactions near the film surface (*reactive sputtering*).



Figure 3.1: AJA International ATC-2000F sputter deposition system.

The Krivorotov group sputtering chamber (AJA International ATC-2000F) consists of a circular arrangement of seven tilt-adjustable sputtering sources (AJA A320 or A300)– sometimes called guns– which each hold a 2” diameter target of raw material (99.9+% purity). The target is placed on the copper cathode block of the sputtering source which is then shielded by a shuttered housing assembly called a chimney (Fig. 3.2). Each sputtering source is connected to an individual DC or RF power supply that can provide a voltage between the target and the rotating stage on the chamber lid which holds the substrate at anode. A typical deposition process begins by flowing inert Ar gas into the sputtering chamber which is under high vacuum via a turbomolecular pump. At a certain pressure ($\sim 2\text{mT}$) regulated by a gate valve in front of the turbomolecular pump, a voltage between the cathode of a particular gun and the anode ionizes the Ar atoms in the chamber to produce Ar plasma.

The positively charged Ar ions bombard the negatively charged cathode holding the target, causing atoms of this material to be ejected everywhere inside of the chamber when the chimney shutter is opened. Magnets behind the cathode confine the electrons of the Ar plasma to the target which prevents them from bombarding the substrate. Optional Ar/O₂ gas may be injected near the substrate for reactive growths.



Figure 3.2: Seven sputtering guns on the ATC-2000F deposition system are shown housed in chimneys. Chimney shutters are swung open when making a deposition. As targets reach the end of their lifetime, deep circular rings become prominent on their surface.

Based on the known deposition rate of the target and the length of time the chimney shutter is opened while the target is sustaining plasma, film thicknesses can be precisely controlled while sputtering. Deposition rates are typically determined by sputtering material onto a bare substrate for a fixed amount of time and power to the target, followed by an X-ray

reflectivity measurement to determine thickness (see section 3.2.2). The deposition rate of the target at the given power level is then calculated as the ratio of measured thickness to deposition time with units of *nm/sec*. Here it is worth noting that changing the tilt of the gun, height of the stage, pressure of Ar plasma, or percentage of power supplied to the target will all substantially change the sputter deposition rate. Rates require re-calibration if any of these conditions change.

Every material has unique growth requirements to consider before making a deposition. For instance, conductive materials can be sputtered using DC or RF power but insulators require strictly RF (13.56 MHz with an impedance matching network) in order to eliminate charge buildup on the target surface. The high ionization energies of most metals (~ 10 eV) means they can also be sputtered at higher deposition rates than insulators [1]. Even magnetic materials may be deposited by sputtering provided the sputtering cathode itself is magnetic, which is a re-configurable property in the Krivorotov group system (guns 1-3 are currently magnetic). For comprehensive details on the operation of the Krivorotov group AJA system, see Appendix A.

When purchasing targets, thickness is a critical factor. The AJA A320 and A300 sources are designed for 2" diameter targets of 0.25" thicknesses. Conductive, non-magnetic materials (e.g., Al, Cu) can be purchased exactly 0.25" thick, but magnetic materials (e.g., Fe, Py, Ni) and oxides (e.g., MgO) must generally be thinner (~ 0.125 "). If the amount of pure material is < 0.25 " thick, an adapter ring is placed on top of the target to reach the 0.25" threshold needed for operation with the A320 and A300 sources. Oxide and semiconducting targets are further restricted in thickness since they require a conductive backing plate to facilitate proper cooling. Based on these requirements, targets should be appropriately purchased such that total thickness (i.e., pure material thickness + adapter ring thickness + backing plate thickness) reaches exactly 0.25". With repeated depositions targets naturally erode over time, leading to the formation of deep circular rings on their surface as visible in Figure 3.2.

If caution is not taken to properly monitor this erosion, it is possible to entirely penetrate through the target and begin sputtering the backing plate, or worse, the cathode block of the sputtering source itself.

Four major parameters influence the quality of a sputtered film: the power supplied to the target, plasma pressure, chamber base pressure, and growth temperature. Increasing power and plasma pressure will generally increase the deposition rate of a material, but there exists limits above which the target can become damaged or the plasma unstable. Base pressure inside of the sputtering chamber is typically in the high vacuum ($<5E-9$ Torr) range which prevents residual gases like water or oxygen from adversely impacting the film chemistry. A residual gas analyzer (RGA) inserted inside of the chamber is a useful probing tool to identify and quantify these gases (see Appendix B). Depositions may also be performed at room temperature or while heating the substrate. Amorphous, polycrystalline, and epitaxial thin films are all achievable by sputtering (Fig. 3.3).

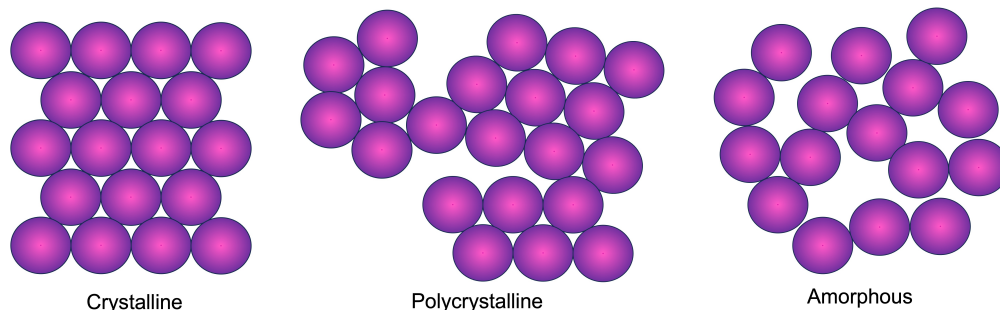


Figure 3.3: The atoms of a single-crystal (epitaxial) film are periodically arranged, whereas a polycrystalline film consists of smaller "crystallites" and long-range atomic order is fully absent in an amorphous film.

Epitaxial Thin Film Growth

Of central importance to this thesis is thin film epitaxy: a growth mode in which crystalline layers of a material are deposited with a well-defined orientation with respect to an underlying crystalline seed layer or substrate. The film and seed materials can be the

same (homoepitaxy) or different (heteroepitaxy). In semiconductor applications, epitaxial thin films are often advantageous over polycrystalline or amorphous types since their physical properties (e.g., conductivity) tend to be controllable by the conditions of their growth (temperature, doping, substrate, etc.).

Most film and substrate combinations will not yield epitaxial growth unless the mismatch ε between the in-plane lattice constant a of the film and substrate, calculated as

$$\varepsilon(\%) = \frac{a - a_{\text{substrate}}}{a_{\text{substrate}}} * 100, \quad (3.1)$$

is minimized. Note that in some cases a may be related to $a_{\text{substrate}}$ by a 45° , 30° , or 60° in-plane rotation. If ε is large ($>10\%$), lattice strain that increases with thickness begins to form in the film layer and makes epitaxy difficult to achieve. This accumulation of strain eventually relaxes at a critical thickness which is inversely related to ε (i.e., if ε is large relaxation occurs at a small film thickness). Because minimization of ε is critical, epitaxial film growth places limitations on the choice of substrate.

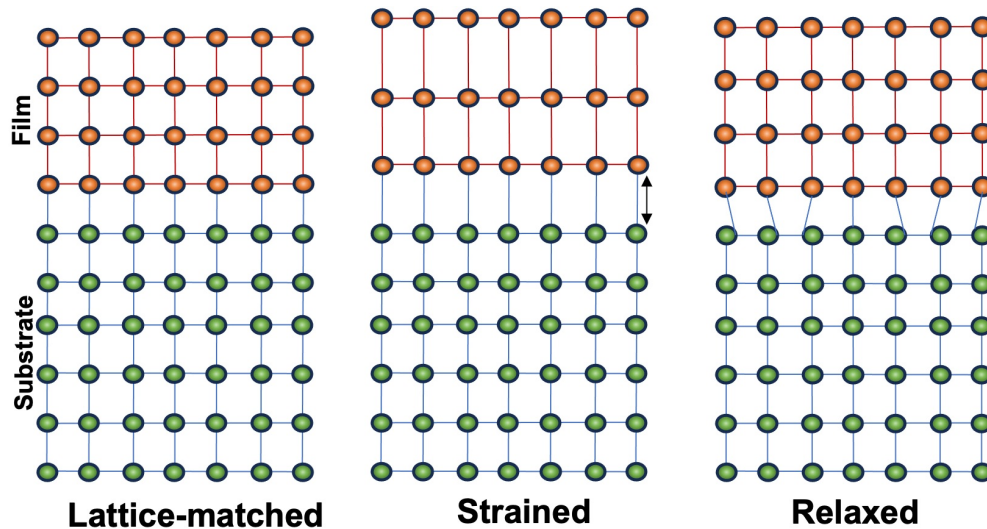


Figure 3.4: When there is an in-plane lattice mismatch an epitaxial film must strain to accommodate to the substrate. Strain relaxes at a certain film thickness.

A crystalline substrate is also described by the Miller index $[hkl]$ of its surface lattice plane,

which has a direct influence on the crystallographic orientation of the film layer grown upon it. Based on the desired orientation of the film (e.g., (100), (110), (111)), the substrate should be purchased with its surface cut along the appropriate Miller index. Because no substrate can be cut perfectly along a crystallographic plane, the substrate will always have a small miscut. The miscut– or angle of deviation between the surface normal of the substrate and the crystallographic plane of its surface– is generally within $\pm 0.5^\circ$ and should be stated by the substrate manufacturer. It can also be independently verified by an X-ray diffraction rocking curve measurement.

Although epitaxial growth details vary by material and require consultation with the existing literature, several comments are broadly applicable. Firstly, the smoothness of the interface between film and substrate is imperative. Substrates should be purchased with one side polished and a surface roughness $<5 \text{ \AA}$. For added cleanliness one may choose to sonicate the substrate sequentially in acetone, methanol, then isopropyl alcohol, and/or subject the substrate to a brief RF plasma cleaning in the sputtering system prior to deposition (60 seconds, 20 W). Second, epitaxial growths are commonly performed at elevated temperatures which can be made up to 700°C maximum in the AJA sputtering system. It is advisable to always ramp the temperature down from elevation since cooling to room temperature rapidly can impart additional strain into the film. Furthermore, it is good practice to use low deposition rates and Ar plasma pressures ($\leq 1\text{mT}$) while sputtering as these tend to promote the formation of large epitaxial grains. And lastly, when depositing an epitaxial film series it is crucial to keep the conditions of the main chamber as stable as possible. Depositions should be made in the quickest succession feasible with zero interruptions in between. If re-production in film quality proves difficult, it may be necessary to condition the chamber prior to growth by sputtering a getter material such as Ta to reduce the amount of residual gas in the chamber.

3.1.2 Ion Mill Etching

Etching is the process of removing material during the fabrication of nanodevices and can be broken into dry or wet regimes. Dry etching is a physical process that typically removes material using plasma, while wet etching is a chemical process that uses liquid chemicals or etchants. Dry etching is generally a more repeatable and controllable process which makes it advantageous over wet techniques.

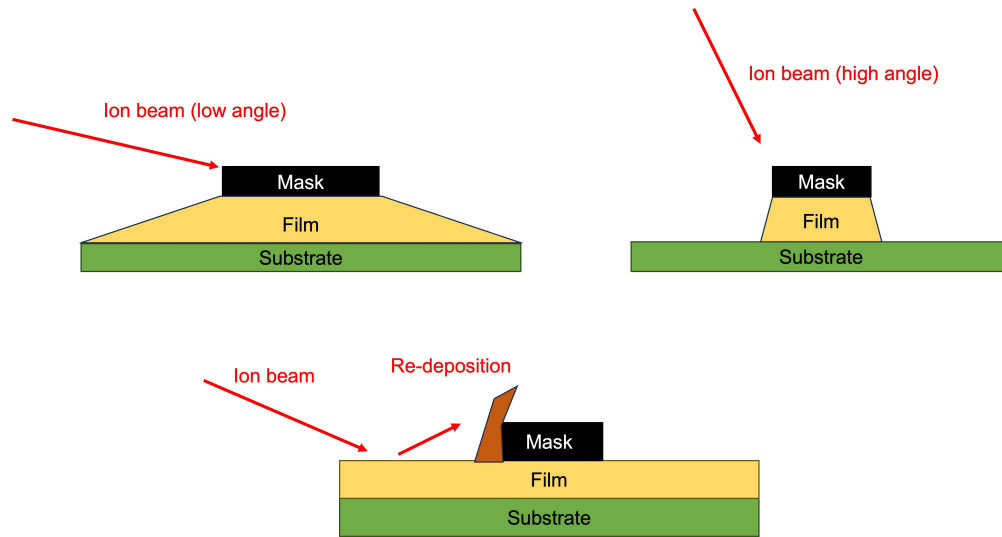


Figure 3.5: Difference in pattern transfer when etching at low versus high angles. Re-deposition of milled material often builds up at the edge of a mask.

An ion mill is a form of dry etching that uses a beam of Ar ions accelerated from an ion source to bombard the surface of a sample, driving away material to some desired depth in the process. The milling is done in high-vacuum while the sample is continuously rotated at a fixed angle with respect to the incident beam. To minimize heating of the sample during this process, a shutter cyclically opens and closes for a fixed time interval specified by the duty cycle parameter. Similar to sputtering rates, etching rates are material-specific and strongly depend on the incident angle of the ion beam with respect to the sample surface. By choice of angle, nanodevices with straight sidewalls and well-defined features can be created. All etching done in this thesis was performed using the Intlvac Nanoquest I ion mill in the

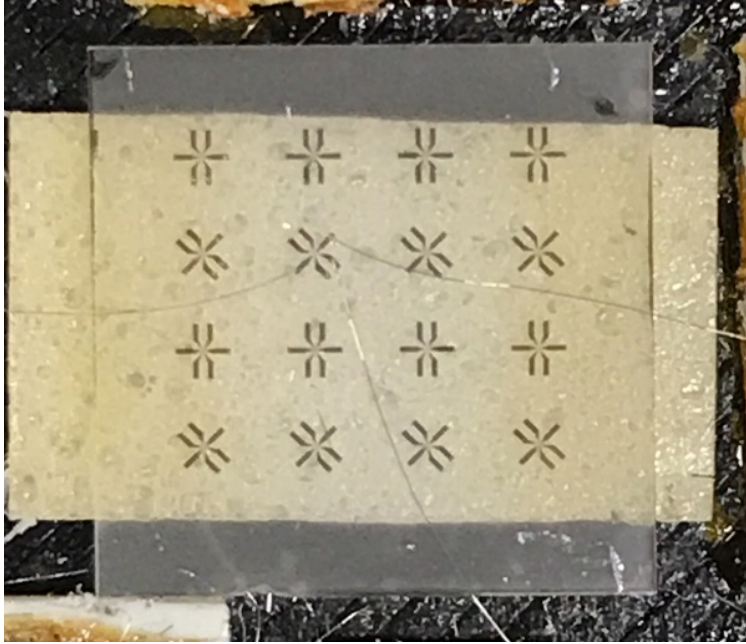


Figure 3.6: Hall bars were defined by etching away all exposed metal until the substrate (clear) becomes visible.

Krivorotov lab.

Typical etching parameters are listed in Table 3.1. As stated, the choice of etching angle varies by need. A near-normal etch of 80° is a good general-purpose choice for defining things like alignment marks, Hall bars, or other micrometer-scale features since shadowing effects are minimal at this angle. Unavoidably during an etching process, there is re-deposition of the etched material onto the side of the structure which can lead to electrical shorts down

Parameter	Setting
Beam Voltage	400 V
Beam Current	30 mA
Acceleration Voltage	80 V
Emission Current	34 mA
Stage Temperature	10°C
Duty Cycle	30 s
Base Pressure	$<5\text{E-}7$ Torr
Spin Speed	20

Table 3.1: Standard ion milling parameters.

the line (Fig. 3.5). This can be prevented by adding a 30 second clean-up etch at low-angle (10°) after the completion of the 80° etch. Low-angle etches can also be utilized to trim the dimensions of resist masks (e.g., reducing the diameter of a circular mask from 50 nm to 20 nm). This is apt when the desired dimensions of the mask are difficult to achieve by lithography directly, which is often the case where sub-30 nm features are concerned. Switching back and forth between two etching angles in a single process is an additional possibility.

3.1.3 Electron Beam Evaporation

Another method of thin film growth is electron beam evaporation which is a form of physical vapor deposition. High current and moderate voltage applied to a filament under vacuum produces a thermal beam of electrons that is accelerated into a pocket filled with a particular material. Once the beam strikes the pocket the material inside heats until transformed to its gaseous phase, at which point it vaporizes from the pocket and coats the sample sitting above it (Fig. 3.7). To promote uniform heating of the source material, the beam is continuously swept around the contents of the pocket. The direction of material accumulation onto the sample is controlled by the stage angle. An angle of 45° with respect to the beam is standard as this ensures all areas of the sample, including sides, are coated.

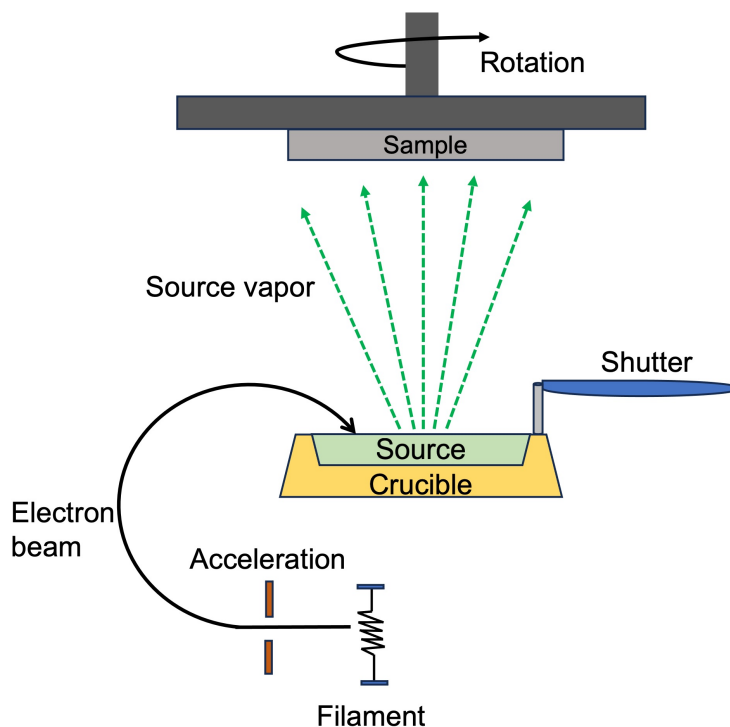


Figure 3.7: Electron beam evaporation under high-vacuum.

The Krivorotov group Intlvac evaporator system, conveniently attached to the ion mill, was utilized in this thesis for purposes of lead deposition or device passivation immediately after etching. Thick (30+ nm) evaporations should be performed in the Angstrom Engineering EvoVac Glovebox Evaporator at IMRI.

3.2 Structural Characterization Tools

3.2.1 Atomic Force Microscopy

Scanning probe microscopes (SPM) are designed to measure physical properties like height, magnetism, and topography using a probe. A probe tip rasters over a specified area of the sample while the physical property of interest is read out in real time. Atomic force

microscopy is a specific type of SPM commonly used to collect surface feature information with resolution up to fractions of nanometers.

Measurements are performed in either contact or non-contact scanning modes. Contact scans directly drag the probe tip across the sample surface which can be destructive. Non-contact (tapping) mode is less invasive and works by alternatively touching then retracting the probe tip from the sample in quick succession as the tip moves across the scan line. In both cases, data is obtained using a laser deflection feedback loop where a photodiode laser is aimed at the back of the probe tip and reflected onto a light sensitive detector. The detector records changes in the laser position and converts this to a DC signal that ultimately reveals the sample topography. In contact mode, the force applied to the sample is kept constant and the image is generated based on the z-motion of the tip. In non-contact scans, the probe tip oscillates with a fixed amplitude and the change in oscillation amplitude as the tip encounters peaks or valleys is used to identify features.

Atomic force measurements taken in this thesis were done using the Anton Paar Tosca 400 AFM located in MC2. The following subsection outlines how the Tosca 400 may be utilized to perform a height measurement with tapping mode.

Anton Paar Tosca 400 AFM Operation

- Open Tosca Control software
- Remove the actuator for holding the probe tip (Fig. 3.9)
- Insert AFM probe tip (App Nano, ACT-20) into the actuator using the Anton Paar insertion tool (Fig. 3.8)
- Re-insert the actuator into the AFM
- Load samples onto the stage using double-sided carbon tape

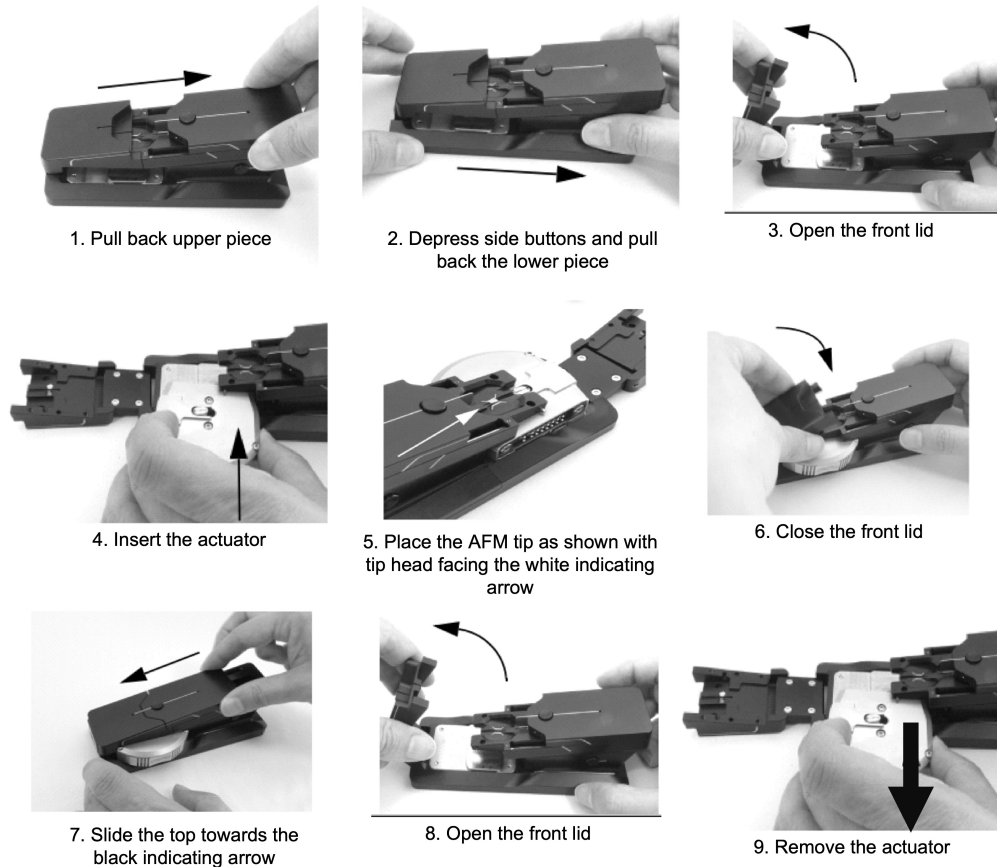


Figure 3.8: AFM tip loading procedure using Anton Paar insertion tool.

- Close the AFM lid
- Under Cantilever Setup, choose Tapping Mode
- Under Deflection Module, double-click to place the red crosshairs over the AFM tip
- Perform Auto-Alignment
- Perform Cantilever Tune, making sure to enter the frequency range specific to the AFM tip as specified by the manufacturer (200-400 kHz)
- Ensure a resonance peak is seen during cantilever tuning, otherwise the tip may be defective
- On the amplitude vs. frequency curve, choose a frequency slightly adjacent to the

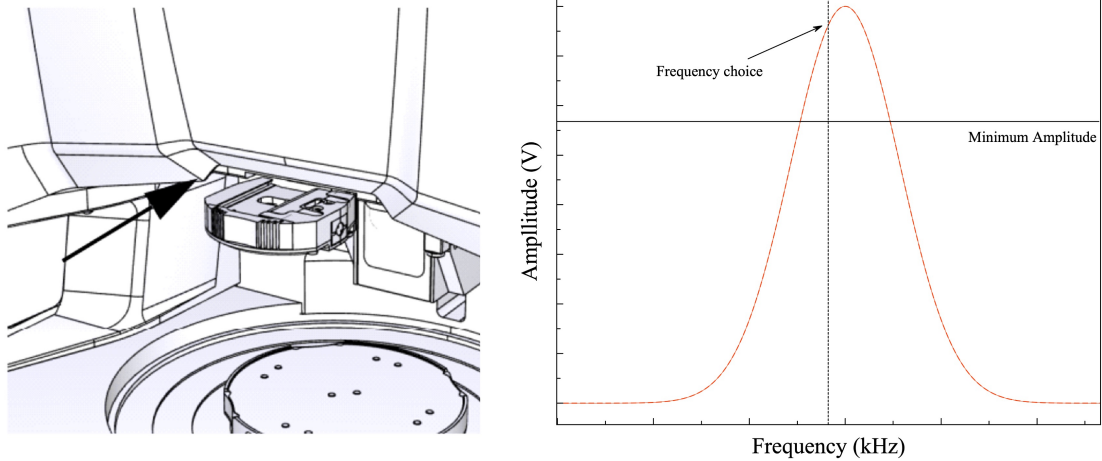


Figure 3.9: The AFM actuator (left) holds the probe tip and is slid into or out of the AFM during a tip exchange. The ideal frequency choice of the tip is slightly off-resonance (right).

resonant frequency peak which is also above the minimum amplitude level shown in the software (Fig. 3.9)

- Under Macro Navigation, navigate to the sample of interest (before measuring real samples, it is advisable to measure a calibration sample of known height to ensure the AFM itself is working accurately)

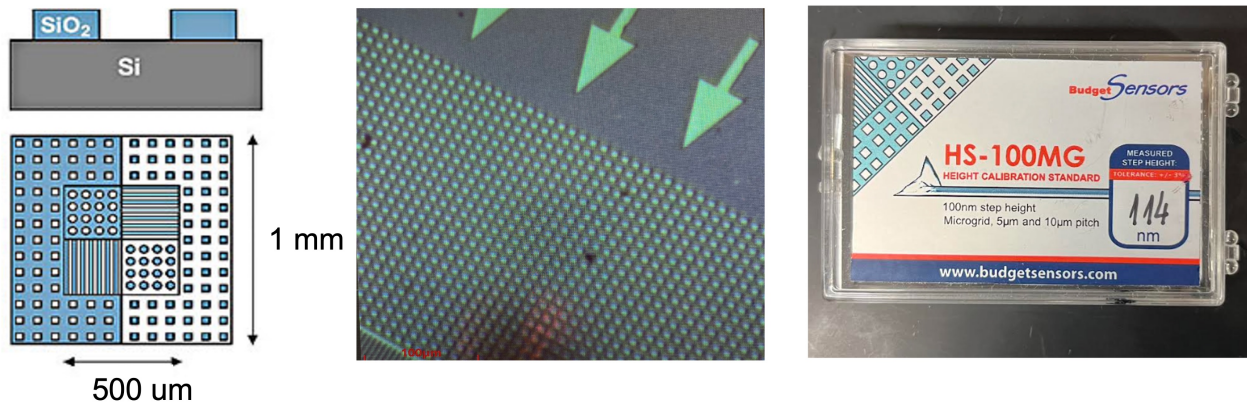


Figure 3.10: Layout of the Ted Pella HS-100MG calibration stub (left)–kept in the AFM tool box– and an actual portion of it as seen under the AFM (center). All features on the stub have a step height of 114 +/- 3% nm as specified on the backside of the stub box.

- Under Coarse Approach, lower the AFM tip to the surface of the sample– do not crash the actuator into the sample!



Figure 3.11: Silhouette of the AFM tip while being lowered to the sample surface using the Head Stage controls. Lower the tip to within one notch mark of the sample surface.

- Under Micro Navigation, move to the feature of interest and adjust the focus of the AFM microscope (under Camera Control) until clear
- When ready to measure, select Engage
- Measurement parameters including scan rate, resolution, and scanning area (0.001-100 μm) should be adjusted to needs (for tapping mode, gain should be set somewhere between 50 to 100 and rarely above 400)
- Select Start to image and Stop when finished
- If additional measurements are needed, disengage then navigate to the next location
- If fully finished, disengage, slide out the actuator, and remove the AFM tip using the insertion tool
- In Tosca Analysis (Gwyddion is an alternative software), open the image
- Under Operators, choose Extract Layers to extract the height trace scan

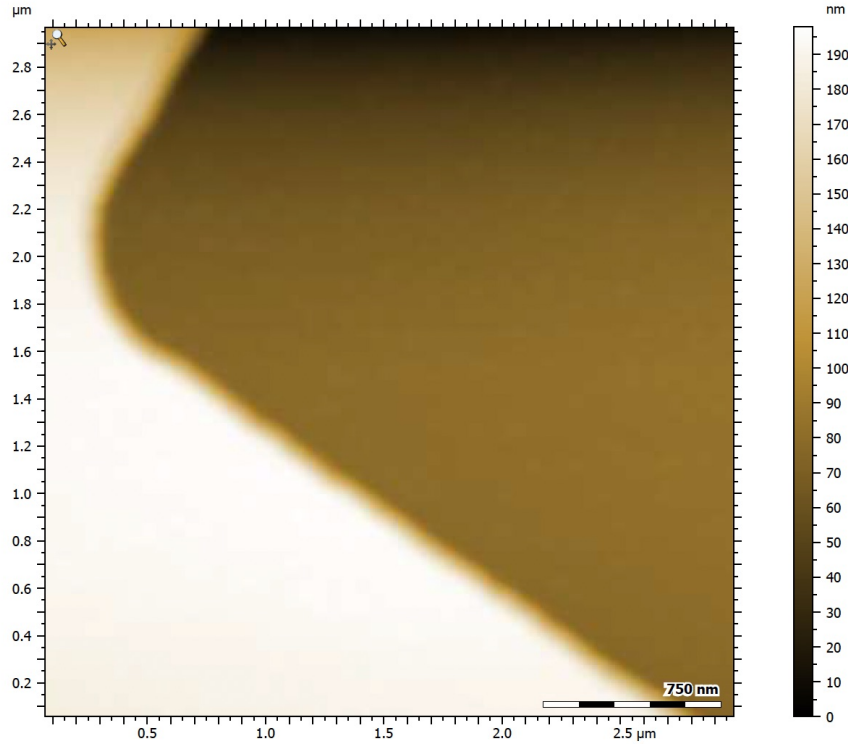


Figure 3.12: AFM image of a step height used for calibration.

- Choose Level then Leveling method of plane defined by 3 points
- Level the image by defining a plane which encloses an area known to be of approximately equal height
- Choose Extract profile to draw a line across the image and extract its height profile

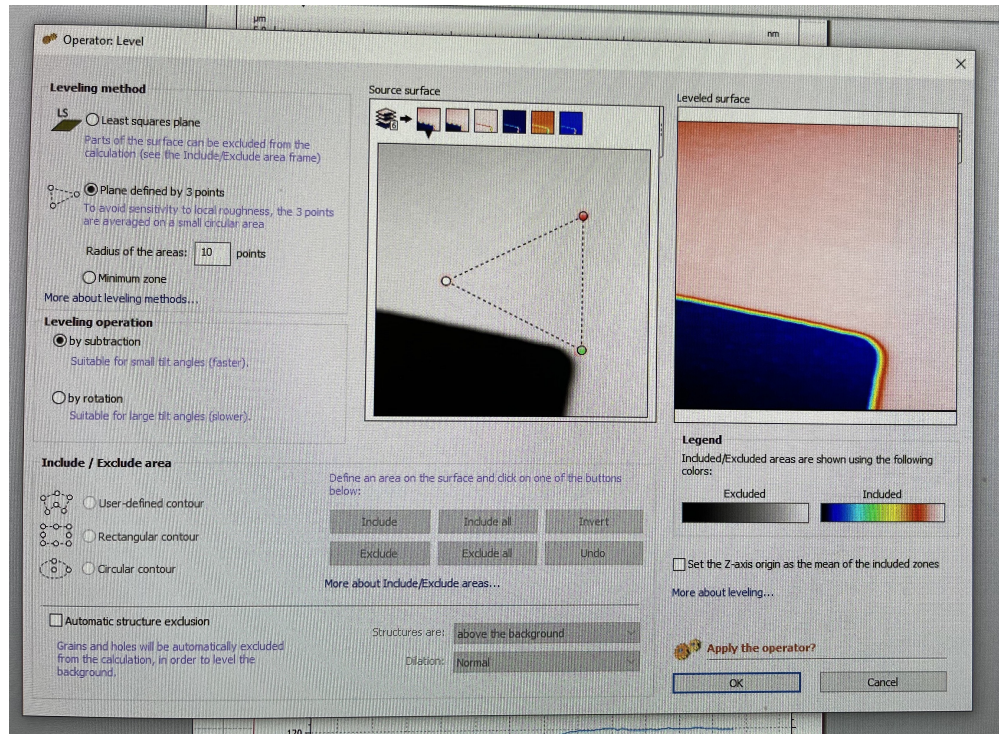


Figure 3.13: A raw AFM image (grey) must be leveled in order to acquire accurate height information. This is done in the Tosca Analysis software by defining a 3-point plane on the image which encompasses an area known to be of equal height. The leveled image is shown in color.

AFM tips are stored in a manufacturer-supplied gel pack where they are individually labeled by a number (1-20). To track the amount of times a given tip has been used, a user adds a tally mark to the usage record which is logged directly on the cover of the gel pack. From personal experience, the quality of an AFM tip begins to degrade around the five tally mark. Indications of a shoddy AFM tip— aside from direct impact by lowering it too rapidly into the sample— include the inability to find its resonance frequency or image artifacts.

Artifacts, or features that appear in the AFM image but are not present in the actual probed sample, fall into two main categories. The most common AFM artifacts arise from the probe itself. Since the AFM image is a convolution of the probe and the sample, the health of the probe directly impacts the data quality. Ideally the probe tip diameter should be smaller than the required resolution [2]. The tip must also be isotropic and sharp, otherwise imaged

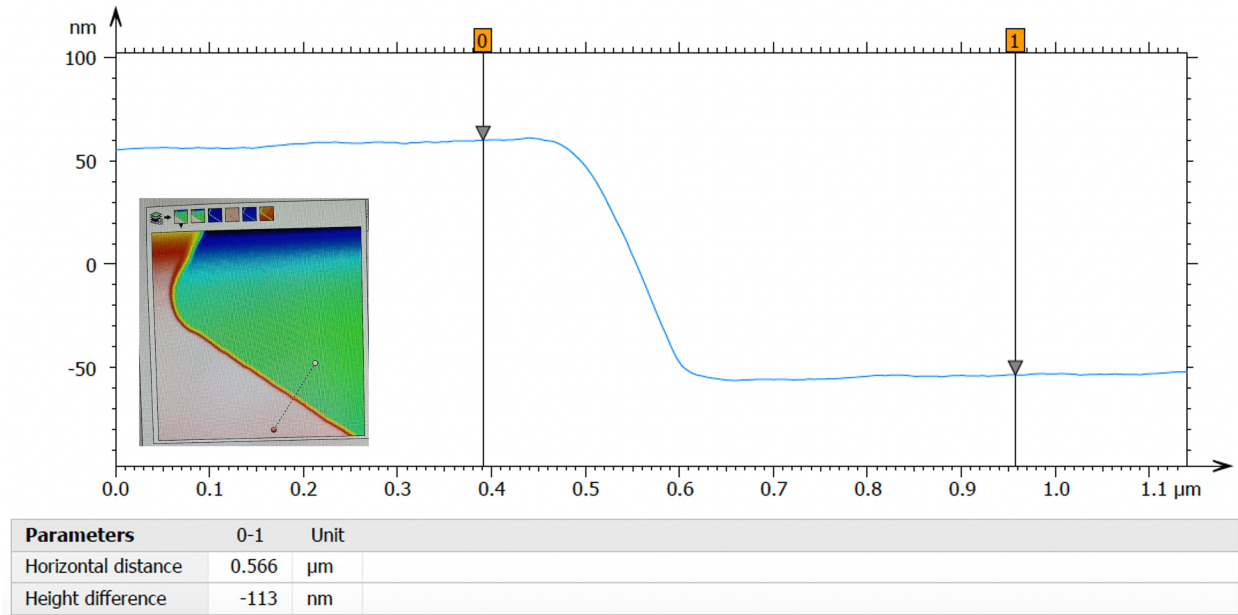


Figure 3.14: A line drawn across a leveled AFM height image (inset) yields a step profile from which feature height can be deduced.

features by that probe can appear artificially smaller or larger. Distortions in the shape of an imaged object or unusual repetitive patterns are signs of probe contamination, which can occur from something as small as a small piece of dust. These issues are generally worse, and appear with greater frequency, for scans in the x - y plane of the sample versus the z (or height) direction. The second artifact category that gives rise to noise in AFM images is vibration. Vibrational artifacts, which can also be acoustic, usually appear as random lines or streaks across the image. The AFM sits atop a vibration isolation table to directly combat this issue but it is far from perfect. Data should always be collected with the lab door closed and extraneous equipment or noise sources removed from the measurement area.

3.2.2 X-Ray Diffraction (XRD)

A *crystalline solid* is a material whose atoms are ordered in a regularly repeating array to form a crystal lattice that extends in all directions throughout the solid. When X-ray

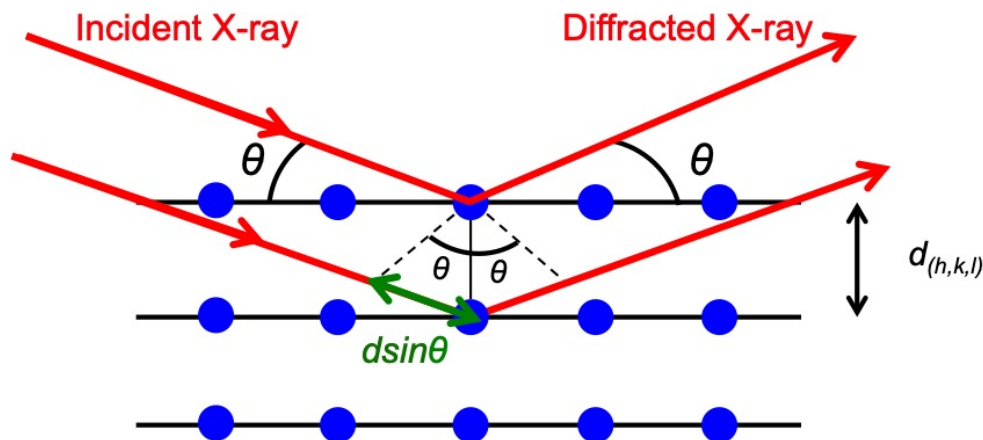


Figure 3.15: X-ray radiation of wavelength λ is scattered by two different atoms of a crystalline solid. The lower incident beam must travel an extra length of $2d \sin(\theta)$ compared to the top beam. When this length is equal to an integer multiple of λ , the two scattered waves constructively interfere.

radiation passes through a crystalline solid, the rays become scattered by these atoms. The pattern generated by the diffracted X-rays reveals information about the crystal such as its lattice parameters, structural order, and crystallographic orientation. X-ray reflectivity can also be used to measure thin film thickness, roughness, and density. The physics behind XRD is governed by Bragg's law (Fig. 3.15). As an X-ray strikes an atom, a set of waves are produced via elastic scattering. Since the scattering sites in this case are regularly spaced atoms, the resulting set of waves are also regularly spaced. Constructive interference between these waves occurs when Bragg's Law

$$2d \sin \theta = n\lambda \quad (3.2)$$

is satisfied, where d is the spacing between lattice planes (hkl), λ is the wavelength of the incident radiation, θ is the incident angle, and n is a positive integer.

The following subsections explain the various XRD measurement geometries in further detail. All XRD measurements performed in this thesis were done with a Cu $K\alpha$ radiation source ($\lambda=1.5405 \text{ \AA}$) using the Smartlab X-Ray Diffractometer located at IMRI. In all measurements

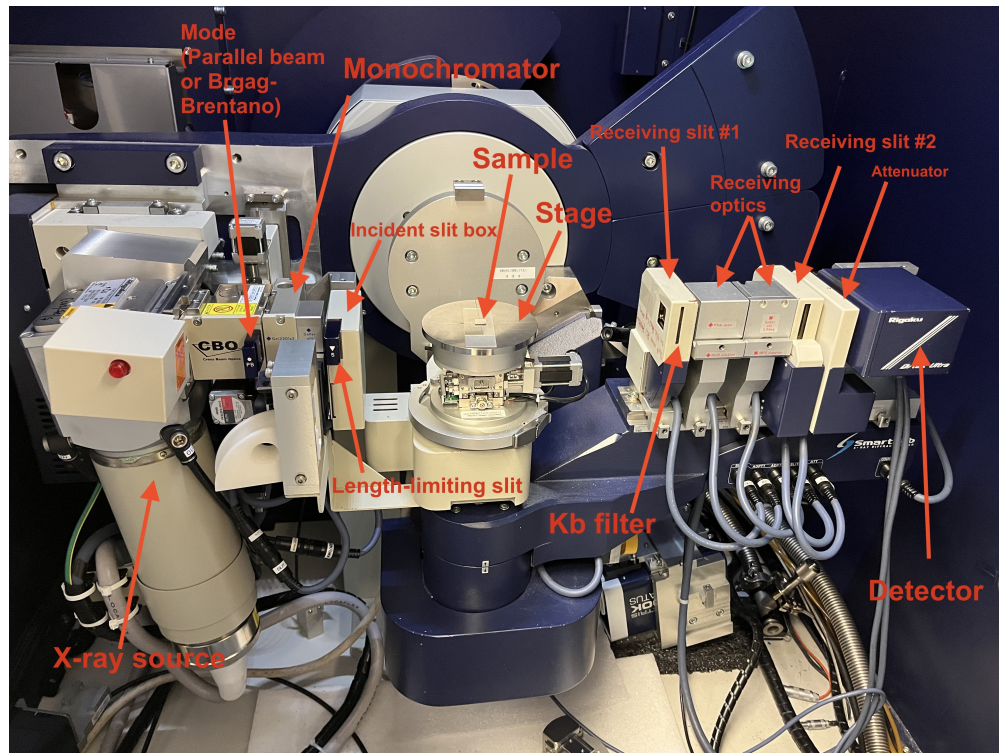


Figure 3.16: Rigaku Smartlab goniometer. Optical alignment for any measurement is automated through the Rigaku software.

a filter was used to minimize $K\beta$ X-ray emission. For 2θ scans, a Ge(220)-x2 monochromator was used to obtain high resolution data and reduce the beam divergence.

2θ - ω Measurement

The 2θ - ω measurement geometry (sometimes referred to as 2θ or θ - 2θ) is commonly used to identify the crystalline phase of thin films. The measurement is carried out by uniformly moving an incident X-ray source and scintillation detector through various angles with respect to the plane of the sample. The result is a plot of intensity versus angle 2θ , where the various peaks correspond to values of 2θ for which Bragg scattering from a particular lattice plane (hkl) is satisfied in accordance with Equation 3.2.

Diffraction from specific crystallographic planes can be understood in terms of a diffraction

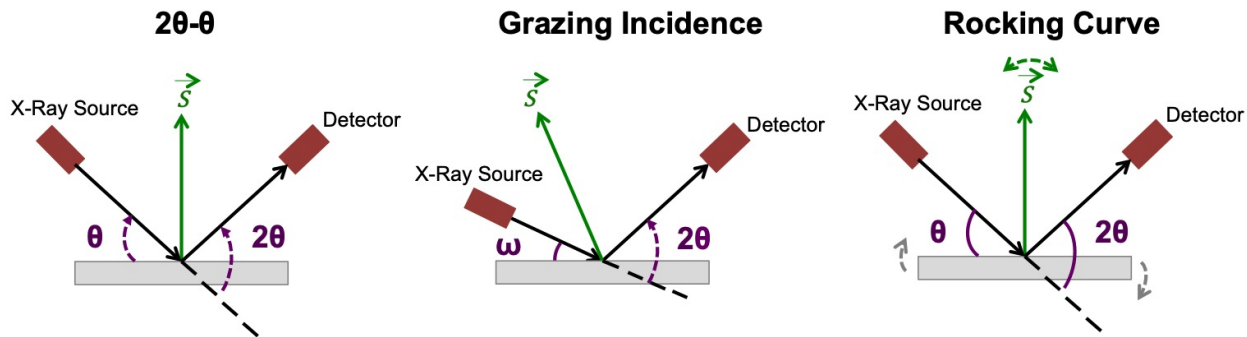


Figure 3.17: Common XRD measurements and their geometries. In $2\theta-\omega$, the diffraction vector \vec{S} is fixed and only crystal planes parallel to the sample surface are probed. In GIXRD, \vec{S} continually changes direction and planes that are tilted with respect to the sample surface are probed. In rocking curves, \vec{S} is finely rocked about a fixed position to study diffraction from a single plane.

vector \vec{S} that bisects the angle between the incident and diffracted X-ray (Figure 3.17). When \vec{S} is parallel to the normal direction of a particular plane (hkl), a diffraction peak is produced. If \vec{S} and the normal of (hkl) are not parallel, no diffraction occurs. In the $2\theta-\omega$ setup, the diffraction vector is always perpendicular to the sample plane and only crystal planes parallel to the sample surface will be detected. Although the incident X-ray beam probes deeply into the sample during this measurement, it can also produce a large signal from the highly crystalline and much thicker substrate which can overshadow peaks from the film of interest. For this reason, grazing incidence data is typically collected in conjunction with $2\theta-\omega$.

For $2\theta-\omega$ scans of amorphous or polycrystalline thin films, a user trained on the Smartlab diffractometer should be able to execute the measurement by selecting General (medium resolution PB) in the Rigaku software (Figure 3.18) and following the automated optical alignment prompts. In the final step of the work flow, the user will be brought to the screen shown in Figure 3.19 and asked to define the scan parameters. The range of 2θ angles over which to scan should be chosen based on the known 2θ peaks of the materials within the sample. This information can be found by consulting the Inorganic Crystal Structure Database (ICSD) on the Smartlab desktop. Based on the size of the scan range, the scan

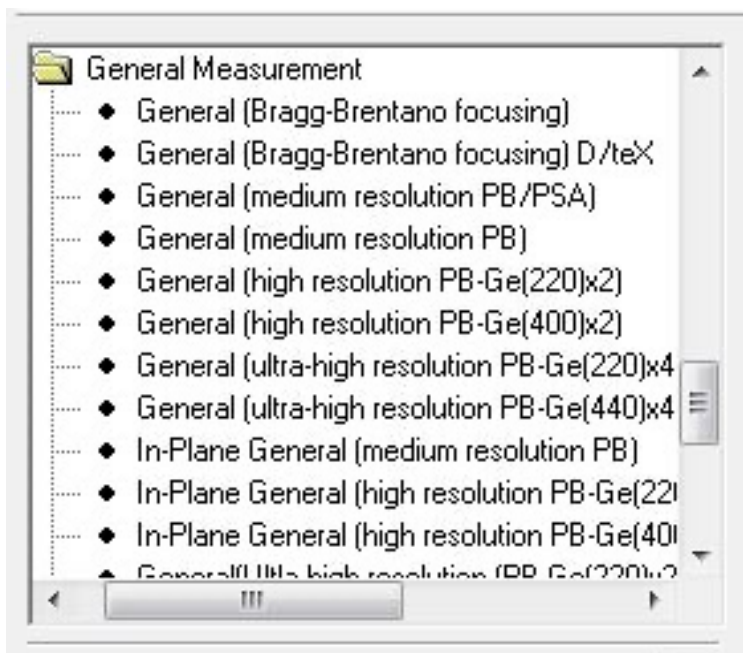


Figure 3.18: Measurement packages available in the Rigaku software.

speed should be adjusted to the desired measurement duration. A one hour scan is usually sufficient to get cursory information about the sample.

For 2θ - ω scans of epitaxial or single-crystal thin films, special care must be taken to align the optics to the diffraction peak of the substrate such that the 2θ - ω scan of the film is made relative to this substrate peak. Firstly, insert the Ge(220)x2 monochromator into the diffractometer then select Rocking Curve/Reciprocal Space Mapping (high resolution PB-Ge(220)x2) under the list of measurement packages (see IMRI staff for monochromator access). Follow the workflow shown in Figure 3.20 up to the Rocking Curve Pre-Measurement step. In the rocking curve pre-measurement dialogue box, set all parameters identically to Figure 3.20 with the exception of 2θ and ω . The 2θ angle must be set to the 2θ angle of the substrate peak based on its crystal orientation (e.g., (100), (110), (101), etc.). This angle is usually given directly by the substrate manufacturer or can be found in the ICSD if the crystal orientation of the substrate is known. Change ω to be exactly one half of 2θ then execute the pre-measurement step. When the pre-measurement step is complete, select the General (high resolution PB-Ge(220)x2) measurement package and skip directly to General

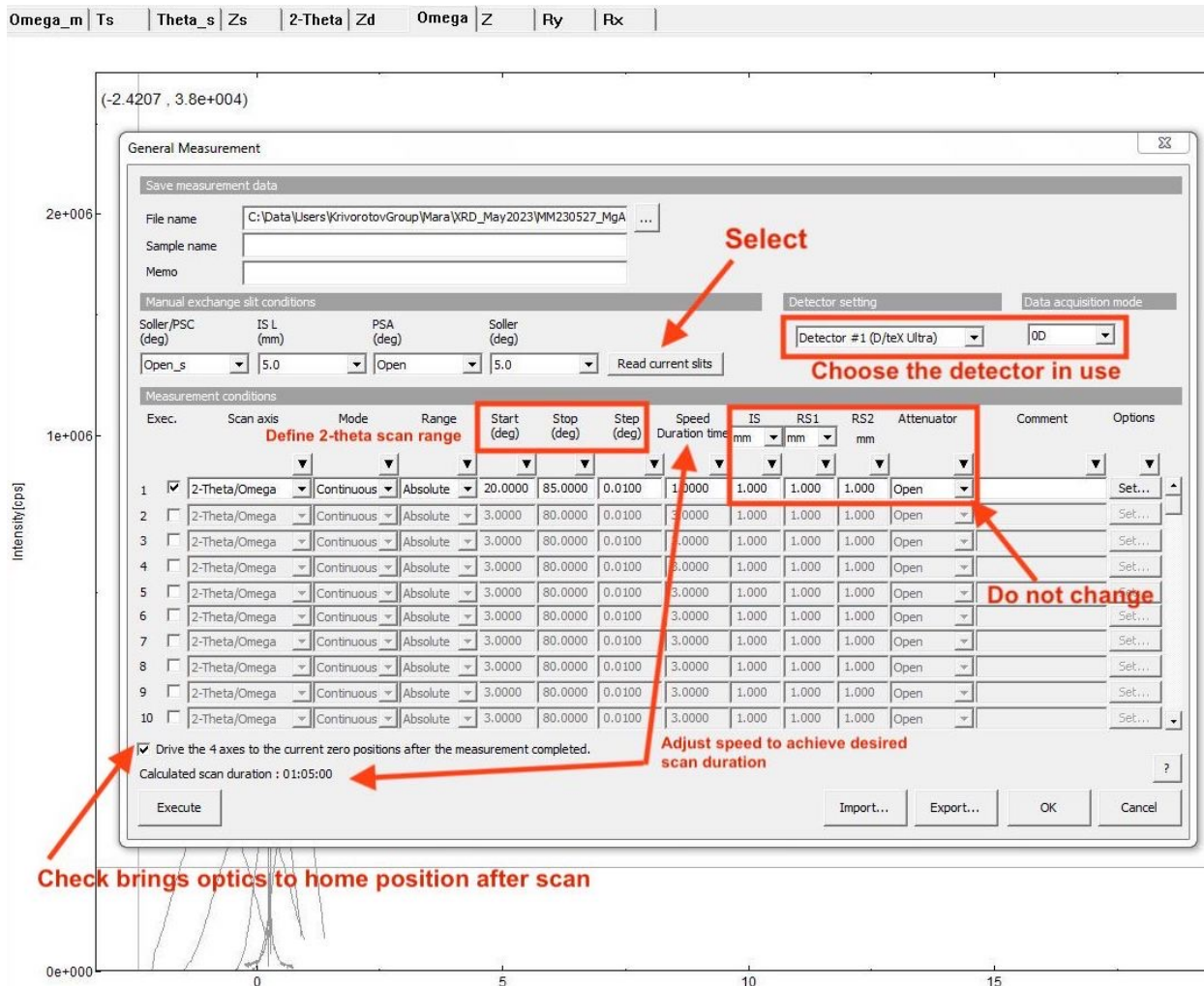


Figure 3.19: Dialogue box for setting 2θ - ω measurement conditions. If using a scintillation detector, select data acquisition mode 1D.

Measurement on the workflow. The substrate alignment step will be saved so the user may enter the parameters of their scan and execute the measurement (Figure 3.19).

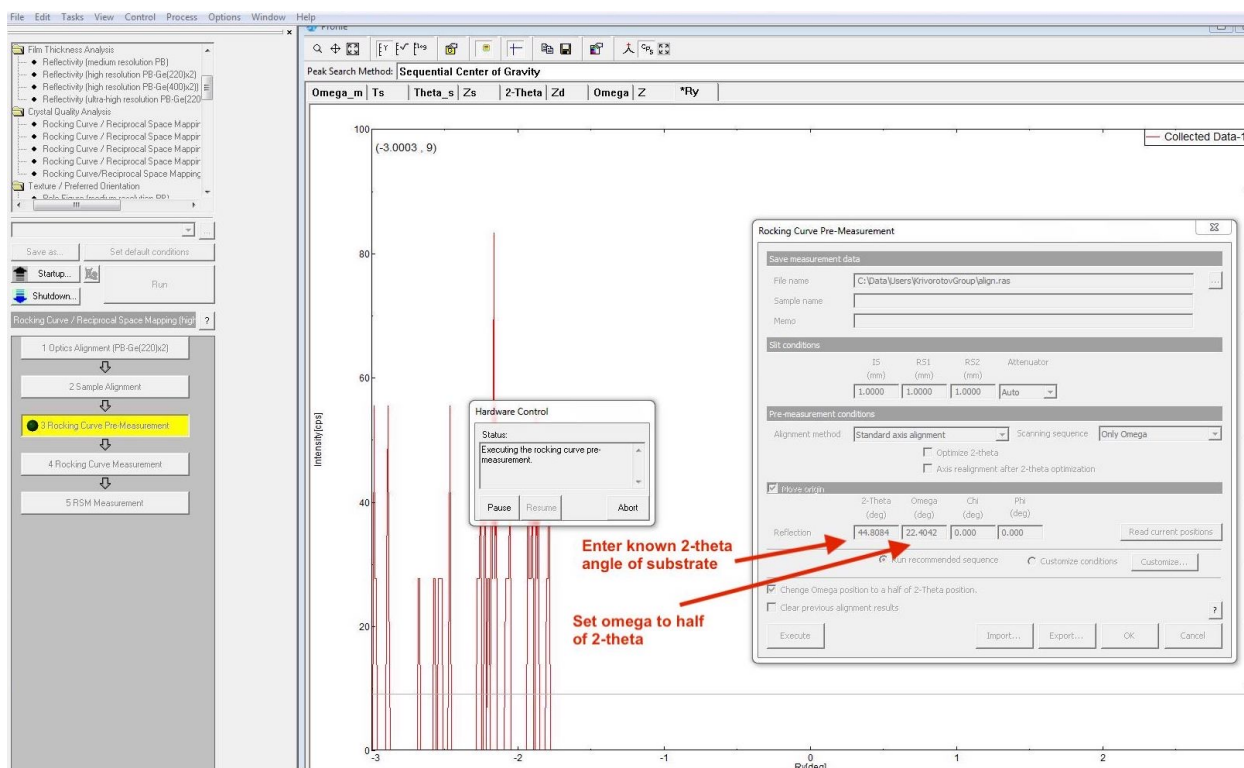


Figure 3.20: To align the goniometer to the known 2θ value of a crystalline substrate, follow the rocking curve measurement workflow in the Rigaku software from steps 1 through 3.

Grazing Incidence Measurement (GIXRD)

This measurement geometry keeps the incident angle of the X-ray source fixed at a shallow angle ($\theta < 1^\circ$) and moves only the detector arm such that the contribution from the substrate is minimized. Because the direction of the diffraction vector \vec{S} changes throughout the scan, only the crystal planes that are inclined with respect to the surface of the sample are probed. This makes GIXRD unsuitable for identifying orientation in thin films but useful for confirmation of perfect crystallinity or epitaxy. A perfect crystal with all crystal planes sitting parallel to the sample surface should return a GIXRD spectrum with no peaks.

Rocking Curve (ω) Measurement

A rocking curve (ω scan) is a method for studying perfection in thin films. The X-ray source and detector are fixed at a specific angle that satisfies the Bragg condition for diffraction from a particular crystallographic plane of interest. The sample is then gently rocked about the angle ω in a series of fine steps while the detector records the intensity of the diffracting beam. The resulting plot of intensity versus ω yields a single, sharp peak corresponding to the crystal plane being scanned and is generally fit to a linear combination of a Gaussian $G(x)$ and a Lorentzian $L(x)$ curve

$$V(x) = \eta G(x) + (1 - \eta)L(x) \quad (3.3)$$

which is weighted by a parameter η between 0 and 1. Analysis of the peak provides information about mosaicity, strain, and dislocations. Rocking curves of highly crystalline films typically have full-width-at-half-maximums $\ll 1^\circ$ after instrumental broadening effects are accounted for.

X-Ray Reflectivity Measurement (XRR)

Thickness, surface roughness, interface roughness, and density of single and multilayer thin films can all be experimentally determined through an X-ray reflectivity (XRR) measurement. This technique reflects X-rays off of the sample surface at shallow incident angles while a detector records the intensity of reflected X-rays at an angle equal to the incident angle. As the arms move in unison through a small range of angles (about 0 - 12°), internal reflection will occur at some critical angle in accordance with the laws of Fresnel reflectivity. If the interface between substrate and film (or between films in a multilayer) is not perfectly smooth, reflected X-rays will constructively or destructively interfere and create oscillations in the intensity versus 2θ curve. Fitting of the resulting XRR profile yields

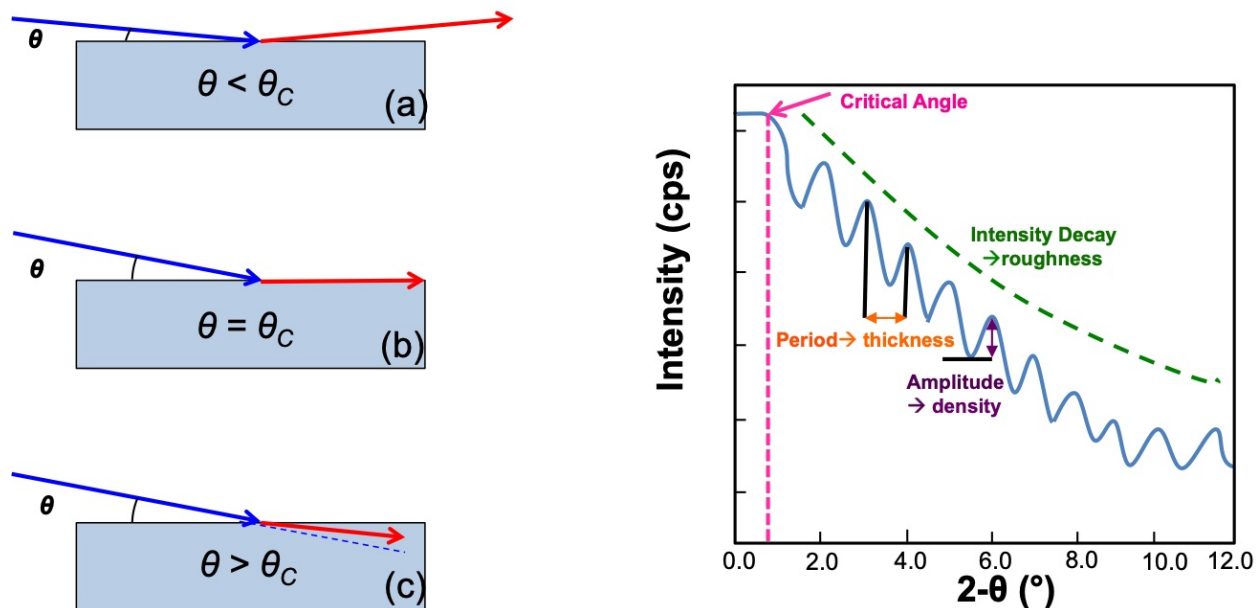


Figure 3.21: Behavior of an incident X-ray for various incident angles (left) and an example of an XRR profile (right). In (a), an incident X-ray (blue) is completely reflected (red) from the sample surface and does not penetrate into the film; in (b), the incident X-ray propagates along the sample surface at a critical incident angle θ_C ; in (c), incident X-rays refract into the sample when $\theta > \theta_C$.

valuable information about the material parameters of the films.

Experimental reflectivity data may be analyzed in the software GlobalFit. Data in the form of a .ras file should first be loaded into GlobalFit under Load Measured Data (Fig. 3.22). Next a layer structure should be defined to account for every layer in the sample. In the Create Layer Structure workflow, choose Edit Layers to add layers one by one (the substrate should always be layer zero). For each layer, load in the density of the material by choosing (...) next to Material Database and performing a search. Under Structure Parameters, set thickness to the expected value, roughness to 0.5 nm, but do not adjust density. Check the Refine box to allow a parameter to be adjusted during the fitting procedure—do not allow density to be refined yet. Under the Common tab, enable background refinement. Select GlobalFit to perform a least-squares fit to the reflectivity profile. When a rough fit has been found, choose Refine under the workflow to improve the fit further. Here one may now choose to allow density to be refined. An acceptable fit should have a chi-squared value

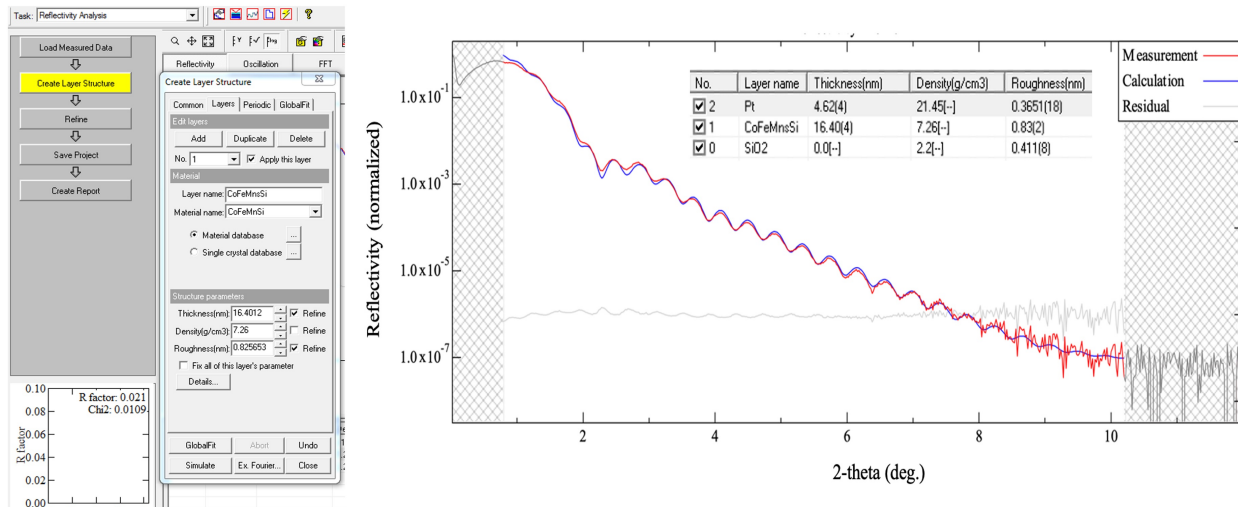


Figure 3.22: GlobalFit software (left) and an example XRR fit with best fit parameters (right).

around 0.02 or lower. Although GlobalFit may find a best fit, it is important to verify that the parameters it returns are sensible. For instance, the roughness of a layer should not be greater than the thickness of the layer itself, and density values should not be wildly different from expectation.

3.3 Lithography Techniques

3.3.1 Electron Beam Lithography (EBL)

Electron beam lithography (EBL) is a widely used fabrication tool for defining nano- and micron-scale structures. A sample coated with an electron beam sensitive resist and placed under the vacuum of a scanning electron microscope (SEM) with EBL capability is selectively exposed to an electron beam that has been programmed to draw out a particular design. Only places along the chip where the beam has traversed have been exposed. When the sample is removed from the SEM, it appears unchanged until it has undergone a development process which is typically done chemically. If a negative tone resist was used, areas that were

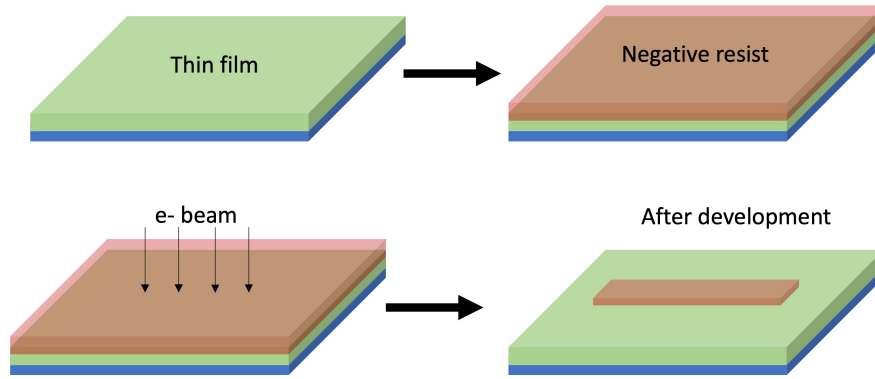


Figure 3.23: A resist mask fabricated with negative tone electron-beam resist.

Resist	Tone	Dosage ($\mu\text{m}/\text{cm}^2$)	Spincoat
MAN-2401	Negative	200-400	3500 RPM, 45 sec
PMMA	Positive	250-500	4500 RPM, 45 sec
PMMA	Negative	30,000-50,000	4000 RPM, 45 sec
MMA/PMMA	Positive	250-500	4500 RPM, 45 sec
MMA	Positive	200-500	3500 RPM, 45 sec
HSQ	Negative	2000-6000	4000 RPM, 45 sec

Table 3.2: Electron beam resist options (MAN-2401 doubles as a photoresist).

exposed to the beam will remain after development. If a positive tone resist was used, areas that were exposed to the beam will vanish after development. The resulting resist mask is then utilized in subsequent deposition or etching steps for patterning devices. The choice of negative or positive tone resist will therefore depend upon the nature of the fabrication step being performed. Some common resists and their typical dosages are listed in Table 3.2.

Laurell Spin Coater Operation

Any EBL step requires spreading resist onto the sample which is accomplished using the Laurell Technologies WS-650MZ-23NPP spin coater in the Krivorotov group fume hood.

- Sign in on the logbook
- Open the right-most nitrogen cylinder next to the soldering station and verify its output

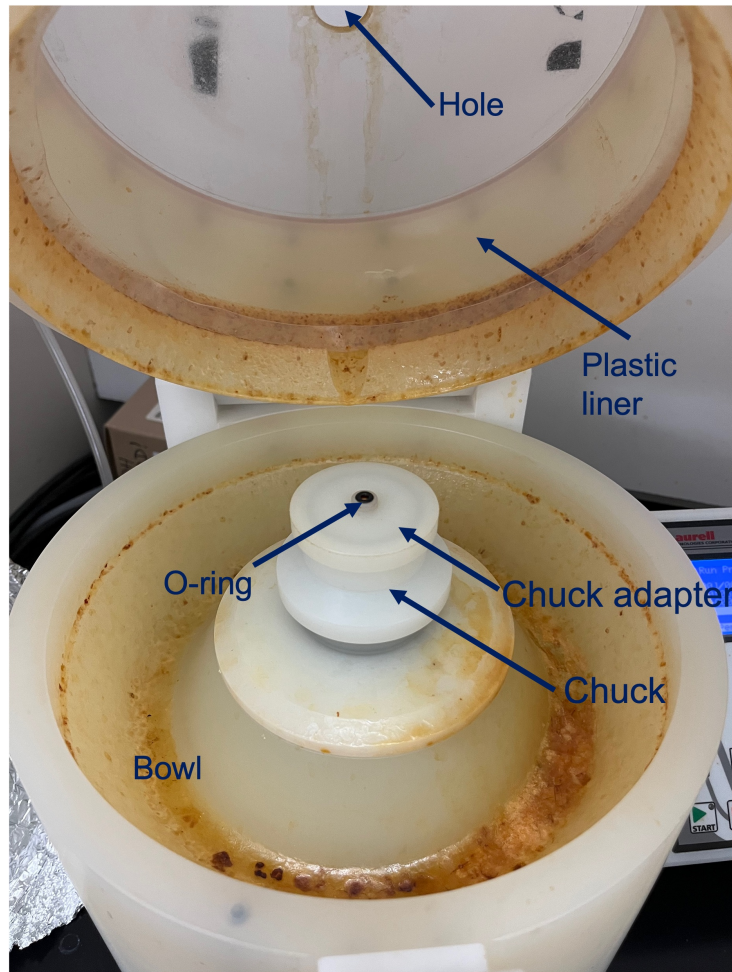


Figure 3.24: The spin coater has clearly seen a long life. It is critical to follow the cleaning protocol to avoid further degradation.

pressure is 60 psi

- On the left side of the spinner are two clear, plastic tubes– open the black valve on each (Fig. 3.25)
- The spin coater display should change from Need CDA to Need Vacuum
- Hit Select Process on the keypad and use the arrow keys to navigate to a desired process
- Select a process by hitting Run Mode (this will not automatically start the program yet)



Figure 3.25: Black valves for controlling vacuum level (left) and keypad controls (right).

- If creating a new process:
 - Choose Edit Mode on the display
 - Use the arrow keys to select a field then tab to edit (the editable field should now be blinking)
 - Use the up/down arrows to change values and left/right keys to change digits
 - To create a multi-step process, choose the Steps field and edit as desired (use the FWD and REV keys to toggle between steps)
 - Press Run Mode when finished
- Remove the aluminum foil from the top of the spinner
- Depress the white clamp on the front of the coater to open its lid
- Place the sample centrally on the O-ring of the wafer chuck and close the lid
- Press Vacuum on the keypad (the Vac reading will be ≥ 15 and say "Ready" – if Vac is < 15 make sure the nitrogen tank is at 60 psi)

- Take a plastic pipette from the box at the back of the fume hood
- Compress the pipette and blow the tip with nitrogen (do not release compression)
- Keeping the tip compressed, bring the pipette into the resist bottle without touching the sides
- Release compression slightly to draw a small amount of resist into the pipette
- Release 2-3 drops of resist onto the sample—enough to cover its surface—through the circular hole on the spin coater lid
- Press Start
- Do not open the spinner until it is stopped and Time on the display reads zero
- Press Vacuum on the keypad, open the lid, and retrieve the sample
- Close the black valves
- With a Beta-wipe and IPA, clean the process bowl (do not use acetone!)
- Remove the wafer adapter on top of the chuck
- Clean the top of the wafer chuck and bottom of the adapter with an Alpha-wipe and a small amount of IPA (do not use acetone!)
- Clean the lid liner with an Alpha-wipe and a small amount of IPA (do not use acetone!)
- Close the lid and put the aluminum foil back on the spinner lid
- Throw away used pipette
- Close the nitrogen tank
- Sign out on the logbook

Magellan EBL Operation (Overview)

The EBL writing process using the FEI Magellan 400 SEM located at IMRI is run through the control software Nabity Pattern Generation System (NPGS). Users can familiarize themselves with NPGS in the Krivorotov lab office where it is also installed on one of the desktops. While not exhaustive, the outline below serves as a guide to beginners on the operational basics of EBL with the Magellan assuming they have been trained on the SEM. Nanofabrication requiring multi-step alignment procedures will be detailed in future chapters.

The first part of any writing process is the setup of the electron beam. The working conditions for EBL require a 30 kV beam voltage and 7 mm working distance, but the choice of beam current is a free parameter that should be selected based on the dimensions of the feature to be written. Large beam currents are generally used to write large features. When nanoscale features are needed, smaller beam currents are best. The user must be able to make a decently focused image of their sample, by adjustment of the microscope focus, stigmator, and lens alignment, at every beam current with which they plan to write their pattern. Before beginning, the user should always measure the beam currents with a Faraday cup since they are known to deviate from expectation.

Starting

- Enable the SEM reservation and log into the SEM computer
- Re-start the separate EBL computer but do not log back in yet
- Mount the sample on an SEM stub with copper clips
- Scratch at least 3 corners of the chip using a diamond scribe— this will assist in focusing later
- Screw the SEM stub into the quick-loader stub

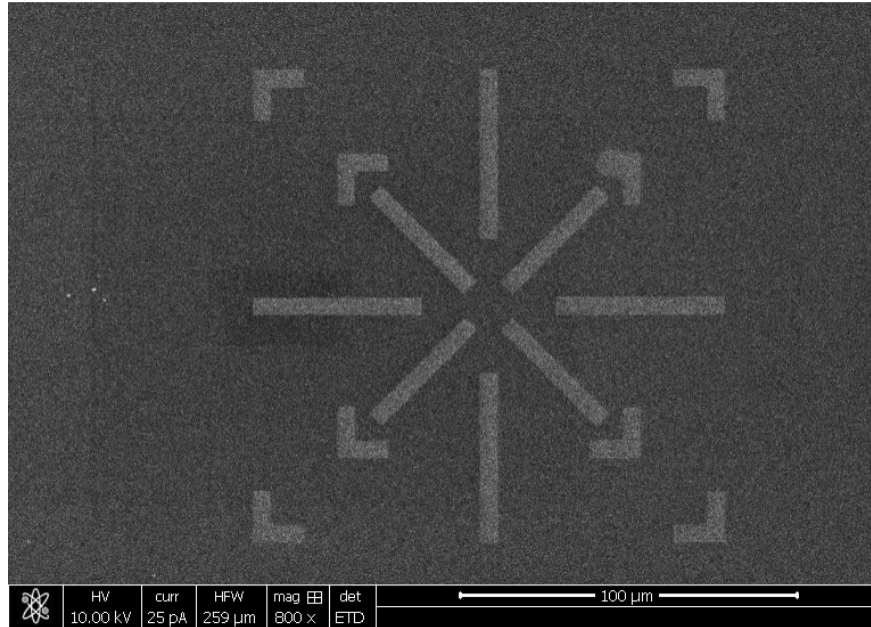


Figure 3.26: SEM image of a global alignment mark made with PMMA resist. Large features such as these should be written with a large beam current (6.4 nA) which reduces write time.

- Press V on the SEM quick-loader to vent the sample loading space
- Open the quick-loader lid and release the loader arm from position 2 to position 1
- Mount the quick-loader stub onto the spring-loaded arm and return the loader arm to position 2
- Close the quick-loader lid
- Press P on SEM to move the internal stage to the loading position
- When the bottom half of the SEM icon– located in the bottom right of the SEM GUI–turns yellow, open the quick-loader door
- Follow the position sequence labeled on the loader arm to transfer the sample into the SEM, watching in real-time via the SEM camera
- Retract the arm following the position numbers labeled on the loader arm

- Close the quick-loader door
- In the SEM GUI go to Stage→ Take Nav-Cam Photo to take a CCD picture of the sample for navigation

Beam Setup

- Move to the top left corner of the sample by double-clicking the corner of the Nav-Cam image
- Set the beam voltage to 30 kV and beam current to the smallest value to be used in the write
- Turn on the beam
- Roughly focus on the corner where you have scratched
- Now log into the EBL computer and follow the prompts for the auto-beam alignment procedure (a set of horizontal stripes should raster down the SEM viewing panel during this time)
- When the procedure finishes open NPGS on the EBL computer
- On the SEM computer, re-focus on the scratch and link the Z-height
- Set the Z-height to 7 mm (good practice is to keep finger over ESC key when adjusting Z-height to abort if the stage somehow gets too close to the SEM pole piece)
- Go to Direct Adjustments and check that the crossover for every beam current being used is centered → return to the lowest beam current when finished
- Move to the top left corner of the chip and store this position (1) then move to the adjacent corner and store this position (2)

- Return to position (1)
- Go to Stage→ XT-Align Feature→place the first point at (1)→ move to (2)→ place the second point at (2) (this aligns the chip along the (1)-(2) direction)
- Return to the top left corner of the chip and focus on the scratch → it is only necessary to focus on something that is close to the size of the feature that is going to be written at that current
- Periodically link the Z-height during focusing, which must be maintained at 7 mm
- Go to Direct Adjustments and adjust the stigmatism and lens modulation as well (if adjusted, you may need to re-focus after)
- When the beam is focused at all beam currents and working distance is 7 mm, return to the lowest beam current
- Go to Stage → Unlink Z-Height
- Choose Direct Stage Control in NPGS→ press enter twice to collect new data → press Space bar to acquire the first data point → move to the next corner of the chip and focus on the scratch (*Only* adjust the focus during this process)→ press Space bar to acquire point two → move to the third corner and focus on the scratch→ press Space bar to acquire point three → press Enter twice then Esc to quit→
- Return back to the top left corner of the sample
- In the NPGS software, select NPGS Mode → the SEM window should say External and the light on the top of the SEM should turn from green to yellow

Writing

- Open your .dc2 pattern (made in LayoutEditor) using the DesignCad software on the EBL desktop

- Select a feature from layer 1 of the pattern then choose the Information icon
- Ensure that the layer mode is set to Dashed (repeat the same check for all layers in the .dc2 file)
- Save any changes then exit DesignCad
- From inside your NPGS project folder, right-click your .dc2 file
- Choose Run File Editor which opens the window shown in Figure 3.27 and set the conditions listed in Table 3.3

Parameter	Setting
Non-Stop Writing Mode	Yes
Allow Advanced Modes	Yes
Disable X-Y Focus Mode	No
Disable Automated Stage Control	No
Disable Digital SEM Control	No
Enable Global Rotation Correction	No

Table 3.3: Run File Entity settings.

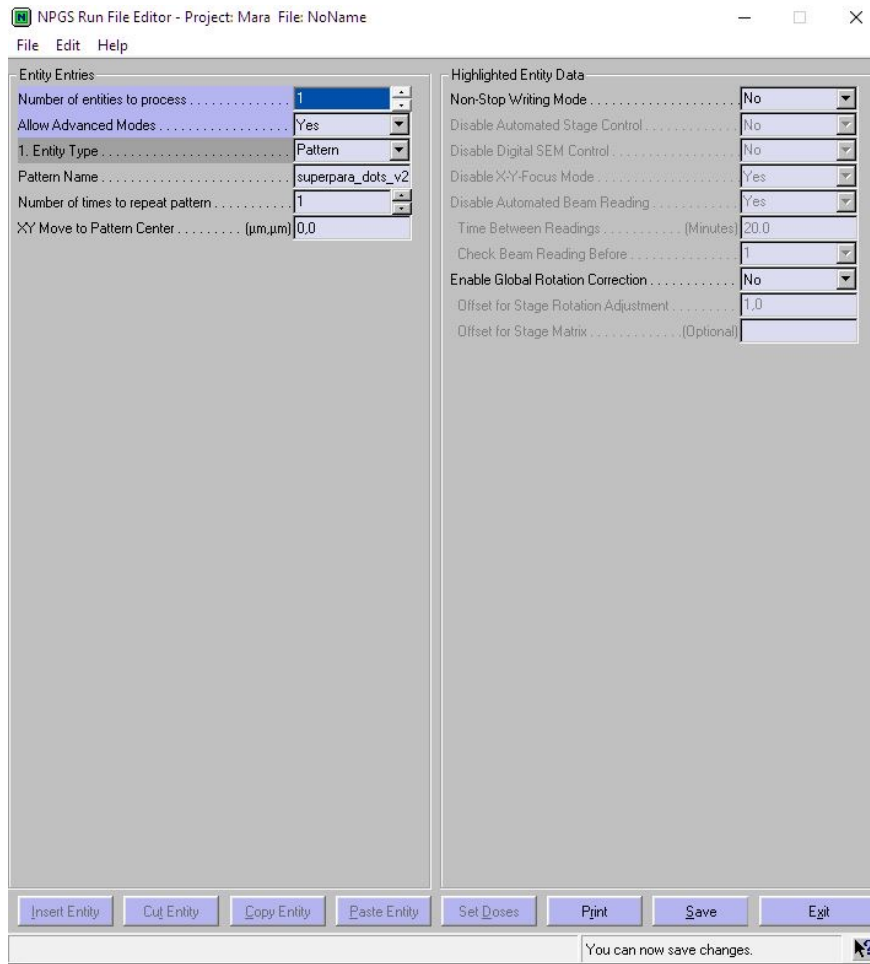


Figure 3.27: Modify the parameters under Highlighted Entry Data according to Table 3.3

- Highlight the section Entity Type
- Specify the writing conditions for each layer in the write pattern (Table 3.4)

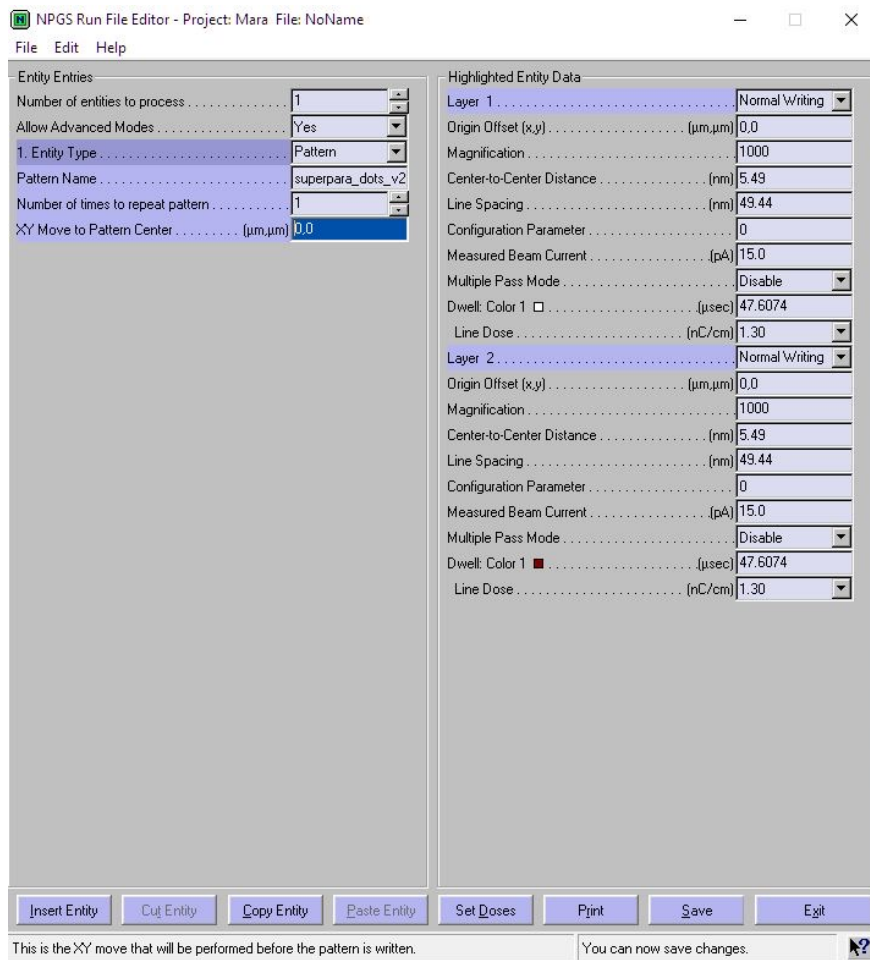


Figure 3.28: Entity type can be set to Pattern (singular) or Array.

- Save the run file as a .RF6
- From the SEM GUI, move the sample stage to the desired writing location
- From NPGS, run the .RF6 file

Ending

- Navigate back to one of the sample corners
- In NPGS, select SEM Mode
- Roughly focus on something and then link the Z-height to ensure it is FWD

Parameter	Setting
Origin Offset (x,y)	0,0
Magnification	Maximum
Center-to-Center Distance	Pattern dependent (5-50 nm typical)
Line Spacing	Center-to-Center Distance
Configuration Parameter	See caption
Measured Beam Current	Faraday cup value
Multiple Pass Mode	No
Area Dose	Resist dependent
Dwell	Auto-fills based on Area Dose

Table 3.4: Center-to-center distance and line spacing dictate the space between points in the electron beam. Smaller spacing improves resolution but increases write time. The configuration parameter, in parentheses, specifies the beam current: 1.6 pA(-9), 3.2 pA(-8), 6.4 pA(-7), 13 pA(-6), 25 pA(-5), 50 pA(-4), 100 pA(-3), 200 pA(-2), 400 pA(-1), 800 pA(0), 1600 pA(1), 3200 pA(2), 6400 pA(3).

- Turn off the beam

- Lower the Z-height to 9 mm

- Press P on the SEM quick-loader

- When the SEM icon on the GUI turns yellow in the lower half, open the quick-loader door

- Follow the position numbers labeled on the loader arm to remove the sample, watching in real-time with the SEM camera

- Close the quick-loader door

- Press V to vent the quick-loader and retrieve the sample

- Log out of IMRI reservation and the SEM computer

3.3.2 Photolithography

Photolithography is a UV-based lithography technique for fabricating devices of micrometer size. It is a faster and cheaper alternative to EBL best suited for applications where nanoscale features are not required. All photolithography performed in this thesis was accomplished with the Karl Suss MA6 mask aligner located in the INRF cleanroom.

Karl Suss MA6 Mask Aligner Operation

Using MA6 is made simpler when one first understands its general operation. Once the photomask is inserted into the aligner the mask will remain stationary and only the position of the wafer with respect to the photomask can be changed using the X, Y, and rotation control knobs on the sides of the tool (Fig. 3.29). Two microscopes (left and right) connected to a split-screen television monitor are used for viewing— their focus and separation may be changed using the coarse focus knob on the very top of the aligner and the objective knobs on the respective microscopes. After accurately positioning the wafer into the alignment marks on the photomask, the sample is exposed to a flood of UV light from a mercury lamp and then taken out to be developed.

Because MA6 is intended for 4 inch wafers, a 10 x 10 mm chip should be mounted onto a 4 inch dummy wafer using a small amount of vacuum grease as shown in Figure 3.30. The chip should be placed as close to the center of the wafer as possible for easiest alignment.

- Power on MA6 and the television monitor and wait until "Ready for Load..." message appears (Fig. 3.32)
- Use the arrow keys to toggle to TSA mode
- Use the Edit Parameter key to set: alignment gap = 25 microns, exposure mode =

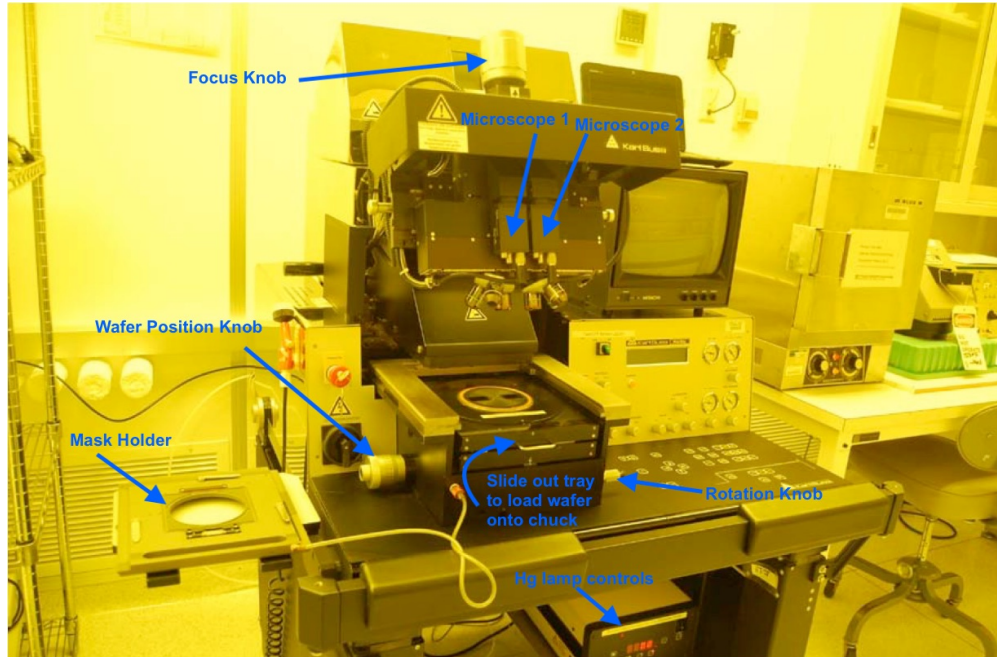


Figure 3.29: Full layout of MA6.

Soft, wedge error correction (WEC) = Cont, and exposure time = 30 seconds

- Select Channel 2 on the Hg lamp (10 mW/cm² and 365 nm wavelength)
- Select Change Mask key
- Place the photomask onto the mask holder against the stop pins (chrome/orange side of mask facing up towards user)
- Select Enter to toggle the mask vacuum on
- Flip the mask holder over (orange side now face down), slide it into MA6, and press Change Mask key again
- Select Load key and wait until “Pull slide and load substrate onto chuck” message appears
- Pull out the slide, place the dummy wafer (with mounted chip) onto the wafer chuck, and slide back in

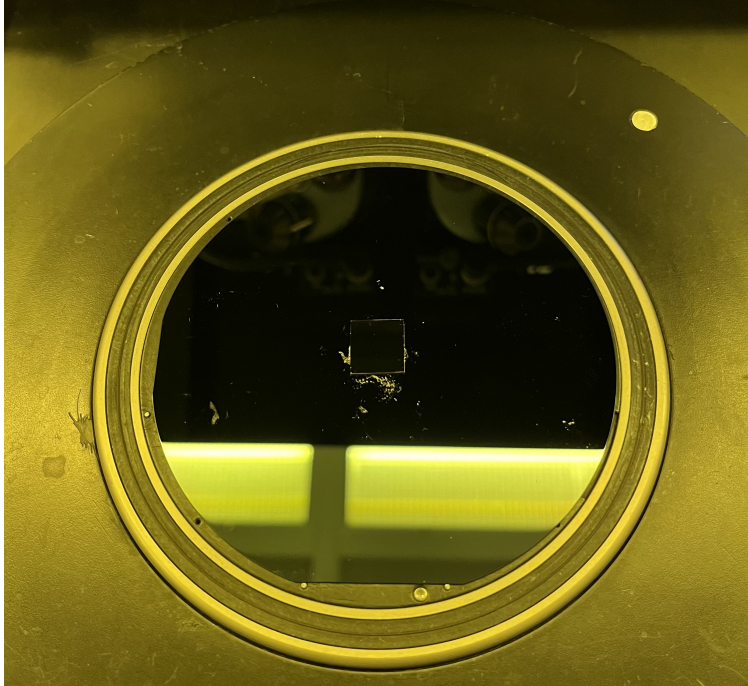


Figure 3.30: Because MA6 is intended for 4 inch wafers, smaller samples should be mounted to a dummy wafer with vacuum grease.

- Select Enter key and wait until the microscope lowers (press F1 if it does not do so automatically)
- Make sure that the BSA Microscope key is disabled
- Adjust the microscope focus knob (top) until both the photomask and chip come into view on the monitor
- Use the X, Y, and rotation knobs to align the four corners of the chip into the center of the L-shaped alignment marks on the mask
- Select the Exposure key when ready
- Once prompted, slide out the wafer chuck and remove the sample
- Select Change Mask key and take out the mask holder
- Select Enter to toggle the mask vacuum off and remove it from pins



Figure 3.31: MA6 control panel.

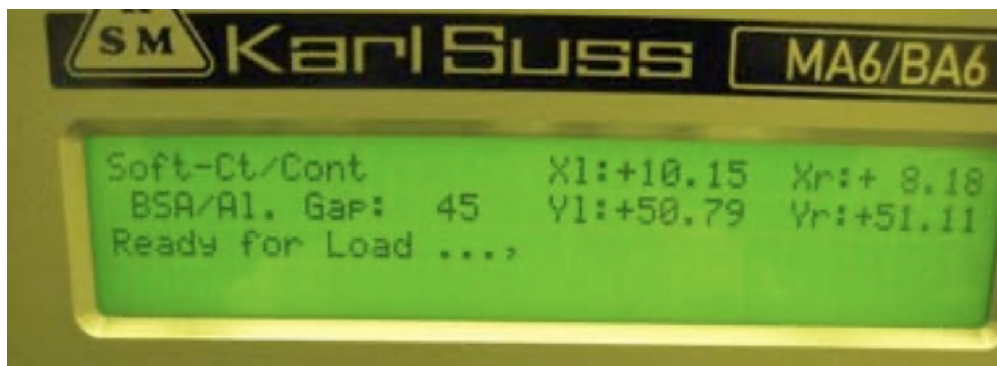


Figure 3.32: "Ready for Load" message on MA6 screen.

- Power off MA6 and monitor

3.4 Magnetic Characterization

3.4.1 Anomalous Hall Effect

In 1879, Edwin Hall placed a current-carrying conductor in a magnetic field and noticed that a voltage transverse to the applied field developed across it. This discovery became

eponymously known as the ordinary Hall effect (OHE), or simply Hall effect. Years later, Hall swapped out his nonmagnetic conductor for a ferromagnet and found that the effect was nearly doubled in strength. While the origin of the OHE would eventually be linked to the classical Lorentz force, the anomalous Hall effect (AHE) in ferromagnets could only be explained by relativistic quantum mechanics.

The origin of the AHE is typically associated with two different mechanisms: extrinsic scattering of spin-polarized electrons due to spin-orbit coupling and intrinsic effects connected to Berry curvature of the electronic bandstructure. Phenomenologically, the AHE is described by the equation

$$\rho_{\text{H}} = R_0 H_z + R_{\text{H}} \mu_0 M_z \quad (3.4)$$

where ρ_{H} is the Hall resistivity, H_z is the perpendicular component of the applied field, M_z is the perpendicular component of magnetization, and R_0 and R_{H} are the ordinary and anomalous hall coefficients, respectively [3, 4]. The first term in Equation 3.4 is the ordinary contribution while the second is the anomalous contribution. The important feature of Equation 3.4 is that the out of plane component of magnetization is proportional to Hall resistivity, meaning M_z can be probed using a simple DC Hall setup. This type of measurement is particularly well-suited for systems with large perpendicular anisotropy, in which case the second term in Equation 3.4 is significantly larger than the first.

AHE Measurement Setup

Anomalous hall measurements were conducted at the Crushinator station using Hall crosses fabricated by electron beam lithography. DC current is passed along one arm of the cross (Yokogawa 7651) while a nanovoltmeter records voltage (Keithely 2400) along the other, all while an external field swept from positive to negative saturation is applied out of the sample plane. An R vs. H hysteresis loop is produced by conversion of voltage to resistance in the

measurement script.

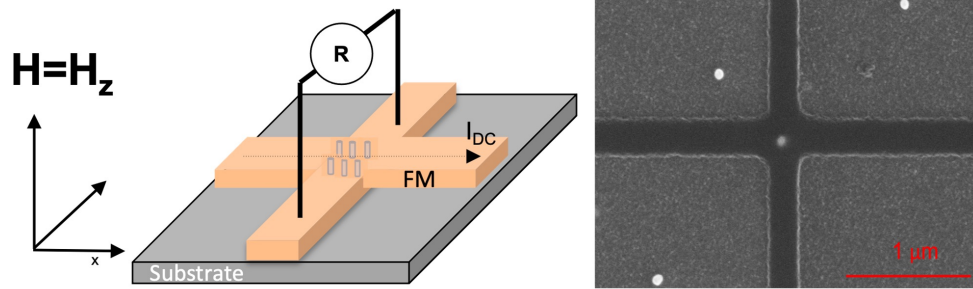


Figure 3.33: A nanopylar oriented at the center of a Hall cross to be probed by the anomalous Hall effect.

In the setup, the sample is mounted by epoxy onto a CPW and suspended vertically between the pole pieces of a magnet (Fig. 3.34). The voltage arm of the cross is wirebonded to one side of the CPW which connects to the nanovoltmeter and the current arm is wirebonded to the other side of the CPW which connects to the current supply. The two SMA ports of the CPW are isolated from one another by taking a razor and peeling off a roughly 2 mm wide slice of conductive gold layer on the front and back of the CPW as depicted in Figure 3.34. The CPW ports are then connected to the Yokogawa current source and nanovoltmeter individually and the sample is suspended between the pole pieces. The maximum field that can be achieved with this setup is about 18 kOe or 1.8 Tesla. A field of this magnitude is typically needed to saturate samples with large PMA, which means the pole gap is quite small. Given the dimensions of the CPW, this has the unfortunate consequence of inhibiting angular dependent measurements. While not a necessary requirement for AHE measurements, angular capabilities is an area for improvement.

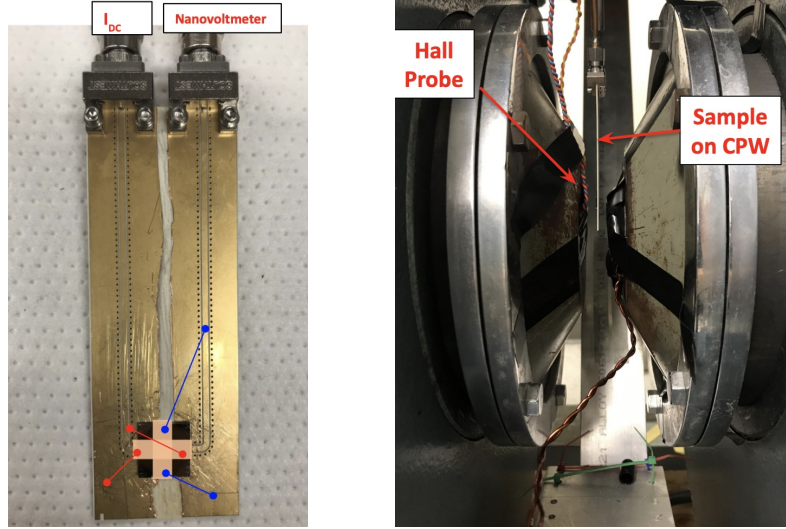


Figure 3.34: A sample is mounted onto the CPW (with backside similarly sliced) using epoxy and then suspended vertically between the pole pieces.

3.4.2 Ferromagnetic Resonance (FMR)

Ferromagnetic resonance (FMR) is a technique for probing both static (anisotropies, saturation magnetization) and dynamic (Landé g -factor, damping) magnetic properties of ferromagnetic thin films. In a conventional broadband (1-70 GHz) FMR setup, the sample is mounted on a coplanar waveguide (CPW) and placed in a DC magnetic field H . An AC microwave signal of given power and frequency f_{drive} is sent through the waveguide, creating a small field H_{RF} around the sample that causes its magnetization to precess according to the LLG equation (Equation 2.9). This precession will undergo resonance at a particular field $H = H_{res}$ and frequency f_{res} . When f_{res} and f_{drive} are equal, the sample absorbs some of the microwave power. The decrease in power due to absorption by the ferromagnet is experimentally measured for a constant f_{drive} while H is swept. For maximum signal, H and H_{RF} should be perpendicular to one another. Similarly, one can also measure FMR at a constant H while sweeping f_{drive} though this requires a slightly modified setup to the one described below.

CPW-FMR Measurement Setup

The experimental setup for in-plane, field-domain FMR with field modulation is shown schematically in Figure 3.36. The purpose of field modulation is to help distinguish the FMR signal from all other frequency sources in the room and thus improve the signal-to-noise ratio. This is accomplished by supplying AC current via an audio amplifier to a set of modulation coils near the poles of the electromagnet to generate a small field modulation h_{mod} to H . With the help of a lock-in amplifier referenced to this modulation frequency, the FMR signal can then be isolated more easily.

The sample is first mounted film-side down onto the CPW using a thin strip of Kapton tape (Fig. 3.35). Alternating microwave current is sent from the output of a microwave generator (Rhode & Schwarz; Hittite) to one port of the CPW to produce a field H_{RF} around the sample. The other CPW port attaches to a microwave diode that converts transmitted microwave current into a DC voltage to be read by the input of a lock-in amplifier (Signal Recovery Systems). The lock-in is referenced to the modulation frequency of the AC current being sourced by the audio amplifier (Behringer Europower EP4000), monitored by an ammeter, and ultimately fed to the modulation coils. A 1 kW resistor is installed in series with the coils in order to match load impedance and prevent them from overheating. Lastly, the lock-in analog output and Kepco power supplies for the electromagnet (GMW) are connected to a DAQ for control via computer.

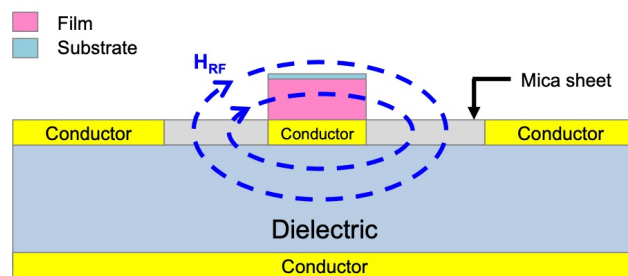


Figure 3.35: A thin film sample is placed film-side down on the coplanar waveguide.

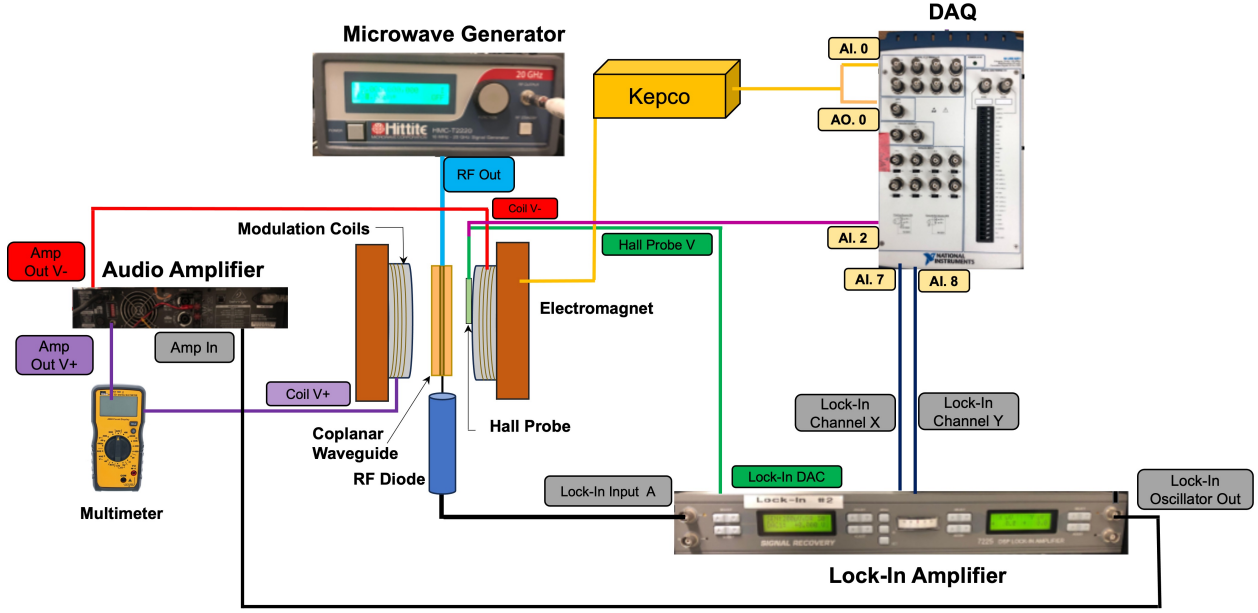


Figure 3.36: Schematic of connections for FMR with field-modulation.

CPW-FMR Analysis

Experimental FMR signals (Fig. 3.37) can generally be fit using a sum of symmetric L_S and anti-symmetric L_A Lorentzian functions given by

$$V(H) = SL_S(H) + AL_A(H) \quad (3.5)$$

where $L_S = \frac{1}{1+(H-H_{\text{res}})^2/\Delta H^2}$, $L_A = \frac{(H-H_{\text{res}})/\Delta H}{1+(H-H_{\text{res}})^2/\Delta H^2}$, S and A are symmetric and antisymmetric Lorentzian amplitudes, and ΔH is the FMR linewidth (half-width-at-half-maximum). However, under field-modulation—specifically when h_{mod} is smaller than ΔH —the measured signal is actually proportional to the field derivative of $V(H)$:

$$\frac{dV(H)}{dH} \propto S \frac{dL_S(H)}{dH} + A \frac{dL_A(H)}{dH}. \quad (3.6)$$

[5, 6].

The condition for resonance is determined by the derivatives of the total free energy density

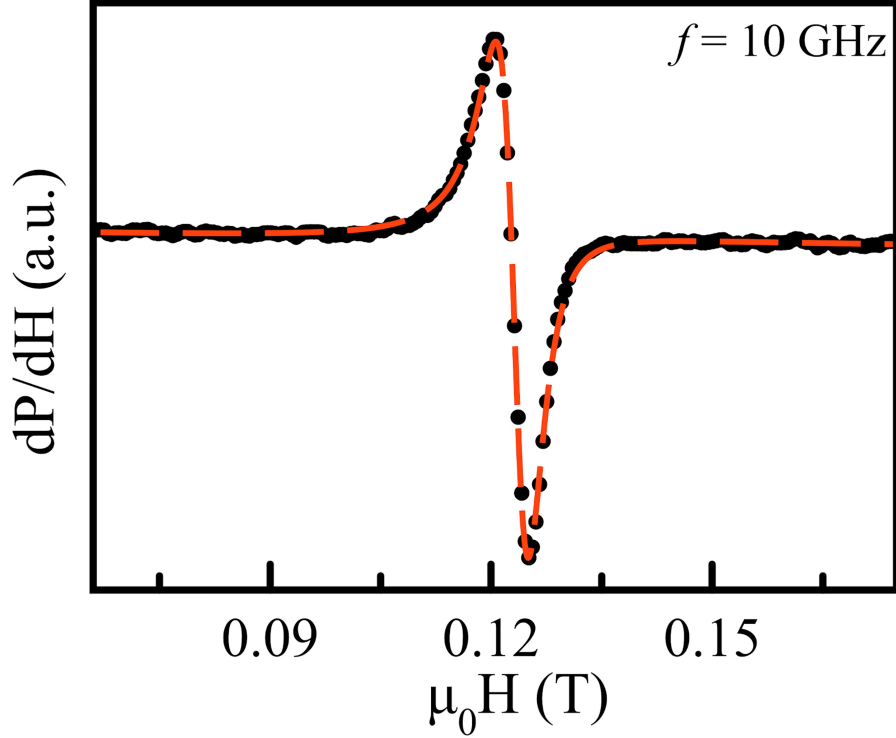


Figure 3.37: Typical FMR resonance peak of Lorentzian form.

F [7]:

$$\left(\frac{2\pi f_{\text{res}}}{\gamma}\right)^2 = \frac{1}{M^2 \sin^2 \theta} \left[\frac{\partial^2 F}{\partial \theta^2} \frac{\partial^2 F}{\partial \phi^2} - \left(\frac{\partial^2 F}{\partial \theta \partial \phi}\right)^2 \right] \quad (3.7)$$

where γ is the gyromagnetic ratio, θ and ϕ are the spherical coordinates of the magnetization, and the partial derivatives ∂F are evaluated at the equilibrium angles θ_{eq} and ϕ_{eq} which are obtained from minimization of F , i.e., $\frac{\partial F}{\partial \theta} = 0$ and $\frac{\partial F}{\partial \phi} = 0$. In experiment, one is mainly concerned with obtaining H_{res} for different driving frequencies f_{drive} and fitting to Equation 3.8 to obtain γ and the quantity $4\pi M_{\text{eff}}$:

$$\frac{\omega}{\gamma} = \sqrt{H_{\text{res}}(H_{\text{res}} + 4\pi M_{\text{eff}})}. \quad (3.8)$$

Similarly, FMR linewidth ΔH vs. f_{drive} provides information about magnetic damping and

inhomogeneities within the system. Linewidth data is typically fit using [8]:

$$\Delta H = \Delta H_0 + \frac{4\pi\alpha f_{\text{drive}}}{|\gamma|} \quad (3.9)$$

where α is the Gilbert damping parameter and ΔH_0 is the frequency-independent, inhomogeneous linewidth broadening due to sample imperfections. Non-linearity in ΔH due to effects like field dragging and two-magnon scattering may also be observed [9].

3.4.3 AC Magnetoresistance

Wheatstone Bridge Operating Principle

Magnetoresistance measurements (four-point) with sensitivity down to 1 part per 10^5 were made by means of a lock-in amplifier and Wheatstone bridge. The advantage of a Wheatstone bridge is that resistance changes as small as 1 m Ω can be detected, thereby enabling the measurement of extremely small signals. The Wheatstone bridge circuit is shown in Figure 3.38 and consists of two parallel paths.

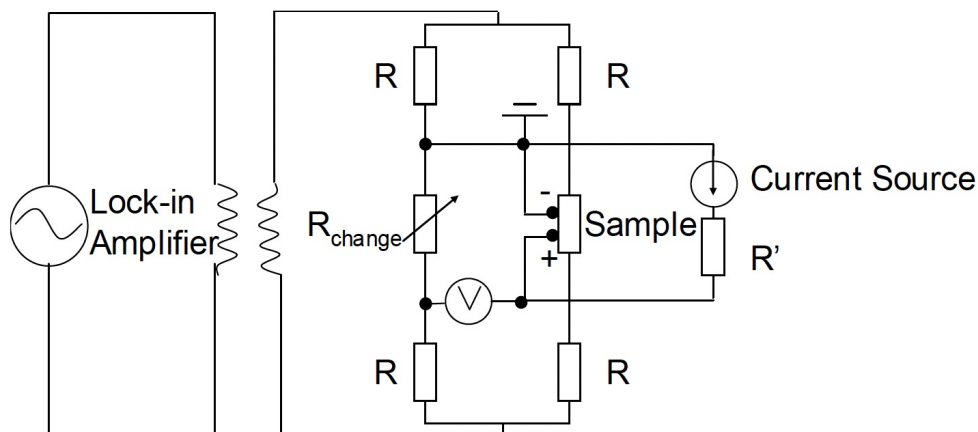


Figure 3.38: Wheatstone bridge circuit diagram.

On the left path are two adjustable resistors R and a variable resistor R_{change} . On the right path are two adjustable resistors R and the sample whose resistance R_{sample} is to be measured. Both paths are connected to the output of the lock-in amplifier, via an audio transformer, which supplies a small AC voltage to the circuit. When the adjustable resistors are chosen to be two– but no more than three– orders of magnitude larger than R_{sample} (R can be set from 10 k Ω to 1 M Ω via knobs on the front of the bridge), the RMS current flowing through the left and right paths of the circuit is approximately constant ($I = \frac{V_{\text{osc}}}{2R}$). The input of the lock-in amplifier is connected between R_{change} and R_{sample} which share a common ground. The lock-in input, acting as a voltmeter, reflects the voltage difference $V = I(R_{\text{sample}} - R_{\text{change}})$ between R_{change} and R_{sample} . When R_{change} is set equal to R_{sample} , the voltage read by the lock-in is very close to zero. If an external stimulus is then applied to the sample (via temperature, applied field, etc.), the lock-in can detect the change in R_{sample} with extreme sensitivity.

Sample Preparation

Samples were patterned into 6-contact Hall bars via photolithography with the Karl Suss MA6 mask aligner. As shown in Figures 3.39 and 3.40, there are two photomask options to choose from, each intended for samples of 10 x 10 mm dimensions. The caterpillar design is particularly suitable when current needs to be applied at various angles with respect to a specific crystallographic direction of the sample. After lithography, the Hall bar should be mounted onto a chip carrier using a small amount of vacuum grease.

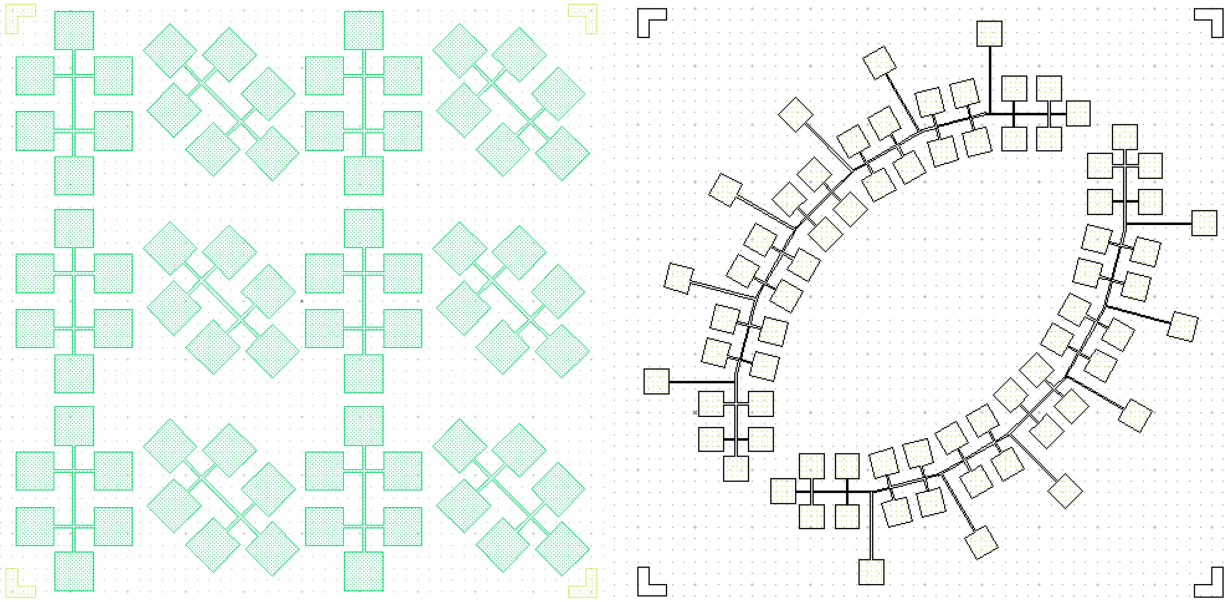


Figure 3.39: LayoutEditor designs of the conventional Hall bar photomask (left) and the caterpillar Hall bar photomask (right). The caterpillar segments 1 through 7 wind in 15° increments.

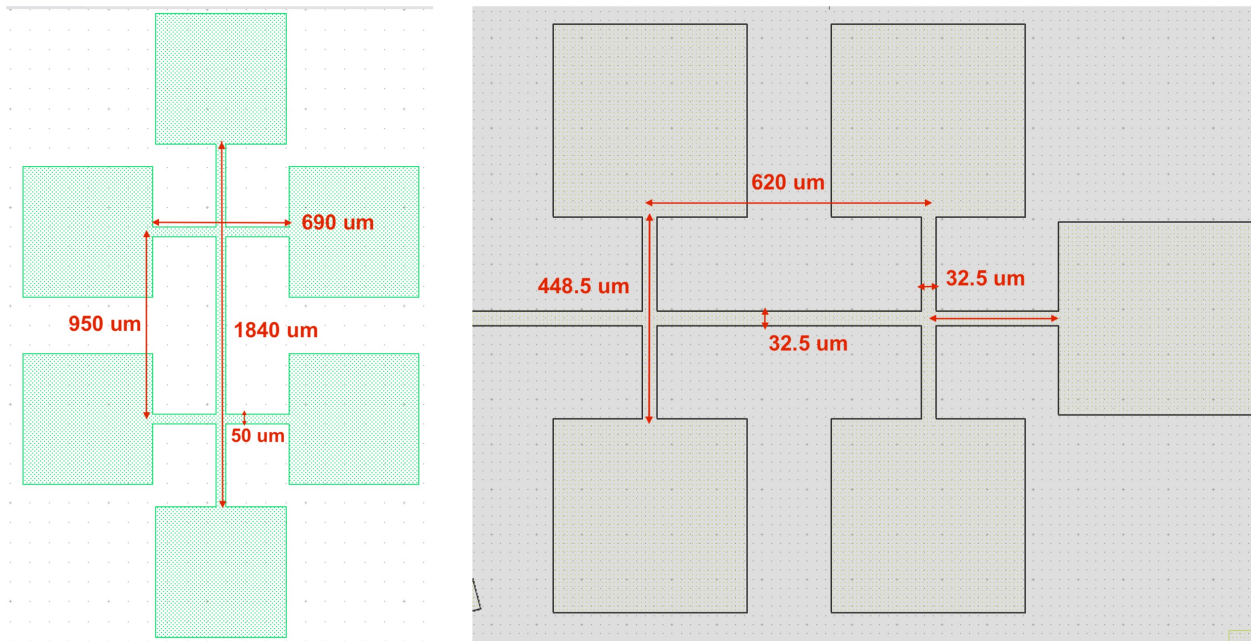


Figure 3.40: Dimensions of the conventional Hall bar photomask (left) and caterpillar variety (right). Both photomasks are intended for 10 x 10 mm samples.

To prevent temperature drift, the magnetoresistance measurement is carried out inside of

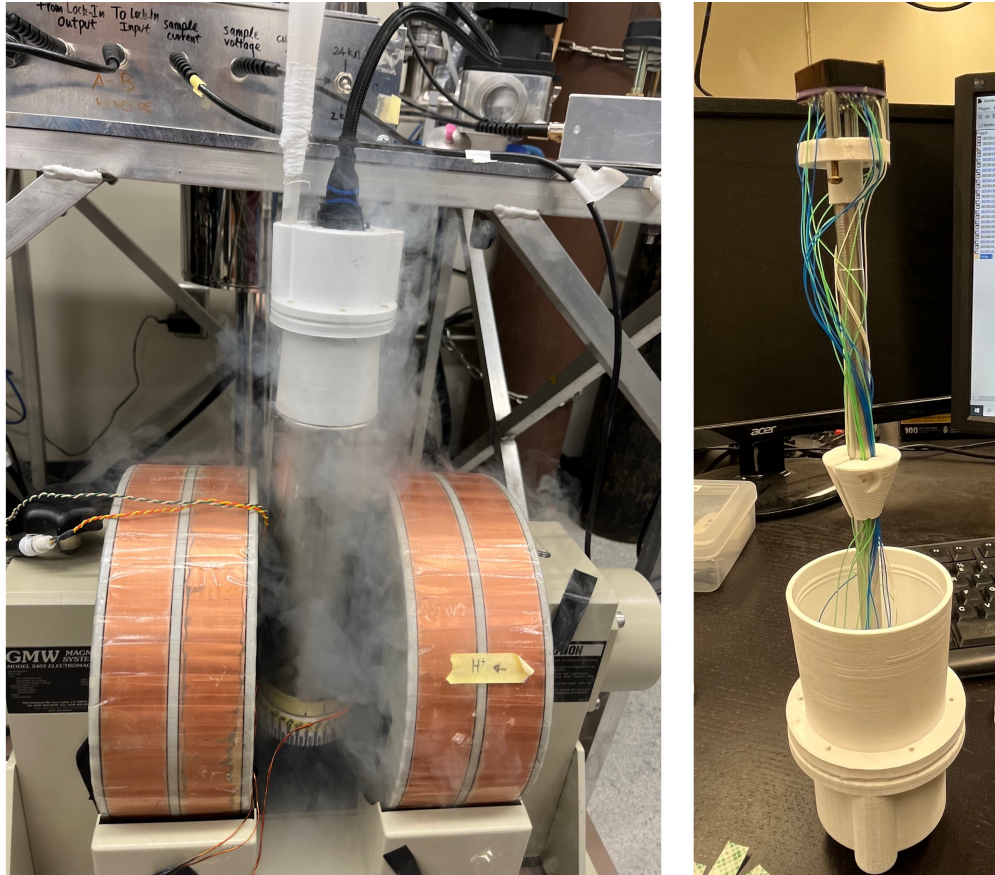


Figure 3.41: Resistance versus field angle (AMR) is measured by rotating the dewar between the pole pieces. Similarly, resistance versus field data collected at a particular field angle may be used to determine sample saturation. Measurements can be taken at 77 K by funneling in liquid nitrogen through a small opening on the top of the dewar lid. The HDMI-compatible dewar lid with carrier socket is shown right.

a nitrogen dewar with a custom-built lid. As shown in Figure 3.41, the lid has a central metallic rod with a carrier socket fashioned to its bottom that connects the pins of the chip carrier to an HDMI port. An HDMI cable then feeds to a switchbox (to be discussed later) that enables permutation of the measurement contacts. The Hall bar contacts on the sample, numbered 1 through 6 with reference to Figure 3.42, have the following correspondence to the pin numbers of the chip carrier:

- Hall bar contact 5 → chip carrier pin 2
- Hall bar contact 6 → chip carrier pin 22

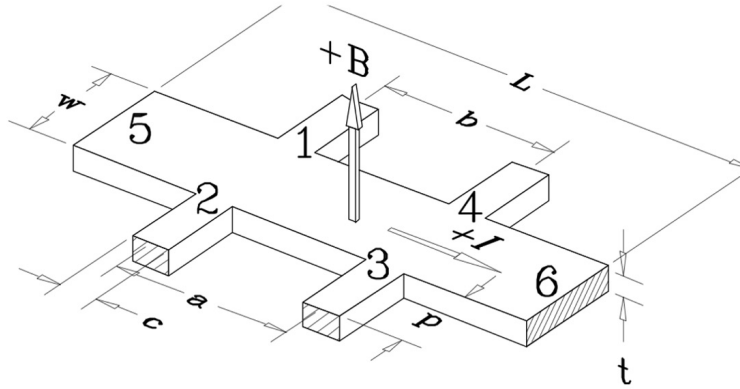


Figure 3.42: Numerical labeling of the Hall bar contacts. The bar is of thickness t , length L , and width w , with contact separation $a = b$ (figure taken from Appendix A of Lake Shore 7500/9500 Series Hall System User's Manual).

- Hall bar contact 1 → chip carrier pin 40
- Hall bar contact 2 → chip carrier pin 11
- Hall bar contact 3 → chip carrier pin 13
- Hall bar contact 4 → chip carrier pin 35.

This wirebonding scheme is shown pictorially in Figure 3.43. It is identical for either Hall bar design, with the exception that the voltage contacts (Hall bar contacts 1 through 4) on the caterpillar are made to individual segments at a time and the current contacts (Hall bar contacts 5 and 6) can be made at the ends of the caterpillar or at intermediate points on the outermost arc (Fig. 3.39). After wirebonding, the chip carrier should be inserted into the carrier socket on the dewar lid exactly as shown in Figure 3.44. This is accomplished by placing the chip carrier atop the socket and pushing it into the socket using the four-legged insertion tool.

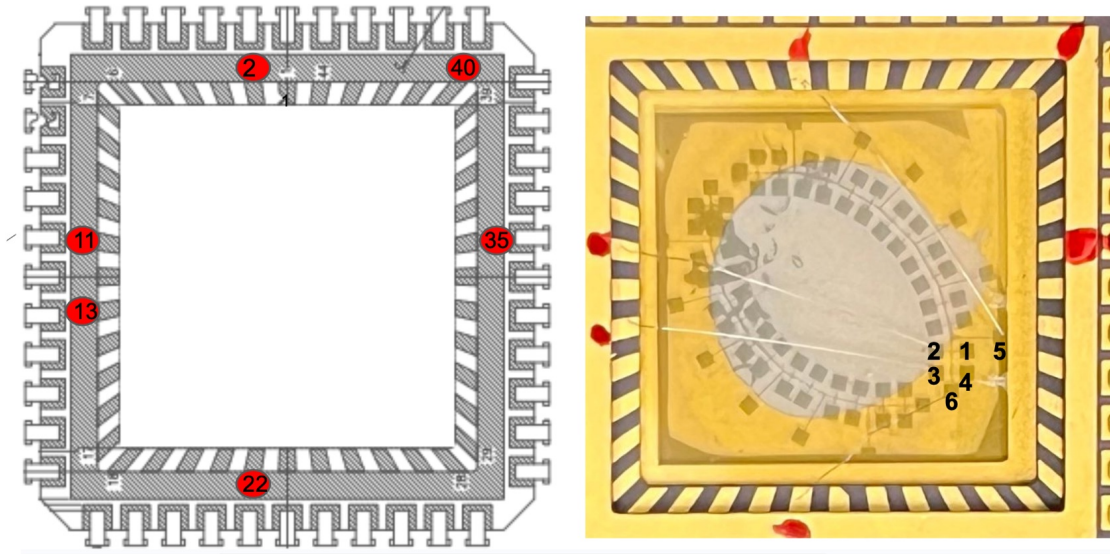


Figure 3.43: Numbered red circles are the chip carrier pins to which Hall bar contacts 1 through 6 should be wirebonded to as detailed in the text. A real example is shown right.

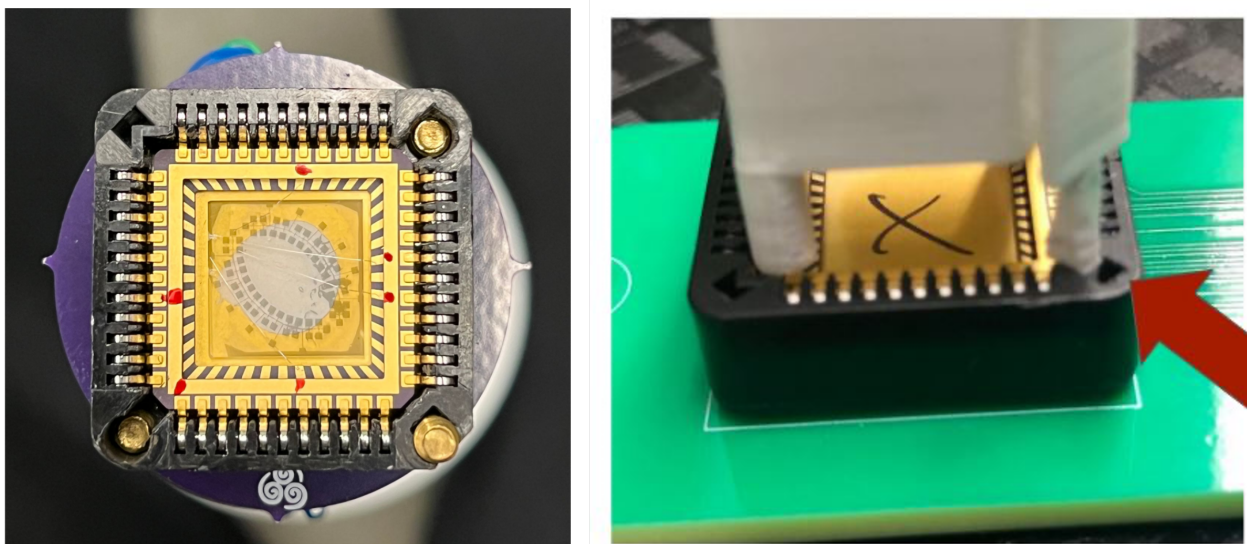


Figure 3.44: Samples are mounted to the chip carrier with vacuum grease and must be inserted into the carrier socket in the exact orientation shown left. When using the 3D-printed insertion tool (right), its thicker leg must face the crown-shaped feature that appears on only a single corner of the socket.

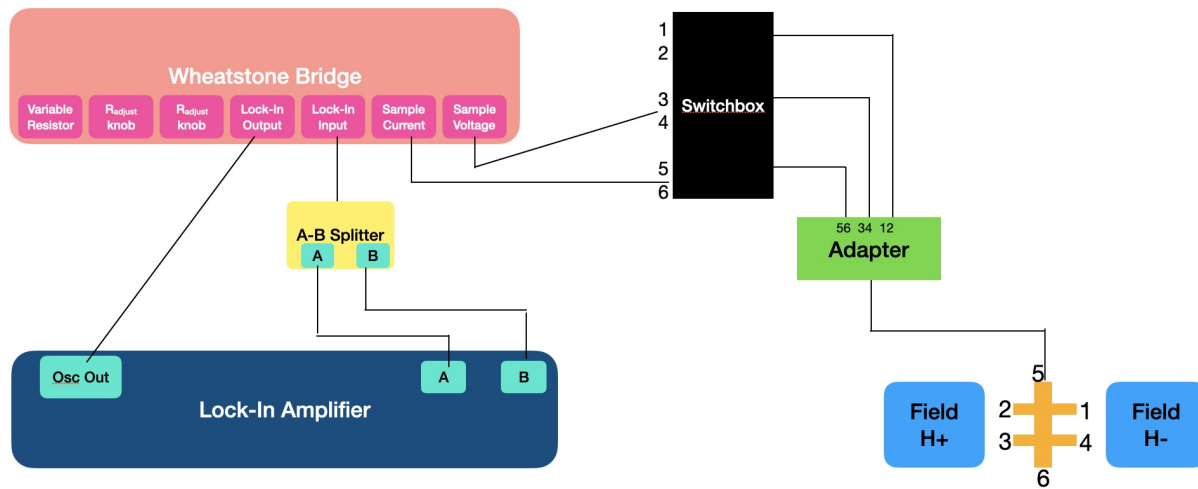


Figure 3.45: Full schematic of connections for the low-noise AMR measurement using a Wheatstone bridge.

Equipment Settings

The required measurement equipment, with connection schematics depicted in Figure 3.45, is as follows: lab-made Wheatstone bridge, lab-made switch box with adapter (Fig. 3.48), 1:1 audio transformer (Hammond 801), lock-in amplifier (Stanford Research Systems 830) plugged into an isolation transformer (TrippLite), A-B splitter box, and liquid nitrogen dewar with an HDMI compatible lid. The lock-in (Fig. 3.46) should be set to A-B measurement mode, AC coupling, floating, and FET (for sample resistances $< 10 \text{ k}\Omega$, bipolar may be used). Care should next be taken to ground the chassis of the Wheatstone bridge by connecting its metallic lid to a grounding box via banana cable as shown in Figure 3.48. To minimize capacitive coupling, the oscillation frequency of the lock-in should be set to a prime number between 50-1200 Hz. To measure voltage across specific Hall bar contacts, the "sample voltage" BNC port on the bridge should be connected to the appropriate ports labeled 1 through 6 on the switchbox via banana cables. The "sample current" BNC port on the bridge should always connect to ports 5 and 6 on the switchbox. With current along contacts 5 and 6 and field applied in-plane, AMR can be measured across contacts 1 and 3, 1 and 4, 2 and 3, or 2 and 4 (Fig. 3.42).



Figure 3.46: A-B splitter (left) and lock-in measurement settings (right). User beware that this Signal Recovery lock-in has problems above 30 dB gain– replace with SRS 380 or use with caution.

Resistance vs Angle Measurements

For the R_{sample} vs field angle measurement, it is important that the segment of the Hall bar which passes electrical current is as close to parallel with the direction of the applied field as possible before starting measurements. This is critical in terms of keeping track of AMR sign, which can be positive or negative based on this alignment. Any hope of utilizing the caterpillar design for its intended purpose depends upon the ability to precisely align the direction of applied current with the direction of applied field.

One way to ensure alignment of current and field is to perform a preliminary test using a Hall bar of Py which has a large, positive AMR that obeys the typical $\sim \cos^2 \theta$ dependence. First, insert the Py sample into the dewar with current and field aligned very roughly by eye as follows:

- Ensure the sample is oriented in the chip carrier as shown in Figure 3.44
- Insert the lid straight into the dewar with the spiral logo in Figure 3.44 pointing opposite you when looking top down along the carrier rod
- Hold the *lid steady* with one hand and *screw the dewar* into the lid with the other

- Rotate the dewar counter-clockwise by 90°

Before continuing, a brief aside is now needed on how to operate the Wheatstone bridge. With the sample connected to the bridge and all knobs on the switchbox set to "live," set R_{change} to 0Ω via the variable resistor box on the bridge (Fig. 3.48). Using the two black knobs, set the adjustable resistors to be two orders of magnitude larger than R_{sample} (this rule applies for low resistance samples of several Ohms like Py). On the other hand, if the sample is highly resistive ($\sim \text{k}\Omega$) it is not advised to use large adjustable resistors since they will contribute significant noise to the measurement upon heating. In this case, the adjustable resistors should instead be set lower ($\sim 10 \text{ k}\Omega$). The trade-off to this is that it can no longer be assumed that the RMS current flowing along the left and right paths of the bridge circuit are approximately equal. This adds an added layer of complexity to the analysis, but can be accounted for later as will be discussed. For maximum signal, set the lock-in oscillator voltage to its 5 V limit. Put all signal into the lock-in X(V) channel by using the auto-phase feature and then increase the phase by 180° . Next zero/balance the bridge by adjusting R_{change} until the lock-in channel X is as close to 0 V as possible— this value of R_{change} should be very close to R_{sample} if R_{sample} is low. If R_{sample} is large, R_{change} will be quite different from R_{sample} when the adjustable resistors are $\leq 10 \text{ k}\Omega$. Lastly, set the lock-in to the lowest sensitivity and highest gain possible without overloading. Allow the sample 1-2 minutes to come to thermal equilibrium before beginning a measurement. As the sample heats up its resistance may increase slightly and the value of R_{change} may need to be re-adjusted to fully zero the bridge.

Returning to the discussion of sample alignment using Py, a resistance maximum should be observed as a function of applied field angle when current and field are parallel. This angle should now be pinpointed by rotating the dewar about its starting position until a maximum voltage reading on the X(V) channel is observed. This position is likely to be only $\pm 15^\circ$ away from the starting angle. Record the angle of maximum resistance θ_{max} then remove

the sample from the dewar. Draw a line on a piece of tape and place it on the dewar. Then draw a line on the dewar lid, ensuring that after tightening the lid onto the dewar the two aforementioned lines are exactly parallel.

The θ_{\max} found using Py located the angle at which H is parallel to current. In the context of the caterpillar design, this corresponds to current and field aligned along segment 1 when the dewar is at θ_{\max} and the sample is inserted in the following way:

- Ensure the sample is oriented in the chip carrier as shown in Figure 3.44
- Insert the lid straight into the dewar with the spiral logo in Figure 3.44 pointing to the left when looking top down along the carrier rod
- Screw the dewar lid onto the dewar such that both lines drawn on the dewar and lid are parallel
- Set the dewar to θ_{\max} found using the Py test sample
- Rotate the dewar counter-clockwise by the winding angle of the Hall bar— for instance, rotate the dewar by 30° counter-clockwise to apply field along current segment 3 on the caterpillar (Fig 3.39)

Good sampling parameters for data collection consist of a high number of averages (10000) taken at a 100001 Hz sampling rate for 1 s per data point. A lock-in time constant of 300 ms and oscillation frequency of 513 Hz were found to yield a low noise floor. For R vs angle measurements that may now commence, the sample should always be rotated in the clockwise direction. One can choose to measure R_{sample} vs H (at fixed field angle) or R_{sample} vs field angle (at fixed H) using the bridge method. As mentioned, swapping the pair of Hall bar contacts across which to measure is accomplished by inserting banana plugs into the ports on the switchbox correspondingly labeled 1 through 6. If changing contacts, it is not necessary to re-phase the bridge.



Figure 3.47: A 1:1 audio transformer is soldered to the back of the Wheatstone bridge. This is a crucial component which seems to be removed from the several spare bridges currently in lab storage!



Figure 3.48: Components of the AMR setup: grounded Wheatstone bridge (left), switchbox (middle), and adapter (right).

Since the lock-in amplifier measures voltage, the actual resistance of the sample must be calculated from raw voltage $X(V)$. This is accomplished using a Mathematica code which has fully solved the bridge circuit using Kirchoff's laws (Appendix D). To use the script requires the following additional resistance measurements— with reference to Figures 3.42 and 3.43— to be taken using a nanovoltmeter and current supply (assuming AMR is being measured on contacts 2-3 in Figure 3.42): $R_{52} = \frac{V_{52}}{I_{52}}$, $R_{36} = \frac{V_{36}}{I_{36}}$, $R_{23} = \frac{V_{23}}{I_{23}}$, $R_{56} = \frac{V_{56}}{I_{56}}$,

$R_{53} = \frac{V_{53}}{I_{53}}$, $R_D = \frac{V_{23}}{I_{56}}$. The value of R_{change} must also be documented. Lastly, an optical image of the sample should be taken after measurements to extract the misalignment angle of the sample with respect to the chip carrier. Based on these inputs, the Mathematica code returns a coefficient c by which the raw $X(V)$ data should be multiplied to give the measured change in sample resistance dR_{sample} .

AC Magnetoresistance Troubleshooting

A useful test to check the functionality of the Wheatstone bridge is to replace the sample with a resistance substitution box and verify that the R_{change} that zeroes the bridge matches the resistance set on the substitution box. A change in the resistance substitution box by 1Ω should equal the lock-in voltage reading predicted by calculation (Appendix D).

The full setup may also be tested using a standardized sample with known AMR. The Py Hall bar used for sample alignment is permanently stored with the bridge for this purpose (AMR $\sim 2\%$). Furthermore, if—beginning from 0Ω —increasing R_{change} causes the lock-in $X(V)$ to increase, rather than decrease, there is a problem with one of the sample connections. This can be a bad wirebond or a scratch across the Hall bar, two things that can also manifest as voltage fluctuations on the lock-in. Additionally, the bottom of the dewar is fixed to the rotational base between the pole pieces using double-sided tape. Though it is sufficiently strong to keep the dewar from slipping during rotations, one should be mindful of this as a potential source of error in angular-dependent data. Furthermore, a linear background in R_{sample} vs angle is a sign of heating and additional time should be given to allow the sample to reach thermal equilibrium.

In general, resistivity measurements at zero applied field can also be made independently from the bridge using a DC current source (Yokogawa 7651) and nanovoltmeter (Keithley 2182A) using Hall bars. The "sample current" BNC cable on the bridge should be disconnected and fed to the Yokogawa, while the "sample voltage" BNC cable should be connected

to the nanovoltmeter. Following the nomenclature of Figure 3.42, the voltage between 2 and 3 should be measured for positive (+) and negative (-) polarities of DC current applied along 5 and 6. The process should then be repeated on 1 and 4 with current still along 5 and 6. Sample resistivity is then calculated by taking the average of Equations 3.10 and 3.11. If there is large disagreement between ρ_A and ρ_B , the Hall bar should be inspected for inhomogeneities.

$$\rho_A = \frac{V_{56,23}^+ - V_{56,23}^-}{I_{56}^+ - I_{56}^-} \frac{wt}{a} \quad (3.10)$$

$$\rho_B = \frac{V_{56,14}^+ - V_{56,14}^-}{I_{56}^+ - I_{56}^-} \frac{wt}{b} \quad (3.11)$$

References

- [1] Johnson, M., Bloemen, P., Den Broeder, F. & De Vries, J. Magnetic anisotropy in metallic multilayers. *Reports on Progress in Physics* **59**, 1409 (1996).
- [2] Eaton, P. & Batziou, K. Artifacts and practical issues in atomic force microscopy. *Atomic Force Microscopy: Methods and Protocols*, 3–28 (2019).
- [3] Gerber, A. *et al.* Extraordinary Hall effect in magnetic films. *Journal of magnetism and magnetic materials* **242**, 90–97 (2002).
- [4] Nagaosa, N., Sinova, J., Onoda, S., MacDonald, A. H. & Ong, N. P. Anomalous hall effect. *Reviews of modern physics* **82**, 1539 (2010).
- [5] Gonçalves, A. *et al.* Spin torque ferromagnetic resonance with magnetic field modulation. *Applied Physics Letters* **103**, 172406 (2013).
- [6] Harder, M., Cao, Z., Gui, Y., Fan, X. & Hu, C.-M. Analysis of the line shape of electrically detected ferromagnetic resonance. *Physical Review B* **84**, 054423 (2011).
- [7] Farle, M. Ferromagnetic resonance of ultrathin metallic layers. *Reports on progress in physics* **61**, 755 (1998).
- [8] Kalarickal, S. S. *et al.* Ferromagnetic resonance linewidth in metallic thin films: Comparison of measurement methods. *Journal of Applied Physics* **99**, 093909 (2006).
- [9] Zakeri, K. *et al.* Spin dynamics in ferromagnets: Gilbert damping and two-magnon scattering. *Physical Review B* **76**, 104416 (2007).

Chapter 4

Quantitative measurements of AMR in PtMn antiferromagnet

4.1 Introduction

Discovered by Lord Kelvin in 1856, anisotropic magnetoresistance (AMR) is an electrical detection mechanism of magnetic order which has found extensive use in modern FM spintronics, enabling for instance the detection of magnetization dynamics generated by spin torques and the readout of current-driven spin torque oscillators [1–4]. A current goal of spintronics research is to find analog phenomena using AFM materials whose exchange-dominated dynamics stand to offer faster switching speeds than their FM counterparts. Methods to efficiently control and detect AFM order are therefore critically needed. The identification of candidate AFM materials with appreciable AMR is one potential stepping stone towards this end.

Metallic AFMs are a particularly relevant material class for study, since the interplay of their electronic, magnetic, and optical degrees of freedom can lead to the complex spin-orbit and

magneto-optical phenomena fundamental to the operation of spintronic devices [5]. Given the difficulty of probing AFM dynamics using magnetic fields, the number of AFM metals in which magnetoresistance effects have thus far been experimentally reported is limited [6–12].

Here we present room temperature detection of AMR in epitaxial layers of the metallic AFM PtMn using exchange-coupled FM/AFM bilayers. Our interest in PtMn is based on theory prediction of AMR as large as 10%, in addition to reports of a large spin Hall angle and tunable magnetic anisotropy via voltage and strain [13–18]. Similarly, the spin dynamics in PtMn are predicted to be of THz order which exceeds the GHz frequencies of most FMs [19]. PtMn is also known to be CMOS-compatible and already functions as a pinning layer in several magnetic technologies [20–22].

To rotate AFM magnetic order by applied field it is necessary to overcome the magnetocrystalline anisotropy (MCA) and exchange energies of the AFM itself. Given the moderate MCA of PtMn, we choose to utilize PtMn/CoFeMnSi bilayers to probe AMR in PtMn so that the formation of an interfacial exchange field assists in re-orienting the direction of AFM magnetic order and thereby lowers the applied field requirements. Importantly, the ferromagnetic Heusler compound CoFeMnSi—promising in its own right for low Gilbert damping and signatures of spin gaplessness—is a half-metal that exhibits negative AMR at room temperature: its AMR can be minimized to nearly zero by thickness or deposition temperature to ensure a majority AMR contribution from PtMn in the PtMn/CoFeMnSi bilayers [23–26].

Here we present the first quantitative measurements of AMR in a collinear, high-temperature antiferromagnet PtMn. A novel detection method based on the exchange coupling of an AFM to a zero-AMR FM is put forth, and may plausibly extend to other FM/AFM systems beyond the one studied here. A growth procedure for epitaxial PtMn thin films by sputter deposition is also provided. Our results contribute to the general body of knowledge surrounding AFM material properties and may find future application as an electrical readout method of superparamagnetic switching in an AFM or of magnetization dynamics in AFM-based spin

torque oscillators.

4.2 PtMn Thin Films

4.2.1 Physical Properties

Mn-based metallic alloys are a desirable choice for magnetoresistance studies considering Mn carries the largest magnetic moment among the transition metals ($3.65 \mu_B$) and many of its alloys order antiferromagnetically (e.g., IrMn, FeMn, NiMn, and PdMn) [13, 15, 27]. PtMn is another such alloy known to have T_N as high as 975°K and exhibit collinear antiferromagnetism over a large range of atomic compositions [19, 28, 29]. Since heavy Pt atoms tend to possess large spin-orbit coupling, PtMn is also an interesting platform for studying phenomena arising from magnetic anisotropy [15].

When deposited at room temperature, PtMn films are paramagnetic and chemically disordered with face-centered-cubic structure. The antiferromagnetic state is only achieved through high temperature deposition or annealing, which induces a phase transition to the ordered, face-centered-tetragonal (FCT) structure also known as the $L1_0$ phase. Ordered, FCT PtMn consists of two Mn and Pt sub-lattices (Fig. 4.1) where the magnetic moments on Mn lattice sites may point along the c or a axes based on alloy composition or strain [18]. The magnetization axis, or order parameter, of bulk PtMn is reported to lie along the $[001]$ direction in the ground state [30].

4.2.2 Epitaxial Growth

Single crystal thin films of PtMn are a necessary starting point for the AMR measurements to follow. When grain size in the AFM is large, the AFM order parameter is thermally

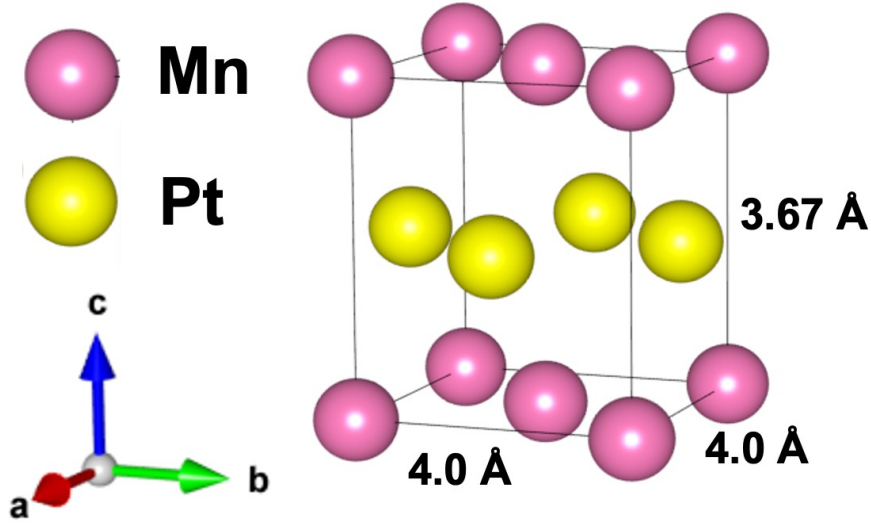


Figure 4.1: Crystal structure of tetragonal PtMn with nominal lattice constants [31].

stable along a particular crystallographic direction that is typically determined by substrate orientation, stoichiometry, or lattice strain. Only with a large distribution of these stable AFM grains does AFM AMR become apparent on a measurable scale.

PtMn(001) films were co-sputtered from individual Pt₁₈Mn₈₂ at.% and Pt targets onto cubic spinel MgAl₂O₄(001) substrates chosen for their 1.5% lattice mismatch to PtMn in the film plane ($a_{\text{PtMn}} = 3.98 \text{ \AA}$; $a_{\text{substrate}} = 8.08 \text{ \AA}$). The 10 x 10 mm MgAl₂O₄ substrates (MTI Corporation) were taken directly from their individual packaging and loaded into the sputtering chamber with no intermediate cleaning steps performed. The substrate temperature was then ramped to 650°C at a rate of 30°C/min. Upon reaching 650°C, the substrate was left to soak for 10 minutes to ensure temperature stability prior to deposition. Pt₅₀Mn₅₀ at.% films—calibrated to equiatomic composition using Rutherford backscattering data (RBS)—were then deposited at a rate of 0.243 Å/s using a 1.1 mT Ar plasma. Films were immediately capped with 2 nm of Ta to prevent oxidation before ramping down temperature at an identical rate. Details regarding the calibration of growth rates necessary for the co-deposition can be found in Appendix C.

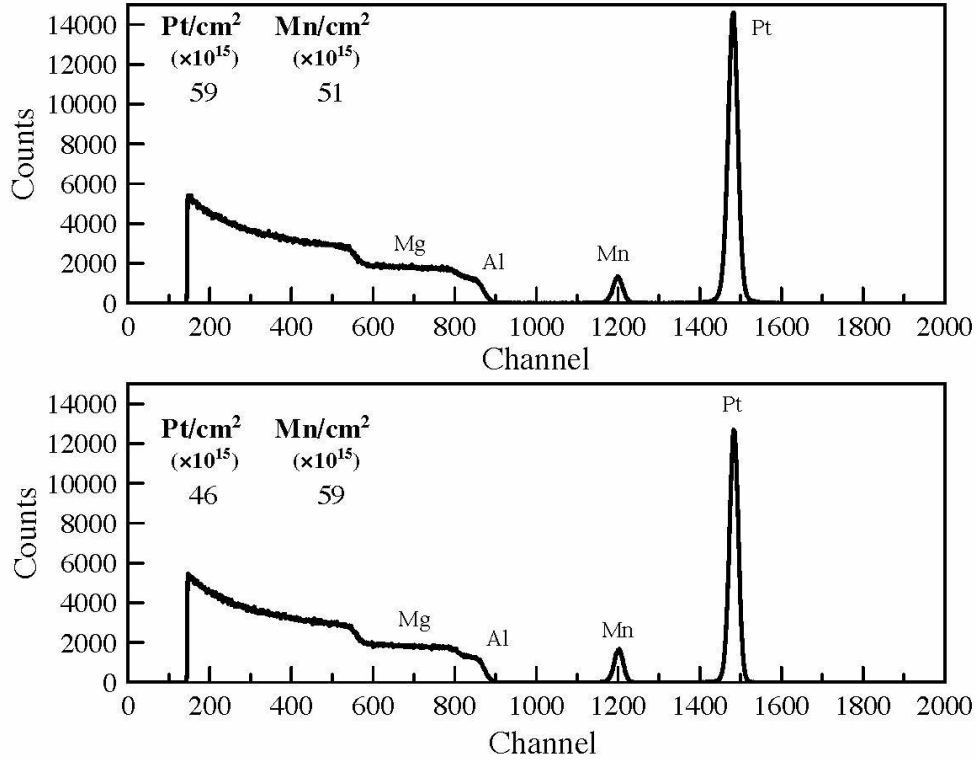


Figure 4.2: RBS spectra ($2.3 \text{ MeV } ^4\text{He}^{++}$) of 16 nm films of $\text{Pt}_{53.6}\text{Mn}_{46.4}\text{at.}\%$ (top) and $\text{Pt}_{43.8}\text{Mn}_{56.2}\text{at.}\%$ (bottom) were used to calibrate films to equiatomic composition. Measurements are courtesy of Rutgers University.

4.2.3 Film Characterization

The crystallographic properties of sputter-deposited $\text{Pt}_{50}\text{Mn}_{50 \text{ at.}\%}$ films were investigated by X-ray diffraction (XRD) with a Cu $K\alpha$ ($\lambda=1.5405 \text{ \AA}$) X-ray source and Ge(220)-x2 monochromator. Diffraction coming exclusively from the $(00l)$ family of planes in the 2θ scan demonstrates that the PtMn layer has identical orientation as that of $\text{MgAl}_2\text{O}_4(001)$ (Fig. 4.3a). The absence of diffraction at grazing incidence (inset Fig. 4.3a) is a further indication that the PtMn layer is single crystal with all $(00l)$ planes oriented parallel to the sample surface. Next a ϕ scan along the PtMn(100) direction was taken to establish the in-plane crystallographic orientation of PtMn (Fig. 4.3b). Fourfold-symmetric peaks with 90° periodicity are a reflection of a square in-plane lattice and corroborate good epitaxial

growth of PtMn on MgAl₂O₄ despite their 1.5% lattice mismatch. By rocking curve analysis, the miscut angle of the bare substrate was found to be 0.18° and does not appear to impede the epitaxial growth of PtMn [32, 33].

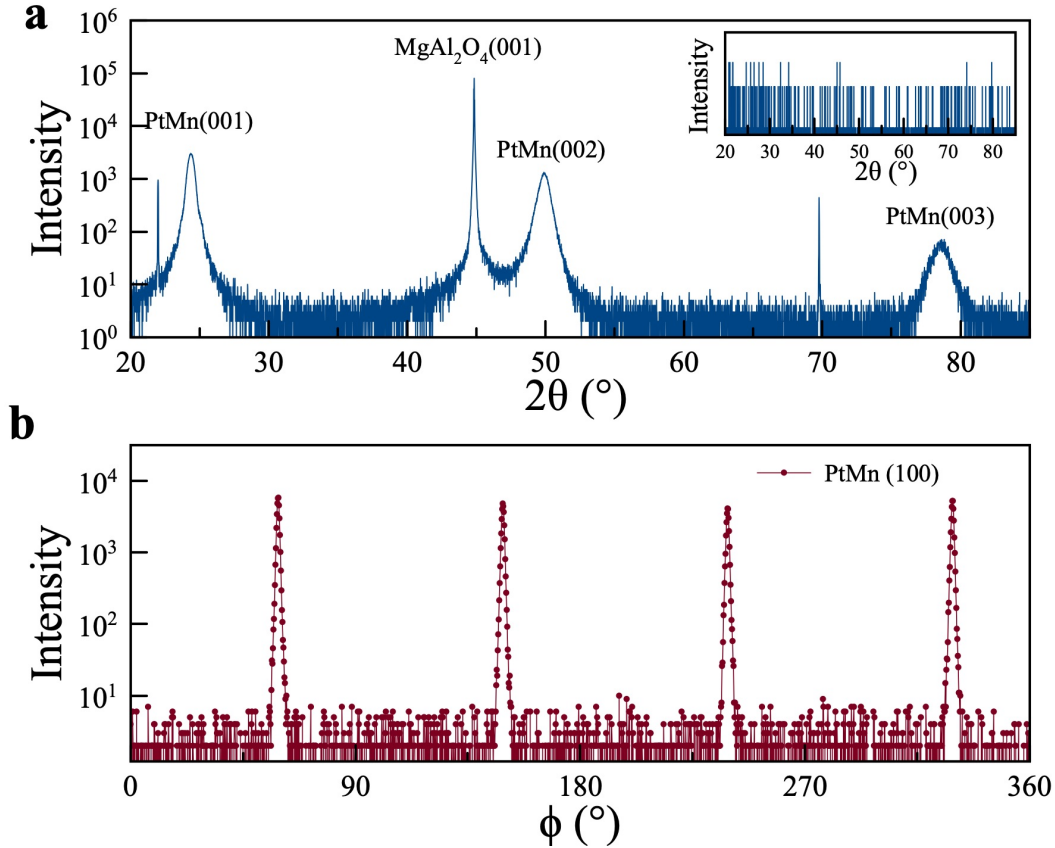


Figure 4.3: (a) XRD 2θ scan of an MgAl₂O₄/PtMn(16 nm)/Ta(2 nm) film shows a preferred (001) texture. Epitaxy is also corroborated by a flat grazing incidence spectrum. (b) In-plane ϕ measurement on the film of (a) taken from 0° to 360°.

For a crystal of tetragonal symmetry, the in-plane and out-of-plane lattice constants, a or c , can be calculated using

$$\frac{1}{d^2} = \frac{h^2 + k^2}{a^2} + \frac{l^2}{c^2} \quad (4.1)$$

where the crystal lattice spacing d is determined from a fit to the various (hkl) peaks in the 2θ scan. A lattice constant of $c = 3.65 \text{ \AA}$ extracted from the data in Figure 4.3a is in close agreement to literature values corresponding to the antiferromagnetic phase of PtMn with

1: 1 composition [34]. We may assume that the PtMn layer is relaxed given that c is closer to the PtMn bulk value (3.71 Å) than that of MgAl₂O₄ (8.808 Å).

Images of the PtMn film surface with and without a Ta cap were taken by atomic force microscopy over a 1 x 1 μm scanning area (Fig. 4.4a-b). A similar surface morphology revealing island-like growth can be seen in both the capped and uncapped film varieties. This is a known growth mode of sputtered thin films deposited at elevated temperatures. The RMS roughness S_q of the PtMn(16 nm)/Ta(2 nm) and PtMn(16 nm) film surfaces are 1.57 nm and 1.41 nm, respectively, which likely includes a layer of surface oxide in both cases. The surface of a 20 nm PtMn film with 2 nm Ta cap was also imaged by scanning electron microscopy (SEM). Large PtMn grains over 200 nm long in the film plane are readily apparent (Fig. 4.4c). Their formation is likely assisted by the slow deposition rate and low Ar plasma pressure used during deposition of the PtMn layer. In view of these grain sizes, the high S_q are not unexpected given that roughness is known to increase with grain volume. In the out of plane direction, the average PtMn grain size was confirmed to be thickness limited by XRD Scherrer analysis.

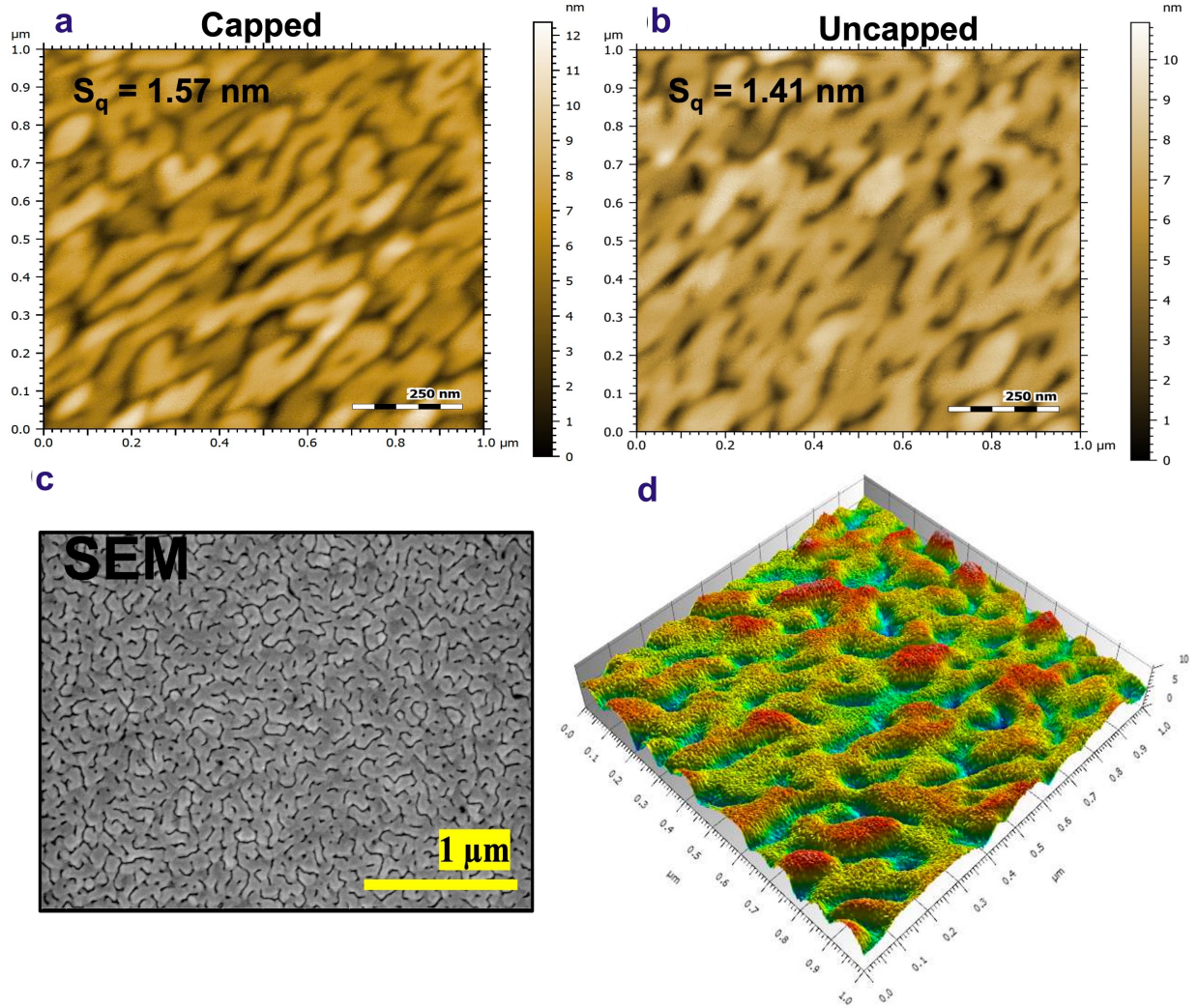


Figure 4.4: AFM images of a 16 nm PtMn film (a) with a 2 nm Ta cap and (b) without a cap, where S_q is RMS roughness. (c) SEM image of a PtMn(20 nm)/Ta(2 nm) film. (d) 3D surface of the un-capped PtMn film shown in (b) as measured by AFM.

4.3 Experimental Results

4.3.1 AMR in CoFeMnSi

To promote a maximal AMR contribution from PtMn in PtMn/CoFeMnSi bilayers it is first useful to minimize the AMR in single films of CoFeMnSi. We deposit a series of

Property	Value	Reference
T_C	763-826 C	[25, 36]
M_S	530-630 emu/cc	[26, 37]
$a = b = c$	5.609 Å	[36]
ρ at RT	269 $\mu\Omega$ -cm	[25]

Table 4.1: CoFeMnSi physical properties.

MgAl₂O₄/CoFeMnSi(3 nm)/Ta(2 nm) films by sputtering as a function of CoFeMnSi growth temperatures spanning 400-450°C and subsequently pattern them into Hall bars for measurements (section 3.4.3). For consistency, we utilize the same Hall bar geometry that will be used to facilitate the application of current along specific crystal axes of PtMn in later PtMn/CoFeMnSi bilayers, wherein the applied current direction is parameterized by the angle α (Fig. 4.5b). Device schematics and the definition of all relevant angles throughout our work are shown completely in Figure 4.5.

Room temperature AMR measurements were carried out in a saturating field of 3300 Oe using the low-noise Wheatstone bridge setup described in section 3.4.3. Since the growth of CoFeMnSi on MgAl₂O₄ is not expected to be crystalline given their lattice mismatch, any dependence of CoFeMnSi AMR on the angle α is not expected. This is confirmed in Figures 4.6a-b which demonstrate that AMR in a representative CoFeMnSi film, patterned into the structure of Figure 4.5b, is equal when measured at two different α . The possibility of shunting through the Ta cap is considered negligibly small due to the formation of a naturally occurring surface oxide of approximately 2 nm [35].

We observe a transition from positive to negative AMR in 3 nm films of CoFeMnSi for a growth temperature between $425^\circ\text{C} < T_{\text{CoFeMnSi}} < 435^\circ\text{C}$ (Fig. 4.7). The angular-dependent resistance data was fit to the equation,

$$R(\theta) = R_0 + \Delta R \cos^2(\theta + \phi_2) \quad (4.2)$$

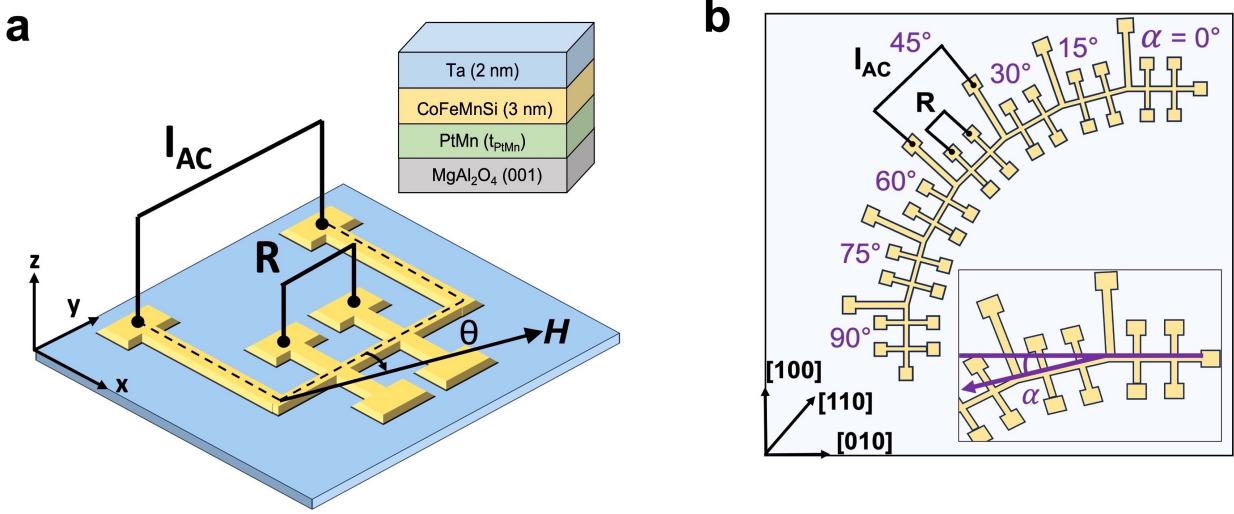


Figure 4.5: (a) Measurement schematics for an arbitrary segment of the Hall bar shown fully in Figure 1.5b. The longitudinal component of sample resistance R was measured under an AC current I_{AC} applied along specific crystallographic directions of PtMn in a saturating field H , where θ is the angle between H and I_{AC} . (b) All films in our work, including the bare CoFeMnSi films, were patterned into the extended Hall bar geometry shown which turns in 15° intervals. The angle α (magnified inset for clarity) represents the angle of applied current with respect to the $[010]$ direction of PtMn. AMR measurements conducted at each α allows AMR to be probed along the various crystallographic directions of PtMn.

where R_0 is the background sample resistance, ΔR is the change in sample resistance, ϕ_2 is the phase, and the AMR ratio is obtained as $\Delta R/R_0$ [38, 39]. The transition in AMR sign as shown in Figure 4.7 pinpoints the onset of half-metallicity– hallmarked by negative AMR at room temperature– and suggests that zero AMR can be achieved in CoFeMnSi through control of deposition temperature. Based on a linear fit to Figure 4.7, the CoFeMnSi growth temperature that yields the smallest AMR was found to be 433°C .

4.3.2 AMR in PtMn/CoFeMnSi

We next investigate AMR in PtMn(t_{PtMn})/CoFeMnSi(3 nm) bilayers as a function of PtMn thicknesses t_{PtMn} between 2-20 nm. The multilayer stack is depicted in Figure 4.5a, wherein the CoFeMnSi and 2 nm Ta cap were deposited at the optimized 433°C . As previously

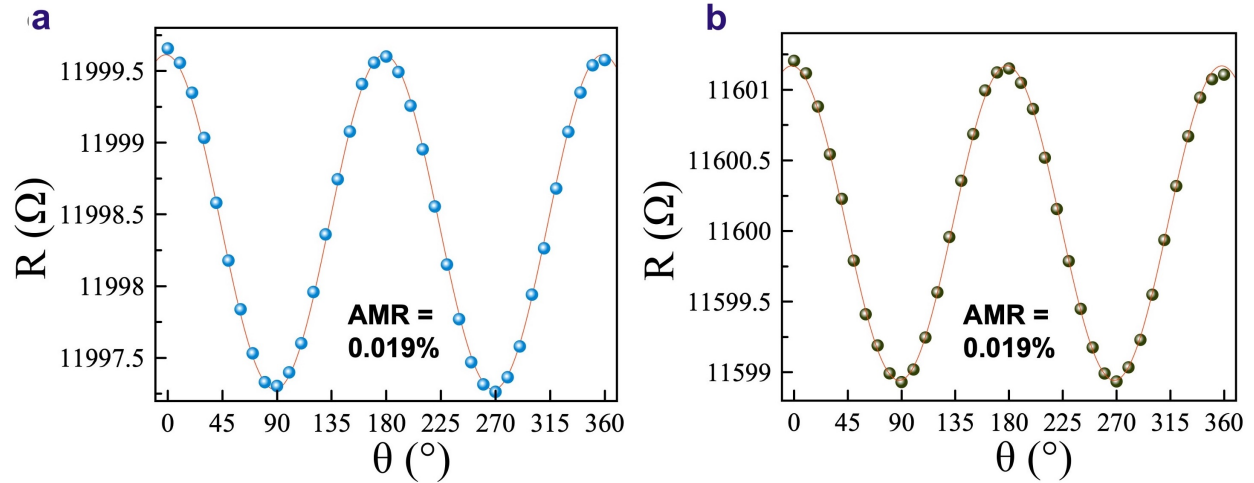


Figure 4.6: Resistance versus angle of CoFeMnSi(3 nm)/Ta(2 nm) films grown on MgAl₂O₄ at 400°C for I_{AC} along (a) $\alpha = 0^\circ$ and (b) $\alpha = 45^\circ$. Equal AMR percentages confirm that CoFeMnSi AMR does not depend on α .

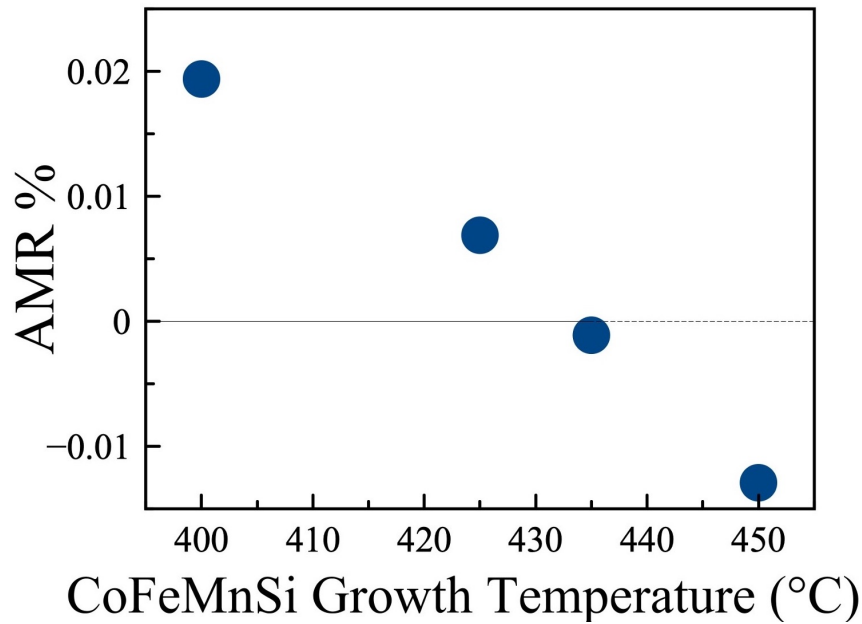


Figure 4.7: AMR percentage versus growth temperature in 3 nm films of CoFeMnSi.

discussed, samples were patterned into the winding Hall bar geometry of Figure 4.5b where the angle α (magnified inset Figure 4.5b for clarity) represents the angle of I_{AC} with respect to the [010] direction of PtMn.

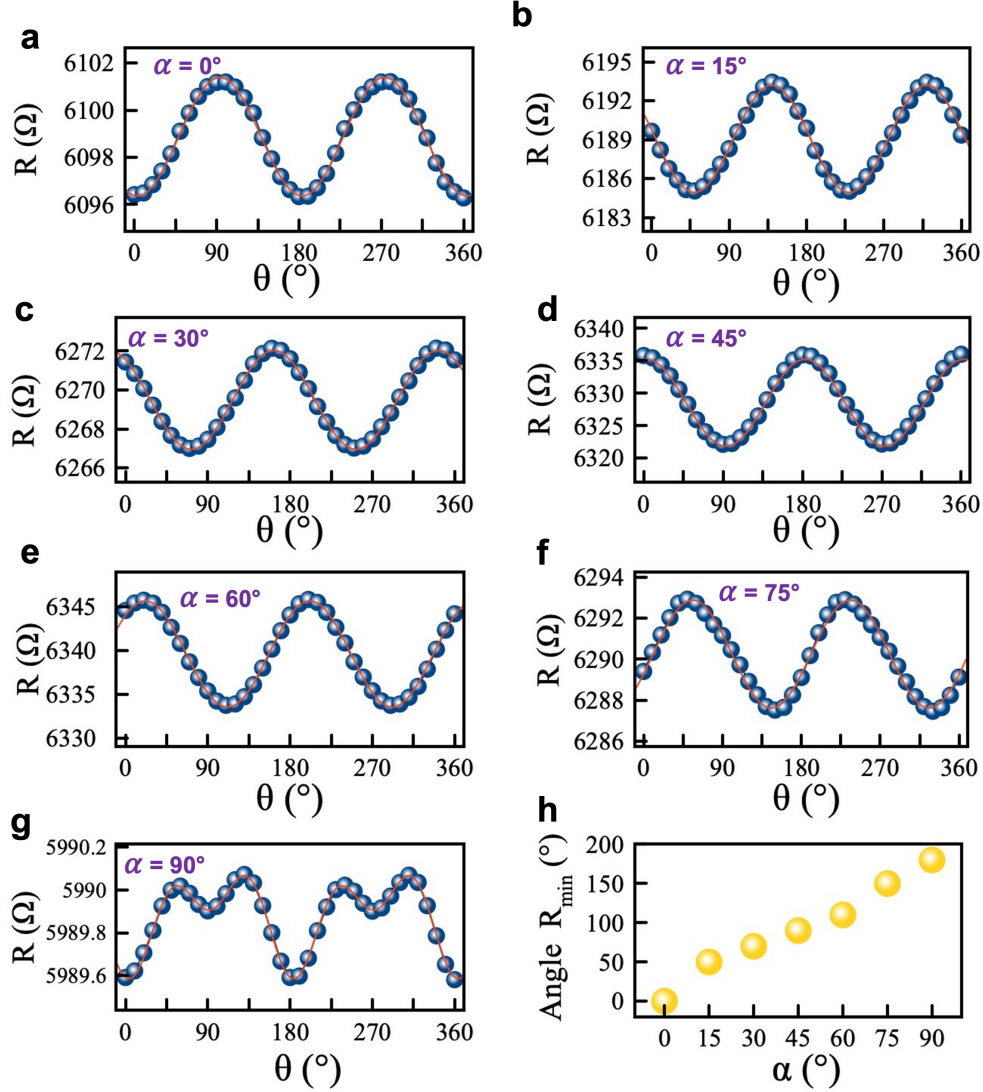


Figure 4.8: Angular-dependent resistance for t_{PtMn} bilayer when (a) $\alpha = 0^\circ$ (b) $\alpha = 15^\circ$ (c) $\alpha = 30^\circ$ (d) $\alpha = 45^\circ$ (e) $\alpha = 60^\circ$ (f) $\alpha = 75^\circ$ and (g) $\alpha = 90^\circ$. (h) Angle between resistance minimum and $\theta = 0^\circ$ versus α .

The AMR of the bilayers was measured in a 3300 Oe applied field at multiple α . Across bilayers with $2 \text{ nm} \leq t_{\text{PtMn}} \leq 20 \text{ nm}$, the largest AMR is observed for $t_{\text{PtMn}} = 4 \text{ nm}$ at $\alpha = 45^\circ$. AMR measurements at $\alpha = 45^\circ$ taken on bilayers with thicker and thinner t_{PtMn} are shown in Figures 4.10a-b for completion. Representative angular-dependent resistance plots at each α for the bilayer with $t_{\text{PtMn}} = 4 \text{ nm}$ are displayed in Figure 4.8. For $t_{\text{PtMn}} = 4 \text{ nm}$, the AMR magnitude reaches 0.2% when $\alpha = 45^\circ$ (Fig. 4.8d) and reduces in size by

approximately two orders of magnitude when $\alpha = 90^\circ$ (Fig. 4.8g). An additional fourfold component arising from higher-order resistance effects is also apparent when $\alpha = 90^\circ$ [6, 40]. While less discernible by eye, a small fourfold component is also present for $\alpha = 45^\circ$ based on a poor fit to Equation 4.2. Therefore the $R(\theta)$ data, where applicable, is fit to a modified version of Equation 4.2 that includes a fourfold term ΔR_4 ,

$$R(\theta) = R_0 + \Delta R \cos^2(\theta + \phi_2) + \Delta R_4 \cos^4(\theta + \phi_4) \quad (4.3)$$

where ϕ_4 is the phase of the fourfold magnetoresistance component.

The magnitude of the AMR ratio, expressed as a percentage, is plotted against α for $t_{\text{PtMn}} = 4$ nm in Figure 4.9a and against all t_{PtMn} for three crystallographic directions of PtMn ($\alpha = 0, 45, \text{ or } 90^\circ$) in Figure 4.9b. The AMR percentage reported in both Figures corresponds only to the twofold component of magnetoresistance which arises exclusively from AMR and excludes the fourfold component from higher order effects.

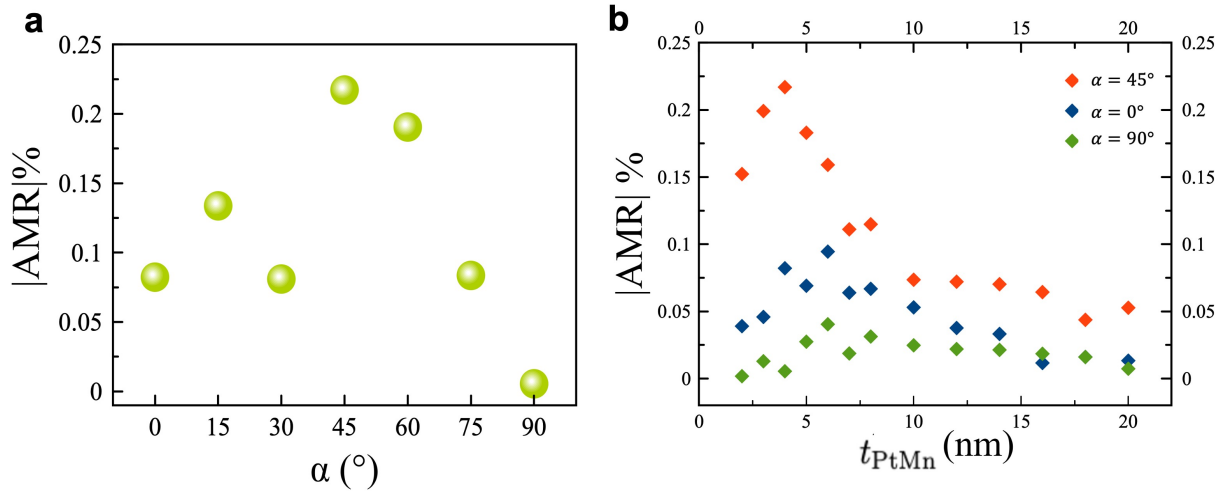


Figure 4.9: (a) Dependence of AMR magnitude on α in a PtMn/CoFeMnSi bilayer with $t_{\text{PtMn}} = 4$ nm. (b) AMR magnitude as a function of t_{PtMn} when $\alpha = 0, 45, \text{ and } 90^\circ$. The corresponding PtMn crystal directions are: [110] ($\alpha = 45^\circ$), [010] ($\alpha = 0^\circ$), and [100] ($\alpha = 90^\circ$).

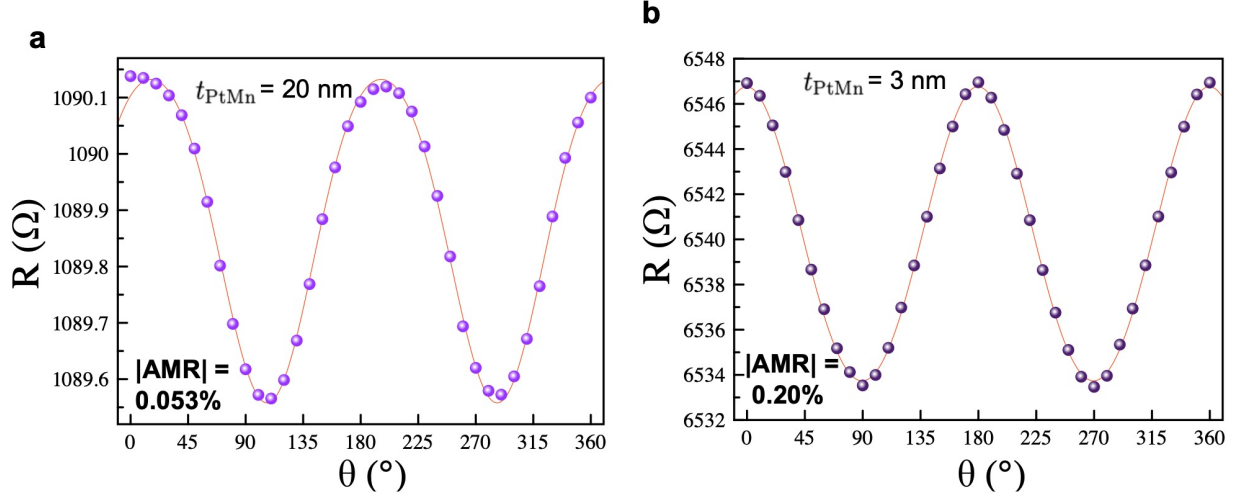


Figure 4.10: Resistance versus applied field angle when $\alpha = 45^\circ$ in bilayers with (a) $t_{\text{PtMn}} = 20 \text{ nm}$ and (b) $t_{\text{PtMn}} = 3 \text{ nm}$.

Compared to single layers of CoFeMnSi(3nm) which have $\text{AMR} \leq 0.02\%$ (Fig. 4.7), the AMR of 0.2% observed for $\alpha = 45^\circ$ in the $t_{\text{PtMn}} = 4 \text{ nm}$ bilayer is already ten times larger (Fig. 4.9b). This is an indication that the intrinsic/bulk AMR of PtMn is giant. Here it is worth noting that the AMR contribution from PtMn in our bilayer resistance data is only a fraction of its intrinsic value. As will be discussed, the AFM order parameter is never rotated through a full 360° in the film plane during measurements. However the analytical model to be described next allows us to quantify the intrinsic AMR of PtMn from our experimental results.

4.4 Data Analysis and Modeling

The respective magnetoresistance contributions from CoFeMnSi and PtMn must be separated from the bilayer magnetoresistance data to isolate the intrinsic AMR of PtMn. This was performed using a combined parallel resistance and Fuchs-Sondheimer (FS) model, wherein the FS theory provides a theoretical description of electron transport in thin films that takes

into consideration interfacial scattering processes [41, 42]. Under the FS model, resistance of the bilayer due to scattering processes can be modeled as:

$$R(t, \lambda, p) = \left(\frac{1}{R_{\text{FM}}} + \frac{w \cdot t}{L} + \frac{1}{FS(t, \lambda, p)} \frac{1}{\rho_{\text{AFM}}} \right)^{-1} \quad (4.4)$$

where λ is the mean free path of PtMn, p is the scattering specularity, FS is the Fuchs-Sondheimer corrective factor, ρ_{AFM} is the PtMn bulk resistivity, w is the Hall bar width, L is the Hall bar length, and t is the bilayer thickness. A fit of bilayer resistance versus t_{PtMn} to Equation 4.4, using a least squares method, returns $\lambda = 4.1$ nm and $\rho_{\text{AFM}} = 165$ μm when diffuse scattering $p=0$ is assumed (Fig. 4.11a). In this approach, we assume that the Ta cap does not contribute to resistance and that the FM layer thickness is held constant at 3 nm as t_{PtMn} is varied between 2-20 nm.

To next isolate the PtMn twofold magnetoresistance contribution within the bilayer magnetoresistance data, we combine the FS model of Equation 4.4 with a parallel magnetoresistance model under two additional assumptions: AMR in CoFeMnSi is uncorrelated to PtMn thickness and $R_{\text{AFM}}(t)$ can be modeled as an exponential as evident by the trend in Figure 4.11a. The resistance of our bilayers R can thereby be separated into magnetoresistance contributions MR_{FM} and MR_{PtMn} from the respective CoFeMnSi and PtMn layers as,

$$R(t, \lambda, p) = \left(\frac{1}{\text{MR}_{\text{FM}}(\theta)} + \frac{1}{\text{MR}_{\text{PtMn}}(t, \lambda, p, \theta)} \right)^{-1} \quad (4.5)$$

where $\text{MR}_{\text{FM}} = R_{\text{FM}} + \Delta R_{\text{FM}} \cdot \cos^2(\theta)$, $\text{MR}_{\text{PtMn}} = FS(t, \lambda, p) \cdot R_{\text{AFM}}(t) + \Delta R_{\text{AFM}}(t) \cdot \cos^2(\theta)$, and $R_{\text{AFM}}(t) = a + be^{-t/c}$. Least squares minimization between the bilayer ΔR and Equation 4.5 is shown for for $\alpha = 0^\circ$ and 45° in Figure 4.11b and enables the extraction of MR_{PtMn} . This analysis was performed for all α , allowing us to isolate the AMR contribution from the PtMn layer as a function of t_{PtMn} for any α (Fig. 4.12a).

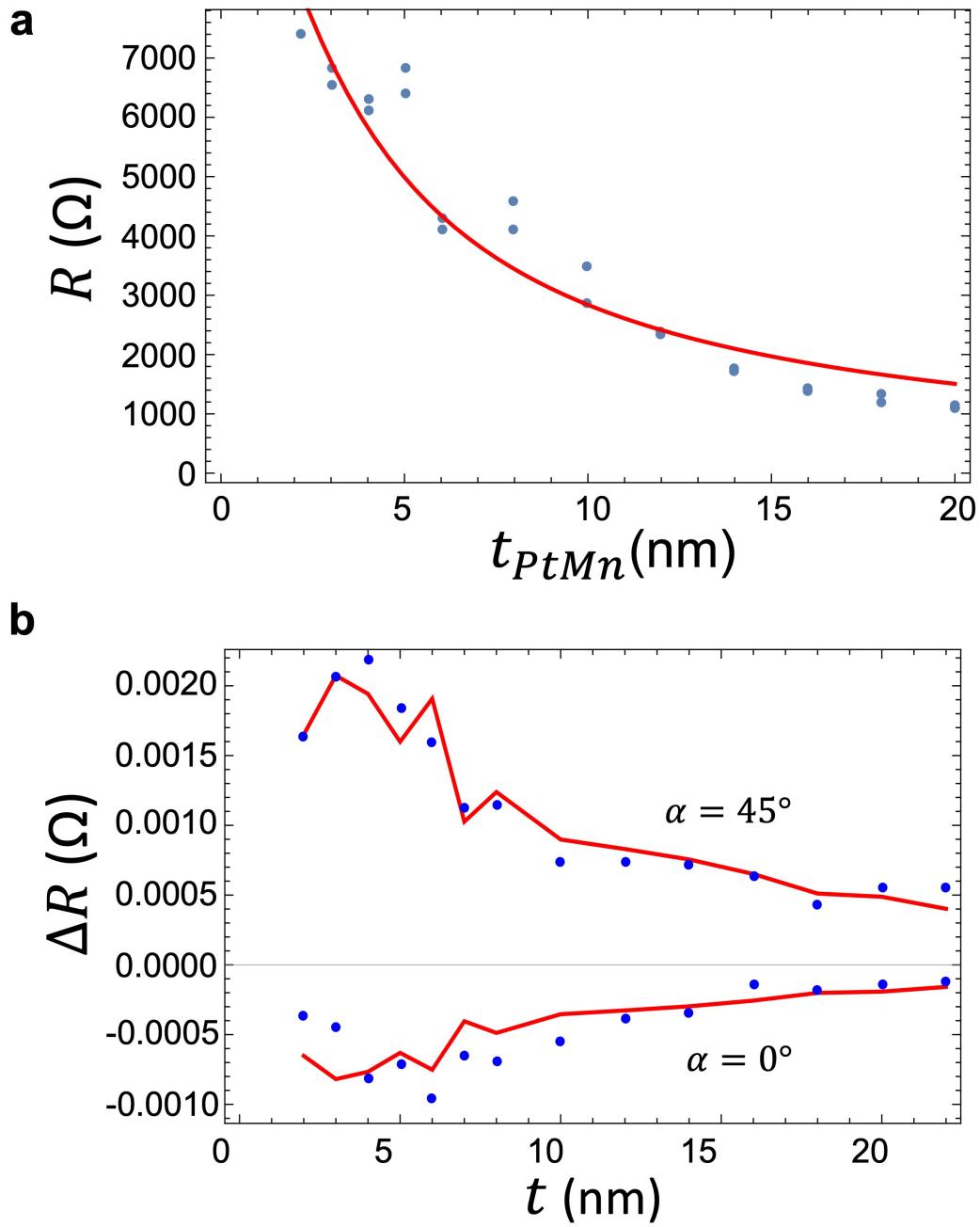


Figure 4.11: (a) Bilayer resistance versus t_{PtMn} (blue) fit under a combined parallel resistance and FS model (red). (b) Thickness dependence of bilayer magnetoresistance ΔR (blue) modeled with Equation 4.5 (red).

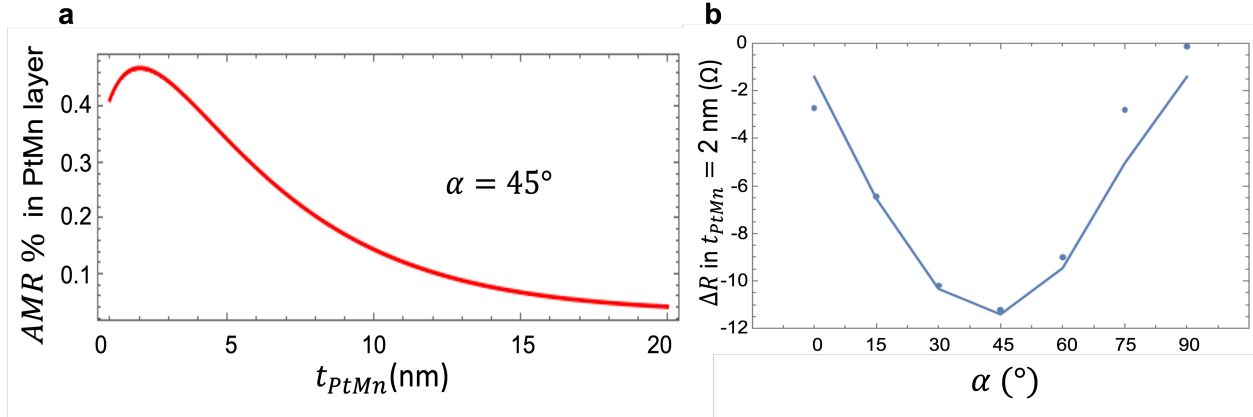


Figure 4.12: (a) Isolated AMR percentage from the PtMn layer in PtMn/CoFeMnSi bilayers as a function of t_{PtMn} when $\alpha = 45^\circ$. (b) Bilayer ΔR for t_{PtMn} (points) with fit line (blue) predicted by 3D atomistic model.

Lastly, intrinsic AMR of PtMn was calculated from the extracted $MR_{PtMn}(t)$ using a 3D atomistic model that establishes a relationship between the measured properties of CoFeMnSi and the intrinsic properties of PtMn. Specifically, the atomistic model accounts for the following in PtMn: inter- and intralayer AFM exchange interactions, nearest-neighbor FM exchange interactions, fourfold magnetic anisotropy within the PtMn ab plane, and the influence of an AFM/FM exchange bias field on two AFM domain populations (Fig. 4.13). Under this model, a trendline in close agreement to the bilayer ΔR versus α for a chosen t_{PtMn} was predicted and subsequently used to calculate an intrinsic AMR of $-10 \pm 3\%$ in PtMn (Fig. 4.12b). Our experimentally measured, giant AMR agrees closely to theoretical prediction of 10% AMR calculated elsewhere by first-principles [13].

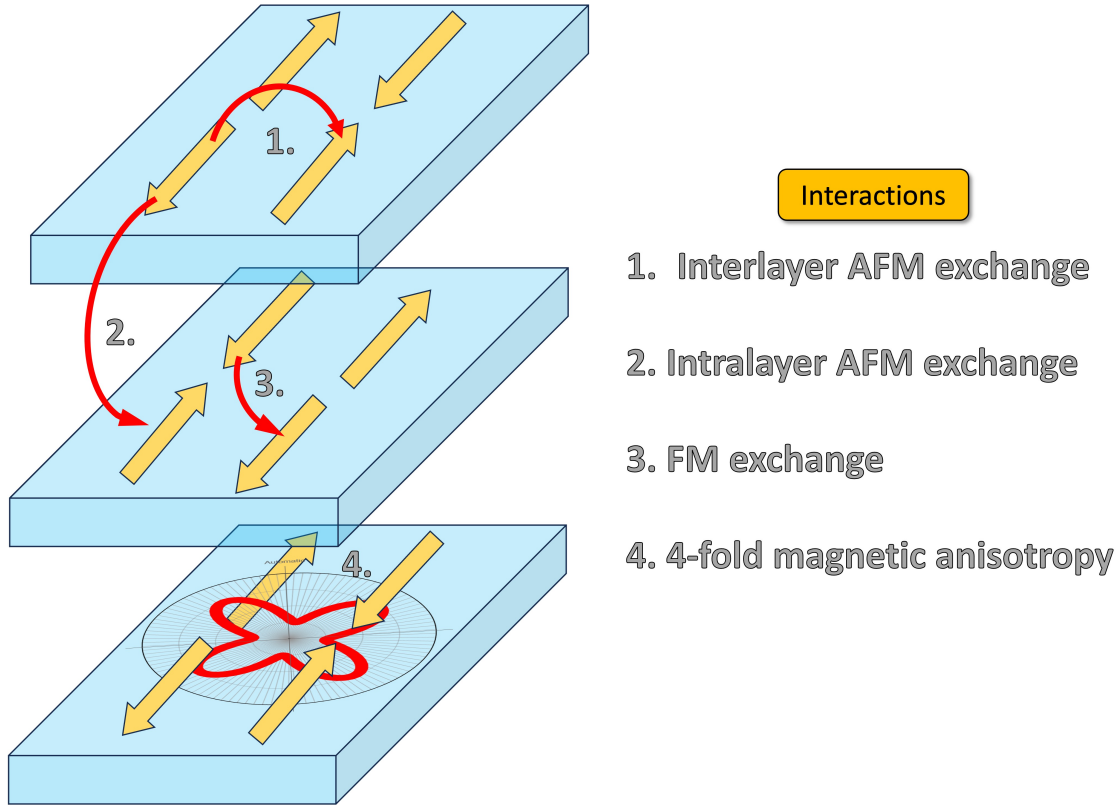


Figure 4.13: Interactions within and between atomic layers of PtMn.

4.5 Discussion

Single crystal films of PtMn are a necessary component for the detection of its AMR. The energy barrier ΔE to reverse the direction of AFM magnetic order is dependent on the grain volume V_{AFM} and anisotropy energy K_{AFM} as $\Delta E = V_{\text{AFM}} K_{\text{AFM}}$. When AFM grain size is large, the order parameter is thermally stable along a particular crystallographic direction and superparamagnetism is avoided. A large distribution of stable AFM grains enables AMR to become apparent on a measurable scale. In this respect, epitaxial grains are highly desirable. Our detection of large AMR along PtMn[110] ($\alpha = 45^\circ$) for t_{PtMn} as small as 2 nm is an indication that there are a significant fraction of thermally stable AFM grains with in-plane order parameter even in the ultra-thin regime.

In Figures 4.8a-g, the AMR curves appear to possess a "phase shift" when measured at different α . This is an artifact of the measurement geometry that does not correspond to any real physical effect. As shown in Figure 4.5a, θ is defined as the angle between I_{AC} and H . The direction of I_{AC} necessarily changes between the various α . However, θ is not defined with respect to a fixed direction of I_{AC} that is consistent across all α . As a result, there exists a fictitious "phase shift" or lag in the R versus θ curves displayed in Figures 4.8a-g. This arises solely from the definition of the experimental coordinates. Figures 4.8a-g can be fully reproduced when the definition of I_{AC} (and thereby θ) is made to share a common reference frame with α through an appropriate coordinate transformation.

In exchange-coupled AFM/FM systems, there is a tendency for FM magnetization to align perpendicular to an AFM easy axis by energy minimization. This perpendicular coupling between FM magnetization and AFM order is generated by an exchange field H_{ex} that exists in the film plane of our system. As an applied field rotates the direction of FM magnetization, the direction of H_{ex} is naturally changed and the AFM order parameter is inclined to move in order to maintain a 90° orientation to H_{ex} at all times. Despite an H_{ex} of roughly 200 kOe, the AFM order parameter is unable to complete a 360° rotation with respect to I_{AC} during any of our AMR measurements. Instead, the AFM order parameter is only slightly deflected away from its equilibrium position due to the magnetocrystalline anisotropy K_{AFM} and applied field limitations. As a result, only a fraction of the intrinsic AMR of PtMn contributes to the AMR measured in our bilayers. The total intrinsic AMR of PtMn is determined from the experimental data separately using the model described in section 4.4.

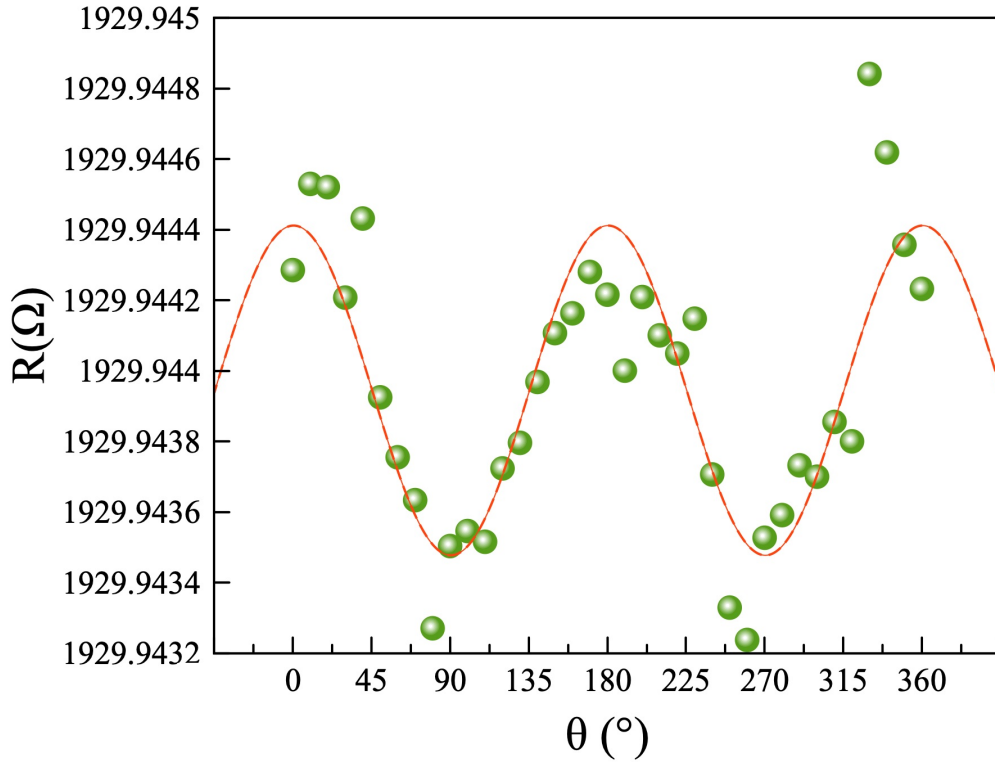


Figure 4.14: The sensitivity of the magnetoresistance measurement setup is highlighted by our ability to detect AMR as small as $4.8\text{E-}5\%$ in a 16 nm film of PtMn.

Our detection of small-angle deflections of the AFM order parameter is enabled by the low-noise magnetoresistance setup described in section 3.4.3, wherein resistance changes of 1 part per 10^5 are within measurable limits. Given the sensitivity of our measurement setup using a Wheatstone bridge, an AMR of $4.8\text{E-}5\%$ in a bare 16 nm PtMn film is within detectable limits. However the signal is much noisier compared to any of the resistance data in the bilayer configuration. This underscores the importance of the CoFeMnSi layer which greatly improves the signal-to-noise ratio and is essential for the reliable detection of AMR in PtMn especially to low t_{PtMn} .

The largest AMR in our PtMn/CoFeMnSi bilayers is seen for $t_{\text{PtMn}} = 4$ nm when $\alpha = 45^\circ$ and decreases with increasing t_{PtMn} . Because the size of the exchange field H_{ex} decays with distance from the FM/AFM interface, this result is in agreement with expectation. For

thicker PtMn layers, there is little AFM motion in the bulk and thus a smaller AMR is observed. Below $t_{\text{PtMn}} = 4$ nm, other factors including surface roughness, the compensated or uncompensated nature of the AFM layer at the interface, and interlayer diffusion become more significant. The lower AMR seen for $t_{\text{PtMn}} < 4$ nm is likely a result of such effects.

A qualitative understanding of our main results can also be illustrated with the help of Figure 4.15. Two equivalent AFM domains represented by solid green arrows exist in the film plane. In the ground state, these domains lie along the AFM easy axes represented by black dashed lines. Applied current I_{AC} is fixed at the angle $\alpha = 45^\circ$ for demonstration. The magnetization of the FM layer M is assumed to be parallel to the applied field H . When M is oriented at 45° with respect to both AFM domains (Case I), both AFM domains deviate away from their respective easy axes to become more perpendicular to M . In Case II, M is parallel to one AFM domain and perpendicular to the other. The domain parallel to M experiences zero torque, while the domain perpendicular to M will experience only a negligible amount of spin canting since the H in our study is weak. Therefore the effect of M on the perpendicular AFM domain is also effectively zero.

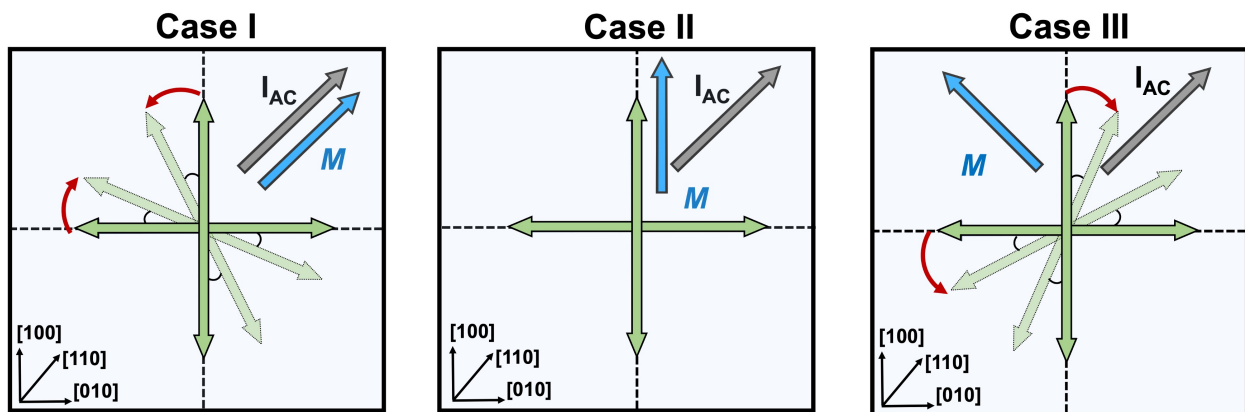


Figure 4.15: Cartoon illustration depicting the influence of FM magnetization direction (blue) on two in-plane AFM domains (green) when $\alpha = 45^\circ$.

In Case I, the AFM domains in their *deviated* state (light green) are furthest from parallel to the direction of I_{AC} . In a material with positive AMR, a resistance minimum would

ordinarily be observed as a result. However, Case I corresponds to a resistance maximum in the experimental data which indicates that the intrinsic AMR in PtMn is negative (see $\theta = 0^\circ$ in Figure 4.8d). In Case II, neither AFM domain is appreciably deviated by M though a larger fraction of AFM domains are parallel to I_{AC} than in Case I. This yields a resistance decrease. In Case III, the AFM domains are maximally parallel to I_{AC} , which results in a resistance minimum. The cartoon in Figure 4.15 agrees with what is experimentally reported in Figure 4.8d.

While the direction of I_{AC} in Figure 4.15 may change based on α , the motion of the AFM domains as depicted does not. Accordingly, the same cartoon may be used to explain why a resistance minimum is observed when I_{AC} is rotated to the $[010]$ axis for example (i.e., $\alpha = 0^\circ$). In this case, I_{AC} along $[010]$ makes an effectively equivalent orientation with respect to the canted domains in Case I and III such that no net change in resistance is produced between the two cases. Furthermore, there is effectively zero deviation in the AFM domains in Case II— even with $\alpha = 0^\circ$ —which is needed to produce AMR. These descriptions explain why AMR is experimentally tiny for $\alpha = 0^\circ$. The fact that AMR is non-zero at $\alpha = 0^\circ$ can be ascribed to unequal populations of the two types of AFM domains.

Figure 4.9a shows the AMR magnitude, expressed as a percentage, plotted against α for $t_{PtMn} = 4$ nm. Starting from $\alpha = 0^\circ$, the AMR trends upwards, reaches a maximum at $\alpha = 45^\circ$, and steadily declines from $\alpha = 45^\circ$ to $\alpha = 90^\circ$. In terms of the crystallographic axes, this corresponds to a maximum AMR for I_{AC} along PtMn $[110]$ and minimum AMR along $[100]$. This trend is consistent for all t_{PtMn} .

The unequal AMR percentages for $\alpha = 0^\circ$ and $\alpha = 90^\circ$ is an unexpected finding in the experimental results. Although these correspond to equivalent PtMn crystallographic directions $[100]$ and $[010]$, the AMR percentages between these two directions are different, in some cases, by as much as 0.07% (Fig. 4.9b). As demonstrated in Figure 4.8a and g, there exists a larger fourfold component at $\alpha = 90^\circ$ compared to $\alpha = 0^\circ$ which is a trend observed across

all t_{PtMn} . A complete understanding of this experimental finding is presently lacking and necessitates further study. Future improvements to our work will also include obtaining experimental values of several material parameters, including the fourfold magnetic anisotropy constant of PtMn, through ferromagnetic resonance. These will in turn be used to improve the 3D atomistic model and thereby reduce the error bar on the $-10\pm 3\%$ intrinsic AMR of PtMn reported.

4.6 Conclusions

To summarize, our work provides the first quantitative measurements of AMR in a high temperature, collinear antiferromagnet PtMn. Our theoretical model is in good qualitative agreement with the experimental data and allows us to report a giant intrinsic AMR of $-10\pm 3\%$ in PtMn. In pursuit of this goal, we utilize epitaxial thin films of PtMn grown by co-sputtering. Further, we disclose a general method for detection of AMR in AFM materials by means of exchange-coupling an AFM to a zero-AMR ferromagnet. This detection scheme can plausibly be adapted to other AFM/FM material systems to enable quantification of AMR in the AFM layer. Giant AMR in an AFM holds promise for antiferromagnetic spintronic devices with AMR-based readout which may include current-driven spin torque oscillators [3, 4].

References

- [1] Chappert, C., Fert, A. & Van Dau, F. N. The emergence of spin electronics in data storage. *Nature materials* **6**, 813–823 (2007).
- [2] Juretschke, H. Electromagnetic theory of dc effects in ferromagnetic resonance. *Journal of Applied Physics* **31**, 1401–1406 (1960).
- [3] Siddiqui, S. A. *et al.* Metallic antiferromagnets. *Journal of Applied Physics* **128**, 040904 (2020).
- [4] Duan, Z. *et al.* Nanowire spin torque oscillator driven by spin orbit torques. *Nature communications* **5**, 5616 (2014).
- [5] Fukami, S., Lorenz, V. O. & Gomonay, O. *Antiferromagnetic spintronics* 2020.
- [6] Fina, I. *et al.* Anisotropic magnetoresistance in an antiferromagnetic semiconductor. *Nature communications* **5**, 1–7 (2014).
- [7] Wadley, P. *et al.* Electrical switching of an antiferromagnet. *Science* **351**, 587–590 (2016).
- [8] Bodnar, S. Y. *et al.* Writing and reading antiferromagnetic Mn 2 Au by Néel spin-orbit torques and large anisotropic magnetoresistance. *Nature communications* **9**, 1–7 (2018).
- [9] Marti, X. *et al.* Room-temperature antiferromagnetic memory resistor. *Nature materials* **13**, 367–374 (2014).
- [10] Kriegner, D. *et al.* Multiple-stable anisotropic magnetoresistance memory in antiferromagnetic MnTe. *Nature communications* **7**, 1–7 (2016).
- [11] Galceran, R. *et al.* Isothermal anisotropic magnetoresistance in antiferromagnetic metallic IrMn. *Scientific reports* **6**, 35471 (2016).
- [12] Park, B. G. *et al.* A spin-valve-like magnetoresistance of an antiferromagnet-based tunnel junction. *Nature materials* **10**, 347–351 (2011).
- [13] Liu, Q., Yuan, H., Xia, K. & Yuan, Z. Mode-dependent damping in metallic antiferromagnets due to intersublattice spin pumping. *Physical Review Materials* **1**, 061401 (2017).
- [14] Zhang, W. *et al.* All-electrical manipulation of magnetization dynamics in a ferromagnet by antiferromagnets with anisotropic spin Hall effects. *Physical Review B* **92**, 144405 (2015).
- [15] Dyakonov, M. I. & Khaetskii, A. *Spin physics in semiconductors* (Springer, 2017).

- [16] Shao, Q. *et al.* Roadmap of spin-orbit torques. *IEEE Transactions on Magnetics* **57**, 1–39 (2021).
- [17] Chang, P.-H., Fang, W., Ozaki, T. & Belashchenko, K. Voltage-controlled magnetic anisotropy in antiferromagnetic MgO-capped MnPt films. *Physical Review Materials* **5**, 054406 (2021).
- [18] Umetsu, R., Sakuma, A. & Fukamichi, K. Magnetic anisotropy energy of antiferromagnetic L10-type equiatomic Mn alloys. *Applied physics letters* **89**, 052504 (2006).
- [19] Kang, K., Cahill, D. G. & Schleife, A. Phonon, electron, and magnon excitations in antiferromagnetic L10-type MnPt. *Physical Review B* **107**, 064412 (2023).
- [20] Nozieres, J. *et al.* The role of interfaces in NiFe/Cu/NiFe spin valves. *Journal of magnetism and magnetic materials* **121**, 386–389 (1993).
- [21] Lederman, M. Performance of metallic antiferromagnets for use in spin-valve read sensors. *IEEE Transactions on magnetics* **35**, 794–799 (1999).
- [22] DuttaGupta, S. *et al.* Spin-orbit torque switching of an antiferromagnetic metallic heterostructure. *Nature communications* **11**, 5715 (2020).
- [23] De Groot, R., Mueller, F., van Engen, P. v. & Buschow, K. New class of materials: half-metallic ferromagnets. *Physical review letters* **50**, 2024 (1983).
- [24] Bainsla, L. *et al.* Spin gapless semiconducting behavior in equiatomic quaternary CoFeMnSi Heusler alloy. *Physical Review B* **91**, 104408 (2015).
- [25] Fu, H. *et al.* Structures, magnetism and transport properties of the potential spin-gapless semiconductor CoFeMnSi alloy. *Journal of Magnetism and Magnetic Materials* **473**, 16–20 (2019).
- [26] Bainsla, L. *et al.* Low magnetic damping for equiatomic CoFeMnSi Heusler alloy. *Journal of Physics D: Applied Physics* **51**, 495001 (2018).
- [27] Shick, A. B., Khmelevskiy, S., Mryasov, O. N., Wunderlich, J. & Jungwirth, T. Spin-orbit coupling induced anisotropy effects in bimetallic antiferromagnets: A route towards antiferromagnetic spintronics. *Physical Review B* **81**, 212409 (2010).
- [28] Ladwig, P. F. *et al.* Paramagnetic to antiferromagnetic phase transformation in sputter deposited Pt–Mn thin films. *Journal of applied physics* **94**, 979–987 (2003).
- [29] Umetsu, R. Y., Fukamichi, K. & Sakuma, A. Electrical and magnetic properties, and electronic structures of pseudo-gap-type antiferromagnetic L10-type MnPt alloys. *Materials transactions* **47**, 2–10 (2006).
- [30] Su, Y., Li, M., Zhang, J., Hong, J. & You, L. Voltage-controlled magnetic anisotropy in antiferromagnetic L10-MnPt and MnPd thin films. *Journal of Magnetism and Magnetic Materials*, 166758 (2020).

- [31] Krén, E. *et al.* Magnetic structures and exchange interactions in the Mn-Pt system. *Physical review* **171**, 574 (1968).
- [32] Wang, J. *et al.* Quick determination of included angles distribution for miscut substrate. *Measurement* **89**, 300–304 (2016).
- [33] Wang, J. *et al.* Quick determination of included angles distribution for miscut substrate. *Measurement* **89**, 300–304 (2016).
- [34] Brun, K., Kjekshus, A. & Pearson, W. Equiatomic transition metal alloys of Manganese: I. The tetragonal PtMn phase. *Philosophical magazine* **10**, 291–299 (1964).
- [35] Montoya, E. *et al.* Spin transport in tantalum studied using magnetic single and double layers. *Physical Review B* **94**, 054416 (2016).
- [36] You, C. *et al.* Fabrication and intrinsic physical property of spin-gapless like Heusler alloy CoFeMnSi single crystal. *Materials Research Bulletin* **133**, 111044 (2021).
- [37] Fu, H., You, C., Ma, L. & Tian, N. Large and temperature-stable anomalous Nernst effect under a favorable out-of-plane thermal gradient in the epitaxial Heusler spin gapless-like CoFeMnSi thin film. *Materials Research Express* **6**, 116119 (2019).
- [38] McGuire, T. & Potter, R. Anisotropic magnetoresistance in ferromagnetic 3d alloys. *IEEE Transactions on Magnetics* **11**, 1018–1038 (1975).
- [39] Thomson, W. XIX. On the electro-dynamic qualities of metals:—Effects of magnetization on the electric conductivity of nickel and of iron. *Proceedings of the Royal Society of London*, 546–550 (1857).
- [40] Ahadi, K. *et al.* Anisotropic magnetoresistance in the itinerant antiferromagnetic EuTiO₃. *Physical Review B* **99**, 041106 (2019).
- [41] Sondheimer, E. H. The mean free path of electrons in metals. *Advances in physics* **50**, 499–537 (2001).
- [42] Fuchs, K. *The conductivity of thin metallic films according to the electron theory of metals* in *Mathematical Proceedings of the Cambridge Philosophical Society* **34** (1938), 100–108.

Chapter 5

Development and characterization of nanopillar arrays

5.1 Introduction

A disturbance in the magnetic order of a magnetic material propagates in the form of a spin wave whose quanta are known as *magnons*. The scientific interest surrounding magnons stems from their ability to be excited without the translational motion of the electron. By encoding information into the phase or amplitude of their motion, magnons can be used as data carriers that produce zero energy waste through Joule heating.

Novel phenomena can arise when many individual magnetic elements are combined into a larger periodic structure as in the case of a magnonic crystal. A magnonic crystal is defined as a periodic spatial arrangement of artificial magnetic media—reminiscent of the crystal structure inside a solid—whose spin wave properties can be tailored by changing the geometric or magnetic parameters of the array elements. These factors directly influence the magnon band structure inside the crystal and thereby dictate the frequency and spin

wave modes that are allowed to propagate through it. The magnetization of certain magnonic crystals can also be changed dynamically by application of an external field which gives them a further degree of freedom. Because magnonic crystals are highly tunable, they pave a path towards the development of new processing devices based on magnons which may include filters, logic gates, transistors, and more. Implementing these components into memory devices and computing schemes is a large goal of magnonics [1].

Two-dimensional magnonic crystals comprised of perpendicularly magnetized nanopillars represent a particular class of static crystals. These systems are predicted to have rich spin wave dynamics which include non-reciprocity and topologically protected collective edge modes. Several requirements, which have been carefully defined in the theoretical literature, must be met for such behavior to exist: individual nanopillars must be in sufficient proximity to dipolarly interact; the pillars must have a non-zero out-of-plane component of magnetization M_z ; and the crystal must have a complex periodicity with at least 2 nanopillars per primitive cell [2–5]. Meeting all three of these requirements simultaneously is experimentally challenging.

Beyond magnonic crystals, tall nanopillars are useful in the creation of magnetic tunnel junctions (MTJs) with perpendicular magnetization. These have gained popularity due to scaling limitations associated with in-plane versions. For instance, the magnetostatic field of in-plane MTJs increases as their sizes shrinks below ~ 50 nm which leads to issues with stability, and their elliptical shape, which keeps their magnetization in-plane, limits their packing density. Accordingly, research efforts have moved towards perpendicular varieties which have already succeeded in producing tunneling magnetoresistance ratios above 100% at room temperature [6].

Here we put forth a nanofabrication recipe for micron-scale, square arrays of high aspect ratio nanopillars by electron beam lithography. We subsequently characterize the out-of-plane component of magnetization in the arrays by anomalous Hall effect (AHE) measurements as

a function of pillar diameter and separation. We utilize a typical magnetic tunnel junction stack possessing a thick CoFeB layer (≥ 20 nm) such that shape anisotropy, rather than material or interfacial properties alone, assists in pulling magnetization out of the film plane [7].

5.2 Fabrication of Nanopillars

5.2.1 Overview

Micron-scale arrays ($10 \times 10 \mu\text{m}$) of nanopillars were fabricated via electron beam lithography from multilayers deposited by Everspin Technologies (Fig. 5.2). A thick CoFeB ferromagnetic layer was used in the stack for the purpose of enhancing the pillar aspect ratio (height:diameter). Nanopillars with diameters as small as 30 nm were defined using ion mill etching and hydrogen silsesquioxane (HSQ) electron beam resist developed in a mixture of NaOH, NaCl, and DI water.

The adhesion of this HSQ dot mask to the multilayer is the pivotal difficulty in the fabrication process. Since the mask of resist must be thick enough to withstand long etching and the dot diameter must be tiny, the aspect ratio of the mask itself is high (around 2.5) and prone to toppling. This is a challenge that makes the lithography of nanopillars much different than typical nanowire devices, where wire widths may be 30-40 nm but lengths are >100 nm. The following recipe outlines the procedure for fabricating micron scale arrays of nanopillars onto Hall crosses for anomalous Hall measurements.

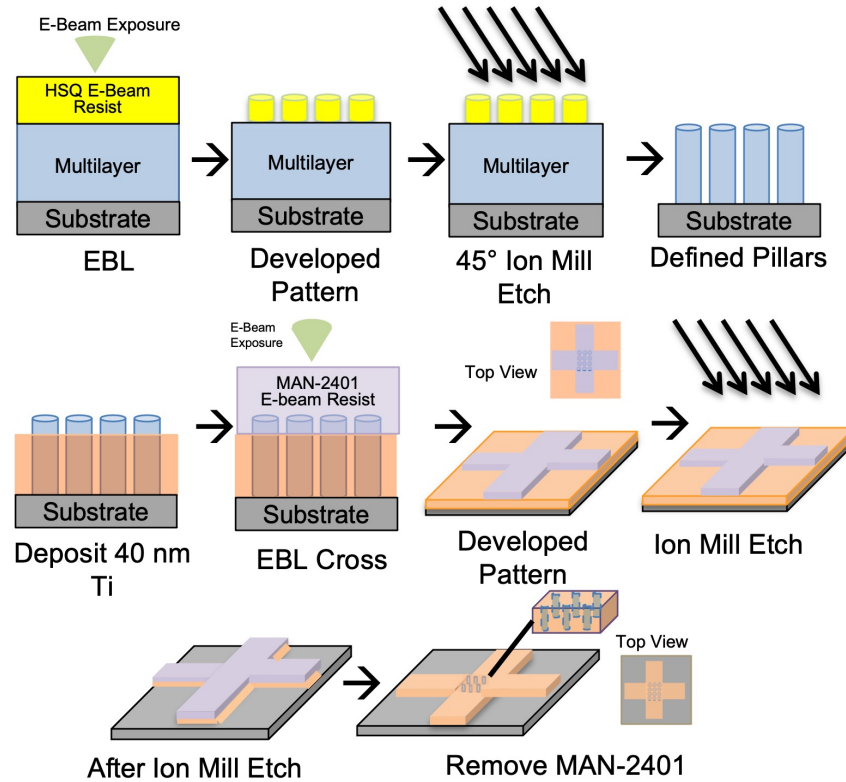


Figure 5.1: Step-by-step nanopillar fabrication process.

5.2.2 Preliminary Steps

Etching rate of multilayer

The ion beam etching rate of the entire multilayer is critical to know since pillars must ultimately be etched down to the substrate. The etching rate of the multilayer can be determined by dicing a piece of the multilayer and measuring its thickness before and after a prolonged amount of etching using XRR or an optical profilometer. The milling time through the multilayer will depend on the choice of etching angle. As will be discussed later, a 45° etching angle was found to be most suitable for pillars and thus the milling time through the multilayer should be determined for this angle.

Aside from XRR or profilometry, one can also get rough approximations of whether conductive material remains on the sample post-etch using a four-point resistance measurement or

by visually comparing the sample to a color chart (these exist mainly for SiO_2). While these options will not yield numerical values of thickness, they can serve as quick checks to ensure the multilayer has been completely etched to the substrate.

Etching rate of HSQ Resist

The highest resolution electron beam resist that is currently available commercially is negative tone HSQ. Capable of producing features as small as 10 nm, it is an ideal choice for making nanopillars, or other features, of sub-100 nm dimensions. It should be noted that HSQ requires high dosages ($\sim 6000\text{-}8500 \mu\text{C}/\text{cm}^2$) and also reacts with air and light, so it is advised that the time between spincoating, lithography, and development be kept under 2 hours when working with it. Nanopillars in this thesis were fabricated using Dow Corning XR-1541 4% which has a spin-on film thickness between 55-115 nm depending on RPM (1000-5000 RPM). Thicker and thinner formulations of HSQ are also available through Dow or more recently Applied Quantum Materials.

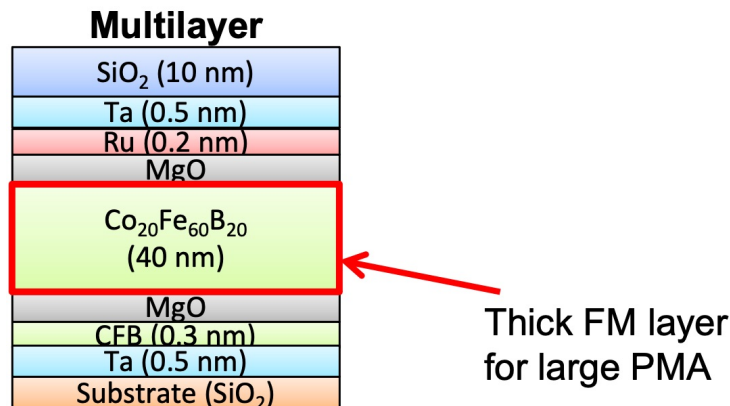


Figure 5.2: Three 10” wafers with the multilayer stack depicted were deposited by Everspin with a CoFeB layer of 20, 40, or 50 nm.

The etching rate of HSQ at 45° (the milling angle which will be used to define the pillars) must be determined: if the resist can be entirely etched away before the multilayer finishes etching then the pattern transfer of the dot mask will not work. The etching rate can be

found using a two-step nanofabrication with subsequent AFM characterization. In the first step, a series of vertical HSQ stripes are fabricated on the multilayer via EBL as shown in Figure 5.3. After development, a series of horizontal stripes made of MAN-2401 resist are fabricated on top of the vertical HSQ lines. The result is a crosshatch pattern where the the HSQ lines are covered by MAN-2401 at certain locations. By etching the sample then removing the lines of MAN-2401 with acetone, the etching rate of HSQ can be found based on step height measurements taken on the crosshatch via AFM (Figs. 5.5 and 5.4).

- Sonicate a piece of SiO₂ substrate in acetone then IPA for 5 minutes each
- Blow dry with nitrogen gas
- Spincoat the substrate with HSQ at 3000 RPM for 45 seconds (Program 19)
- Write a pattern of vertical stripes 5 μm wide using EBL (Fig. 5.3) (I = 6.4 nA , dose = 6000 μC/cm²)

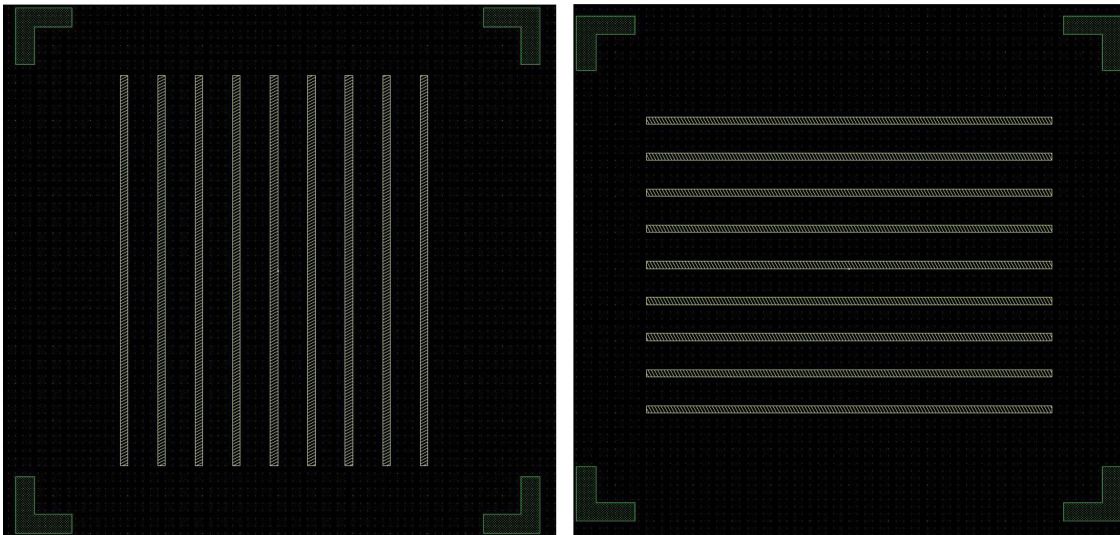


Figure 5.3: LayoutEditor designs for the crosshatch pattern. Vertical HSQ stripes of 5 micron widths are patterned by EBL onto the sample. Lines of MAN-2401 are then patterned horizontally overtop the vertical lines in a separate EBL step. To avoid headaches, it is useful to make one set of lines slightly wider than the other.

- Develop HSQ in the diluted salty developer according to section 5.2.4

- Spincoat chip with MAN-2401 at 3600 RPM for 45 seconds (Program 5)
- Bake sample 90°C for 60 seconds
- Write a pattern of horizontal stripes 3 μm wide using EBL ($I = 6.4 \text{ nA}$, dose = 250 $\mu\text{C}/\text{cm}^2$)
- Place the sample in a glass beaker
- Pour maD-525 developer into the beaker and develop for 60 seconds
- Transfer sample to DI water to stop development (leave the sample undisturbed for 3 minutes)
- Blow dry with nitrogen gas
- Etch sample briefly in ion mill at 45° (long enough to remove a measurable amount of resist but not all of it– 5 minutes maximum should be sufficient)
- Remove the MAN-2401 by sonicating in acetone then IPA for 5 minutes each
- Blow dry with nitrogen gas
- Use AFM to measure the step heights between specific areas of the crosshatch pattern according to Fig. 5.5

It is important to note that this process utilizes two negative tone resists and will require modification if interested in finding the etching rate of a positive resist. In doing so, it is also relevant to consider the developers that will be used. Here MAN-2401 was specifically chosen for protecting the HSQ resist because its developer—and the acetone and IPA that removes MAN—does not harm the HSQ in any way.

If the etching rate of HSQ turns out to be faster than that of the multilayer sample and a thicker HSQ formulation is not available, there are a few workarounds to increase its

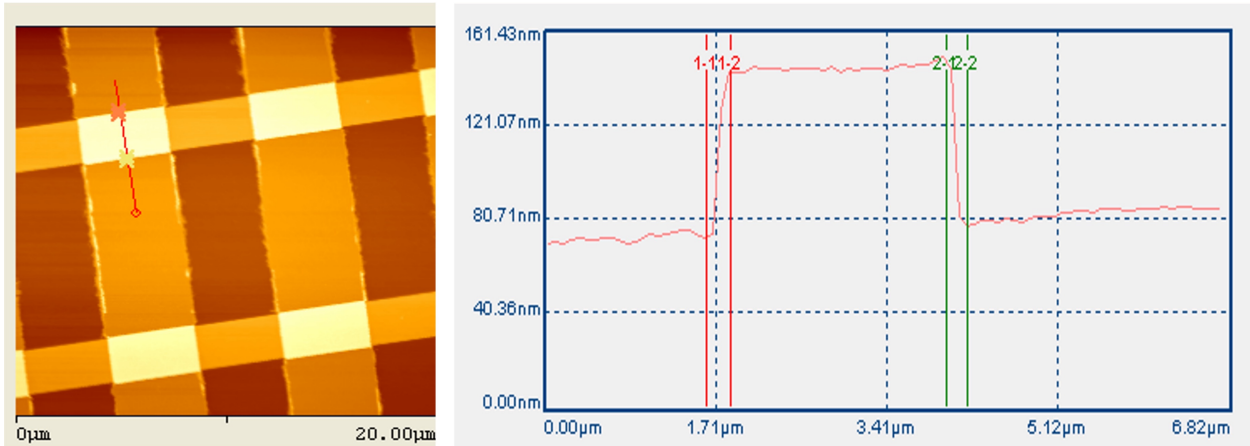


Figure 5.4: AFM image of the crosshatch with a step height measurement.

thickness. The first and simplest choice is to spincoat at a slower RPM, consulting the manufacturer's thickness vs. RPM charts as a guide. From experience, attempting to go any slower than the minimum recommended RPM always results in undesirable streaking patterns across the chip. The second method to increase resist thickness is to spincoat for a briefer amount of time. Spinning HSQ for 45 seconds versus the recommended 60 seconds at an identical RPM can nearly double the height (e.g., a 3600 RPM spincoat at 60 second yields 70 nm thickness while 45 seconds yields 132nm). Interestingly, this created no significant changes in dosages or development time. The third method is to repeat the spincoating process twice. This does not result in films of double thickness but adds around 20 nm of extra height, which may be useful if only needing to extend the etching lifetime of HSQ for an additional minute or so. Spincoating the HSQ onto an underlayer, like PMMA for instance, is unadvised as patterns defined by EBL proved susceptible to cracking (Fig. 5.6).

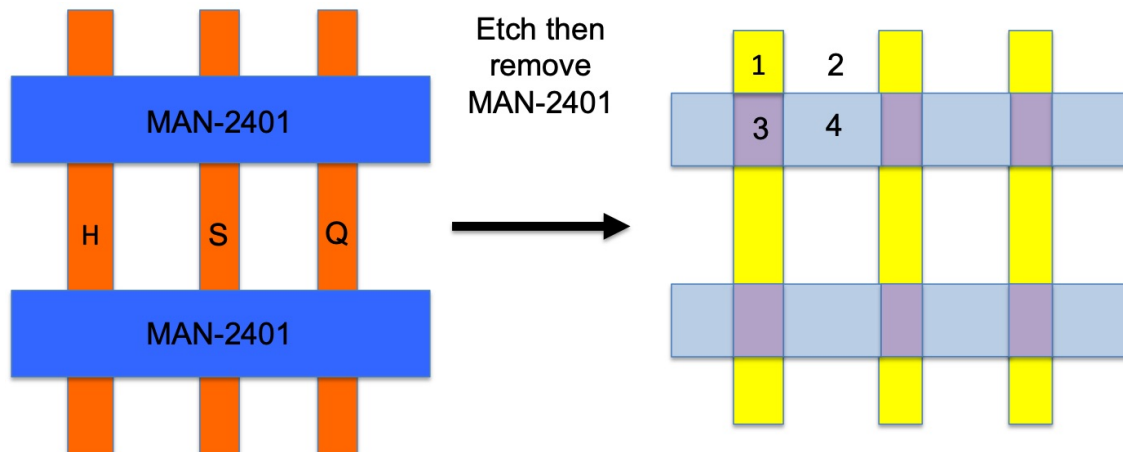


Figure 5.5: Crosshatch pattern on bare SiO_2 substrate (left) used to determine HSQ etching rate. After milling the crosshatch then removing the MAN-2401 (right), the numbered areas represent the resulting regions: etched HSQ (1), etched SiO_2 substrate (2), un-etched HSQ (3), and un-etched SiO_2 (4). The 3-4 step height yields the height of un-etched HSQ while the 1-3 step height yields the the amount of HSQ that has been etched.

5.2.3 Sample Preparation

Cleaning sample

Chips of 10 x 10 mm size were diced from a 10" wafer (Everspin) and sonicated in acetone then IPA for 5 minutes each. This is the only cleaning step performed prior to the fabrication of the dot mask. In most nanofabrication processes a second, more aggressive cleaning step is usually advised since a well-prepared surface promotes mask adhesion. Some easily accessible options include the Gatan Plasma Cleaner at LEXI, pre-baking the chip $>100^\circ\text{C}$ before spincoating to release moisture, or doing an RF bias cleaning in the sputtering system (60 seconds, 40% power). For HSQ in particular, group members have reported luck in improving adhesion with these methods, specifically when fabricating nanowires. However, in the development of this nanopillar recipe all of these pre-treatment choices failed to improve the adhesion of the HSQ dot mask at the sub-50 nm diameter scale. Adhesion could only be promoted by modifying the chemical developer which will be discussed later.

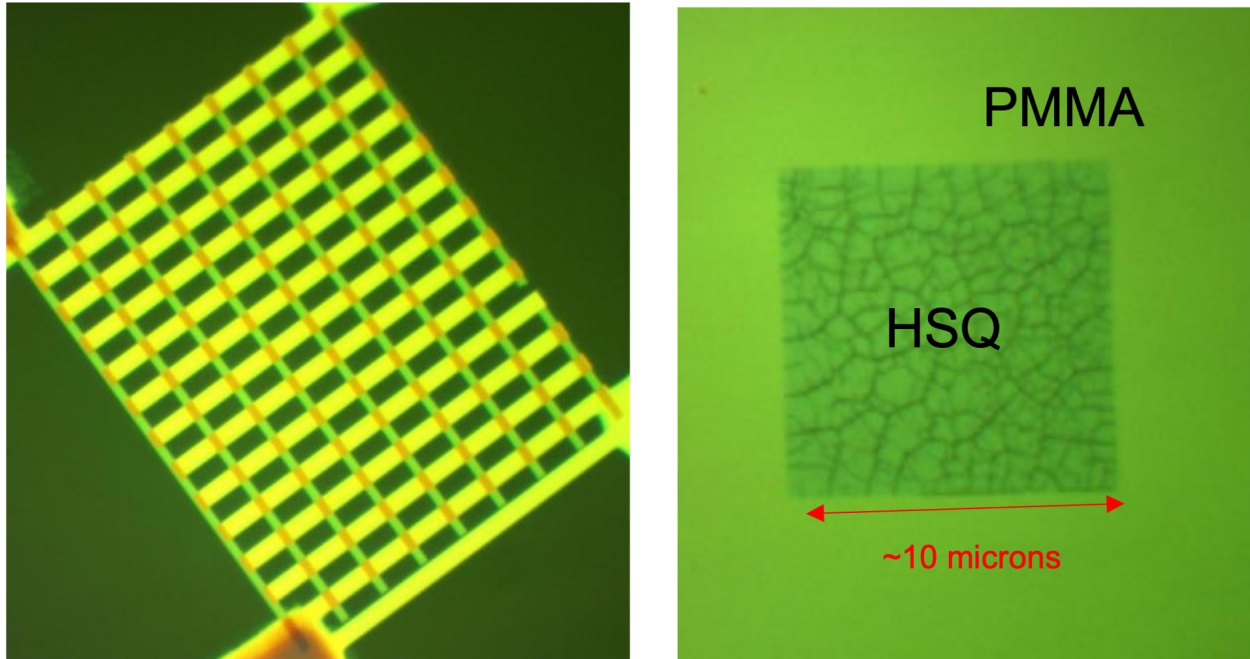


Figure 5.6: Crosshatch as seen under an optical microscope (left). A square patterned by EBL out of an HSQ/PMMA bilayer (right).

Spincoat HSQ

HSQ should be taken out of the chemical refrigerator approximately 15 minutes prior to spincoating and warmed to room temperature. A single coat of HSQ should be spun onto the sample using Program 19 (3000 RPM for 45 seconds) which yields approximately 75 nm of HSQ. No pre- or post-baking was performed. The sample should immediately be brought to the SEM for EBL after spincoating.

5.2.4 Pillar Definition

Write Dot Array

The full design of the nanopillar array with leads is shown in Figure 5.7. The first step is to write the central array of dots framed by larger L-shaped alignment marks. Since

only the nanopillars within the active region of the Hall cross will be probed by the AHE measurement, alignment hassles can (and should) be avoided by simply making the size of the array larger than the active region of the cross (Fig. 5.8).

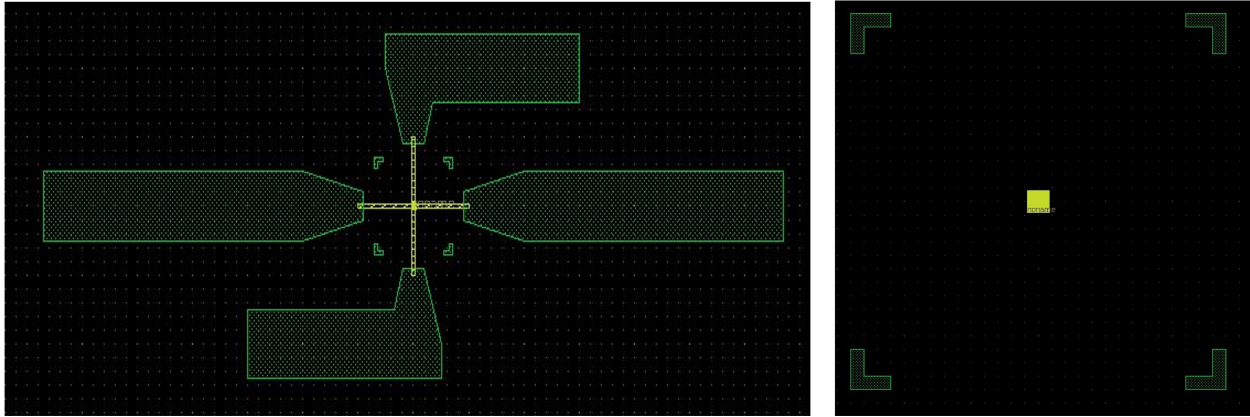


Figure 5.7: Full design of the Hall cross with dot array at its center (left). The first EBL step is to write the array and alignment marks (right).

The center-to-center distance between dots (pitch) should be chosen carefully: too close and shadowing effects from neighboring dots will lead to anisotropic pillars during milling; too large and pillars will not dipolarly interact. An extra $\sim 10\text{-}20$ nm tolerance beyond the calculated shadow length, estimated by simple trigonometry, was found to be a good separating distance. A pitch of 200 nm for a $10 \times 10 \mu\text{m}$ array of 30 nm HSQ dots proved to be a viable choice. Based on the outline provided in Section 3.3.1, the electron beam should be appropriately configured to write the pattern shown right in Figure 5.7 under the following conditions:

- Alignment marks: dose = $6000 \mu\text{C}/\text{cm}^2$, $I = 6.4 \text{ nA}$
- Array: dose = $8300 \mu\text{C}/\text{cm}^2$, $I = 13 \text{ pA}$

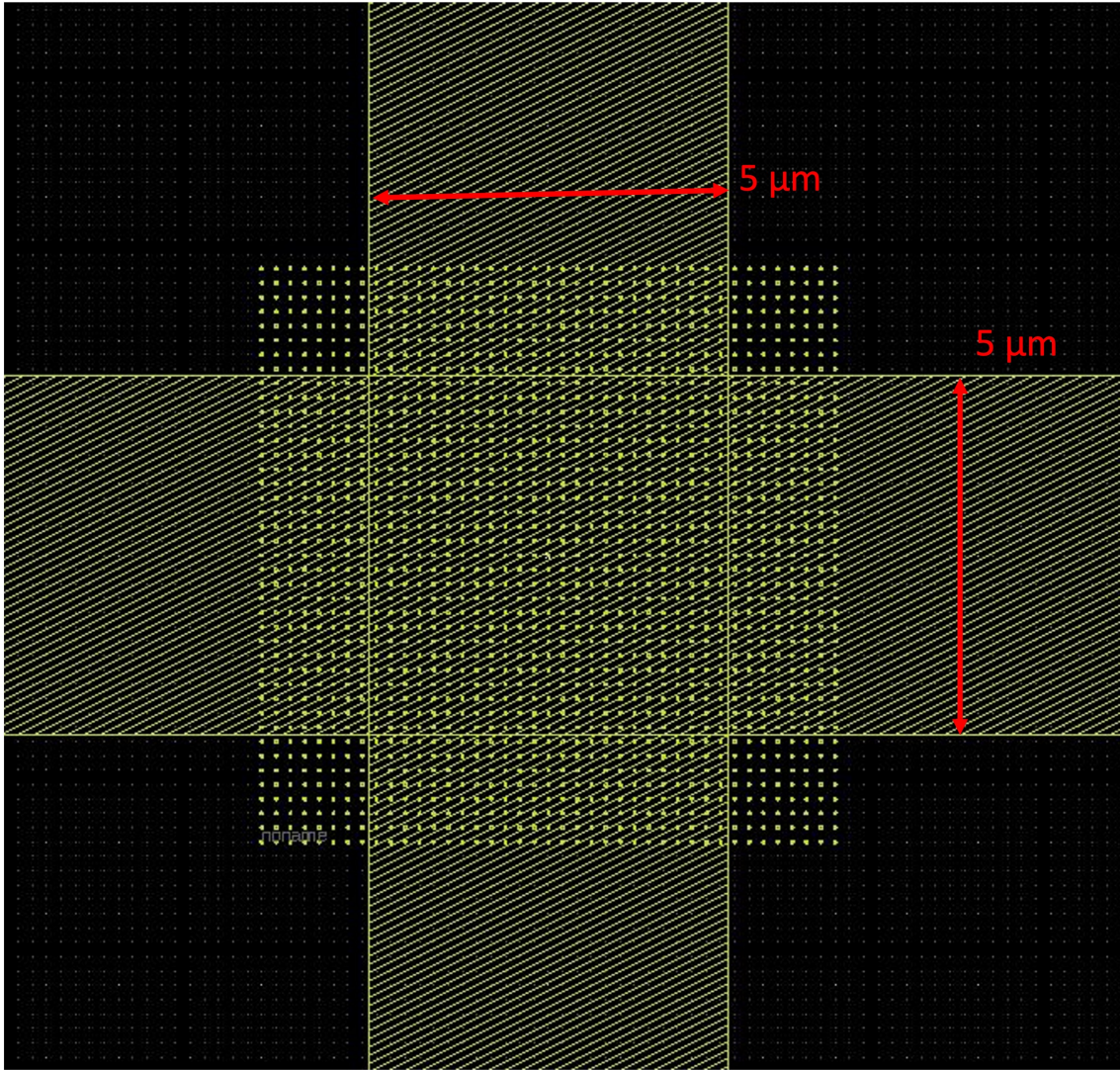


Figure 5.8: The array size should exceed the dimensions of the active region at the center of the cross.

Develop HSQ

The standard recipe for high-resolution salty developer is an aqueous mixture of 1 wt % NaOH and 4 wt % NaCl [8]. However this is an aggressive process that can make high aspect ratio masks susceptible to toppling or washing away (Fig. 5.9). For excellent adhesion of sub-50 nm features, salty developer diluted with additional water was found to work best (Fig. 5.10). In general, HSQ can be developed with either gentle (MF-319) or aggressive (salty) chemical solutions, but MF-319 is not applicable for nanopillar fabrication given its

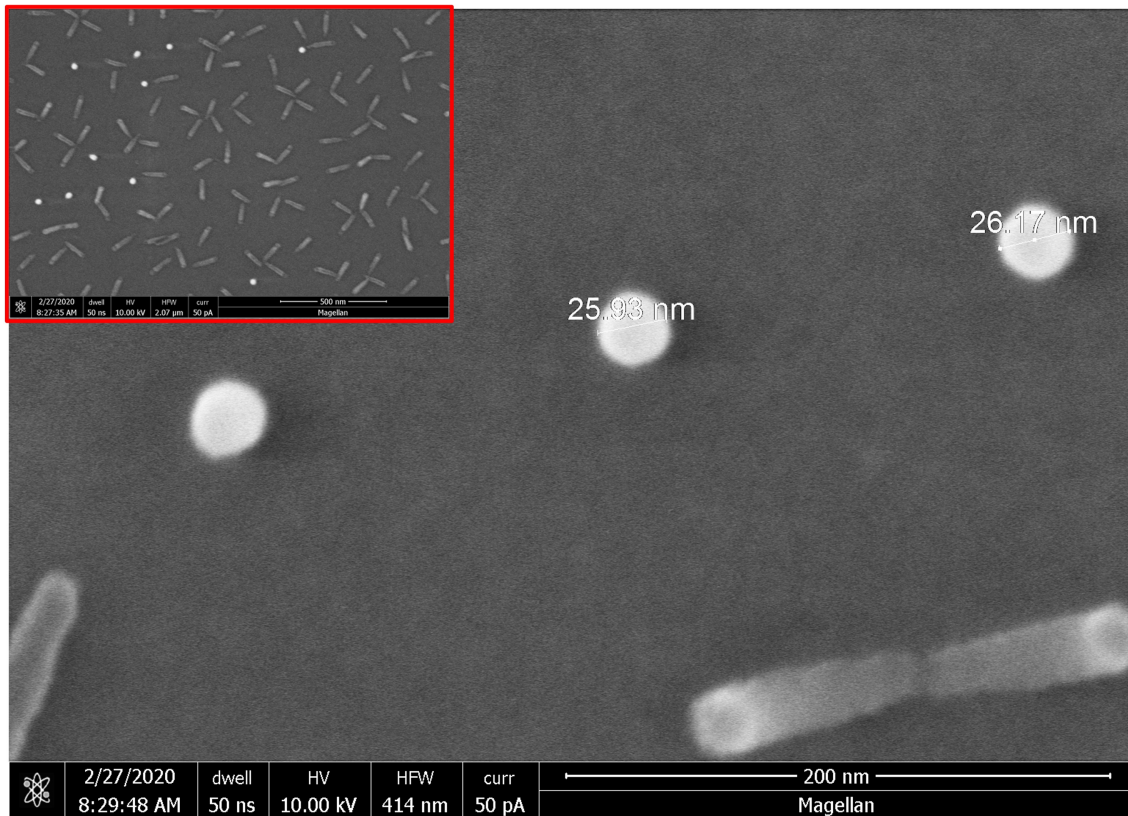


Figure 5.9: High-aspect ratio dot masks developed in the standard aqueous mixture of 1 wt % NaOH and 4 wt % NaCl which have fallen over.

low resolution. Dosages and etching rates will also change significantly if using MF-319.

To make the diluted developer in the fume hood:

- Rinse a new 500 mL HDPE bottle with DI water
- Pour 4 mL NaCL into a graduated cylinder then into the HDPE bottle
- Pour 1 mL NaOH into a graduated cylinder then into the HDPE bottle
- Pour 195 mL DI water into a graduated cylinder then into the HDPE bottle
- Label and date the HDPE bottle
- Store the developer at room temperature

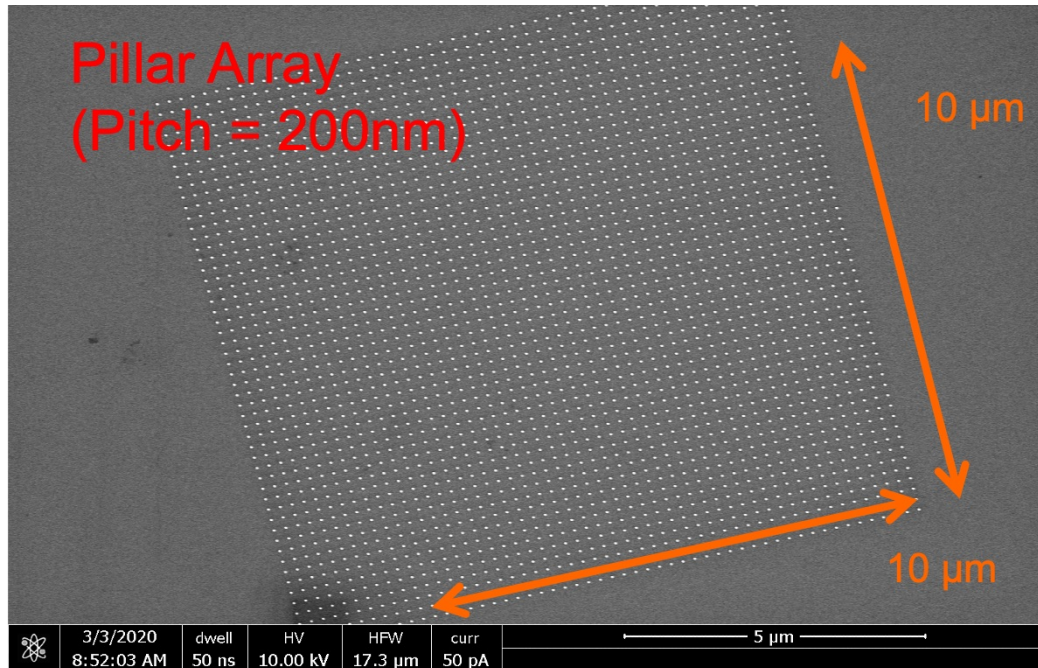


Figure 5.10: HSQ dot array developed in diluted salty developer.

To develop the HSQ:

- Place the sample in a glass beaker
- While holding one corner of the sample down with tweezers, pour the dilute salty developer over top then release tweezers
- Allow sample to develop for 3 minutes (do not swirl)
- Rinse sample with HPLC grade DI water
- Blow dry with nitrogen gas

If considering imaging the dot mask under the SEM, it is advisable to stick to only a small corner of the array. The electron beam is known to interact with the HSQ, even after development, and cause features on the mask to expand undesirably. A single dot will most certainly be deformed after imaging.

Etch Dot Mask

This is ultimately the most important step in the fabrication process and the choice of etching angle is critical. A high angle etch at 80° was tried first but yielded irregular or deformed pillars. The best results for were achieved using a 45° etch followed by a 10° clean-up etch for the last 30 seconds of the milling. Based on the time to etch through the multilayer as determined in section 5.2.2, the sample should be etched for at least as long as it takes to completely mill through the multilayer (and perhaps a little longer to etch into the substrate slightly). After the etch, one should also be sure to consider how much HSQ remains on top of the pillars. This can skew height measurements or even influence electrical measurements if significant since HSQ is electrically conductive. For the nanopillars fabricated from the Everspin multilayers, all of the HSQ was etched away entirely so this was a non-issue.

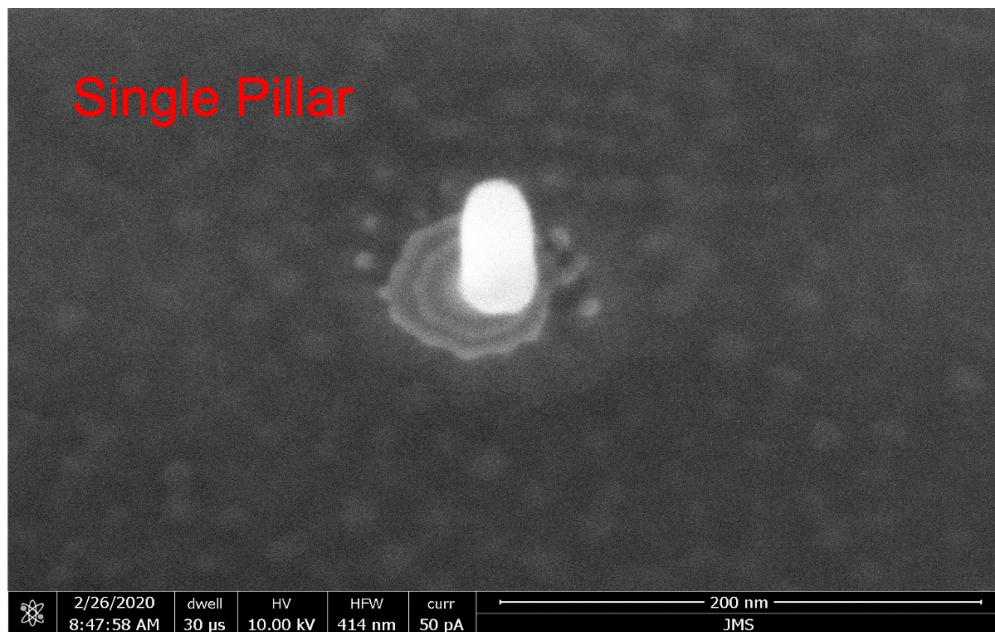


Figure 5.11: SEM image of a single pillar observed using the stage tilt.

If necessary, it is also possible to reduce dot sizes by trimming a larger diameter mask at 10° in the ion mill before proceeding with the pillar-defining 45° etch. In some initial tests, this method was capable of reducing a 50 nm dot down to 30 nm. It is presumably possible to push to diameters <30 nm by this route but it has not been thoroughly tested. It is important

to remember, however, that when trimming an *array* of dots at such low angle, shadowing effects will be quite large and the separation between dots will need to be significant. This could lead to diminished magnetic interactions between neighboring pillars which may be unideal. Nonetheless, mask trimming may be a hack where single pillars are concerned.

Deposit Conductive Layer

A 40 nm blanket layer of conductive Ti was immediately deposited over the sample post-etch via electron beam evaporation, at a rate of 1 \AA/s , to passivate and electrically connect the pillars. The deposition angle for this step was fixed at 45° with respect to the beam (which corresponds to 135° in the ion mill software) to sufficiently coat both the tops and sides of the pillars. Titanium was chosen for the conductive layer since its resistivity is higher than that of the CoFeB layer in the pillars. This ensures that most of the current will flow through CoFeB during the AHE measurement. From experience, it is not necessary to deposit a Ti layer that fully buries the pillars and the height of the Ti need only reach the top of the CoFeB layer. Using a thinner conductive layer also increases its resistivity which is optimal from the perspective of enhancing current flow through CoFeB.

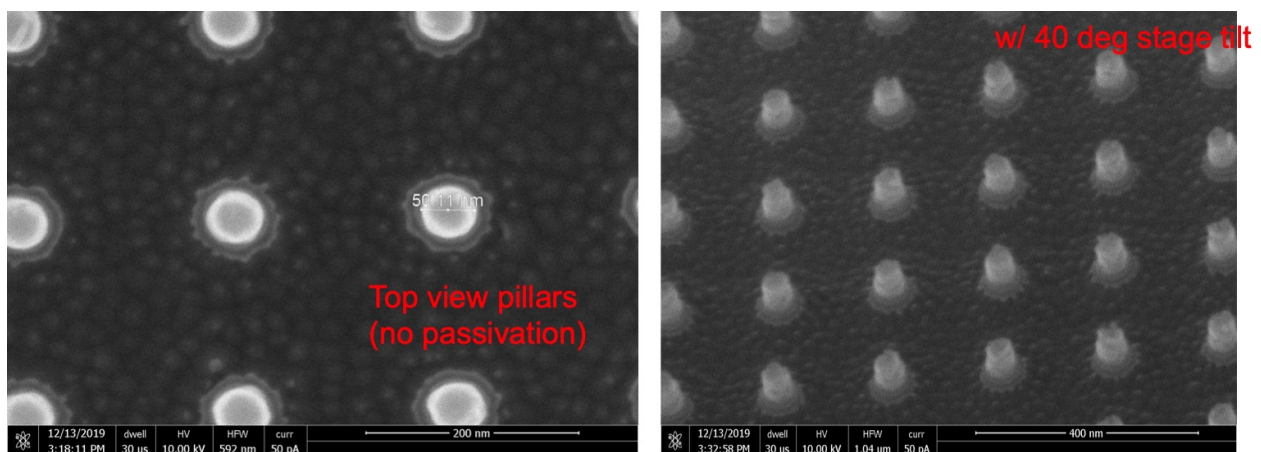


Figure 5.12: Sacrificial nanopillars as seen under the SEM during fabrication development. Without passivation after milling, nanopillars will oxidize upon breaking vacuum.

5.2.5 Hall Cross Definition

Write Leads and Cross

The sample should be spincoated with negative-tone MAN-2401 resist using Program 5 (3600 RPM for 45 seconds) and subsequently baked at 90°C for 60 seconds on the hot plate. The leads and cross, shown left in Figure 5.7, are to be written using the following beam conditions:

- Lead pads: dose = 275 $\mu\text{C}/\text{cm}^2$, I = 6.4 nA
- Cross (5 μm width): dose = 175 $\mu\text{C}/\text{cm}^2$, I = 100 pA

Begin by setting up the electron beam for writing at the aforementioned specifications (see 3.3.1). When ready to write the first cross, navigate to the center of the first dot array on the sample. The electron beam must now be re-positioned with better accuracy to ensure the Hall cross is written centrally over the array. Although the array is wider than the active region of the cross, the SEM is known to have dramatic offsets in position verging on the order on microns. An alignment step in NPGS is therefore a necessary requirement.

Alignment is accomplished using a DesignCad file, independent of the one for writing the pattern, which serves only for alignment purposes. As shown in shown in Figure 5.13, four windows drawn in the alignment file define regions over which NPGS will take an SEM image of the sample and scan for the inset feature in each window (i.e., the alignment marks written on the sample in Section 5.2.4). NPGS will then auto-correct the position of the SEM stage until the feature in the inset of its scanning window is closely matched to the one seen on the sample.

To write the Hall cross using an alignment step, edit the NPGS Run File in the following way:

- Navigate to the pattern Run File (.RF6) created in NPGS
- Insert a new Entity (Fig. 5.14)
- Import the DesignCad file for alignment under Pattern Name
- Change the Entity Type to Alignment
- Set Mode to AutoAlign2
- Ensure the DesignCad file for the cross patten is Entity 2

Upon executing the Run File, NPGS will now perform the alignment scan prior to writing the actual Hall cross pattern. If NPGS has difficulty running the auto-alignment, verify that the scanning windows are large enough to encompass the alignment mark of interest. If all else fails the alignment can be done by the user by setting the mode to Manual and recording the (X,Y) stage coordinates used to position the sample.

Develop MAN-2401

Post-EBL, develop the MAN-2401 using ma-D 525 developer (MicroResist Technology):

- Place the sample in a glass beaker
- While holding one corner of the sample down with tweezers, pour ma-D 525 over top then release tweezers
- Allow the sample to develop for 1 minute (do not swirl)
- Transfer the sample to a beaker of HPLC grade DI water
- Allow the sample to sit for 3 minutes undisturbed

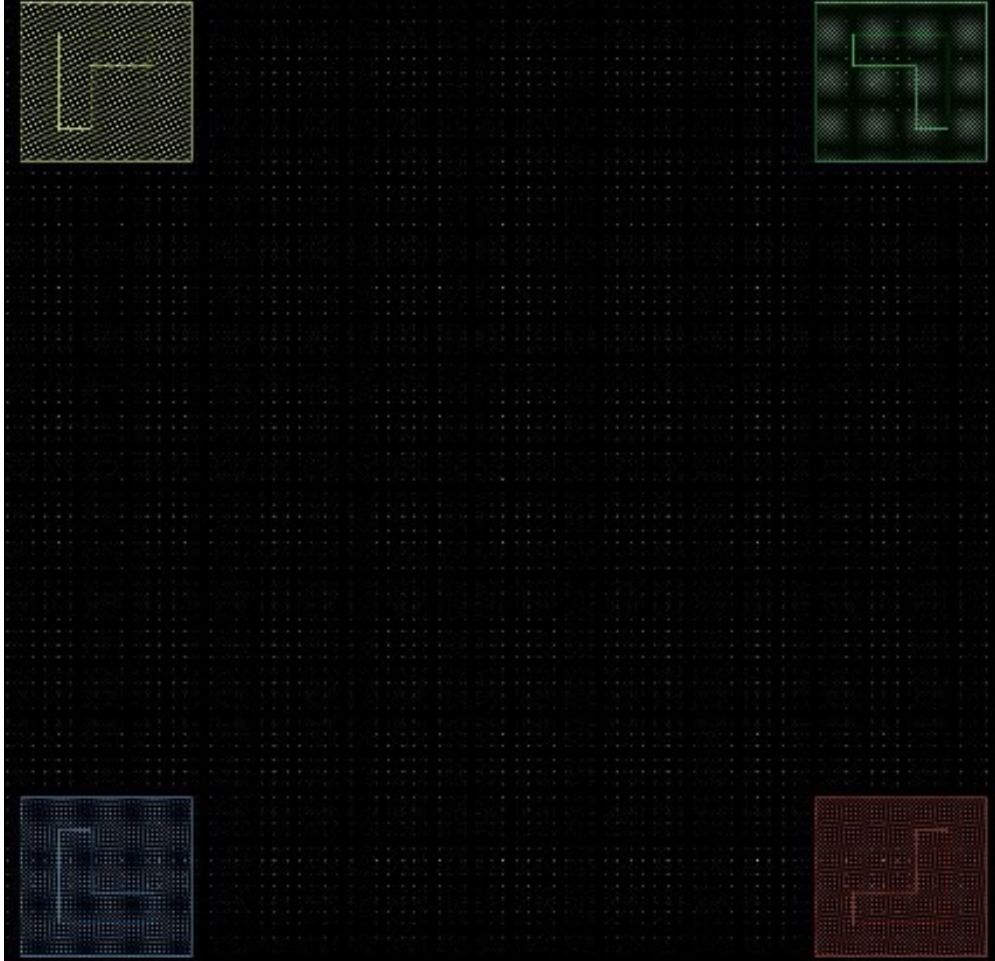


Figure 5.13: NPGS will scan for the L-shaped alignment marks on the sample within the area enclosed by the four square windows. Ensure that all features in the alignment file are written in solid lines (accessible by highlighting the feature and choosing the Information tab). Only dashed lines will be written in NPGS.

- Blow dry with nitrogen gas

Verify with the optical microscope that the Hall cross is written over the dot array which will be hazy but faintly perceptible.

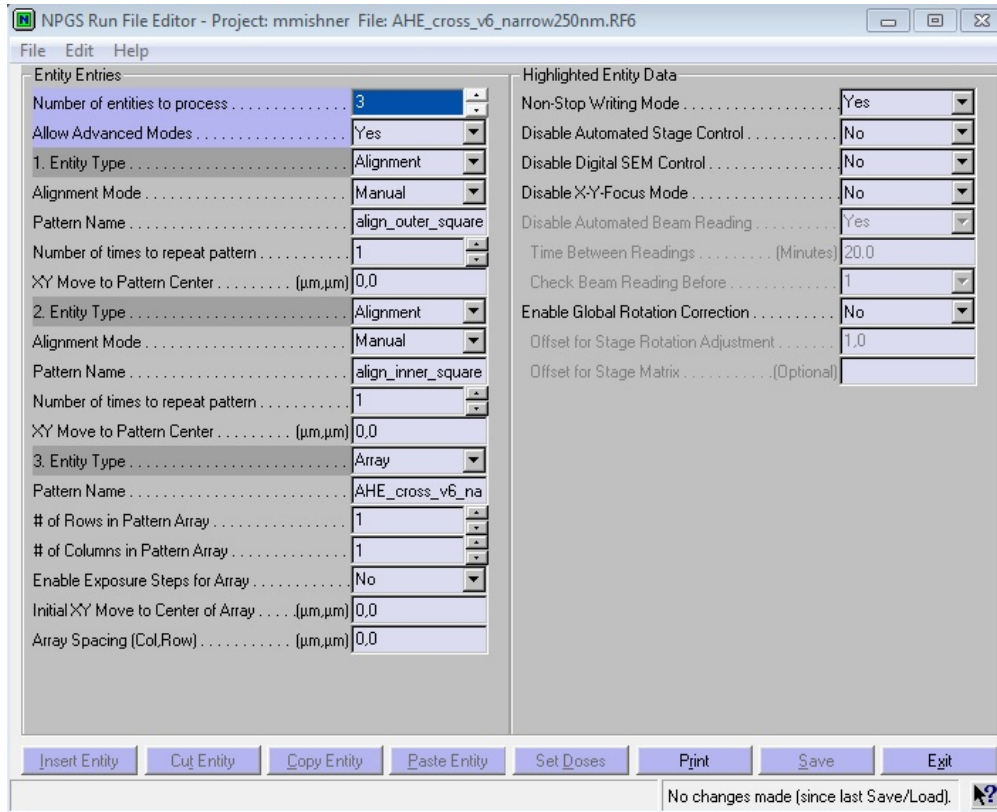


Figure 5.14: NPGS Run File settings with two alignment steps.

5.2.6 Ion Mill Etch to Define Hall Cross

The Hall crosses should be ion milled at 80° until the Ti layer is completely gone. A 30 second clean-up etch at 10° should be included as the last step. After removing the sample from the ion mill, the excess MAN-2401 can be removed by sonicating the sample for 5 minutes in acetone then IPA. Since MAN-2401 is not electrically conductive there is no harm in leaving it on the sample (it can actually serve to protect it from scratches), however wirebonding proved to be easier with the MAN mask fully removed.

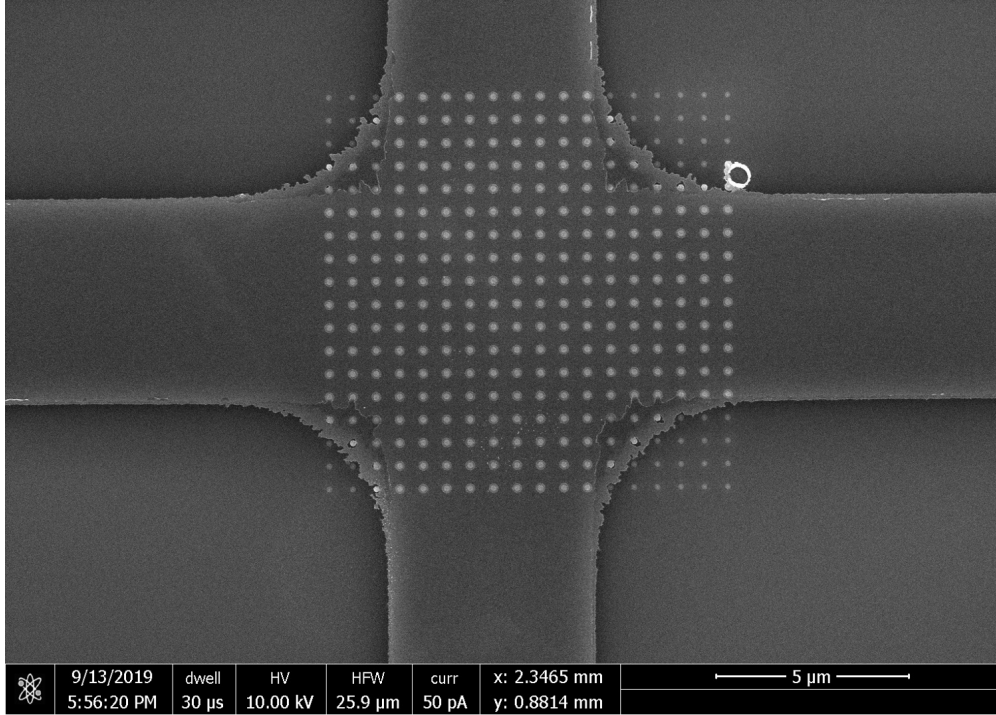


Figure 5.15: Final Hall cross with central array. Some bloating related to dosage is seen near the cross edges.

5.3 Nanopillar Characterization by AHE

For comparison to our nanopillar samples, we first investigate the magnetization of the multilayer itself. Hall crosses made exclusively of the film were fabricated without nanopillars or Ti. Bare films with a 20 nm CoFeB layer were determined to have a saturation magnetization ≈ 1145 emu/cc by vibrating sample magnetometry (Everspin). The out-of-plane R vs H data shows that the films are unsaturated at 17 kOe and that the magnetization of the unpatterned multilayer lies in the film plane (Fig. 5.16).

We next turn to our arrays of nanopillars and study R as a function of H for pillar diameters ranging between 30 to 100 nm. Dipole-dipole interactions between neighboring pillars in the arrays may be ballparked by considering a pillar as a simple point dipole with cylindrical volume. The dipolar field between pillars of 30 nm diameters with $t_{\text{CoFeB}} = 40$ nm is estimated to be 10 Oe (Fig. 5.16). While small, the density with which pillars can be successfully

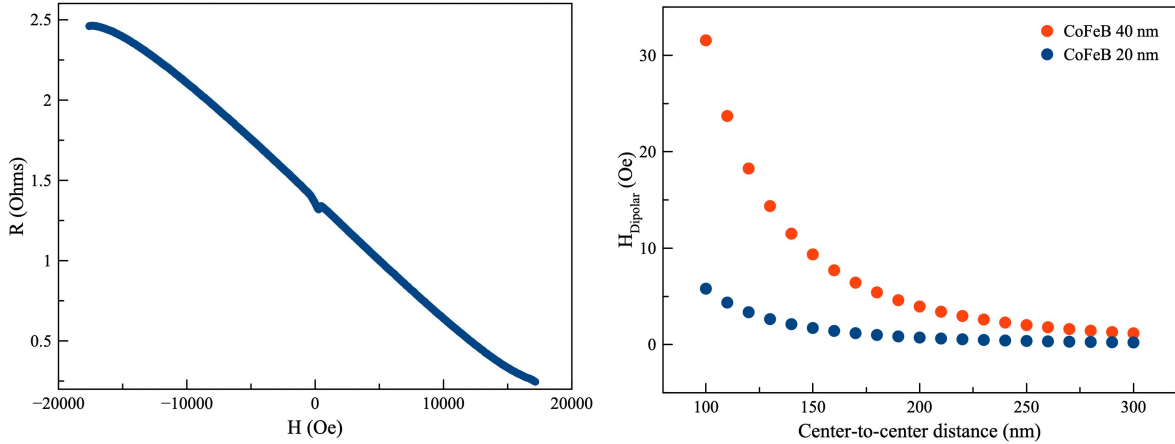


Figure 5.16: R vs H for a blanket film with $t_{\text{CoFeB}} = 20$ nm (left). Estimated dipolar field of 30 nm diameter nanopillars as a function of array pitch (right).

fabricated is restricted by shadowing effects that occur at the ion milling stage for pitches < 150 nm.

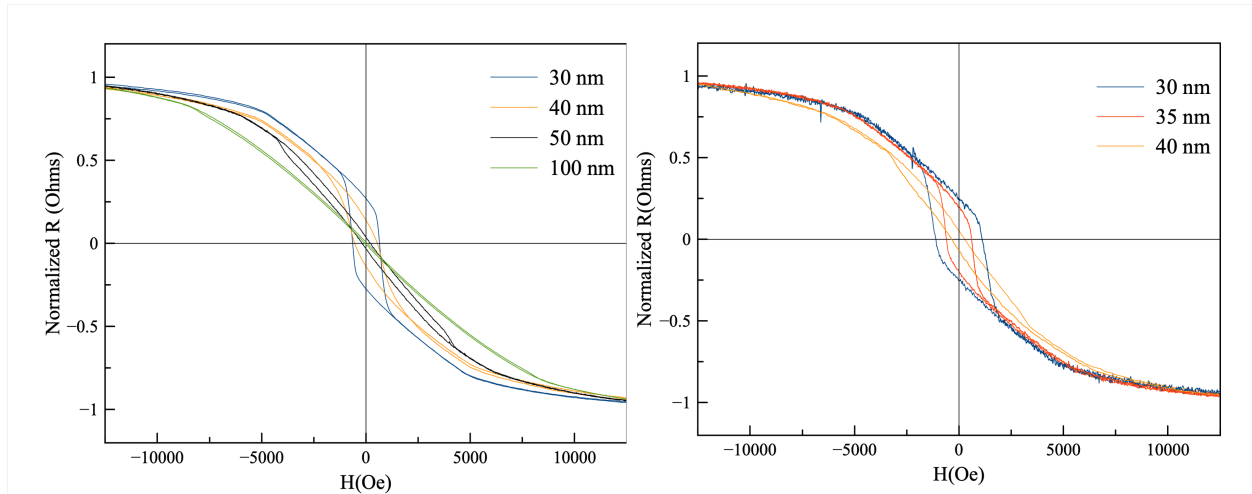


Figure 5.17: R vs H sweeps after linear background subtraction of $10 \times 10 \mu\text{m}$ arrays as a function of nanopillar diameter for $t_{\text{CoFeB}} = 40$ nm and pitch 200 nm (left) or 150 nm (right).

It is apparent from Figure 5.17 that the hysteresis loops of the arrays trend towards squareness as pillar diameter is reduced and that a similar trend exists in arrays of either 200 or 150 nm pitch. The increasing squareness of the loops with a reduction in pillar diameter is an indication that the perpendicular component of magnetization is increasing. This is

Diameter (nm)	H_C (Oe)	Array Pitch (nm)
30	1103 ± 5	150
30	643 ± 3	200
35	602 ± 8	150
40	309 ± 55	150
40	539 ± 2	200
50	202 ± 26	200
100	53 ± 6	200

Table 5.1: Coercive field of the arrays for a given pillar diameter.

to be expected given that narrower pillars should have higher magnetic shape anisotropy. However it is clear that the arrays of either pitch do not reach full magnetic saturation and single domain switching is not observed at any diameter.

AHE measurements were also taken on a single, 30 nm nanopillar centered on a much narrower Hall cross to prevent shunting (Fig. 5.18). Single domain switching is similarly absent, though a weak anomalous Hall signal $\sim 1 \mu\text{V}$ could be detected. Resistance vs time measurements, taken for as long as one hour at several points along select hysteresis loops, also ruled out any thermally activated switching.

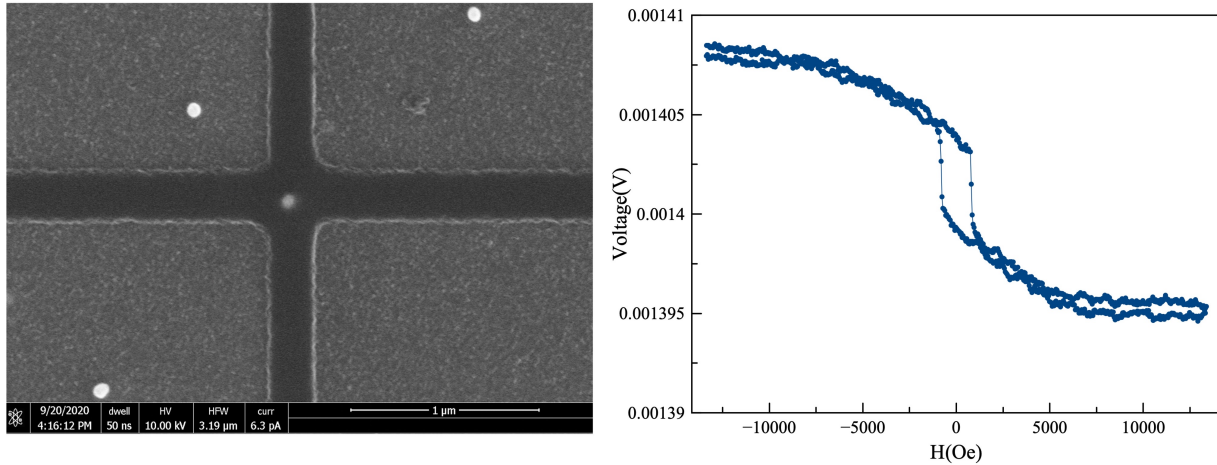


Figure 5.18: V_{AHE} in a 30 nm nanopillar.

While major hysteresis loops represent the bulk within a sample, this form of characterization

lacks detail for multi-particle magnetic arrays. To better understand the mechanism of magnetization reversal, a variation of an R vs H sweep called a first-order reversal curve (FORC) was taken in the out-of-plane direction [9, 10].

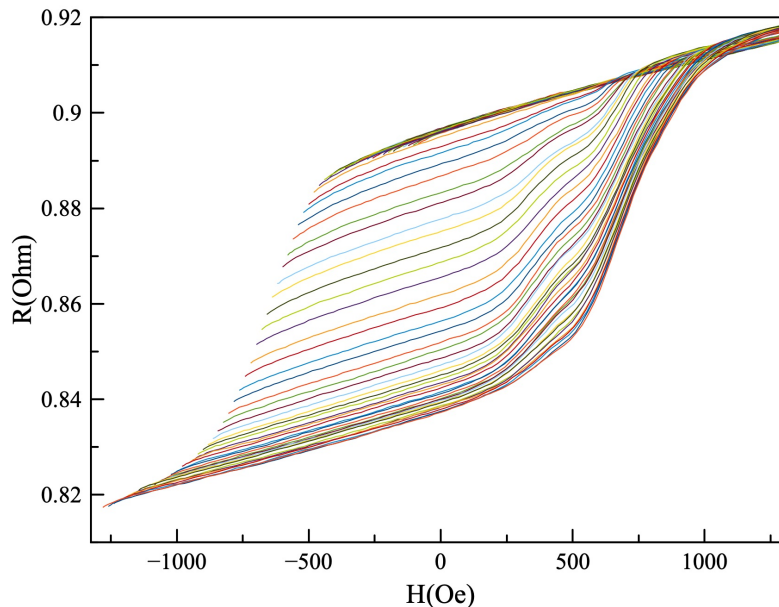


Figure 5.19: FORC curves of a 30 nm nanopillar array with 200 nm pitch. The outer envelope of the FORC defines the major hysteresis loop.

To produce a FORC curve, the sample is saturated in a positive applied field which is then lowered to a pre-defined reversal field H_r . A FORC is the magnetization curve that is produced when the applied field is increased from H_r back to saturation. By collecting FORC curves for a large set of H_r , local interactions between the constituents of a sample can be visualized. As shown in Figure 5.19, there is an intrinsic distribution of coercive fields H_C within a single array. This is different from the single value of H_C concluded from initial observation of the major hysteresis loop alone (Table 5.1). Two kinks, seen ≈ 250 Oe and 500 Oe, clearly suggest that micromagnetic processes are at play within the array. A complete understanding of the non-trivial switching mechanism observed in nanopillars and associated arrays may be gained through computational simulations.

5.4 Discussion and Future Work

We prescribe a nanofabrication recipe for micron-scale arrays of nanopillars made by electron beam lithography with HSQ resist. The adhesion of the tall HSQ dot mask, critical for the definition of pillars via ion milling, was found to lie in the dilution of the NaOH-based chemical developer. While large dipolar interactions within the arrays are expected when pillar density is high, fabrication limitations restrict the array pitch to a minimum of 150 nm. However, improvements to the fabrication process might include hexagonal packing of pillars or optimization of the ion milling angle which may allow for larger dipolar interactions.

From our anomalous Hall characterization, it may be concluded that magnetic shape anisotropy is insufficient to pull the magnetization of pillar arrays with sub-100 nm diameters and pitch ≤ 200 nm fully out of plane. While a smaller pitch is seen to increase H_C , our hysteresis curves would suggest that the magnetization becomes only tilted in the out of plane direction by an applied magnetic field. To further enhance the aspect ratio, and by extension shape anisotropy, sub-30 nm diameter pillars might be considered. This is experimentally challenging, but some preliminary exploration with PMMA electron beam resist— which is known to become negative-tone at high dosage ($30,000+ \mu\text{m}/\text{cm}^2$)—hints that feature sizes of this scale may be plausible [11]. To further promote perpendicular anisotropy, modifications to the multilayer structure might also be considered. For instance, interfacial effects between MgO and CoFeB generally leads to PMA in MTJ-like structures and is known to be controllable by CoFeB composition.

Given the weak dipolar field between pillars in our arrays, it is unlikely that the arrays are suitable candidates for magnonic crystals. However the detection of spin wave modes in arrays and single pillars by spin-torque ferromagnetic resonance is a potential avenue for exploration [12]. By exciting the precession of magnetization via an in-plane microwave field, the perpendicular component of M can be monitored via the anomalous Hall voltage. As

precession amplitude increases, M_z (proportional to V_{AHE}) is expected to decrease and the resulting dips in V_{AHE} versus H correspond to the excitation of spin wave modes. Since the anomalous Hall voltage in our pillar arrays is on the order of 10s of μV , the FMR signal can be expected to be within detectable limits.

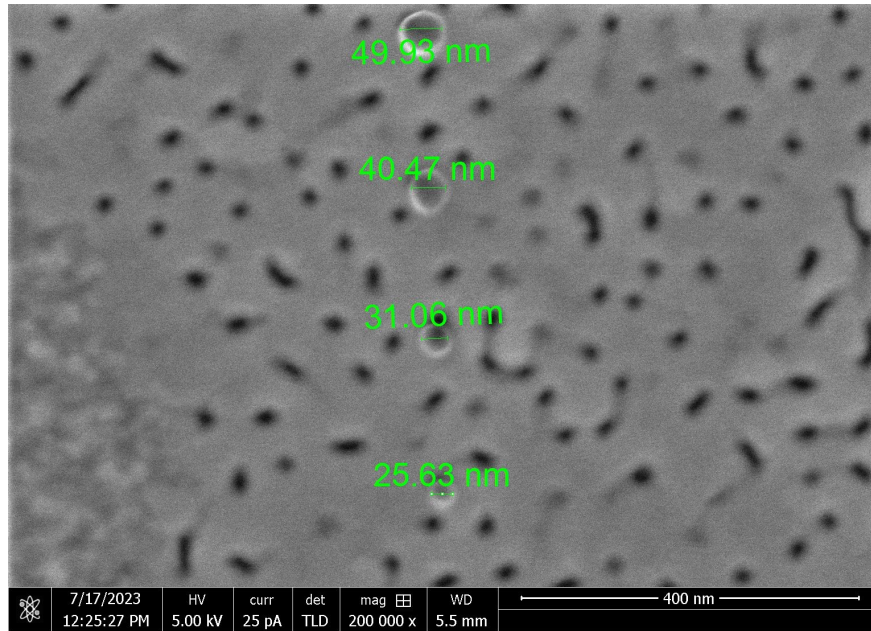


Figure 5.20: PMMA dot masks ($I = 25 \text{ pA}$, dose = $40,000 \mu\text{m}^2/\text{cm}^2$) with attempted diameters of 50, 40, 30, 25 nm (descending) developed in MIBK(1):IPA(3).

References

- [1] Krawczyk, M. & Grundler, D. Review and prospects of magnonic crystals and devices with reprogrammable band structure. *Journal of physics: Condensed matter* **26**, 123202 (2014).
- [2] Lisenkov, I. *et al.* Spin-wave edge modes in finite arrays of dipolarly coupled magnetic nanopillars. *Physical Review B* **90**, 104417 (2014).
- [3] Verba, R. *et al.* Conditions for the spin wave nonreciprocity in an array of dipolarly coupled magnetic nanopillars. *Applied Physics Letters* **103**, 082407 (2013).
- [4] Lisenkov, I., Tyberkevych, V., Nikitov, S. & Slavin, A. Theoretical formalism for collective spin-wave edge excitations in arrays of dipolarly interacting magnetic nanodots. *Physical Review B* **93**, 214441 (2016).
- [5] Louis, S., Lisenkov, I., Nikitov, S., Tyberkevych, V. & Slavin, A. Bias-free spin-wave phase shifter for magnonic logic. *AIP Advances* **6**, 065103 (2016).
- [6] Ikeda, S. *et al.* A perpendicular-anisotropy CoFeB–MgO magnetic tunnel junction. *Nature materials* **9**, 721–724 (2010).
- [7] Watanabe, K., Jinnai, B., Fukami, S., Sato, H. & Ohno, H. Shape anisotropy revisited in single-digit nanometer magnetic tunnel junctions. *Nature communications* **9**, 1–6 (2018).
- [8] Yang, J. K. & Berggren, K. K. Using high-contrast salty development of hydrogen silsesquioxane for sub-10-nm half-pitch lithography. *Journal of Vacuum Science & Technology B: Microelectronics and Nanometer Structures Processing, Measurement, and Phenomena* **25**, 2025–2029 (2007).
- [9] Pike, C., Ross, C., Scalettar, R. & Zimanyi, G. First-order reversal curve diagram analysis of a perpendicular nickel nanopillar array. *Physical Review B* **71**, 134407 (2005).
- [10] Roberts, A. P., Heslop, D., Zhao, X. & Pike, C. R. Understanding fine magnetic particle systems through use of first-order reversal curve diagrams. *Reviews of Geophysics* **52**, 557–602 (2014).
- [11] Hoole, A., Welland, M. & Broers, A. Negative PMMA as a high-resolution resist—the limits and possibilities. *Semiconductor science and technology* **12**, 1166 (1997).
- [12] Kikuchi, N., Furuta, M., Okamoto, S., Kitakami, O. & Shimatsu, T. Quantized spin waves in single Co/Pt dots detected by anomalous Hall effect based ferromagnetic resonance. *Applied Physics Letters* **105** (2014).

Chapter 6

Epitaxial magnesium aluminum ferrite films grown by reactive sputtering

6.1 Motivation

Thin films of magnetic insulators are extensively used in nano-magnonics and spin caloritronics to produce and transmit spin current without the energy loss associated with charge flow. Up to date, most research efforts in these fields employ films of yttrium iron garnet (YIG). While much progress has been made using YIG-based devices, YIG is not ideally suited for certain magnonic applications given its low saturation magnetization and spin wave frequencies [1–3]. Similarly, lattice matching issues and high growth temperatures (600-900°C) make its integration with existing technologies difficult.

Epitaxial magnetic insulators with high saturation magnetization and low Gilbert damping α are highly desirable alternatives to iron garnets. Recently, growth of single-crystal films of magnesium aluminum spinel ferrite $\text{MgAl}_{0.5}\text{Fe}_{1.5}\text{O}_4$ (MAFO) with $\alpha \sim 0.0015$ by pulsed laser deposition (PLD) was reported [4]. Here we have developed a method for the reactive

growth of epitaxial thin films of MAFO by radio-frequency, magnetron sputtering using ArO_2 plasma and report its magnetic properties.

6.2 Film Composition and Growth

Materials with large spin-orbit coupling (SOC) readily dissipate magnetic energy into the lattice which is known to enhance magnetic damping. In this respect, small SOC materials are more ideal and can typically be engineered through chemistry. In the nominal composition of MAFO, Mg^{2+} and Al^{3+} cations possess zero orbital angular momentum ($L = 0$) and magnetism arises primarily from Fe^{3+} . It has been observed in YIG that the effects of an $L \neq 0$ cation structure through doping can increase α by several orders of magnitude [3, 5, 6]. It is likely then that the magnetic properties of MAFO are similarly linked to its chemical arrangement.

MAFO films were reactively sputtered (0.121 nm/s) at 550°C from a stoichiometric target onto (001)-oriented MgAl_2O_4 substrates that were sonicated in acetone, methanol, and isopropyl alcohol prior to loading into the sputtering chamber. Before ramping to temperature, substrates were cleaned under a 60 second RF bias plasma. After a 10 minute soak at 550°C , a mixture of Ar and ArO_2 (10% O_2 + Ar balance) gases was introduced into the chamber at a net flow rate of 20 sccm to generate an ArO_2 plasma (1 mTorr). Through control of the ArO_2 flow rate, MAFO films were deposited under various partial pressures of oxygen to study the effects of oxygen concentration on film quality.

6.3 Structural Characterization

The crystallinity of < 20 nm MAFO films was investigated by X-ray diffraction (XRD). Laue oscillations about the MAFO (004) 2θ peak (Fig. 6.1) demonstrate homogeneity between substrate and film when grown under a 9 sccm ArO_2 flow rate. All crystallographic planes were confirmed to lie parallel to the sample surface by grazing incidence XRD. The high-quality growth of MAFO is further corroborated by its (004) rocking curve. A full-width at half-maximum (FWHM) $\ll 1^\circ$ is close to that of the single-crystal MgAl_2O_4 substrate (FWHM ~ 0.026) and suggests that MAFO films of sub-20 nm thicknesses possess small mosaic spread. Given the 2.7% lattice mismatch in the film plane, the epitaxy between MgAl_2O_4 ($a=8.08 \text{ \AA}$) and MAFO ($a= 8.30 \text{ \AA}$) is rather surprising.

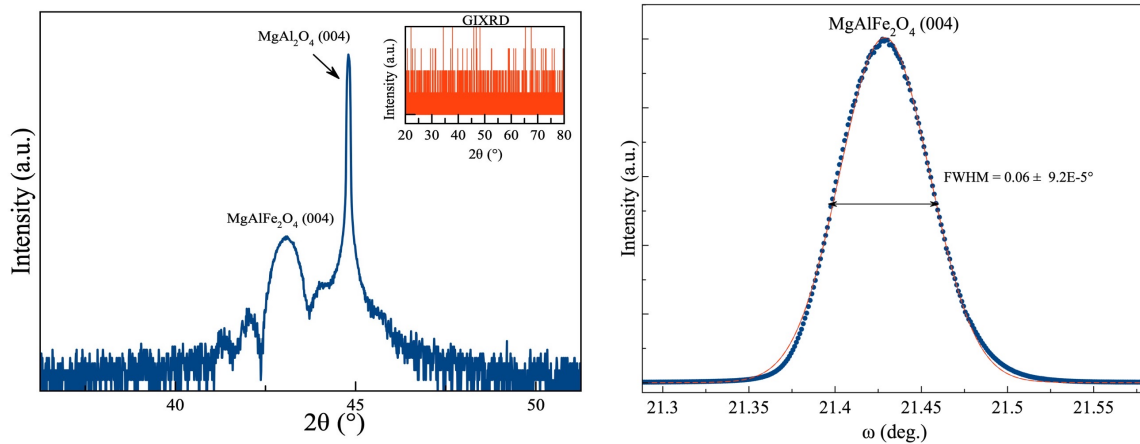


Figure 6.1: XRD 2θ scan of an 18 nm MAFO film (left) with the associated MAFO(004) rocking curve (right).

The growth of MAFO was found to be highly sensitive to the concentration of oxygen in the ArO_2 sputtering plasma. The suppression of the MAFO(004) Bragg peak above or below a 9 sccm flow rate of ArO_2 (Fig. 6.2) suggests there is a critical amount of oxygen needed for epitaxial growth. Deviations as small as 1 sccm away from the ideal ArO_2 flow rate are significant enough to diminish film crystallinity. This result is also reflected in the XRR

roughnesses of MAFO films which can be as much as doubled when grown above or below the critical flow rate (Fig. 6.3).

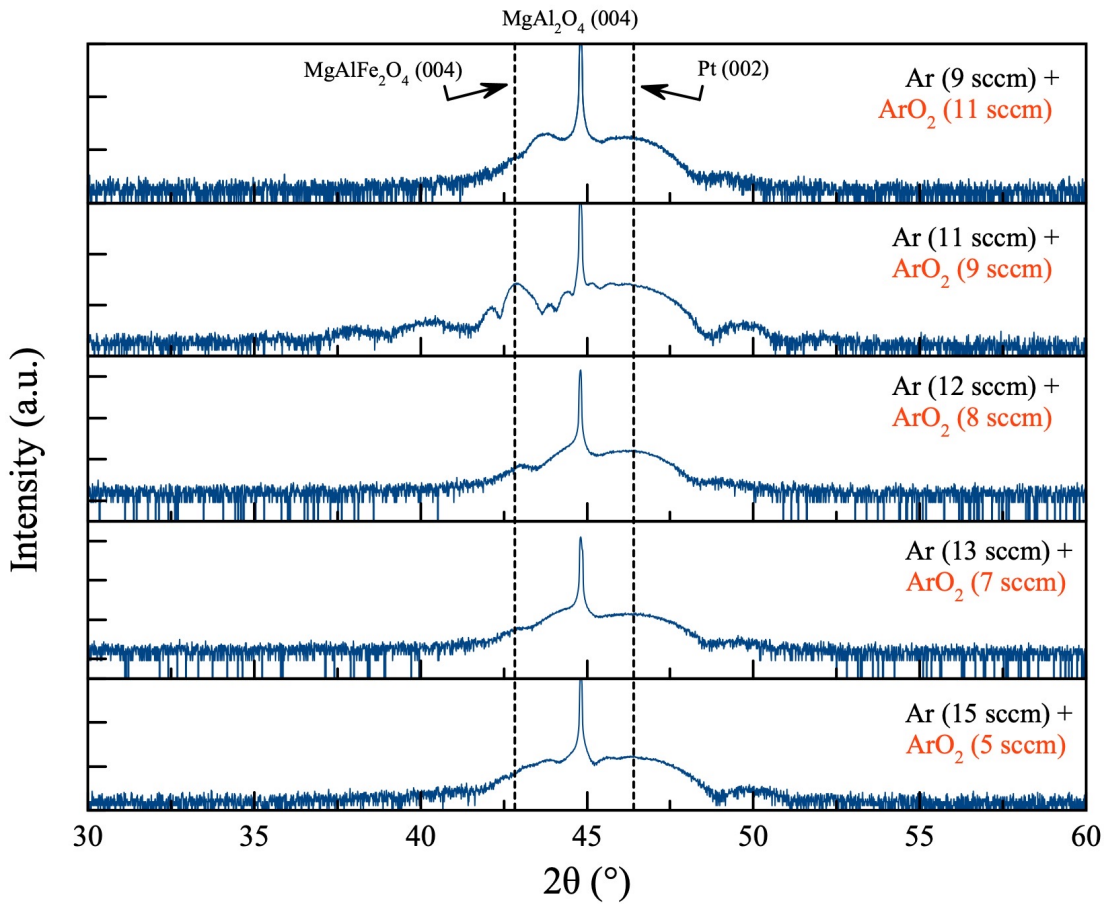


Figure 6.2: In Pt-capped MAFO films, the (004) diffraction peak suppresses as a function of ArO₂ flow rate into the sputtering chamber during deposition.

Prior to the use of oxygen sputtering plasma, two alternative growth methods to synthesize ferrimagnetic MAFO films were attempted. First, 10 nm films were sputter-deposited using exclusively Ar plasma then annealed in situ at 550°C for one hour under a 20 sccm flow of ArO₂ gas. Second, films sputtered with Ar plasma were deposited at ambient temperature and then brought to an oxygen annealing furnace (INRF). Films were ramped to 550°C and left in an environment of oxygen gas (delivery pressure of 480 kPa at 3300 sccm) for one hour up to overnight. In subsequent 2θ scans of films grown by both techniques, Bragg diffraction is only observed from the MgAl₂O₄ substrate. The use of oxygen plasma was found to be

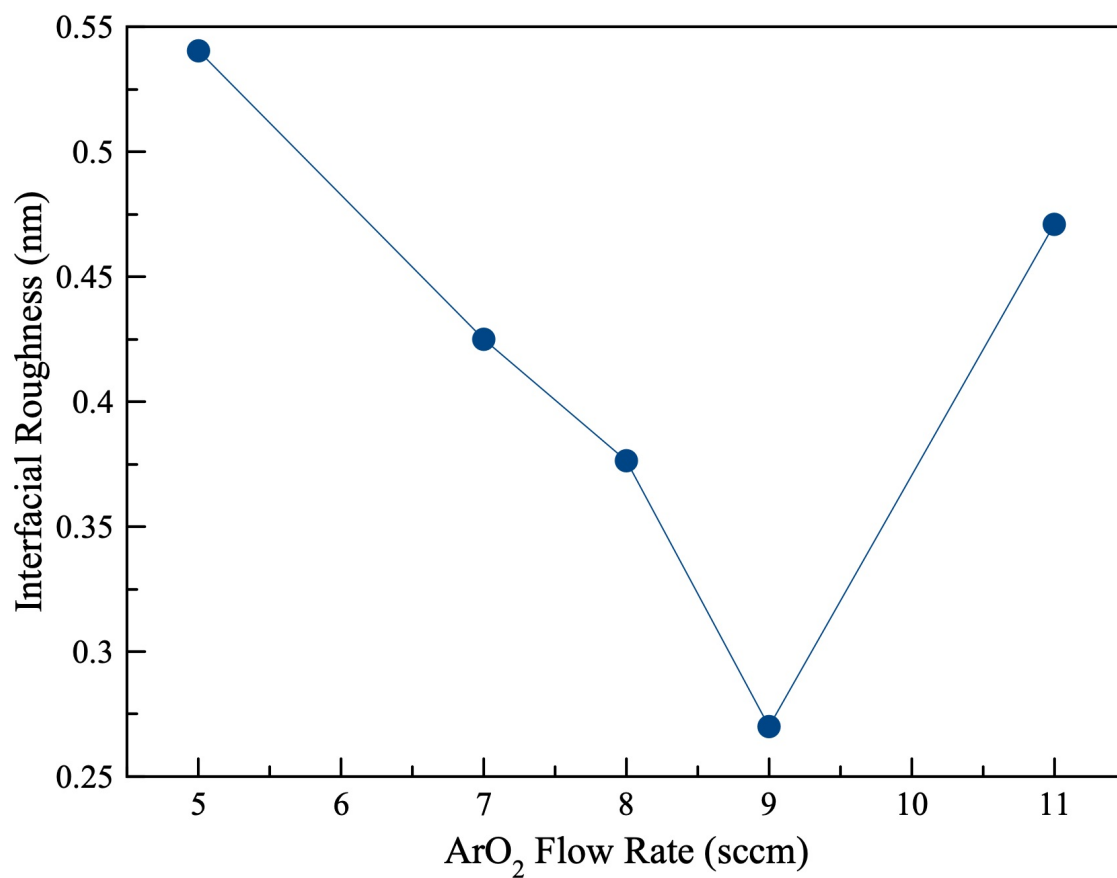


Figure 6.3: Interfacial roughness between MAFO and 2 nm of Pt as. function of ArO₂ flow (left). Roughness values were taken from X-ray reflectivity profiles (right).

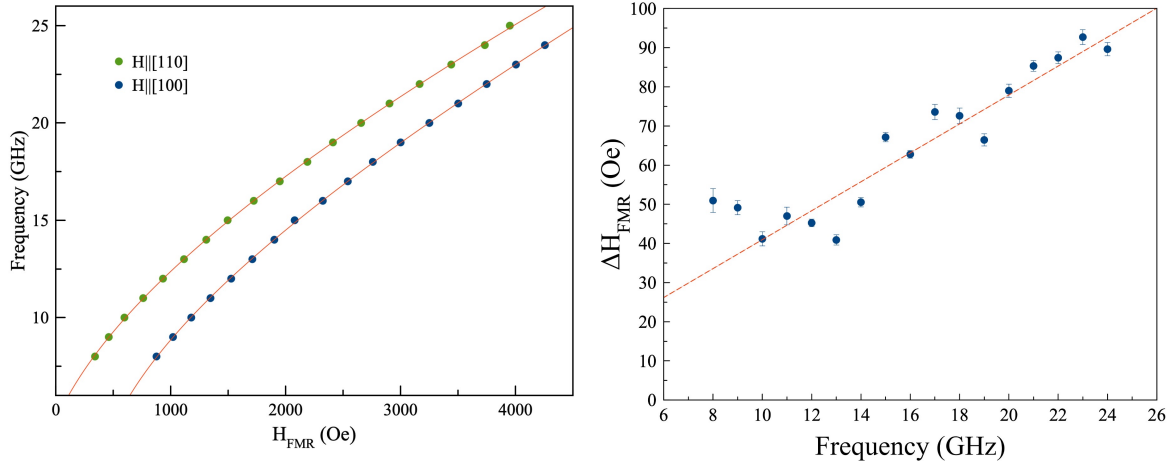


Figure 6.4: FMR resonant field and linewidth data for a 16 nm MAFO film taken along the easy(110) and hard(100) directions.

essential for the growth of MAFO by sputtering.

6.4 Magnetic Characterization

Next the magnetic properties of MAFO were probed by room temperature broadband ferromagnetic resonance (FMR) measurements using a coplanar waveguide setup (Section 3.4.2). The FMR spectra were fit to the sum of symmetric and antisymmetric Lorentzian derivatives (Equation 3.5) to extract the resonance field H_{FMR} and linewidth ΔH_{FMR} . Measurements were taken for applied field H along the easy (110) and hard (100) directions of a 16 nm film (Fig. 6.4).

The lateral shift between the easy and hard axis dispersion in Figure 6.4 indicates strong in-plane magnetic anisotropy and a large $4\pi M_{\text{eff}} \approx 16$ kOe deviates from PLD-deposited MAFO films by about 2 kOe [4]. Similarly, in materials with low SOC a free-electron like g -factor ≈ 2.0 is to be expected. In our MAFO films $g = 1.96 \pm 0.02$, as quantified from a fit to Equation 3.8 along [100], would suggest modest SOC.

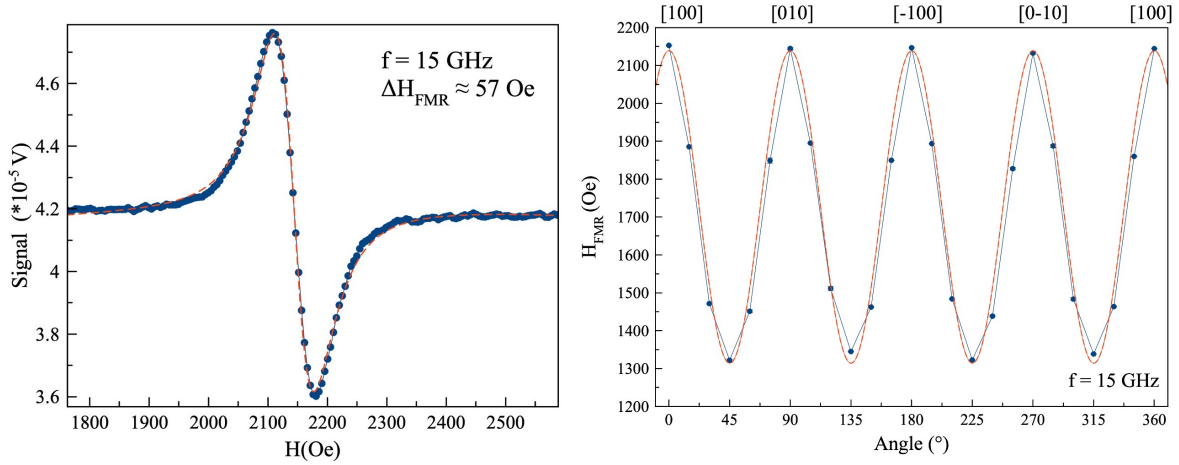


Figure 6.5: Resonance signal and angular dependent FMR (in-plane) measured at $f = 15$ GHz.

For a homogeneous film, the relationship between ΔH_{FMR} and frequency is generally linear (Equation 3.9) and allows for the extraction of $\alpha = 0.01 \pm 4\text{E-}4$ in our 16 nm MAFO film. This is an order of magnitude larger than that seen in MAFO films grown by PLD. However, magnetic inhomogeneities are likely present in sputtered MAFO given the large zero-frequency linewidth ΔH_0 of roughly 14 Oe. This may be an indication of two-magnon scattering which can be created by crystalline defects and sometimes appears as a fourfold anisotropy in angular dependent FMR data [7].

The angular dependence of H_{FMR} was measured as a function of in-plane field angle θ . The fourfold anisotropy seen in Figure 6.5 was found to be ≈ 1.2 kOe through a fit to Equation 6.1

$$f = \frac{g\mu_B\mu_0}{h} \sqrt{(H_{\text{FMR}} + H_4 \cos(4\theta))(H_{\text{FMR}} + M_{\text{eff}} + \frac{H_4}{4}(3 + \cos(4\theta)))} \quad (6.1)$$

where μ_B is the Bohr magneton, μ_0 is the permeability of free space, and h is the Planck constant. The fourfold nature of the magnetic anisotropy is reflective of the spinel crystal structure which has an in-plane cubic unit cell. The magnitude of H_4 may be a product of large epitaxial strain created by the significant lattice mismatch.

6.5 Discussion and Conclusions

We have prescribed an epitaxial growth method of the ferrimagnetic oxide MAFO by reactive sputtering. By FMR, the resulting films are shown to possess large $4\pi M_{\text{eff}}$ and Gilbert damping ≈ 0.01 . The contrast in the magnetic properties of sputter- versus PLD-deposited MAFO films is likely related to the different growth techniques as well as cation chemistry. For instance, the higher α in sputtered MAFO may be a product of growth defects and the non-stoichiometric transfer of target material to the substrate during growth. Additionally, the larger magnetic anisotropy reported here can arise from a different level of epitaxial strain. Nevertheless, sputtered films of MAFO may be useful for exchange-biasing purposes or to study spin-orbit torques from non-magnetic metals like Pt. Improvement of Gilbert damping via control of growth rate, temperature, and composition is an area for future study.

References

- [1] Harris, V. G. Modern microwave ferrites. *IEEE Transactions on Magnetism* **48**, 1075–1104 (2011).
- [2] Mitra, A. *et al.* Interfacial origin of the magnetisation suppression of thin film yttrium iron garnet. *Scientific reports* **7**, 11774 (2017).
- [3] Hauser, C. *et al.* Yttrium iron garnet thin films with very low damping obtained by recrystallization of amorphous material. *Scientific reports* **6**, 20827 (2016).
- [4] Emori, S. *et al.* Ultralow damping in nanometer-thick epitaxial spinel ferrite thin films. *Nano letters* **18**, 4273–4278 (2018).
- [5] Howe, B. M. *et al.* Pseudomorphic yttrium iron garnet thin films with low damping and inhomogeneous linewidth broadening. *Ieee Magnetism Letters* **6**, 1–4 (2015).
- [6] Kehlberger, A. *et al.* Enhanced magneto-optic Kerr effect and magnetic properties of CeY₂Fe₅O₁₂ epitaxial thin films. *Physical Review Applied* **4**, 014008 (2015).
- [7] Rana, B. & Otani, Y. Anisotropy of magnetic damping in Ta/CoFeB/MgO heterostructures. *Scientific Reports* **13**, 8532 (2023).

Chapter 7

Conclusion

In summary, detection of giant AMR in the antiferromagnet PtMn was achieved. In the process of reaching this goal, several types of preliminary work was necessary. First, a growth technique for epitaxial thin films of PtMn was developed. To facilitate AFM/FM exchange coupling, candidate magnetic materials were then explored. These include the half-metal CoFeMnSi and the ferrimagnetic oxide MgAlFe₂O₄, whose crystallographic and magnetic properties were also characterized. Simultaneously, a low-noise magnetoresistance measurement station using a Wheatstone bridge was developed. It was additionally demonstrated that detection of AMR in an AFM material can be achieved by exchange-coupling the AFM to a FM with zero AMR. This broad technique may be applicable to other AFM/FM material systems. Future work will seek to utilize the giant AMR in PtMn as an electrical readout method of superparamagnetic switching or magnetization dynamics in an AFM-based spin torque oscillator.

In a separate venture, a nanofabrication recipe for micron-scale arrays of tall nanopillars was provided. Magnetization in these arrays was probed by the anomalous Hall effect and studied as a function of pillar diameter and pitch. The fabrication technique disclosed lays

groundwork for the development of magnetic tunnel junctions (MTJs) with perpendicular magnetization using electron beam lithography. With further refinements, the detection of spin wave modes in tall nanopillar arrays may also be possible.

Appendix A

Sputtering System Standard Operating Procedure

A.1 System Overview

The AJA International ATC-2000F sputter deposition system has three main user-operated parts: the main chamber, gate valve, and load-lock (Fig. A.1). The load-lock is where the sample is first loaded into the system and subsequently pumped down from atmosphere to high vacuum ($<1\text{E-6}$ Torr). The main chamber, which sits at higher vacuum ($\sim 8\text{E-9}$ – 3E-8 Torr) than the load-lock, is where the deposition takes place. Once the sample has reached high vacuum in the load-lock, the gate valve situated between the load-lock and main chamber is opened to transfer the sample into the main chamber. The sample is removed in an inverse process.

There are four vacuum pumps used in the system. Connected to the back of the main chamber is a Shimadzu turbomolecular pump which is backed by an Adixen Pascal 2021 SD rotary vane roughing pump (Fig. A.2). Similarly, the load-lock has its own Pfeiffer

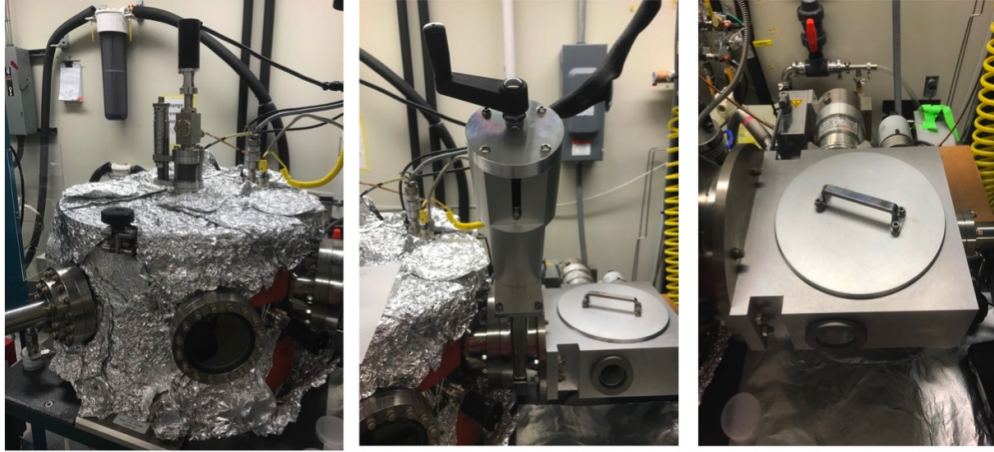


Figure A.1: Main chamber (left), gate valve (center), load-lock (right)

TMH 071P turbomolecular pump which is backed by an Adixen Pascal 2005 SD rotary vane roughing pump (Fig. A.2). Individual roughing pumps assist each turbomolecular pump in reaching vacuum.

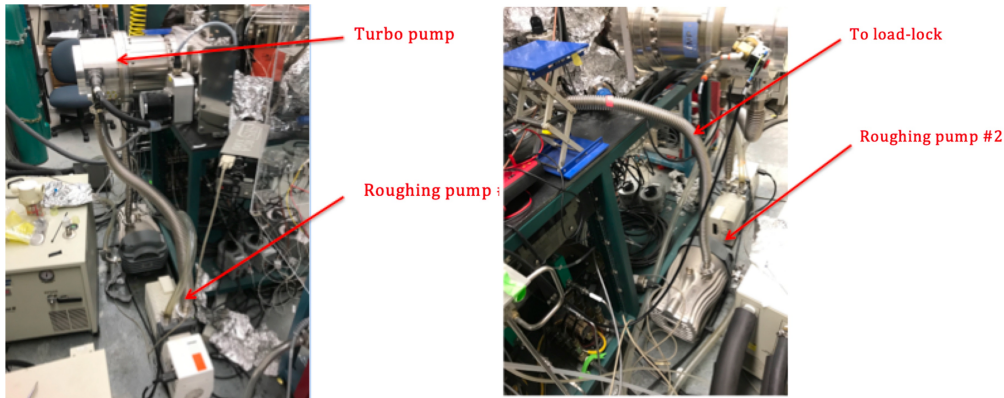


Figure A.2: Vacuum pumps on the sputtering system are shown. The left-most pumps are used for the main chamber while right-side pumps are used for the load-lock.

A.2 Basic Deposition

The following outlines how to set up and run a basic deposition after training by an experienced superuser. For more details on AJA software, refer to the AJA manual on the group Google Drive or in the blue binder next to the system.

A.2.1 Loading Sample

- Ensure that your sample does not contain high vapor pressure materials and is free of any type of grease
- Check that the nitrogen tank on the side of the system is not empty—if it is, replace it and make sure the output pressure is 3-4 psi (Fig. A.3a)
- Vent the load-lock by turning off the load-lock vacuum pump (Fig. A.3b)



(a)



(b)

Figure A.3: (a) Nitrogen tank along back wall of system; (b) Controller for load-lock pump and power– turn vacuum pump switch off to vent load-lock

- Look at the load-lock pressure gauge–parameter 340 on the Pfeiffer display control unit (DCU) in Fig. A.6–and verify that it is increasing towards atmosphere
- Put on lint-free hood, gown, hair net, and gloves
- After 2-3 minutes, the load-lock lid will make a slight popping sound when vented
- Take off the load-lock lid with one hand and remove the sample stage with the other (to minimize potential contamination by skin, eyelashes, etc., do not lean your body over the opening of the load-lock at any point)

- Immediately put the load-lock lid back on
- Place the stage on a clean piece of aluminum foil and inspect it for any semi-loose metallic debris/flakes– if present, contact tool owner immediately
- If stage has no flaking, unscrew the clips and mount your sample
- Open the load-lock lid and place the sample stage into the load-lock as you initially found it (i.e. the sample should be facing down on the transfer arm as in Fig. A.4)

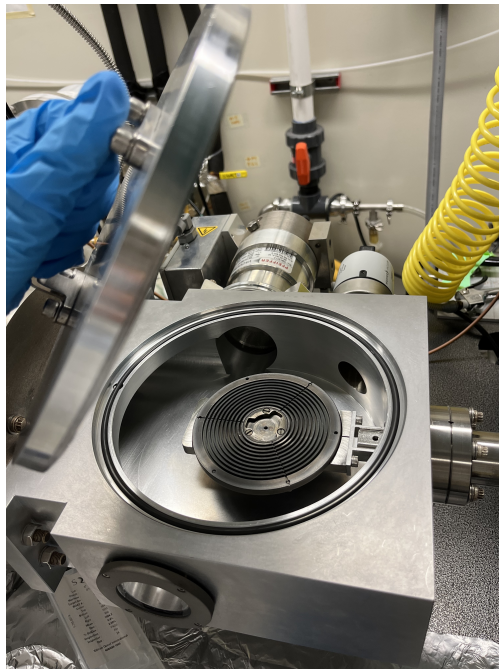


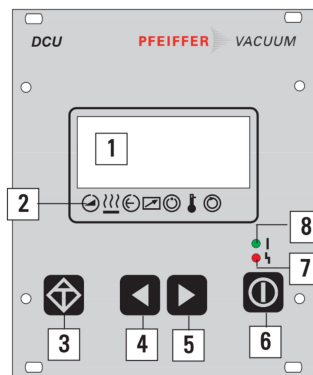
Figure A.4: Remove the load-lock lid with one hand.

- With the held lid in one hand, use the other hand to wipe down the load-lock O ring with IPA and a beta wipe
- Close the lid
- Pump down the load-lock by turning on the load-lock vacuum pump (Fig. A.5) → check the load-lock gauge to ensure pressure is decreasing

- Fill out all parameters listed in the sputtering system log book- the load-lock turbo pump power and current can be accessed on the Pfeiffer DCU by scrolling to parameters 310 (TMP I-mot) and 316 (TMP power) using keys 4 and 5 shown in Figure A.6



Figure A.5: Controller for load-lock pump and power- turn the vacuum pump switch on to pump down the load-lock.



The front panel contains all the operating and display elements.

- 1 LCD display
- 2 Status display (symbol definitions see chapter 4.6.)
- 3 "Error acknowledgement" key
- 4 Key "Left"
- 5 Key "Right"
- 6 "Pumping Station ON/OFF" key
- 7 Red illuminating diode for error status
- 8 Green illuminating diode for operating status



Figure A.6: Use scroll keys 4 and 5 on the load-lock DCU display to read turbo pump power, current, and rotational frequency.

Status request (only readable)		
#	Display	Name, Description
300		Unit remote controlled, not choosable by
301		Oil deficiency turbopump
302		Rotation switch point attained
303	Error code	Actual error code „no Err“ „Errxxx“ or „Wrnxxx“
304		Over temperature Electronic drive unit
305		Over temperature turbopump
306		Set rotation speed attained
307		Turbopump accelerates
308	Set rotspd	Set rotation speed TMP in Hz
309	Act rotspd	Actual rotation speed TMP in Hz
310	TMP I-Mot	Motor current TMP in A
311	TMP Op hrs	Operating hours TMP in h
312	Drv Softw	Software version electronic drive unit
313	TMP DClink	Motor voltage TMP in V
314	Drv Op hrs	Operating hours electronic drive unit
315	TMP finspd	Final rotation speed TMP in Hz
316	TMP power	Motor power TMP in W
319	Cycl count	Cycle counter
331	TMS ActTmp	Heating TMS, actual value in °C
333	TMS steady	TMS regulator engaged ON/OFF
334	TMS maxTmp	Maximum TMS temperature occurred in °C
335	Heat type	Heating type 0=conventional heating, 1=TMS
340	Pressure	Actual pressure value in mbar ³⁾
349	Drv Name	Unit type electronic drive unit
350	Ctr Name	Unit type operating and display unit ³⁾
351	Ctr Softw	Software version Display and Control Unit DCU ³⁾
360	Past Err1	Error storage, Position 1 (last error occurring)
361	Past Err2	Error storage, Position 2
362	Past Err3	Error storage, Position 3
363	Past Err4	Error storage, Position 4
364	Past Err5	Error storage, Position 5
365	Past Err6	Error storage, Position 6
366	Past Err7	Error storage, Position 7
367	Past Err8	Error storage, Position 8
368	Past Err9	Error storage, Position 9
369	Past Err10	Error storage, Position 10

Figure A.7: Readable load-lock turbo pump parameters accessible via the DCU.

- Wait ~30-40 minutes until the load-lock has pumped down to < 1E-6 Torr

A.2.2 Load-Lock to Main Chamber Transfer

- After 30-40 minutes, the load-lock pressure should be ~8.6E-7 Torr (or lower) and ready for transfer of the sample into the main chamber– if pressure hasn’t reached <1E-6 Torr in 1+ hrs, contact superuser
- Slowly open the gate valve so that the main chamber ion gauge reading is increasing steadily—the main chamber pressure does not normally exceed ~8E-8 Torr during this process

Note: There is a difference in pressure between the load-lock and main chamber so by

opening the gate valve you are creating a differential. Creating a big pressure difference very quickly can stress the main chamber turbo pump—if too extreme you can even cause the turbo pump to have a vibration error.

- Make sure the stage height— controlled by the knob on top of the chamber lid— is at least 20 mm or higher (Fig. A.8)

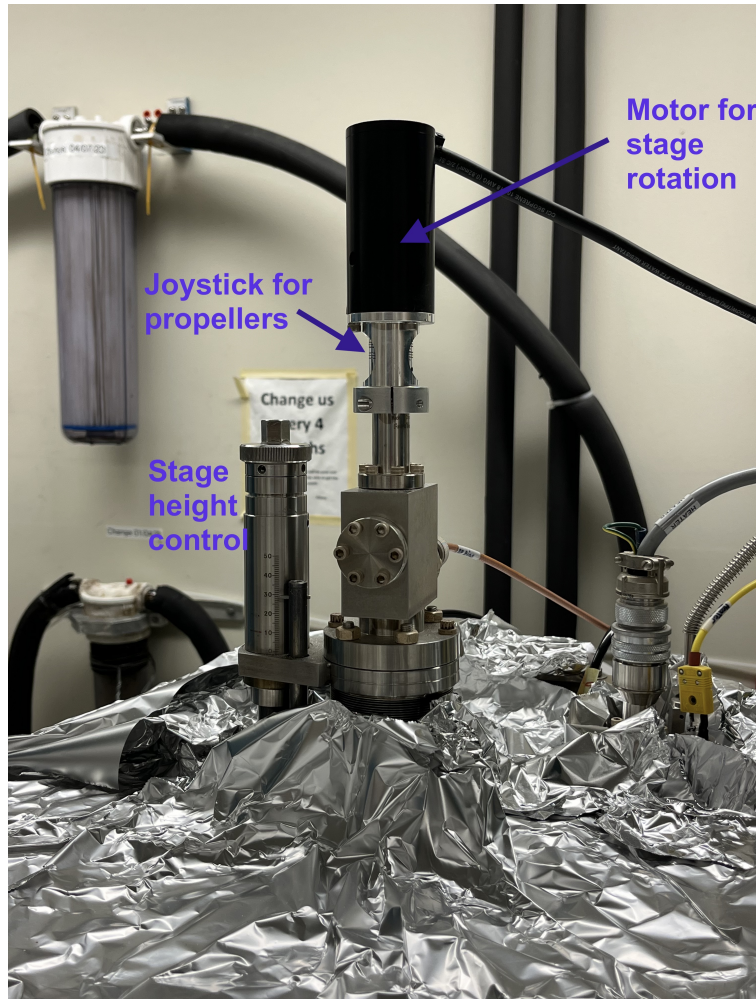


Figure A.8: Sample stage controls.

- While looking through the viewport with the flashlight, grab the black part of the transfer arm behind the laptop and slide it all the way to the left to insert the transfer arm holding the sample

- Again looking through the viewport, lower the stage propellers to ~35 mm using the joystick on the chamber lid
- Slowly rotate the propellers clockwise until they latch into the stage → if you feel too much pressure or have difficulty turning, you should retract the propellers slightly as you are pushing down too hard; if you turn the propellers 360° and feel no latching at all, you should lower the propellers slightly as you are not close enough to the sample holder
- Once the propellers are in, lower them an extra millimeter → turn the propellers clockwise so that they are fully engaged into the recesses on the stage (you can usually see the stage pop slightly upward when this is done properly)
- Now increase the stage height to 10 mm—this is the standard deposition height. **DO NOT GO TO HEIGHTS < 10 mm** which will start to crash the water lines connected to the stage into the top lid of the chamber
- Turn on the stage rotation knob and make sure that the stage is spinning evenly (i.e. there is no uneven gap or wobbliness between the stage and holder) → if uneven, take the stage off the propellers and re-try the mounting process
- Retract the transfer arm from the main chamber and close the gate valve

A.2.3 Making a Process

The main display of the AJA deposition software is shown in Figure A.9. As outlined in yellow, steps of a deposition are defined using "Create Layers," layers are compiled using "Create Process", then a defined process is selected under "Run Process" when ready to be executed. Other system parameters are visible on the home screen as well.

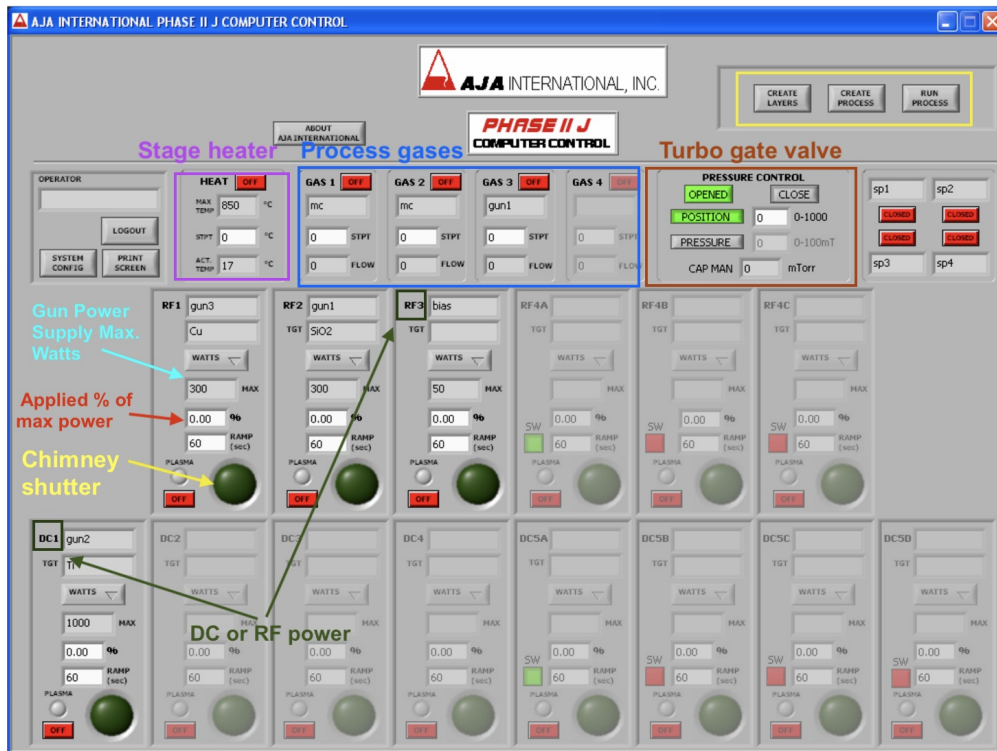


Figure A.9: Main display of the AJA software.

A process generally consists of a “pre-assist” layer followed by a deposition layer. In the pre-assist, the target is ignited with plasma while the chimney shutter remains closed so that all sputtered material stays confined within the chimney. The pre-assist is essentially a warm-up used to make sure the plasma ignites and is stable. Following the pre-assist layer is the deposition layer in which the shutter opens and material is actually sputtered everywhere inside the chamber including onto the sample. The AJA software is nicely outlined in the blue AJA binder and should be read by all users. The following is a general overview of the file parameters. New users must be trained under a superuser before running a deposition by themselves.

Defining Layers

Adjustable layer parameters:

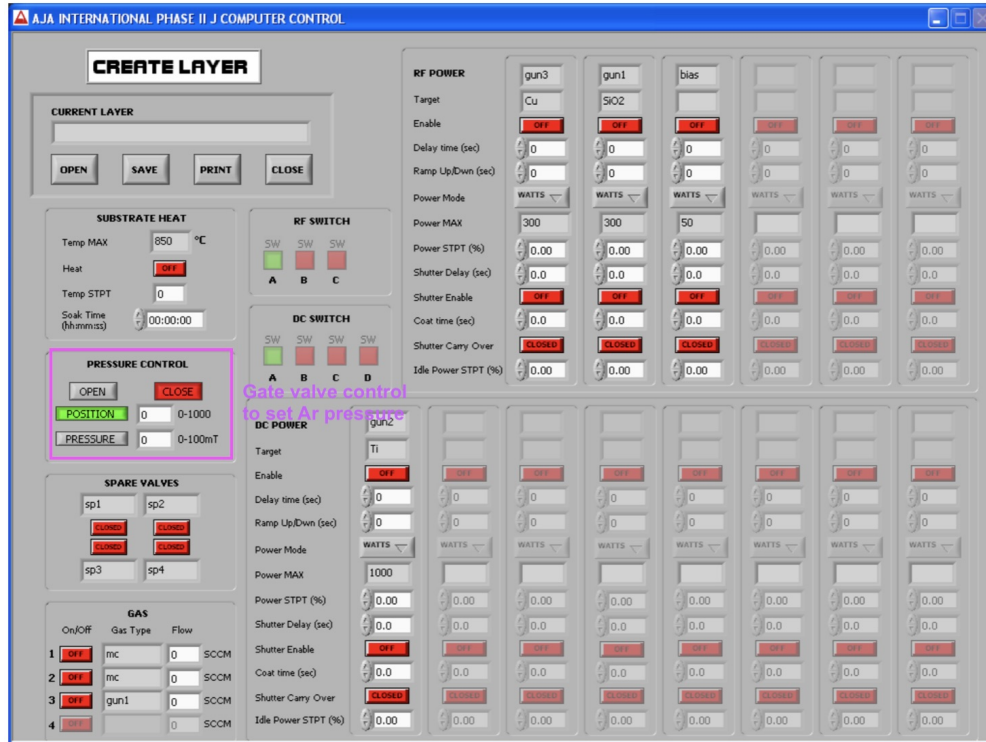


Figure A.10: "Create Layer" screen in AJA software where the user defines the parameters for their deposition.

- Target = material to be deposited
- Enable = enables the gun from which you wish to sputter
- Delay time = wait period after enabling gun (usually set to zero)
- Ramp Up/Down = time to ramp the gun up/down to a specified power (generally 20-30 s)
- Power MAX = maximum power of the gun's power supply (G2-7 = 500 W; G1 = 300 W; Stage bias = 50 W)
- Power STPT = percentage of total power supplied to the gun for a deposition (safe power levels are target-specific– consult ikwiki for historical values)
- Shutter Delay = amount of time to wait before opening chimney shutter

- Shutter Enable = opens chimney shutter
- Coat Time = amount of time to sputter for (film thickness is controlled by coat time which is based on target-specific deposition rates– consult ikwiki values)
- Shutter Carry Over = keeps the chimney open or closed in the following layer
- Idle power = power the gun will ramp to after coat time expires (Typically the idle power in the pre-assist layer should be set to the power you actually want to use in the deposition layer that follows it. In the deposition layer, the idle power should be 0 so that the gun will ramp down when deposition is finished.)
- Pressure = pressure of the Ar plasma (standard is 2 mT and < 0.5 mT is typically unsustainable. Note that changing the Ar pressure will also change your deposition rate.)
- Temperature = temperature of lamps heating the stage (optional)

The user must specify the conditions of their layers the select "Save", give the layer a name, then select "Save" again. The following is an example of typical conditions of a pre-assist and deposition layer:

Parameter	Pre-assist (Layer #1)	Deposition (Layer #2)
Pressure (mT)	20	2
Gas (sccm)	20 -- Ar	20 -- Ar
Enable	On	On
Delay Time (s)	0	10
Ramp Up/Down (s)	20	20
Power STPT (%)	10	5
Shutter Delay (s)	0	10
Shutter Enable	Off	On
Coat Time (s)	15	238
Shutter Carry Over	Closed	Closed
Idle Power STPT (%)	5	0

Figure A.11: Example of the typical layer parameters for making a 20 nm deposition of Ta at 5% power based on its calibrated deposition rate of 0.0841 nm/s. Users must consult ikwiki for up-to-date deposition rates and past records of target-safe power levels. When in doubt, always contact a superuser.

Defining a Process

- Open "Create Process" from main display (Figure A.12)
- Add the pre-assist layer to the process (#1)
- Add the deposition layer to the process (#2)
- Select "Save"
- Name the Process and save it

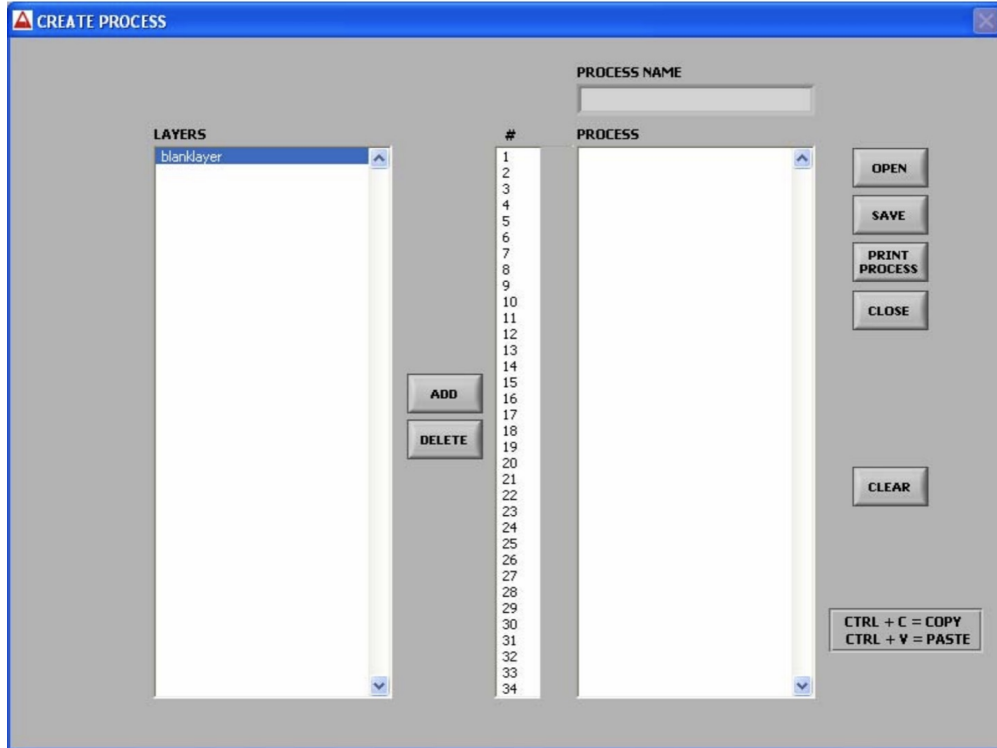


Figure A.12: On the "Create Process" screen, individual layers are compiled into a desired sequence which is saved under a process name.

A.2.4 Starting Deposition

- Make sure the main chamber base pressure is approximately $4\text{E-}8$ Torr or lower
- From the main display, select "Run Process"
- Select your process and enable the Datalog toggle
- Verify the following:
 1. Height of stage is at 10mm (standard – never <10mm)
 2. VAT is in REMOTE mode
 3. Gate valve is closed
 4. Viewport shutter is closed

5. **Ion gauge is off**

6. **Stage rotation is on**

7. **If using a reactive gas, the specific tank is open**

- Select "Run"
- The software will prompt you to check the list above—ensure these items are correct
- Select "OK" to begin deposition (you must be present for the entire deposition)
- During deposition you may click "Abort Process" at any time if there is a problem—contact superuser immediately
- When the process is completed, turn off the ion gauge which will come on immediately

Tips:

- **Tip 1:** Never sputter without the sample holder inside the main chamber and always keep the viewport closed in order to prevent the accumulation of material in unwanted places. The only process that can be run without the sample holder inside is internal baking.
- **Tip 2:** Ignite the plasma in the pre-assist layer using a slightly higher power than you plan to sputter with (e.g. if you plan to sputter at 20%, ignite at 25 or 30% during the pre-assist then set the idle power to 20%)
- **Tip 3:** High temperature growths can be made up to a maximum of 750°C. You **MUST** ramp the temperature in steps—around 10 min for every 100°C is good (the process will fail if you try to start from 16°C and ramp to 750°C in one step/layer). The software considers the time the temperature controller reaches the target temperature to be time "zero" for the layer. In other words, if you define a step to go from 100°C to

200°C in 10 minutes it will really ramp the temperature to 200°C in about 3 minutes and then the controller will sit at 200°C for the 10 minutes you specified. In this way, a nominally 10 minute layer may take closer to 15.

- **Tip 4:** Precious metals (Pt, Au, Rh, Ir, Ag, etc.) must be sputtered conservatively. Pre-assist time must be kept to an absolute minimum and film thicknesses should not exceed 20 nm without permission from the tool owner. A precious target should never be used to assist in igniting plasma in an adjacent target.

A.2.5 Removing Sample

- Once the process finishes it will take about 5 minutes for the chamber pressure to come down again
- After 5 minutes, turn on the ion gauge
- While waiting, enter all of the deposition conditions of your process into the spreadsheet titled "Deposition Rates, Configurations, and Target Lifetime" under tab "Target Lifetime" on the group Google drive. Follow path: ikwiki→Tools→Sputter Deposition System→Logs.
- If a reactive gas was used, close the gas tank
- Turn off the stage rotation
- Monitor the ion gauge until it reaches 4E-8 Torr
- Assuming the load-lock is at $\sim 8.6\text{E-}7$ Torr or lower, slowly open the gate valve between the load-lock and main chamber
- The ion gauge should start increasing and then stabilize near $\sim 6\text{E-}8$ Torr or lower
- Slide the black transfer arm into the main chamber

- Lower the stage onto the transfer arm → making sure that the the stage screws align into the recesses on the transfer arm
- Rotate the the propellers counterclockwise to disengage the stage
- Return the propellers to a height of 20 mm
- Slide out the transfer arm with stage holder on it
- Close the gate valve
- Turn off the load-lock vacuum pump
- Put on lint-free hood, gown, hair net, and gloves
- Lay out a clean piece of aluminum foil on the loading area
- After 2-3 minutes, the load-lock lid will make a slight popping sound when vented
- Take off the load-lock lid with one hand and remove the sample stage with the other (to minimize potential contamination by skin, eyelashes, etc., do not lean your body over the opening of the load-lock at any point)
- Immediately put the load-lock lid back on
- Place the stage on the aluminum foil and inspect it for any semi-loose metallic debris/flakes– if present, contact tool owner immediately
- Unscrew the clips, remove your sample, then re-screw the clips
- Open the load-lock lid and place the sample stage into the load-lock as you initially found it (i.e. the sample should be facing down on the transfer arm)
- With the lid held in one hand, use the other hand to wipe down the load-lock O ring with IPA and a beta wipe

- Close the lid
- Pump down the load-lock by turning on the load-lock vacuum pump (Fig. A.5) → check to see pressure is decreasing

A.3 Target Change

A target change is done whenever materials need to be swapped in or out of the system. Because this requires breaking vacuum and subsequent baking spanning several days, a target change must be properly planned for. This section covers the entire process starting from sandblasting the chimneys to re-conditioning the system after baking. Target changes differ from fully shutting down the system as the main power can still remain on.

A.3.1 Sandblasting

The sandblaster is used to, quite literally, blast sand at the housing and remove the accumulation of old material so that new targets have a clean chimney. Before swapping out targets inside the sputtering system, you first need to verify that there are clean chimneys available *prior* to starting. Since you want to minimize how long the main chamber is open, you do not want to waste time cleaning these. However, depending on how many need to be changed there may be one or two that need cleaning during the change—this is unavoidable.

Our lab sandblaster is located in the Machine Shop (FRH)—go through the front door and straight to the back wall (passing one set of plastic curtains). Their hours as of April 2019 are 6am-2pm.

Getting Started

- Gather the housing that needs cleaning and place it on metal tray
- Put on a lab coat, face mask, and protective eyewear then bring target to sandblaster
- Remove all aluminum and lay out pieces on the metal tray
- Open the left side door of the sandblaster, slide in the tray, and close it
- Make sure that the air hose is connected to the coupler—if not, connect it by pushing back on the coupler, inserting the air hose while still pushing back the coupler, then releasing the coupler (Fig. A.13)

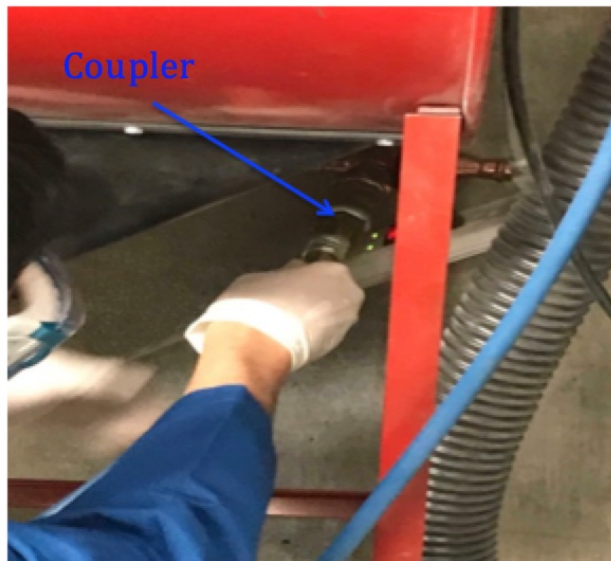


Figure A.13: Coupler being connected underneath sandblaster (red)

- Turn on the extension cord to start air flow
- Place hands inside the holes and grab the gun handle
- Use the foot pedal to start blasting sand
- Since it can be difficult to see inside, you may need to occasionally stop, open the door, and inspect the housing

Tips:

- Focus special attention on the areas where the housing is going to be in direct or close contact to the target
- Sandblasting in one spot for longer is usually more effective than quickly moving over a large area
- If sandblasting is taking significantly longer than usual ($\sim 1-1.5+$ hrs), the tip of the gun may need to be replaced or it may be time to change the sand– notify superusers

After Cleaning

- Remove the tray from inside the sandblaster and re-cover the housing with aluminum foil
- Back in the lab, place the entire housing in a large beaker full of acetone and sonicate for 30 minutes (the metal tray on the sonicator is removable and you may need to slightly lower the water level)
- Follow with 30 minutes of sonication in IPA
- When time is up, lay out two large pieces of aluminum foil (one for drying parts on and one for wrapping up the entire housing)
- Take the housing out of the IPA beaker, place on one piece of aluminum foil, and blow dry with N_2 – make sure it is well dried (i.e. blow directly into screw holes, undersides, etc.)
- Wrap the entire housing in the second piece of aluminum foil and notify superuser once cleaned
- Log your cleaning on ikwiki under "Sputtering System"

A.3.2 Main Chamber Vent

- Vent the load-lock chamber and make sure there is sufficient nitrogen gas (right-most gauge on nitrogen regulator should be reading at least half of the full gauge range– if not, replace the tank with a full one)
- Close the main chamber gate valve: first set the VAT to local by holding down the local button (Fig. A.14)→ hold down the close button → the pressure should start increasing so turn off the ion gauge



Figure A.14: VAT controller which sets the position of the gate valve that sits in front of the turbo pump (visible through the viewport). During normal operation, the gate is fully in the open position. Closing it will increase the chamber pressure.

- Turn off the vacuum pump for the main chamber (Fig. A.15)



Figure A.15: Controller for main chamber vacuum pumps and their power– turn vacuum pump off to stop the turbo pump

- Look at the rotation speed of the pump on the Shimadzu panel and wait until it reaches 0% (takes ~ 5 minutes)
- Open the white Swagelok knob (located on the green system frame near mask aligner arm) in *very* slow steps to bring the main chamber to atmospheric pressure ($\sim 7.7E2$ Torr) → you must loosen the black closure knob on the main chamber lid about 3/4 of the way through this process
- When the chamber is vented, close the Swagelok knob and nitrogen tank
- Remove aluminum foil from outside top of the main chamber
- On the lid of the main chamber are orange heating pads → disconnect these from their grey Variac transformers so that the chamber lid can be fully opened → turn off their extension cord as well
- Set the heat exchanger temperature from $16\sim^{\circ}\text{C}$ to $21\sim^{\circ}\text{C}$ to prevent condensation

A.3.3 Preparation

- Suit up in lint-free gown, hair net, hood, sleeve protectors, gloves, and face mask

- Get out the target change tools from the AJA drawers on the side of the system
- Have the clean chimneys laid out on the workbench and the new targets going into the system nearby
- Carefully open the main chamber lid and line the O ring with aluminum foil for protection
- Inspect the chamber for any abnormalities before proceeding

A.3.4 Starting Target Change

- Adjust the position of the gun towards the chamber walls using the black tilting knob underneath each gun
- Disassemble the gun’s shutter and chimney by removing their screws (refer Fig. A.16)
- For non-magnetic targets, be careful when lifting off the clamping ring as the target may want to slide off the gun — always have your hands in a supportive position to prevent this
- For magnetic targets, slide them off of the surface of the gun GENTLY and with ZERO torque → this means sliding the target with your fingers while “counter-pushing” on the source with your thumbs → be careful during this step as the source is extremely delicate and can be damaged
- Wrap the target in aluminum foil immediately after removing and label it with the name of that material and date
- Also wrap the disassembled housing in aluminum foil and label it by material name as well

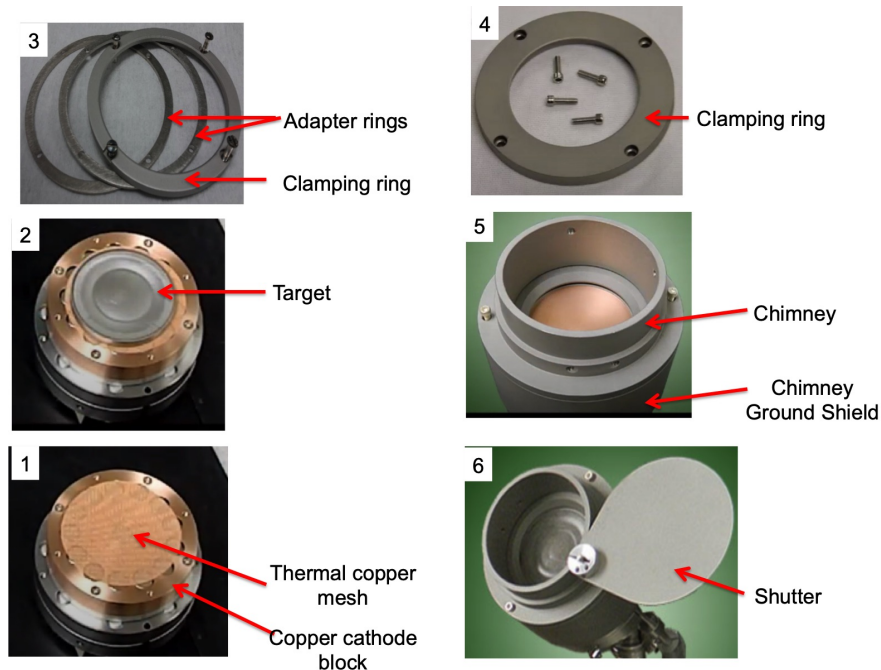


Figure A.16: Order of operations for installing a new target starting from the cathode block.

- Grab the new target and install it in the following order (Fig. A.16): copper mesh (for non-magnetic materials), adapter ring if needed, clamping ring, chimney, then shutter (these should all be freshly cleaned). If the target is magnetic, it should be slid onto the source in the following way:

1. Approach with the target parallel to the cathode surface
2. Make gentle contact between the top edge of the cathode surface and the bottom of the target
3. Carefully slide the target to the center while applying zero torque to the source
4. Choose an appropriate adapter ring such that the total thickness of the target (including backing plate) and ring is 1/4"

Note A: Targets must be 2" diameter and 0.250" thick–this is a total thickness that includes the backing plate if one is used. Insulating or semiconductor targets should be ordered with backing plates to improve heat conduction during deposition. For

thinner targets (like magnetic ones which typically have just 0.125” of source material), an adapter ring of appropriate thickness should be used to reach the 0.250” thickness tolerance. The ring goes between the target and clamping ring.

Note B: We have two different kinds of clamping rings– the standard ring, shown in (Fig. A.16), or a power ring (sometimes called Gen II ring) . The power ring is designed for use with insulating materials and can only be used on targets which have a specially sized copper backing plate from AJA (see Fig. A.17).

- Return the guns to their normal angle, around $\sim 10^\circ$
- Open the shutter of each gun from the AJA laptop and make sure it is level, opens without hitting its neighbors, and covers the chimney top completely
- Next, remove the three screws on the stage propeller and replace them with fresh ones
- If there are flakes on the stage: cover the entire chamber top with aluminum foil for protection, use a razor to shave/peel off these flakes, then remove the aluminum foil and dispose of the catchings
- Vacuum any flakes inside the chamber using the small red Shopvac vacuum with the needle nose attachment
- Finally, use an alpha wipe and IPA to clean the O ring and outer rim of the chamber then dry with another alpha wipe
- If the stage is in the main chamber, remove it in preparation for future baking step
- Close the main chamber lid and secure the closure knob shut



The **AJA** Power Ring & Backing Plate

topgun@ajaint.com | 781-545-7365 | www.ajaint.com



The most effective way to sputter brittle/dielectric targets with RF on an AJA sputter source is to utilize the Power Ring, a design which effectively clamps down the edge of a slightly oversized backing plate with a special, reusable clamp ring. The target is bonded onto the center of this oversized backing plate and its surface is flush with the top of the clamp ring. There is no force exerted on the target itself which minimizes stress on the brittle material. As a result many targets can be operated at up to 50% more RF power than if they are clamped directly. An additional side benefit is that for low sputter yield materials there can be no contamination from the clamp ring at higher pressures since it is no longer exposed to energetic particles.

— The Power Ring & Backing Plate Assembly —



Bonded Target



Power Ring (Backside)



Source with Target & Power Ring

AJA International, Inc. 809 Country Way, N. Scituate, MA 02066

Figure A.17: Power ring technical note from AJA.

A.3.5 Finishing Target Change

- Check Swagelok knob is closed then open nitrogen tank–**Make sure this is correct, otherwise oil from the turbo pump can get pumped into the main chamber**
- Set the heat exchanger temperature from $\sim 21^{\circ}\text{C}$ back to the normal $\sim 16^{\circ}\text{C}$
- Switch VAT back to open position
- Turn on main chamber vacuum pump
- Reconnect heaters and turn extension cord back on
- When the rotation speed of the main chamber turbo reaches 100%, turn on the load-lock vacuum pump
- Update the Target Inventory and Configuration logs on the group Google drive by following the path from "Sputter Deposition System" on ikwiki

A.3.6 Baking

- Verify that all grey Variac transformers beneath the system are off and their output voltage is set to 0
- Check, one at a time, that each Variac is working:
 1. Unplug the grey cables from the heaters into the Variacs
 2. Remove each Variac one at a time from the system
 3. Connect a power cable to the Variac
 4. Insert needle tip probes into the output of the power cable and attach to multi-meter
 5. Plug in power cable to outlet

6. Turn on the Variac (make sure all are in the “on” position– some orange lights may not illuminate)
7. Slowly increase the voltage setting and make sure the multimeter reading is accurate (if not, check that the fuse is not blown), then return it to 0V

Note: The Variacs require a 250V/12A fuse. If we don’t have any, a 250V/10A fuse should be okay temporarily but do not set the voltage near max. Also, do not use a fuse with a higher current rating than 12A.

- After the Variacs have been checked, make sure they are set to 0V and reinsert the grey cables into their respective transformers according to their labels
- Turn on all transformers → slowly increase their voltages from 0V to the number specified on the white label of each transformer

Note: The transformer has a max output of 140V → output voltage=percentage*140V

Table A.1: Multicolumn table

Heater No.	Variac No.	Heater Resistance (Ohms)	Power Percentage
1	4	3	70
2	4	3.4	70
3	4	3.3	70
4	2	2.9	80
5	1	31	70
6	1	61.5	70
7	1	61.6	70
8	2	2.6	80
9	2	2.6	80
10	5	3.3	70
11	5	3.6	70
12	5	3.4	70
Tape	3	85.1	60

- While the system begins its ”outside bake”, the “internal bake” can begin simultaneously

- The internal bake should be done with the stage removed from the main chamber and the propeller rotation on
- First set the temperature controller to HAND (%) mode by pressing the two outside buttons—scroll button (left) and down arrow (right)—at the same time
- Press the indicator then hold the scroll button for 3-5 seconds
- Scroll until you see the actual temperature flashing (top) and bottom display reads HX.XX (where X.XX represents the percentage power output to the lamp)
- Set the percentage power to 0
- In the software, turn the heater on and put the setpoint temperature to 0
- Now increase the percentage power on the temperature controller to 20% for a bakeout
- Monitor the external temperature using a thermocouple thermometer attached to a multimeter and verify the external temperature of the system is reaching $\sim 120^{\circ}\text{C}$
- If okay, cover the outside of the system in aluminum foil
- The system is to be left baking during the daytime (8+ hrs) but not overnight (you can still leave it in HAND mode when you leave for the day, just reduce power to 0; for the Variacs, slowly reduce them to 0V and then turn them off before leaving)
- Monitor the base pressure over the course of the baking until it reaches an acceptable level (it should take 1-2 days but is dependent on how long the system was open for)
- When the base pressure is acceptable, exit HAND mode by pressing the up and down buttons simultaneously
- Turn off the external heaters

- If the base pressure is still high, check the RGA for a leak, try an extra baking, or sputter a getter material (usually Ta). Otherwise it may simply need more time to outgas

A.3.7 Conditioning the Guns

- Since all targets were exposed to air during the change, you will need to sputter off some material from the surface which may have oxidized
- Run a program in which each gun is opened individually and sputtered for ~30sec - 1min (usually at ~20 mT Ar pressure to reduce time) → consult ikwiki for acceptable target power levels/deposition rates
- Make sure the sample holder is inside the main chamber when this is done (as it should always be when running any process)
- The system should now be fully ready to use again

A.4 Shutting Down & Turning On

A.4.1 Shutting Down without Main Chamber Vent

- Vent the load-lock chamber (Fig. A.19a)
- Close the main chamber gate valve: set the VAT to local by holding down the local button → hold down the close button → the pressure should start increasing so turn off the ion gauge (Fig. A.18)

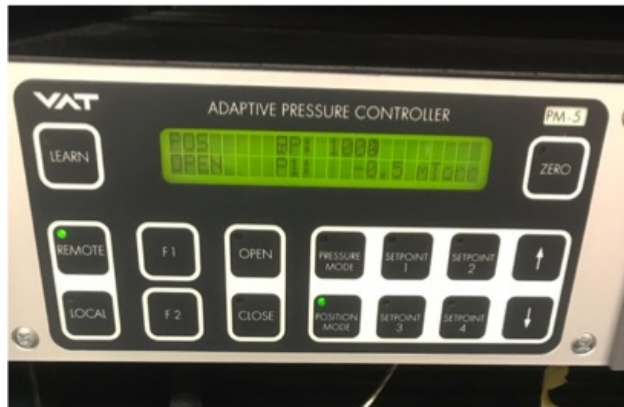
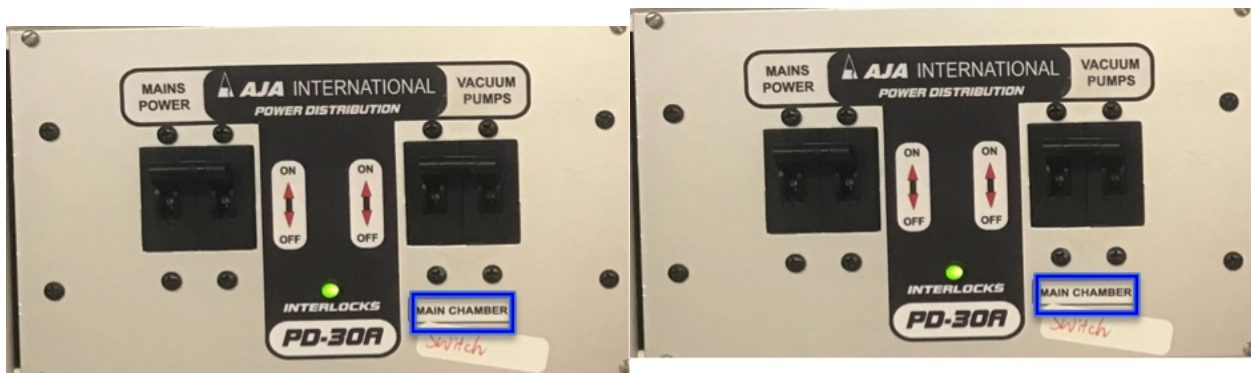


Figure A.18: VAT controller which sets the position of the gate valve that sits in front of the turbo pump (visible through the viewport). During normal operation, the gate is fully in the open position. Closing it will increase the chamber pressure.

- Turn off the vacuum pump for the main chamber (Fig. A.19b)
- Look at the rotation speed of the pump on the Shimadzu panel and wait until it reaches 0% (~takes 5-10 minutes)
- Turn off the main chamber power and load lock power



(a) Controller for load-lock pump and power (b) Controller for main chamber pumps and power

Figure A.19: Separate control panels for main chamber and load-lock powers.

- Turn off main power

A.4.2 Turning on From Shutdown

- If water reset button is illuminated, press it to reset
- Make sure the nitrogen tank is open (and not near empty) and that the Swagelok vent knob is completely closed (it should not have been touched if the main chamber was not vented)
- Turn on the main power
- Turn on the main chamber power and the load-lock power
- Check that the panels of the power supplies are coming on
- Proceed as follows for the particular case:

If the main chamber base pressure is > 1 Torr,

- Vent the main chamber by slowly opening the Swagelok vent knob (nitrogen must be open)→ venting is done to prevent causing stress to the turbo pump if there is a large pressure difference between the turbo and main chamber
- Loosen the black closure knob $\sim 3/4$ of the way through the venting process, but do not open the lid
- When the 2nd gauge reads atmospheric pressure ($7.7E2$ Torr), tighten the black closure knob
- Close the Swagelok vent knob and double check that there is nitrogen flowing
- Set the VAT to local and then open the gate valve
- Turn on the main chamber vacuum pump
- Verify the pressure is going down and wait until the ion gauge comes on
- When the turbo pump is at 100% rotation, turn on the load-lock pump

If the main chamber base pressure is < 1 Torr,

- Turn on the main chamber vacuum pump
- When 100% rotation, verify gate valve position set to 0 in software
- Put VAT in remote
- Open gate valve slowly in small increments (position 50, 100, 200, 500, etc. until 1000–fully open)
- Verify the pressure is going down and wait until the ion gauge comes on
- Turn on the load-lock pump

A.5 Heater Exchanger Maintenance

Every 6 months, the water in the heat exchanger for the turbo pump (directly behind the annealing oven) must be replaced with fresh DI water and the strainer must be cleaned. Any maintenance to the exchanger requires the sputtering system to be shutdown but it is not always necessary to vent the main chamber.

Note: It is normal that the green cooling water light is not constantly illuminated– the heat exchanger works in cycles of cooling and not cooling, hence the cooling light is cyclic. Normal operating temperature and pressure for the exchanger is 60°C and around 72-74 psi.

A.5.1 Cleaning Exchanger Water

- Stop the heat exchanger using the red button on the front panel (the exchanger should stop humming) and then turn off entirely using the black power button
- Loosen the tube clamp on the black water return/recirculating line at the back of the exchanger→ remove the brass nut and hose completely from the exchanger (Fig. A.20)



Figure A.20: Heat exchanger front (left) and back (right)

- Find an empty container or garbage can for dirty water
- Place the hose into the garbage can
- As a precaution, connect a new piece of tubing to the opening where the return hose used to be connected → aim it into the garbage can as well
- Take off the small rectangular lid on the top of the exchanger → unscrew the white cap which is the opening to the water reservoir
- Press the red button on the front panel → the dirty water should now be emptying into the can
- The exchanger will stop running when the water level becomes too low , so another person needs to be coming back and forth with clean DI water from the tap and pouring it into the reservoir
- Press the red button again to empty more water into the can
- Repeat the process of adding clean water and draining old water until you see no more algae in the old water (you will need to periodically stop and empty the garbage can)
- Finish by pouring ~ 300 mL of Optishield Plus kept under the lab sink into the top of the exchanger

- Put the white cap back on, close the top lid, reconnect the hose/fasteners, and turn the red button on

A.5.2 Cleaning Strainer

- The exchanger's reservoir must be drained completely before attempting to clean the strainer
- First shut off the exchanger (system should already be off)
- Disconnect the return and supply connections on the back of the exchanger → these will have residual water inside them so have a bucket to put the hoses in
- Attach a hose from the exchanger's supply to a drain (the drain can be the sink or a bucket that you will periodically dump out)
- Sometimes water can come out of the return line so attach another hose from the return to a bucket to be safe
- Run the exchanger and wait until the low level light comes on and the exchanger stops automatically
- Now turn off the exchanger and unplug it from the socket
- To finish draining the reservoir, unscrew the white reservoir cap and siphon out the rest of the water
- Unscrew the four nuts on the outside frame and lift off the top
- By the brass pump there is a large hex nut behind which is the strainer
- Removing the hex nut will release a fair amount of residual water left in the piping → be prepared with sponges/containers to control the mess

- Once the nut is removed, take out the strainer and sonicate it in MicroPosit until it is clear again
- Re-insert the strainer, tighten the hex nut, and put the exchanger lid back on
- Re-fill the exchanger reservoir (DI water only!) and plug the exchanger back into the socket
- Turn it on again and then turn on the sputtering system (if the water reset button is illuminated hit it to reset)

A.5.3 Flushing Cooling Lines

- Shutdown the system without venting then turn off the heat exchanger
- Go to the backside of the system and look at the pneumatics panel near the floor (Fig. A.22)

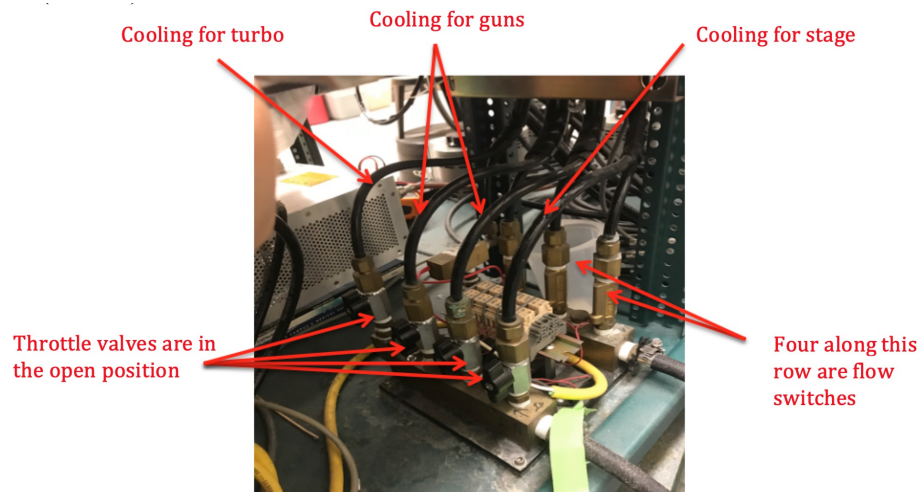


Figure A.21: Pneumatics panel which controls the flow of cooling water to various parts of the system

- There are four black throttle valves each controlling cooling water flow to a particular area (guns 1-3, guns 4-7, turbo pump, and stage)

To flush gun lines using heat exchanger:

- Open all throttle knobs
- Choose one of the series gun loops to measure along first– keep the throttle knob on this line open and close the throttle knob to the other gun line which is NOT being measured
- Choose one gun in the series loop to measure flow rate through first
- Connect the input of the cooling loop line directly into the input of this gun and connect the output of this gun to a piece of tubing that feeds into a bucket (all other guns in the series loop should now be bypassed)
- Run the exchanger and record the time it takes to fill up a 2L jug (i.e. flow rate) as well as the pressure on the heat exchanger – log the information on ikwiki and compare to historical rates
- Now reverse the direction of flow— that is, swap the input and output tubings going through the gun
- Run the exchanger and record the time it takes to fill up a 2L jug (i.e. flow rate) as well as the pressure on the heat exchanger in this ”backwards” direction – log the information on ikwiki and compare to historical rates
- Now repeat this same procedure for the other guns in the loop
- Finally, reconfigure the cooling lines in the loop as normal
- Repeaet this process for the second cooling loop for guns

To flush gun lines using DI water from tap:

- Open all throttle knobs

Table A.2: Measured Flow Rates Through Guns

Gun Number	Flow Rate (Forward) [L/sec]	Flow Rate (Backward) [L/sec]
1	2/46	
2	2/51	2/60
3	2/50	2/51
1-3	2/73	
7	2/55	
4-7	2/88	2/86

- Choose one of the series gun loops to measure along first
- Choose a single gun in this loop to measure first
- Connect the input of the gun directly to the DI tap at the sink and connect the output side of the gun into an empty 4 L bucket
- Measure flow rate by timing how long it takes to fill up a 4 L bucket
- Repeat in forward and backward directions as needed
- Log the information on ikwiki and compare to historical rates

A.6 Leak Testing

A.6.1 Gun Cooling Lines

This procedure is for guns only—do not follow this for leak checking stage or turbo water lines!

- Shutdown without out vent and then turn off the heat exchanger

- Go to the backside of the system and look at the pneumatics panel near the floor (Fig. A.22)

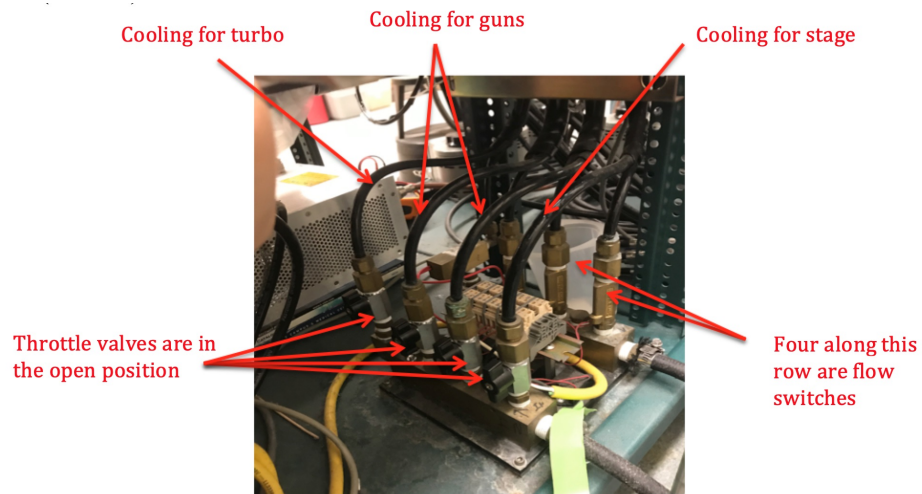


Figure A.22: Pneumatics panel which controls the flow of cooling water to various parts of the system

- There are four black throttle valves each controlling cooling water flow to a particular area (guns 1-3, guns 4-7, turbo pump, and stage)
- Choose which of the gun lines to test first → close only this line by turning its throttle valve 90 °
- To the right of the pneumatics panel is a breakup of the cooling water to their respective areas of the chamber (Fig. A.23)

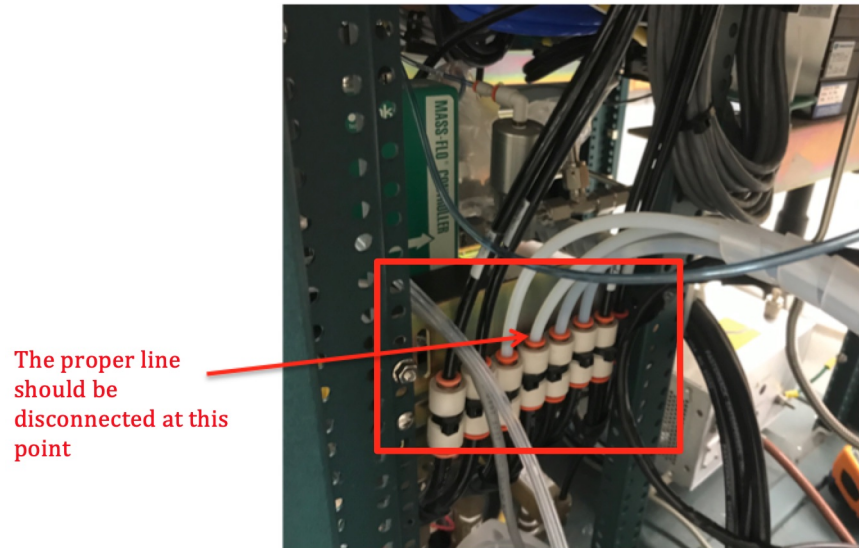


Figure A.23: Individual return and supply lines to guns, turbo pump, and stage

- Trace the lines pictured above until you can identify which are the supply and return for the guns you are interested in testing (note that cooling lines for guns are connected in series)
- Disconnect the proper supply line at the point shown above—if there is an easier connector to remove down this line before it reaches the first gun, you can disconnect at that point instead
- Now disconnect the return line to those same guns either at its respective port pictured above or at a more convenient spot if applicable
- Put a label on the supply and return lines that have been disconnected so you know how to properly re-install them
- The final configuration should look similar to Fig. A.24



Figure A.24: Example of how water lines for guns are connected in series

- Connect a jumper cable between the open ports where the supply and return used to be connected, such that you bypass the guns entirely
- Now turn on the heat exchanger and make sure the new connection does not leak
- Turn on the rest of the sputtering system
- Now blow dry the open gun lines using nitrogen– a full tank is sufficient
- Finally, replace the nitrogen flow with helium and run the RGA to check for signs of a leak
- After leak checking, shut down the system without venting then turn off the heat exchanger
- Remove the jumper cable and reconnect the water lines back to their original configuration
- Turn on the heat exchanger to verify no leaking, then turn on the sputtering system

A.6.2 Stage Cooling Lines

- Shutdown without venting the main chamber, then turn off the heat exchanger
- Disconnect the two black water lines connected to the top of the lid– be prepared with paper towels as these will still have a bit of water in them (Fig. A.40)

Water lines disconnected

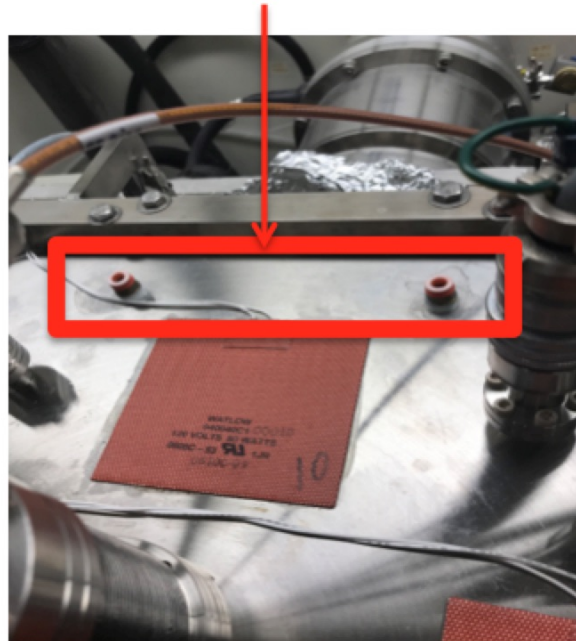


Figure A.25: Empty connections on main chamber lid where water lines to the stage are normally connected

- Connect the removed water lines end to end using a fluid tube connector to form a closed loop (Fig. A.41)
- Place the loop in a bucket for precaution (bucket unpictured in Fig. A.41)

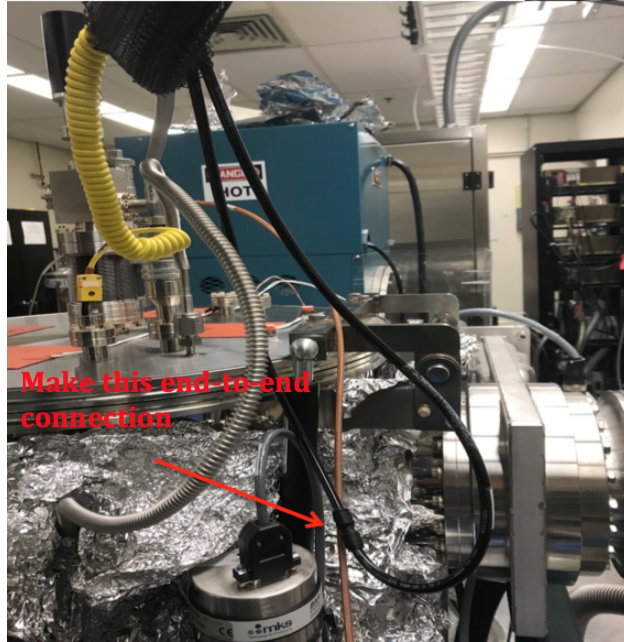


Figure A.26: Connect the water lines together to form a closed loop so that no water is going to the stage

- Run the heat exchanger to make sure the new connection is not leaking—you’ve now bypassed the stage cooling to the system so that it can be tested for a leak
- Now turn on the system again – since system was only off for a short while MC vent is not necessary
- Base pressure should return fairly quickly to its normal value $\sim 1\text{-}2\text{E-}8$ Torr
- The entry points for tubing on the main chamber lid where the black tubes used to be connected (Fig. A.41) need to be dried out
- Connect nitrogen to one of the openings and blow excess water out the other (the line needs to be very dry to do a helium test so typically allow use of an entire nitrogen tank)
- Once this is sufficiently dry, replace the nitrogen with helium gas
- Run the RGA and look for spikes in helium levels:

- If nothing, try adjusting the stage height while helium is flowing as this moves the cooling lines slightly
- If a leak is found, the system needs to be opened and BOTH lines replaced (since it's difficult to pinpoint whether the leak is in the right or left line)
- If no leak is found,
 - Shutdown w/out venting main chamber
 - Turn off heat exchanger
 - Disconnect the black loop end to end
 - Remove the He connection
 - Re-connect each loop to the openings for H₂O on the lid
 - Turn exchanger back on
 - Turn on the system again – since system was only off for a short while, a main chamber vent is not necessary

A.7 Miscellaneous

A.7.1 Replacing Rotary Transfer Rod

- Follow the procedure for opening the main chamber as priorly outlined in this SOP
- Once the lid has been opened, unscrew the three set screws in the stage propellers and remove the propellers
- Next remove the first flange above the bellows on top of the main chamber lid (a plastic piece should come out with it)
- Once removed, you should see a small set screw through the opening that the flange used to cover→this set screw is holding up the transfer rod

- Remove this set screw while keeping a thumb on the base of the transfer rod to prevent it from sliding out into the chamber (or use two people)
- Once unscrewed, safely slide the rod out
- Next close the lid and disconnect the cable to the black rotation motor
- Remove the flange for the black rotation motor
- Once removed, you should notice there is a spring-loaded blockage partially covering the insertion path for the rod (this acts as the contact for transferring RF power through the rod and to the stage)
- Depress the blockage with a flathead screwdriver (one person) and then insert the new transfer rod fully upward through the stage opening
- Spin the rod until the circular opening on the tip of the rod aligns with the opening for the set screw
- Insert the screw then tighten
- Next reinsert the black motor top
- Reattach the stage propellers using fresh screws
- Remove the old gaskets for the two flanges and put in a new one
- Re-seal each flange – use a star pattern when tightening the screws to deform the gasket evenly
- Reconnect the motor's power cable

A.7.2 Flowmeter Removal and Installation

A.7.3 Flowmeter Removal

- Shutdown system without venting
- Make sure the gas tank connected to the flowmeter being worked on is fully closed
- Remove the mounting screws for the flowmeter body (Fig. A.27)

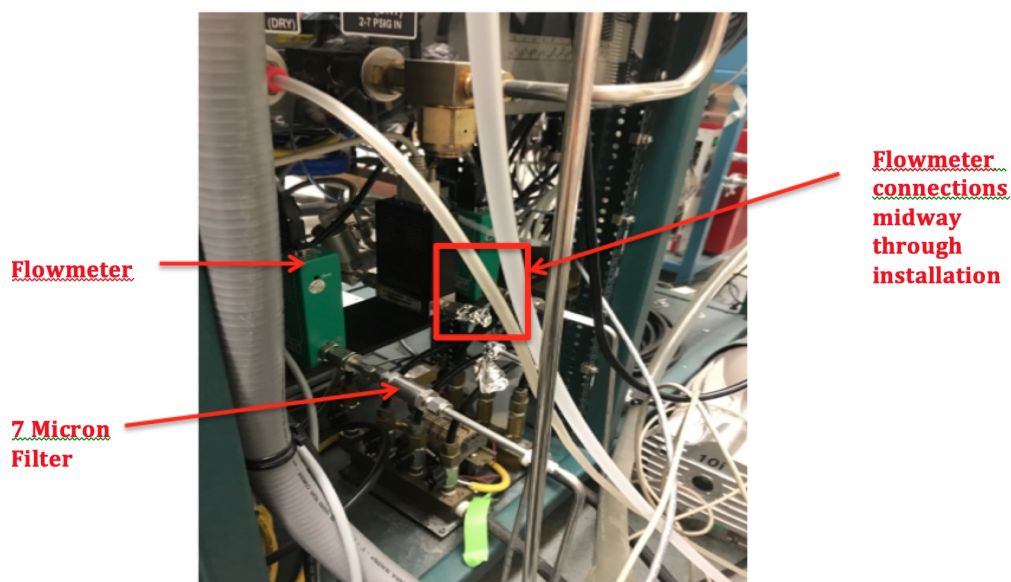


Figure A.27: Flowmeter setup on rear of system: each flowmeter is mounted to the system with removable screws. An incoming gas line is connected to the entrance of each meter with a filter placed in between.

- Now read the VCR or Swagelok instructions for proper tightening and removal procedures of VCR or Swagelok connections before proceeding→these must be strictly followed
- Disconnect back side of meter to where it is currently connected to the diaphragm valve (Fig. A.28)



316L VIM-VAR UHP Diaphragm Sealed Valve, 1/4 in. Female VCR Fitting, SC-01 Cleaned, NC Actuator

Part No: 6LV-DPFR4-P-C

Figure A.28: Diaphragm valve at the exit of the flow meter which then connects to the sputtering system itself. This valve acts like an open/close for incoming gas.

- Cover exposed openings with aluminum foil
- Now come to the other side of the meter where the inline gas connections are made
- Hold the male nut fixed with one wrench and remove the female nut with another wrench(Fig. A.29)

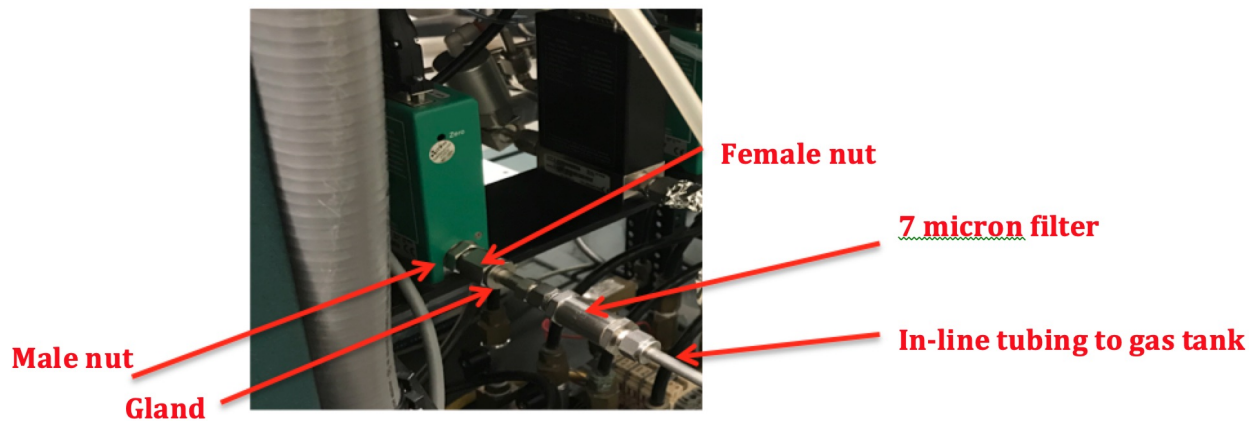


Figure A.29: Connections from gas tank to flowmeter

- Disconnect the 7 micron filter in a similar fashion
- Disconnect the computer cable from the top of the flowmeter and fully unmount the meter

A.7.4 Flowmeter Installation

The necessary components before beginning are: new 7 micron filter, SS-4-VCR-1 female nut, gland (SS-4-VCR-3-2MTW or SS-8-VCR-3-4MTW depending on tube size), and gaskets (SS-4-VCR-2 although sizes should again be double checked against tube size and flowmeter connection size).

- Mount the new flowmeter in place with screws and in the proper flow orientation (the big arrow labeled on the front of the meter should be pointing towards the diaphragm valve)
- Reconnect the backside of the flowmeter to the diaphragm valve
- Now install the new 7 micron filter to the tubing
- Insert the gland through the female nut then reattach this piece to the male nut on the body of the flowmeter
- Insert the other end of the gland into the 7 micron filter then tighten
- Once the connections are sufficiently tightened and the flowmeter is properly installed, open the gas tank
- In the software, start by setting a low flow rate and observing any errors or abnormalities in the base pressure recovery time
- Slowly increase the flow rate and check that the base pressure is still recovering normally
- Now leak check all connections using He gas and the RGA —do not exceed the pressure rating for the RGA though
- This can be done by covering the test piece in a plastic bag and filling it with He, or aiming the end of the tubing at specific areas

A.7.5 Transforming Nonmagnetic/Magnetic Guns


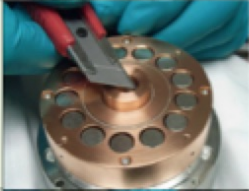


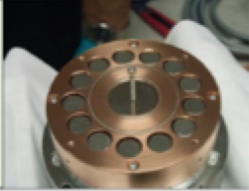
At present, the sputtering system has two magnetic guns for sputtering magnetic materials. However, nonmagnetic guns can be transformed to be magnetic. Extra caution needs to be taken in this process. Despite their metal assembly, the magnetron sources are delicate and have a brittle ceramic ring inside which can be easily damaged by mechanical impacts.

Fig. A.30 is AJA's guide to reconfigure a nonmagnetic gun to a magnetic gun:

AJA INTERNATIONAL, Inc.
P.O. BOX 246, 809 COUNTRY WAY, NORTH SCITUATE, MA 02660 USA
 TEL: 781-545-7365 / FAX: 781-545-4105 / e-mail: topgun@ajaint.com / web: www.ajaint.com

TECHNICAL NOTES & OPERATING TIPS

SUBJECT: CONVERTING A320-XP and ST-20 BETWEEN MAX RATE and MAGNETIC MATERIAL MAGNET CONFIGURATION

<p>1. Remove any shutter, chimney, ground shield, clamping ring, adaptor rings (if necessary), target, and mesh. It should look similar to the photo on the right.</p>	
<p>2. Using clean compressed air. Force the Cu spacer to float up and then grab hold of it and remove it from the gun. If the Cu spacer does not float use a sharp blade to remove the spacer.</p>	
<p>3. Using a pair of needle nose pliers grab the center stack of magnets and remove them.</p>	
<p>4. Thread a 2-56 long screw into the top of the slug. Then holding the screw, insert the slug into the center hole until it makes magnetic contact with the magnetron's pole piece at the bottom of the hole.</p>	
<p>5. The screw should be removed at this point. You can now mount a 3 mm thick x 2.00" diameter magnetic material target directly onto this cathode surface CAREFULLY FOLLOWING the instructions in the source manual. Then position a 0.125" clamping ring adaptor on top of the target, then secure the clamping ring over the top. Finally, reassemble ground shield, gas ring/chimney and shutter and test for continuity as defined in the source manual before use.</p>	

Placing the Target (step 5)

- Targets must be slid onto the source in the following way:

1. Approach with the target parallel to the cathode surface
2. Make gentle contact between the top edge of the cathode surface and the bottom of the target
3. Carefully slide the target to the center while applying zero torque to the source → this means sliding the target with your fingers while "counter-pushing" on the source with your thumbs

Figure A.30: AJA guidelines for configuring a nonmagnetic gun to be magnetic

A.7.6 Replacing Stage Water Lines (VCR)

On the top of the main chamber lid are two black water lines for cooling the stage. These lines are connected directly to two VCR water lines on the inside of the chamber which allow water to reach the stage (Fig. A.43). The raising and lowering motion of the stage causes these internal VCR water lines to move and over time they can form leaks. These VCR lines

are always to be replaced in pairs, as it is too difficult to be tell with certainty which line is leaky.

Note: The reason the stage is never to be lowered past the 10 mm mark is specifically to protect these water lines and the stage assembly. If the stage is lowered past 10 mm, these lines bump into the top of the chamber lid. Not only does this damage the lines but it places stress on the connections to the entire stage assembly.

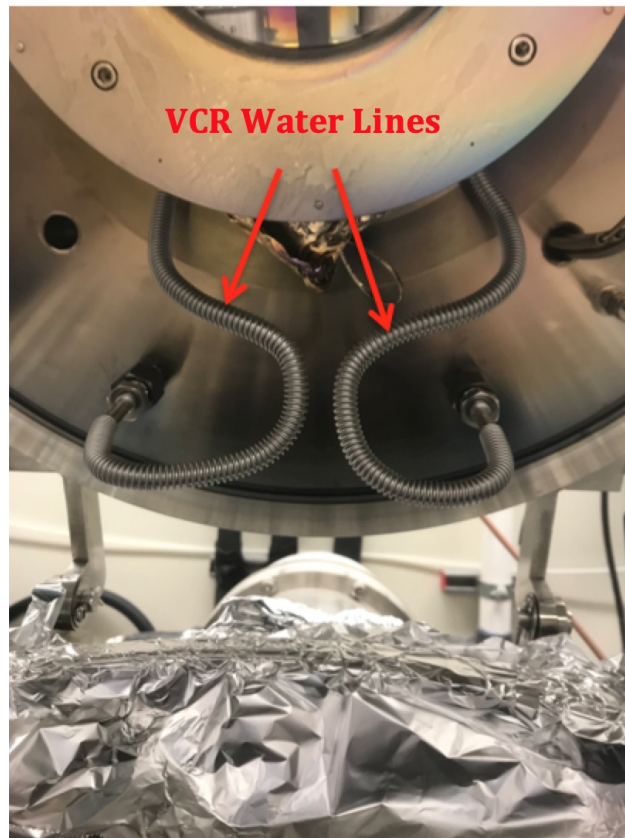


Figure A.31: Internal VCR lines that supply water to the stage

- Shutdown and vent the main chamber, then turn off the heat exchanger
- Close the black throttle knob on the pneumatics panel that goes to the stage
- Disconnect the two black water lines connected to the top of the lid– be prepared with paper towels as these will still have a bit of water in them (Fig. A.40)

Water lines disconnected

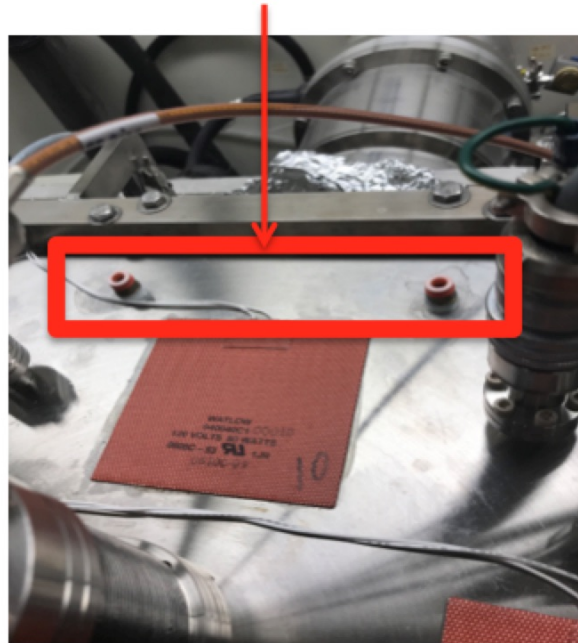


Figure A.32: Empty connections on main chamber lid where water lines to the stage are normally connected

- Connect the removed water lines end to end using a fluid tube connector to form a closed loop
- Place the loop in a bucket for precaution (bucket unpictured in Fig. A.41)

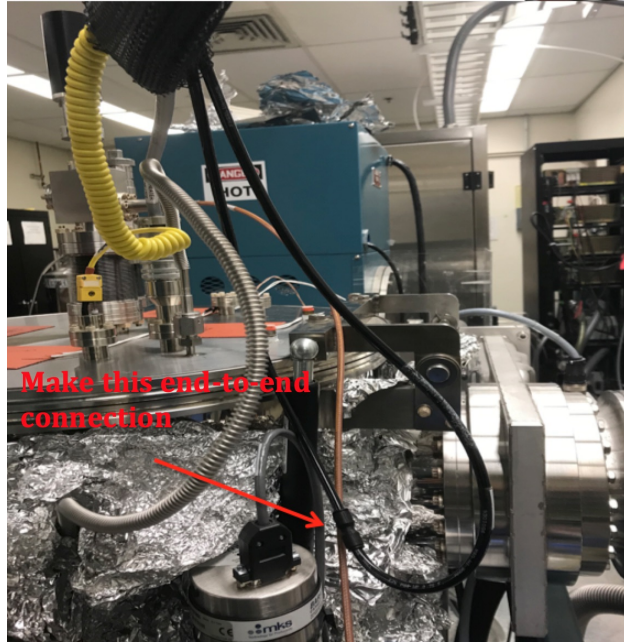


Figure A.33: Connect the water lines together to form a closed loop so that no water is going to the stage

- The inner VCR water lines need to be dried before they are removed—flow nitrogen gas through one of the tubing ports on the chamber lid (Fig. A.40) and out the other one (allow use of an entire nitrogen tank during drying)
- Once dried, open the chamber lid and cover the entire top with aluminum foil
- There are four total VCR connections to disconnect (Fig. A.34)



Figure A.34: Left: Disconnect nut B and the identical one on the opposite side (unpictured). Right: Disconnect these VCR connections at the points shown

- Follow Swagelok VCR protocols for how to properly break VCR connections –Note: The connection in Fig. A.34 (left) should be broken by holding A fixed and rotating B—for reference, Fig. A.49 shows this being done on the reflector box after it has already been removed
- The new water lines should be Swagelok (321-4-X-8FMR) 8” water lines, which must be custom ordered from them. Swagelok sells these lines online only
 - •n 4”, 6”, and 12”. In the past we have used 321-4-X-6FMR but these are not ideal since they require too much bending. Also, purchasing directly from Swagelok instead of AJA will be half the price.
- Replace the removed lines with the new 8” water lines (Swagelok 321-4-X-8FMR) again following VCR protocols—remember to use gaskets (SS-4-VCR-2), see Fig. A.36



Figure A.35: Example of how to disconnect connections pictured in Fig. A.34—hold nut A fixed with one wrench and rotate nut B with a second

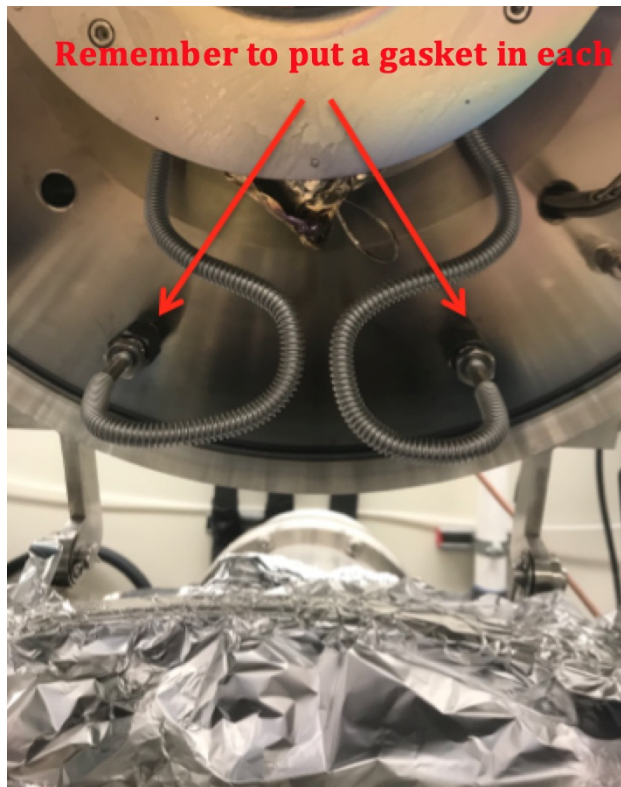


Figure A.36: Install new 8" VCR lines, remembering to use gaskets in the connections with arrows

- Prepare to leak check- first ensure the chamber lid is well covered with aluminum foil and possibly lay down a bit of paper towel to absorb any water droplets that might form (Fig. A.37)



Figure A.37: Ensure the chamber opening is covered and protected before checking for water leaks

- Remove the end-to-end connection (Fig. A.41) and reinsert into chamber lid while it is opened vertically (Fig. A.38)



Figure A.38: Keep the chamber lid vertical and re-insert the water lines back in as normal

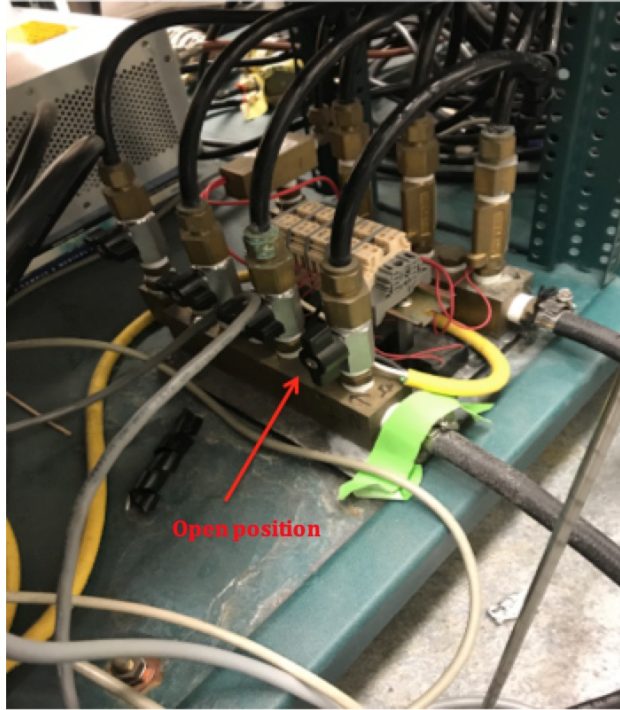


Figure A.39: All throttle knobs are closed except for knob to stage

- Now close all throttling knobs except the one to the stage Fig. A.39
- To prevent condensation from forming since the chamber is at atmospheric pressure, lower the chiller water temperature from 16°C to $\sim 22^{\circ}\text{C}$ on the heat exchanger
- Run the exchanger and look for leaking
- Allow the exchanger to run with the chamber lid still vertical for ~ 20 min.
- If no signs of leaks after this time, remove foil from chamber opening and close the lid
- Run the exchanger for an hour in this position and monitor periodically for leaking
- If no leaking, the installation was successful
- Set the heat exchanger temperature back to 16°C and open all throttle knobs
- Pump the system back down as normal

A.7.7 Removing Reflector Box/Stage Assembly

- Vent the main chamber and shut down the entire system
- Turn off the heat exchanger
- Disconnect the black water lines where they enter the main chamber lid (Fig. A.40)

Water lines disconnected

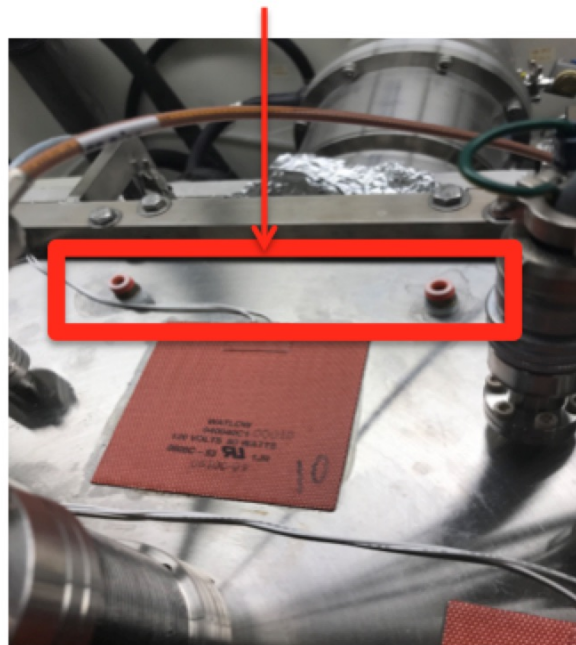


Figure A.40: Empty connections on main chamber lid where water lines to the stage are normally connected

- Connect the removed water lines end to end using a fluid tube connector to form a closed loop
- Place the loop in a bucket for precaution (bucket unpictured in Fig. A.41)

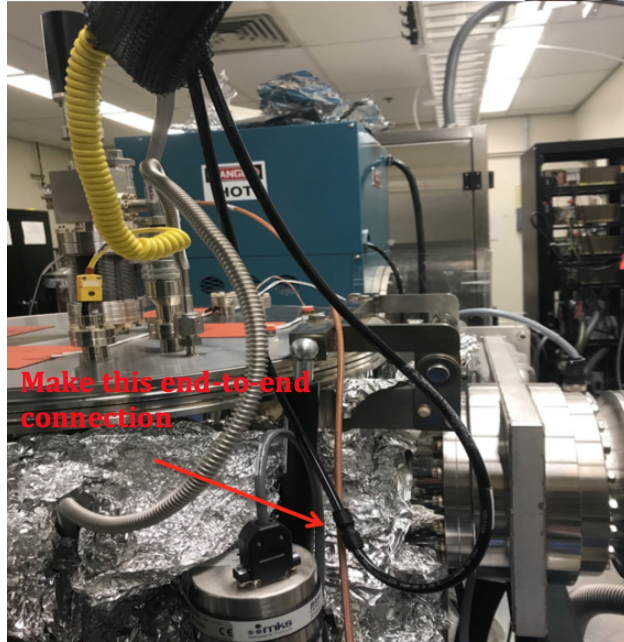


Figure A.41: Connect the water lines together to form a closed loop so that no water is going to the stage

- Connect nitrogen to one of the water line openings on the chamber lid and blow excess water out the other (the line needs to be completely dry so allow use of an entire nitrogen tank)
- Once dried, open the chamber lid and cover the entire top with aluminum foil
- Disconnect the gas line fitting and cover the open connections with aluminum foil (Fig. A.42)

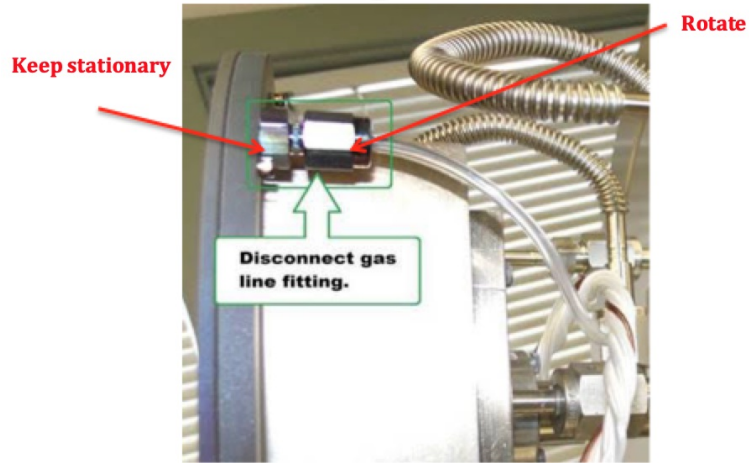


Figure A.42: Gas line to stage

- Disconnect both VCR water lines only at the connections pictured in Fig. A.43 then cover the exposed openings with aluminum foil- remember female nut rotates, male nut is steady

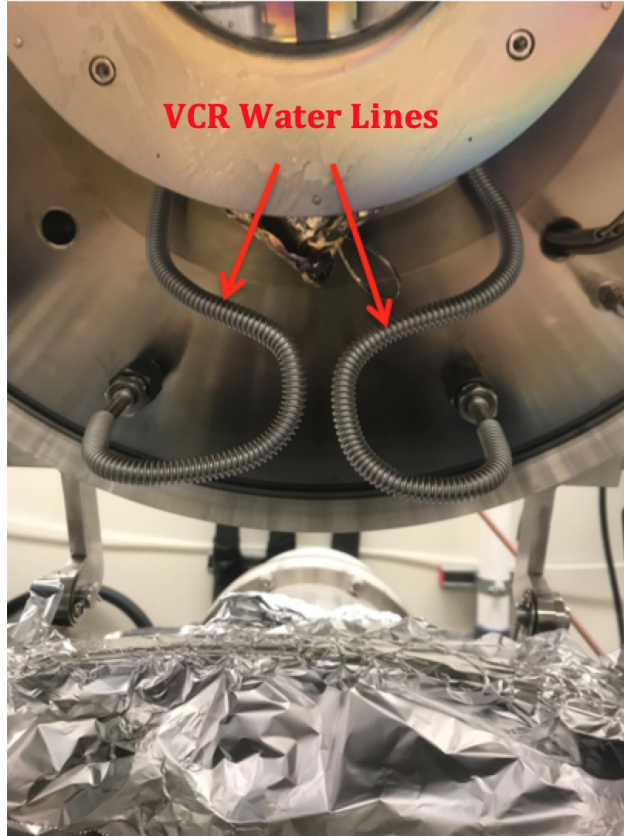


Figure A.43: Internal VCR lines that supply water to the stage— disconnect only the lower two connections pictured

- Next remove the stage propeller (Fig. A.44)

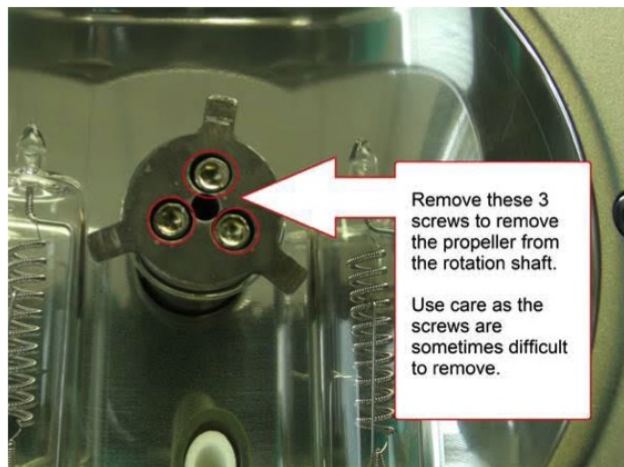


Figure A.44: Stage propellers that hold sample holder

- Unplug the lamp and thermocouple connectors (Fig. A.45—these are to be slid out

manually with some minor force (rocking back and forth slightly helps to loosen these)—and cover with aluminum foil

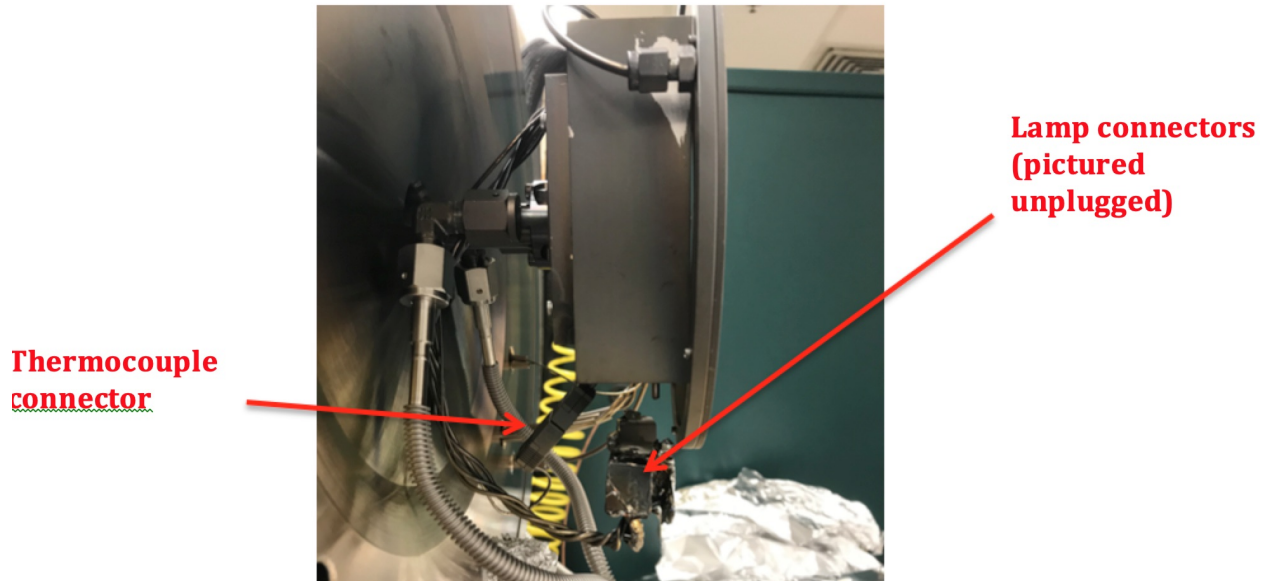


Figure A.45: Thermocouple and lamp connections to the stage are shown

- Next remove the circular support clamp pictured in Fig. A.46 – first remove the side screw then remove the two top screws

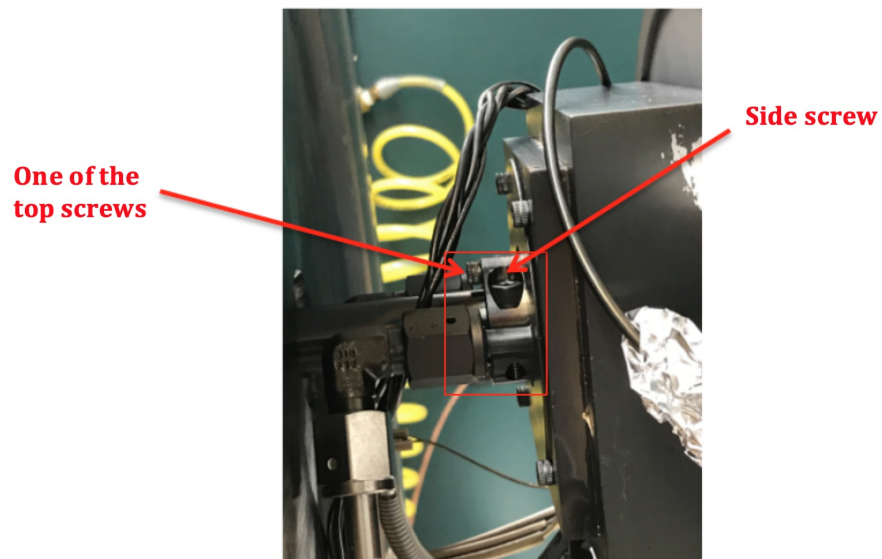


Figure A.46: Top screw and side screws into the support clamp keep the reflector box in place

- The reflector box should be loose now—slide the entire thing forwards to remove from pole piece
- Remaining on the pole piece should be the clamp in Fig. A.47 which also needs to be slid off



Figure A.47: Remaining support clamp after the reflector box has been removed from the pole piece

- If stuck, stick a flat head screwdriver in the slit opening (Fig. A.47) and gently wiggle the clamp until it can be removed—when removed, the chamber should look the same as Fig. A.48

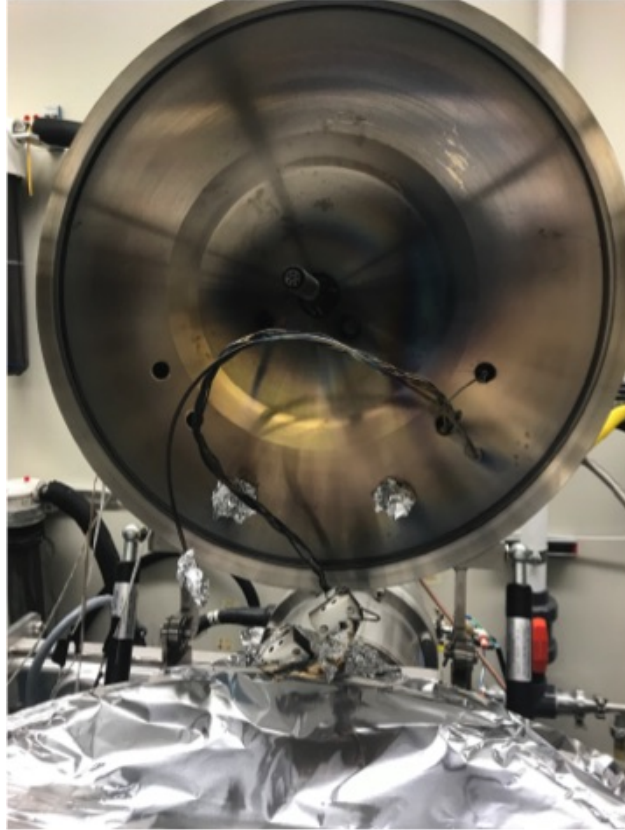


Figure A.48: Chamber lid after reflector box has been successfully removed

- Cover the pole piece with aluminum foil
- Take the reflector box to a workbench and lay it on a sheet of aluminum foil
- Remove the water lines from the elbow tees—hold one wrench vertically on the elbow tee (stationary) and rotate the female nut counter clockwise using a second wrench (Fig. A.49)



Figure A.49: Hold elbow tee fixed with one wrench and rotate the female nut with another

- Cover the elbow tees individually with aluminum foil then wrap the entire reflector box in foil
- Make sure there are no exposed connections inside the sputtering system
- Remove the large sheets of aluminum foil then close lid

Note: If the clamp is difficult to slide back onto the pole piece during reassembly, lightly sand the inner diameter of the ring with a Brillo pad then clean in acetone and IPA

A.7.8 Testing Flow Switches

Flow switches act as sensors for whether there is water flowing through the cooling lines. When water is flowing normally, all switches should read continuous (one should measure this with the system and heat exchanger both on— resistances should be around 0.3 Ohms). If for some reason there is insufficient water flow, the switch will become discontinuous. When the switch is discontinuous for more than 12 seconds, the sputtering system automatically shuts down to protect itself.

Unfortunately, these flow switches can become stuck in the wrong position due to algae buildup or poor water quality. This means that if there is insufficient water flow the system will not be able to tell and will not shut down when it should. This is extremely problematic—overheating can melt circuitry and damage magnets. Therefore these flow switches must be tested regularly.

Here are instructions for how to perform the flow switch test on our system, followed by the general instructions provided by AJA.

Our system:

1. The system should be shutdown and the heat exchanger turned off
2. Notice the terminal block is sectioned into smaller areas labeled 1-1, 2-2, 3-3, etc.
(Fig. A.50)

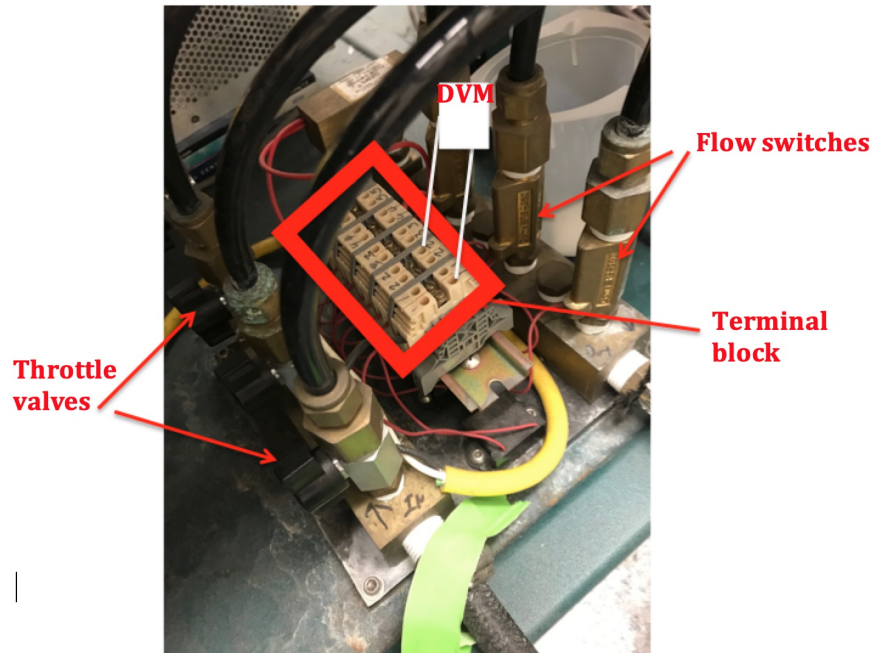


Figure A.50: Pneumatics panel with terminal block pictured. Example of how the digital voltmeter (DVM) should be inserted is shown.

3. Measure the resistance across each flow switch using a multimeter—

- To measure across the first flow switch, insert one prong in a “1” hole and the other in the neighboring “2” hole as pictured above
- Make sure you are placing contact on the metallic screw head
- If all is normal, the reading should be open (“OL” on multimeter or several Megaohms reading)
- If the reading is continuous (a several ohms or kilohms), the sensor is stuck and needs to be fixed immediately
- Measure across the other flow switches in a similar fashion—i.e., putting prongs in 2-3 then reading resistance, then 3-4 and reading resistance

Note: it does not matter which of the two holes in the smaller blocks you choose to put a prong in

AJA Instructions:

Water Flow Switch Testing and Cooling Loop Balancing Procedure

With contaminated cooling water (or over long periods of time) it is possible for flow switches to stick open or closed preventing normal system operation and possibly damaging system components. The purpose of this test is to ensure that each water flow switch is functioning properly.

For Systems with a PD30A box and no EMOC.

Note: Water flow switches are wired in series so that if any one shows discontinuity, your interlock light will not activate and the system power supplies and heater cannot be operated.

For Systems with an EMOC360 or EMOC380.

Note: Water flow switches are wired in series so that if any one shows discontinuity for more than 12 seconds, the main electrical power to your system will shut off and the Blue water alarm light will be on indicating a water alarm. The main electrical power cannot be turned on until the water flow condition has been corrected and the water alarm reset push button is pressed.

1. With a DVM (continuity setting) check all flow switches for continuity. See typical diagram below (systems vary depending on complexity but design concept is identical). You should read "open line" across all flow switches. If one or more flow switches reads positive continuity, it is stuck and you should contact AJA International for further instructions. If all switches read "open line" continue to point 2. Below.

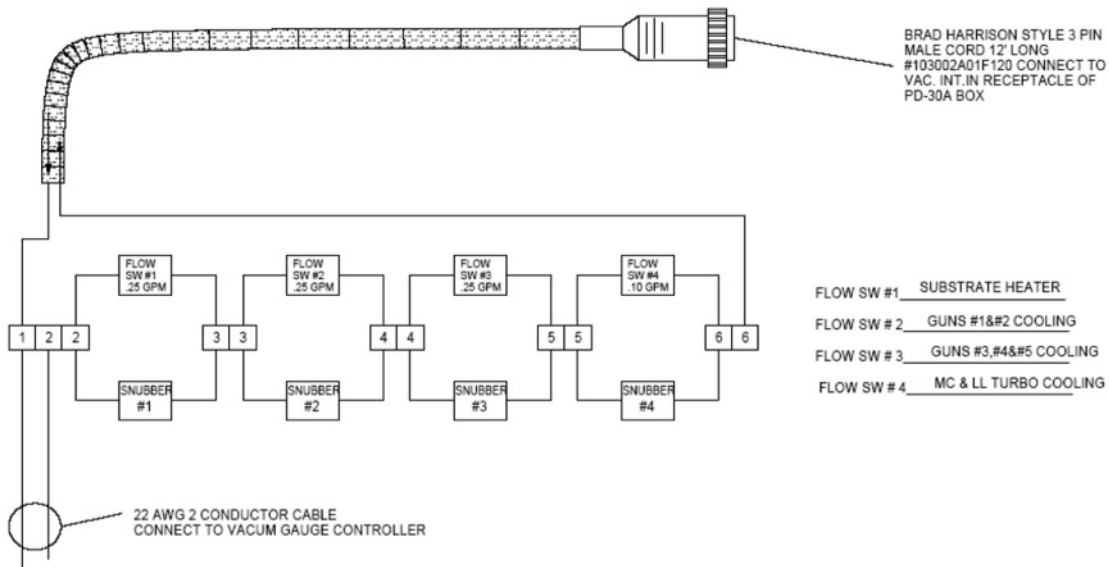
2. Turn on main water supply valve to the system and observe the interlock light on your power distribution system. If your interlock light activates, all switches have closed and your testing has shown all flow switches to be fully functional. Continue to point 4. below.

3. First check for continuity across all flow switches with a DVM. Determine the switch that is preventing completion of the serial interlock circuit. Now close the small throttle valves of the OTHER water loops whose switches show continuity. By doing this you are diverting all the water into the flow sensor that is showing discontinuity. With the DVM measure again to see if this switch now shows continuity. If so, proceed to point 4. below.

If you still show a discontinuity reading when all water is diverted through a particular sensor it is either stuck or there is an obstruction in that particular cooling loop. First, shut off main water valve to system, disconnect the "water out" line at back of system and run this into a bucket so you can measure the flow of coolant leaving the system (X liters/min). Then start the water again and be sure you have sufficient water flowing out of the system through this cooling loop. If the flow is sufficient, you do not have an obstruction in the line, the sensor must simply be stuck. In either case you should contact AJA International for further instructions.

4. Once you have shown all flow switches to be functioning properly, it is necessary to balance the flow in the various cooling loops. First fully open the small throttle valve at the beginning of each cooling loop. Cooling water will take the path of least resistance so the loops with the most conductance (sources, heaters) need to be slightly throttled down to be sure the loops with poor conductance (turbo pump, QCM) have sufficient flow. Therefore, with a DVM reading the continuity of the switch that is not closed, slowly throttle down the other valves to divert more coolant into this loop until it activates. Now throttle down a little more to be sure this sensor is not activating so marginally that it will shut down the interlock circuit with every slight drop in water pressure. Now all flow sensors should be operating properly, your interlock circuit should be completed, the light should be on and you are able to operate the system normally.

NOTE: In balancing the flow and throttling down cooling loops, consider which loops NEED the most cooling and tend to throttle down the other loops first. Consider the maximum, total number of Watts that can go to a particular loop. For heaters, assume 50% of the heat goes into the substrate and chamber and 50% is lost to the cooled reflector box assembly - therefore for a 2000W heater, 1000W needs to be dissipated by the cooling loop. For sputter sources, assume 85% of the power input is transferred into heat and need to be dissipated by the cooling loop - thus for two sputter sources running simultaneously at 500W each (1000W total), assume that 850W need to be dissipated by the cooling loop. In this example, the sputter gun cooling loop can be throttled a little more than the heater cooling loop.



- Another check of whether flow sensors are working is through the water reset light, which should only illuminate when there is insufficient water flow
- With the system safely shutdown and the heat exchanger off, the water reset light should illuminate

- If you press the reset light with the heat exchanger still off, the reset light should remain on—if it turns off something is wrong with the sensors

The specific, piston-type flow switches on our system from Gems Sensors:

FLOW SWITCHES

FS-380 Series

Compact Flow Switch for High Inline Pressure

Part No. 168432
Unit Price \$149.00
Lead Time (Business Days) In Stock




Image is of actual product.

[Add to Cart](#) [OEM Part Modification](#) [Back to Selector](#)

Model	FS-380
Primary Material of Construction	Alloy
Sensor Type	Piston Type
Adjustable Range	N/A
Flow Setting (GPM)	0.25
Body Material	Brass
Port Size	3/8" NPT Male
Switch Type	SPST, N.O. (20VA)
Set Point Accuracy	±20%
Maximum Pressure (PSI)	Over 500
Minimum Temperature (°F)	-20
Maximum Temperature	275
Electrical Termination	22 AWG, 24"-26" long Polymeric Leads
Set Point Differential	20%
Wetted Materials	Brass, PPS Composite, Epoxy, 316 Stainless Steel, Fluorocarbon
Approvals	UL Recognized, CE
Recommended Filtration	100 micron
Minimum Qty (per Release)	1

FLOW SWITCHES

FS-380 Series

Compact Flow Switch for High Inline Pressure

Part No. 181130
Unit Price \$135.00
Lead Time (Business Days) In Stock



Image is of actual product.

[Add to Cart](#) [OEM Part Modification](#) [Back to Selector](#)

Model	FS-380
Primary Material of Construction	Alloy
Sensor Type	Piston Type
Adjustable Range	N/A
Flow Setting (GPM)	0.15
Body Material	Brass
Port Size	3/8" NPT Male
Switch Type	SPST, N.O. (20VA)
Set Point Accuracy	±20%
Maximum Pressure (PSI)	Over 500
Minimum Temperature (°F)	-20
Maximum Temperature	275
Electrical Termination	22 AWG, 24"-26" long Polymeric Leads
Set Point Differential	20%
Wetted Materials	Brass, PPS Composite, Epoxy, 316 Stainless Steel, Fluorocarbon
Approvals	UL Recognized, CE
Recommended Filtration	100 micron
Alternate Stock Item	View Alternate Stock Items
Minimum Qty (per Release)	1

Figure A.51: Top switch (part no. 168432) is used for guns and heaters while bottom switch (part no. 181130) is used for turbo pump. Both are piston-type switches.

A.7.9 Replacing Flow Switches

- Shut down the system
- Turn off the heat exchanger
- Choose which switch to replace first
- Drain this line following the steps below:
 1. Close the black throttle knob to this line
 2. Go to the visual flow indicator corresponding to this line and disconnect it from the black tubing labeled “From Flow Switch”
 3. Use an SMC connector to connect the “From Flow Switch” tube to a longer piece of tubing that drains into a bucket placed away from the system
 4. Put a bucket beneath the visual flow indicator as well for precaution
 5. Open the black throttle knob to this line
 6. Water should begin draining into the bucket—wait until it stops flowing
 7. Close the black throttle knob to this line
- Now disconnect the black tubing entering the top of the flow switch (use a wrench to turn the red arrow in Fig. A.52 counterclockwise)

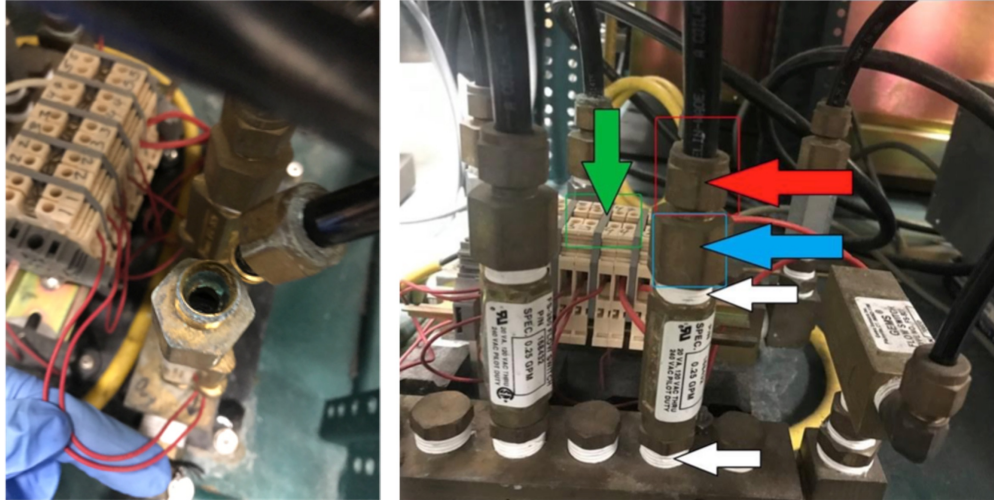


Figure A.52: Left: Removal of tubing going into flow switch. Right: For reference.

- Disconnect the adapter (blue arrow in Fig. A.52) from the flow switch body—again counter clockwise turns of the wrench
- Make note of the red electrical wiring from the flow switch to the terminal block (Fig. A.53 and Fig. A.54)

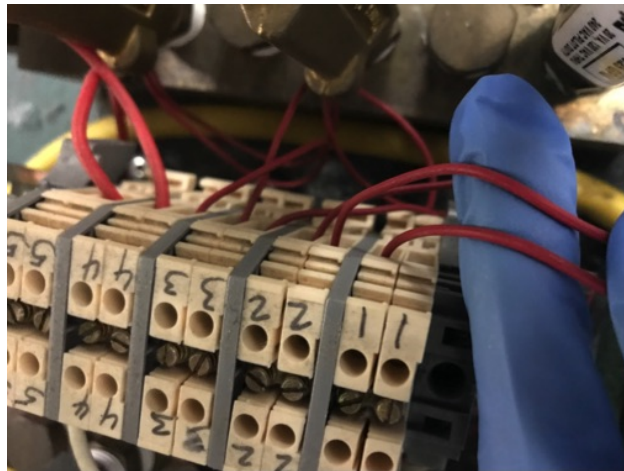


Figure A.53: Red wires connect from the flow switch body into the terminal block pictured.

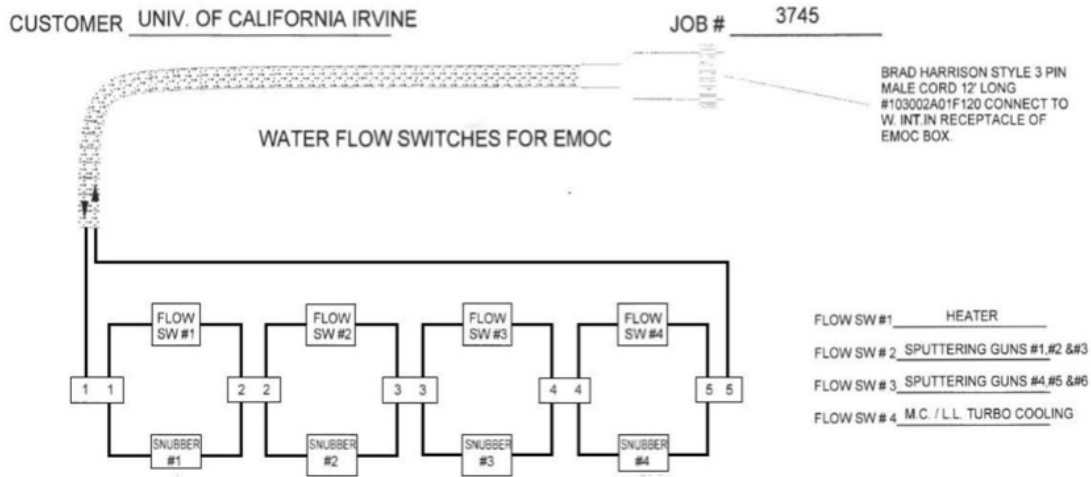


Figure A.54: Terminal block wiring schematic for flow switches on our system

- Using a small screw driver, disconnect the flow switch wires from the terminal block—if stuck, use a cotton swab and some WD-40 around the screw
- Remove the flow switch with a wrench—again counterclockwise turns→ Since there is little clearance, it may be the case that the body of the flow switch comes off while its lower nut (just above lower white arrow in Fig. A.52) stays put→ If so you can remove this nut using a ratchet
- Remove any existing Teflon tape on the opening and from the adapter that was mounted on the flow switch (white arrows Fig. A.52)
- Wrap both ends of the new flow switch with Teflon tape (wrap it using counter clockwise turns)— you do not use Teflon tape on the tubing fitting you disconnected at the red arrow
- Install the adapter onto the top of the flow switch
- Trim and strip the red wire ends so that they will fit nicely into the pneumatics panel
- Install the flow switch

- Connect the wires from the flow switch to the terminal block as disconnected in step above
- Connect the tubing to the adapter on the flow switch
- Once all of the water connections have been made, re-fill the heat exchanger with water
- Turn on the heat exchanger and check for leaks

A.7.10 Load-lock Tubomolecular Pump Removal

- Break the KF connection from the backing pump to the turbomolecular pump by removing the KF clamping ring via thumb screw
- Cover the exposed flanges with aluminum foil
- Remove the ISO flange between the turbomolecular pump and load-lock by unscrewing the four bracket screws, which then drops out the centering ring and O-ring
- Cover the opening of the load-lock with aluminum foil
- Disconnect the line between the pump from the nitrogen vent gas and plug it as shown in Fig. A.55 (this prevents the nitrogen tank from depleting which keeps the main chamber's turbomolecular pump protected in case of a shut down)

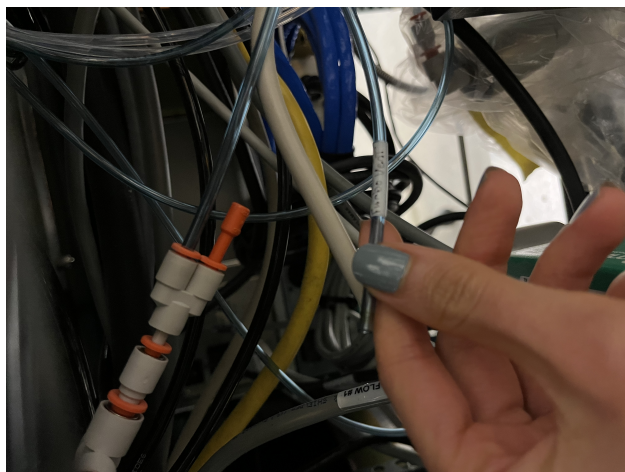


Figure A.55: Nitrogen gas is supplied to both turbomolecular pumps on the system. During load-lock removal, the load-lock nitrogen line in blue should be disconnected and the opening should be plugged as shown in orange.

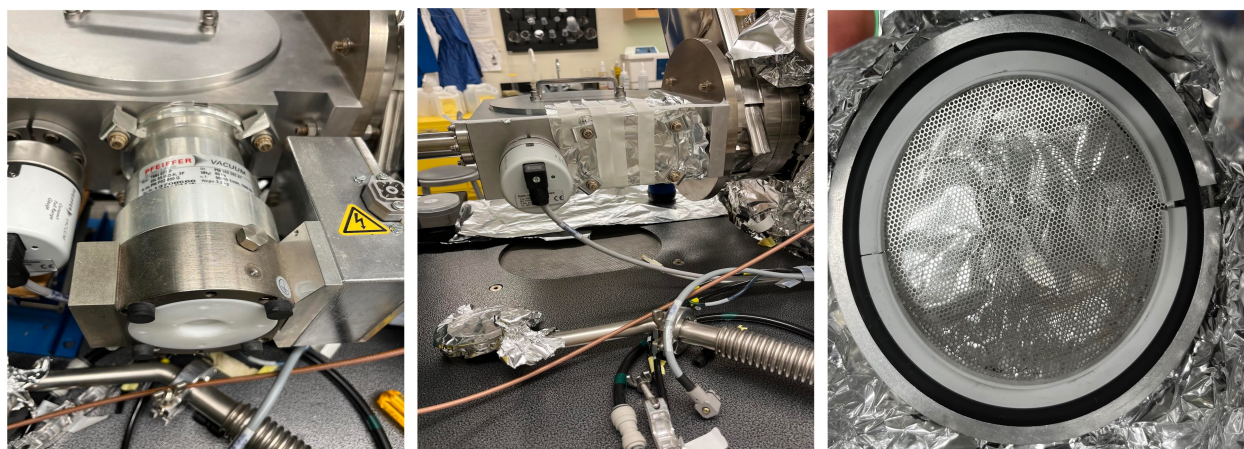


Figure A.56: Left: Load-lock turbomolecular pump still connected (Pfeiffer model: TMH 071 P); Center: after removing pump, cover the exposed opening with foil (the four bracket screws arranged in a square are also visible); Right: centering ring and O-ring

A.8 Troubleshooting

Here are common issues associated with different aspects of the sputtering system and their possible resolutions.

A.8.1 Heat Related

- **Temperature reading in the main chamber is higher than the normal ~16-17°C**

Note: You should preventatively shut down the system if temperature reaches 20°C and the heat exchanger temperature control has not been changed from 16°C

Possible causes:

- Cooling water temperature (i.e. temperature set on the front of the heat exchanger) has been changed to something higher than 16°C
- Blockage in a cooling line (algae buildup—need to flush lines) or poor water quality (need filter change on heat exchanger)
- Flow sensor is stuck in wrong position—if there is insufficient water flow to one of the cooling lines, it may be going undetected and causing excessive heat
- Temperature of facility cooling water has significantly changed – possible but unlikely
- Heat exchanger pump is not working

- **Red light on heat exchanger is illuminated**

Possible causes:

- The cooling water is too hot
- The water in the exchanger reservoir is too low
- To test:

- Shut down without venting main chamber
- Top off water level of exchanger

- Run exchanger (without turning the system back on yet) and see if light returns
- If yes, this indicates a temperature control issue

- **Temperature controller cannot reach set value**

Possible causes:

- Insufficient ramp time– temperature processes can fail if the ramp time is too fast (100°C/10 min ramp time is ideal but 100°C/5 min is usually okay)
- One of the halogen lightbulbs beneath the stage holder is blown out → Open system and replace

A.8.2 Pressure Related

- **Ion gauge reading is abnormally high**

- Use the RGA and see what gas pressures are elevated– high H₂O may indicate a leak in a cooling line (commonly happens to the stage cooling line which is a bit bent), high N₂ or O₂ may indicate an air leak somewhere (main chamber lid may not be tightened sufficiently)
- If base pressure is still within the E-8 Torr range, try sputtering a getter material to lower the pressure—~20-40 nm of Ta and Al are good choices
- If the base pressure creeps up again, there is a source of contamination

- **Ion gauge reading is fluctuating**

Possible causes:

- Fluctuating base pressure usually indicates a periodic leak or outgassing of some contaminant – use the RGA to check which gas levels are elevated

- If the chamber was recently opened or had been opened for an extended period of time, it may be that the system has not been completely baked out
- Try an extra internal bake then check pressure
- Try sputtering a getter material to lower the base pressure—Ta and Al are good choices—and see if the base pressure continues to fluctuate
- If these fail, the chamber should be opened and inspected for source of contamination (possible hair or oil from backing pump or even blown lightbulbs) and then thoroughly cleaned

- **Base pressure is increasing/decreasing with stage height**

Possible causes:

- Most likely leak in the water line to the stage—run the RGA while moving the stage height and see if water spikes

- **Gate valve to the turbo pump cannot reach setpoint**

Possible cause:

- The capacitance manometer is not properly zeroed (it should typically read about -0.5 in the AJA software) → There is a small zero adjust screw hole on the face of the capacitance manometer → Take a screwdriver and slowly adjust until the CAP MAN reading is back to -0.5

- **Appearance of metallic (probably indium) droplets**

- These indicate a serious overheating issue that must be resolved before continuing use of the system
- Typically from the melting of some indium bonding

- Indium can originate from the cooling block which is bonded with indium to the reflector box on the stage

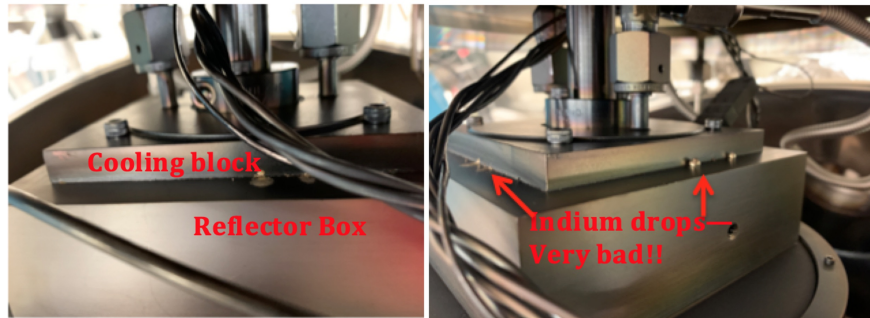
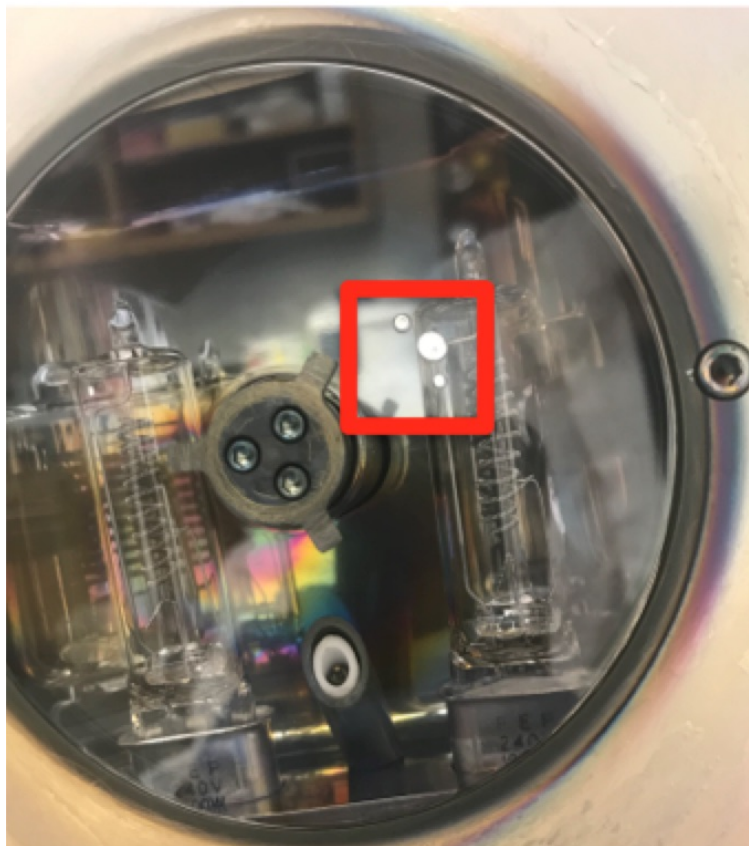


Figure A.57: Reflector box with melted indium droplets.

- Indium can land as far down as the quartz glass stage



- First verify drops are indeed indium—remove drops from stage glass (unscrew the assembly on the face of the stage) or wherever they are found, melt down drops on hotplate to find melting temperature (indium melting temp. = 156°C)

- Quartz glass must be perfectly clear, otherwise can reflect back heat to the lamps and cause overheating

A.8.3 Magnetron Source Related

- **Measuring Resistance of Guns**

- **Method 1 (system can remain on—no venting or shutdown required):**

- Unscrew the coax cable connected to the gun in question on the underside of the system
- Using a multimeter, measure the resistance of the gun by placing one prong directly into the center pin of the gun itself and the other on the outer shield of the connector (Fig. A.58)
- To minimize error from physically moving the prongs, there is also a small coax connector which can be directly screwed to the gun and then fed to the multimeter via a BNC cable—unfortunately it the connector only fits the DC guns though
- In either measuring method, you should read an open circuit

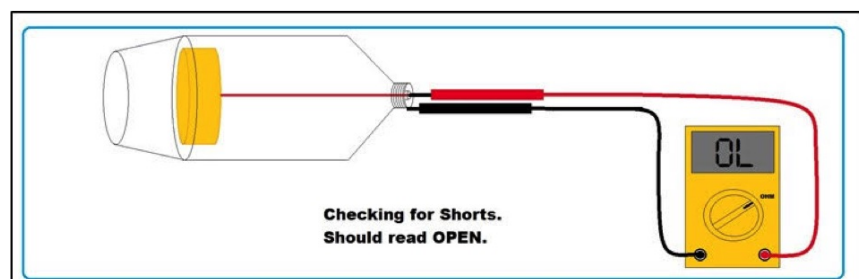


Figure A.58

- **Method 2 (system must be off and vented):**

- Vent and shutdown
- Unscrew the coax cable connected to the gun in question on the underside of the system

- Remove the chimney and target from the gun in question until the cathode surface is exposed
- Measure the resistance of the gun using a multimeter by placing one prong directly into the center pin of the gun itself and the other on the cathode surface (Fig. A.59)
- You should read shorted, or very low resistance (~ 2 ohms or less)

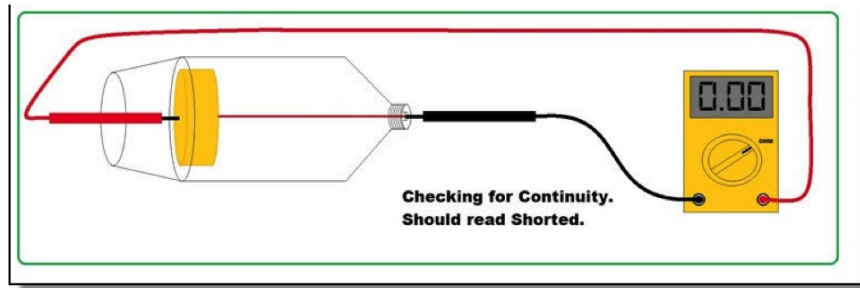


Figure A.59

A.8.4 Load-lock Related

- **Load-lock pump down exceeds 1 hr**

Possible causes:

- Load-lock chamber is dirty (needs vacuum, check for stage flaking, clean lid and O-ring with IPA)
- Inspect load-lock O-ring for lint
- Contamination on the pressure gauge

- **Increase in turbo pump power or current consumption**

Possible causes:

- Increased friction from worn bearings

- Oil reservoir lubricant needs to be replaced
- Check backing pump functionality
- Normal pump parameters are:

DCU Parameter no.	Parameter	Setting
310	TMP I-mot	variable
313	TMP DClink	22.7 V
314	Drv Op hrs	43653 h
312	Drv Softw.	17500
315	TMP finspd	1500 Hz
316	TMP power	variable
319	Cycl count	5365
331	TMS ActTmp	0C
333	TMS steady	no
351	Ctr Softw.	20300
700	TMP RUTime	15min
701	Switch pnt	80%
704	TMSheatset	40C
707	TMProt set	50%
708	DrvPwr set	80%
710	BkP Poff	0 W
717	Stbyrotset	66%
719	Switchpnt2	20%
720	Vent freq	97%
721	Vent time	3600 s
777	PumpRot Max	1500 Hz
794	Param. set	1
795	ServiceLin	340
1	Heating	off
2	Standby	off
4	RUTime ctr	on
10	Pump stat.	on
12	Vent enab	on
13	Brake enab	off
23	Motor TMP	on
24	Conf. Out1	0
25	OpMode BkP	0
26	OpMode TMP	0
30	Vent mode	0
308	Set rotspd	1500 Hz

Turbo current at startup (A)	3.8
Turbo current at steady-state (A)	0.23
Turbo power at startup (W)	78-82
Turbo power at steady-state (W)	5
Turbo voltage (V)	22.7
Load-lock ultimate pressure (Torr)	2.40E-07

Figure A.60

Appendix B



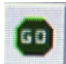
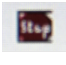
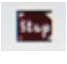

Residual Gas Analyzer (RGA)

The purpose of an RGA is to measure what gases are present inside the main chamber of the sputtering system and in what amounts. It is especially useful when using process gases or if the main chamber pressure is unusually high (often indicative of a leak). Because the RGA is very sensitive to high pressures, it can be instantly destroyed if the sputtering system is used while it is on. By following the SOP below this should never occur.

- Locate the blue plastic folder labeled “RGA SOP” on the side panel of the sputtering system
- Take out the two laminated ”RGA In Use” signs. Place the one with string over the sputtering system glass window and the other on top of the load-lock.
- Look at the ion gauge and verify that the main chamber pressure is better than 9.6E-6 Torr
- Open RGA 3.0 Program on the AJA laptop under the Start menu
- Turn on the RGA (at the back of the sputtering system) by pushing the black power button into the ”1” position. The green power light should come on.



Figure B.1: Proper signage when RGA is in use.

- In the toolbar of RGA 3.0, click the green connect icon 
- Double-click COM3 and verify that its status changes from disconnected to connected
- Click  on the toolbar to begin heating the filament. Let the filament heat for 5-10 minutes. If the main chamber has been opened recently it is best to heat for longer, around 15-20 minutes.
- Select **Mode** on the toolbar and choose P vs T to run a pressure versus time scan. On the toolbar under Scan, select Add Scan Parameters and enter in the gases to scan for (common ones include nitrogen, hydrogen, oxygen, water, carbon dioxide, and helium)
- To start scanning, click  on the toolbar
- To stop scanning, click  at any time
- To save a scan, hit . Go to "Save As" under "File" and save your work in the "RGA data" folder on the Desktop
- Click  on the toolbar to turn off the filament

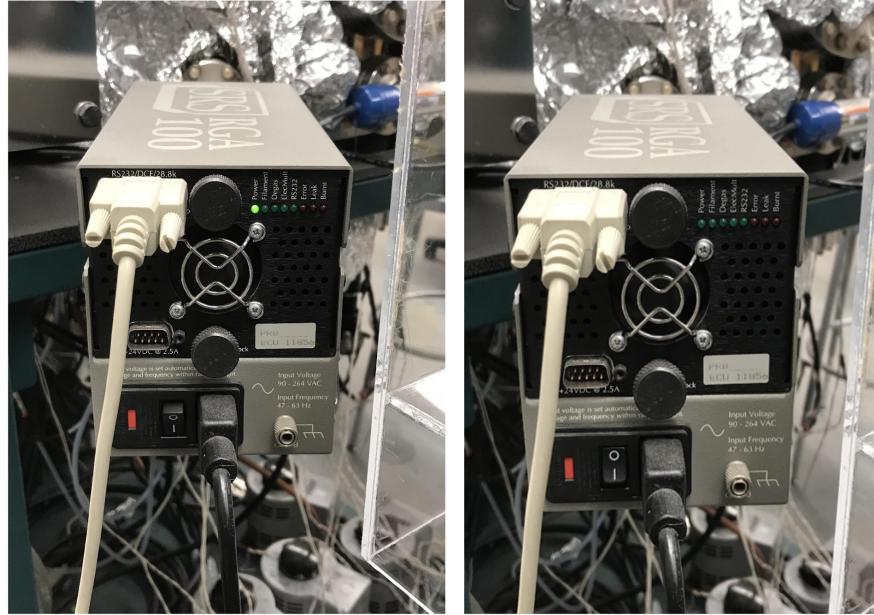



Figure B.2: Power light illuminated.

- Click on the grey  connect button. Double-click COM3 and verify status changes to disconnected.
- Switch the black power button on the back of the RGA to the "0" position and verify the green power light goes off.
- Remove all signs from the sputtering system and place them back in the folder containing this SOP
- Double-check that everything has been shut off properly

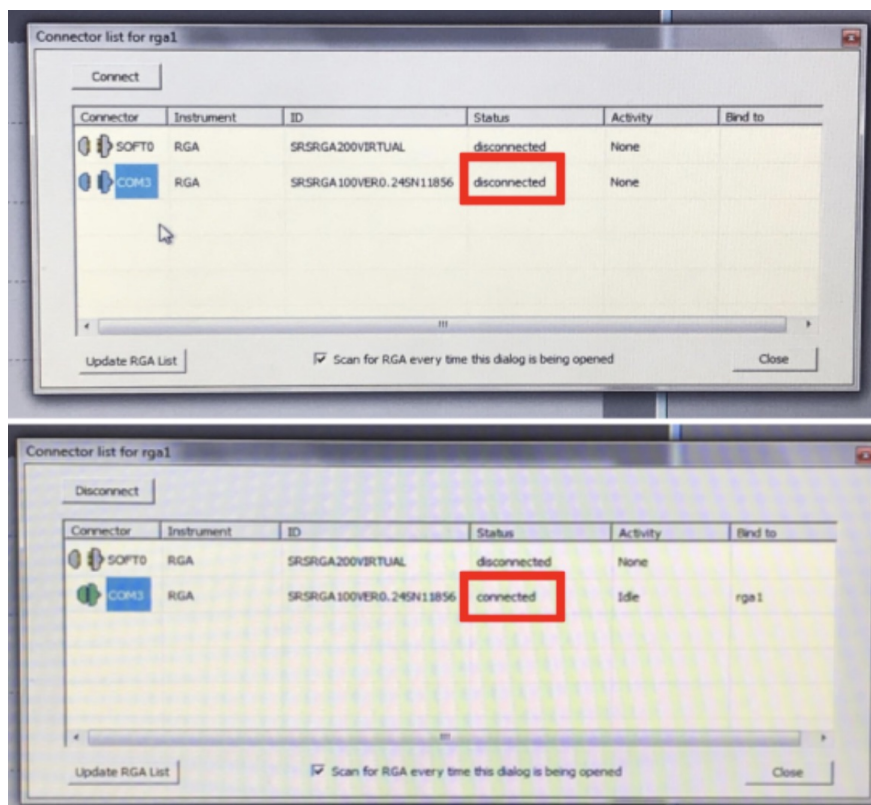


Figure B.3: RGA connection status.

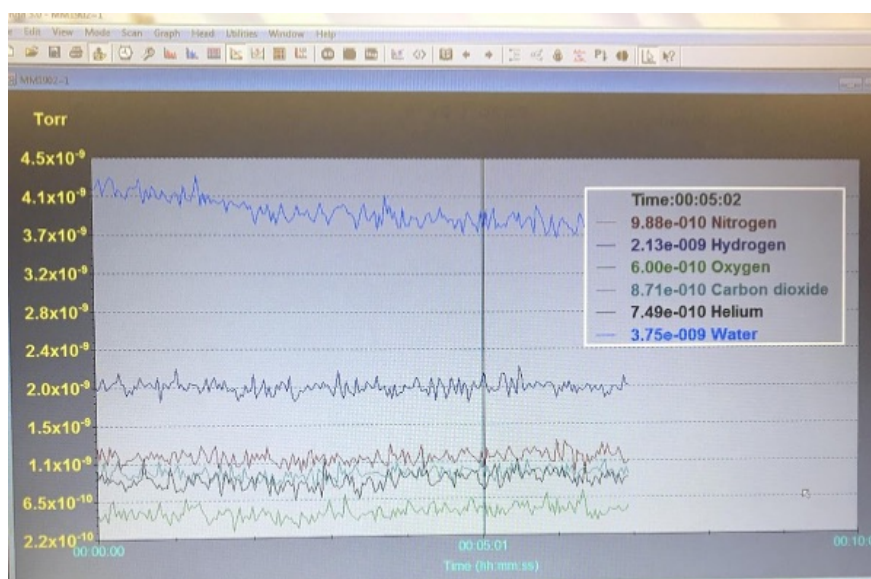


Figure B.4: Pressure vs time plot.

Appendix C

Co-sputtering Mathematica Notebook

The following notebook was used to calculate the sputter deposition rate when making a co-deposition (i.e, sputtering from two targets simultaneously). For each target, the thicknesses of three films grown at three different target powers must be inputted. Targets of Pt and PtMn are used in the code as an example.

Lattice parameters

Input Pt and PtMn lattice constants based on XRD or ICSD data.

```
aPt = Quantity[0.3923, "nm"]; (*lattice constant face-centered cubic (FCC) Pt: aPt=bPt=cPt*)
aPtMn = Quantity[0.385, "nm"]; (*in-plane lattice constant face-centered tetragonal (FCT) PtMn: aPtMn=bPtMn*)
cPtMn = Quantity[0.377, "nm"]; (*out-of-plane lattice constant FCT PtMn: cPtMn*)
```

Calculate unit cell volumes and atom densities.

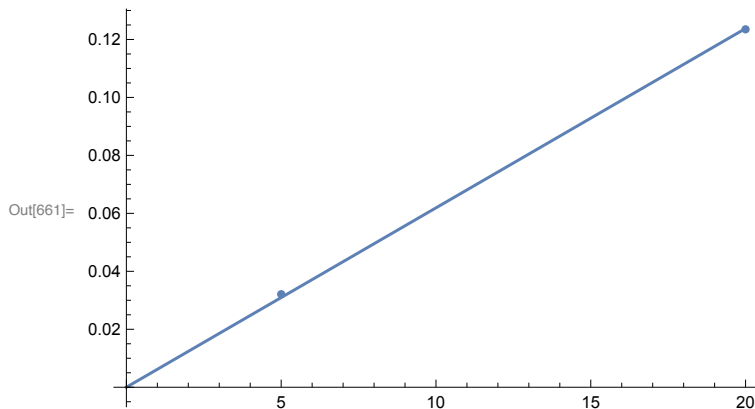
```
VPt = aPt3; (*Pt unit cell volume*)
VPtMn = aPtMn2 * cPtMn; (*PtMn unit cell volume*)
Ptden = Quantity[4, "atoms"] / VPt; (*FCC lattice has 4 atoms per unit cell*)
PtMnden = Quantity[4, "atoms"] / VPtMn; (*FCT lattice has 4 atoms per unit cell*)
```

Thickness rate as function of power for Pt and PtMn (XRR calibration)

Growth rates as function of power with linear fits for Pt and PtMn targets. You can decide if you should force {0,0} and only fit for slope.

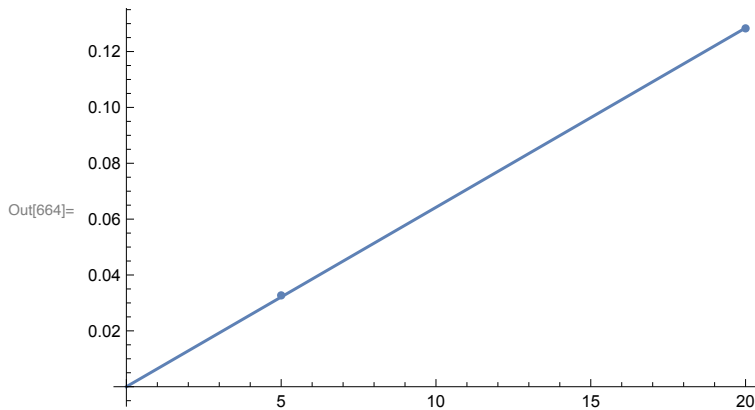
```
In[660]:= PtCal = {{5, Quantity[0.0321, "nm/s"]}, {20, Quantity[0.1235, "nm/s"]}}; (*deposition rates of Pt as a function of power as
PtLMF = LinearModelFit[QuantityMagnitude@PtCal, x, x, IncludeConstantBasis -> False] (*linear fit to deposition rate vs. powe
Show[{Plot[PtLMF[x], {x, 0, 20}, AxesOrigin -> {0, 0}], ListPlot[PtCal]}] (*plot linear fit to deposition rate vs. power*)
ratePt[power_] := Quantity[PtLMF[power], "nm/s"]; (*best fit function for Pt*)
```

```
Out[660]= FittedModel[ 0.00618941 x ]
```



```
In[663]= PtMnCal = {{5, Quantity[0.0327, "nm/s"]}, {20, Quantity[0.1283, "nm/s"]}}; (*deposition rates of PtMn as a function of power*)
PtMnLMF = LinearModelFit[QuantityMagnitude@PtMnCal, x, x, IncludeConstantBasis -> False] (*linear fit to deposition rate vs. |
Show[Plot[PtMnLMF[x], {x, 0, 20}, AxesOrigin -> {0, 0}], ListPlot[PtMnCal]] (*plot linear fit to deposition rate vs. power*)
ratePtMn[power_] := Quantity[PtMnLMF[power], "nm/s"]; (*best fit function for PtMn*)
```

```
Out[663]= FittedModel[ 0.00642235 x ]
```



Atoms per unit area per second

Calculate flux from each target as a function of applied power:

```
NrPt[power_] := Quantity[4, "atoms"] * ratePt[power] / VPt (*NrPt is N Pt atoms per second per unit area.*)
NrPtMn[power_] := Quantity[4, "atoms"] * ratePtMn[power] / VPtMn (*NrPtMn is N PtMn "atoms" per second per unit area.*)
```

Assuming co-sputtering from Pt18Mn82 at.% target,

```
PtFlux[powerPtMn_, powerPt_] := NrPt[powerPt] + NrPtMn[powerPtMn] * .18 (*flux from Pt target*)
MnFlux[powerPtMn_] := NrPtMn[powerPtMn] * .82 (*flux from PtMn target*)
```

Stoichiometry and growth rate

Note: I am assuming small changes in PtMn stoichiometry do not change lattice constant / density

```
StoichiometryPtMn[powerPtMn_, powerPt_] := {
  PtFlux[powerPtMn, powerPt] / (PtFlux[powerPtMn, powerPt] + MnFlux[powerPtMn]),
  MnFlux[powerPtMn] / (PtFlux[powerPtMn, powerPt] + MnFlux[powerPtMn])
}
(*returns stoichiometry of co-sputtered film based on inputted powers,
powerPtMn_ and powerPt_, supplied to the individual PtMn and Pt targets*)
RatePtMn[powerPtMn_, powerPt_] := (PtFlux[powerPtMn, powerPt] + MnFlux[powerPtMn]) / PtMnden
(*total co-sputtering deposition rate based on inputted target powers*)
```

Example calculation:

```
StoichiometryPtMn[2.0, 1.1]  
(*returns {at.% Pt, at.% Mn} of a film co-sputtered from a PtMn target at 2% power and a Pt target at 1.1% power*)  
RatePtMn[2.0, 1.1] (*returns deposition rate of a film co-  
sputtered from a PtMn target at 2% power and a Pt target at 1.1% power*)
```

```
Out[672]= {0.449885, 0.550115}
```

```
Out[673]= 0.0191463 nm/s
```

Appendix D

AMR Analysis with Wheatstone Bridge

AMR measurements taken with the Wheatstone bridge and lock-in return the data as a voltage which must be converted to a resistance. The measured change in sample resistance is calculated as $dR_{\text{sample}} = cV_{\text{measured}}$ where V_{measured} is simply the raw voltage. The following Mathematica notebook will return this conversion coefficient c based on inputted lead resistance values measured according to section 3.4.3. These lead resistances, the lock-in oscillator voltage V_{DC} , and the value of the adjustable resistors R_B are the only inputs needed to run the script.

```
SetOptions[SelectedNotebook[],
  PrintingStyleEnvironment → "Printout", ShowSyntaxStyles → True]
```

```
RDRV = {{}};
```

```
(* Input lead resistances (Ohms) into array in the following order:
```

```
RD, R23 , R56, R52 , R36 , R53 ,
```

```
Rvar -- see Chapter Experimental Methods for definitions
```

```
*)
```

```
In[757]:= i = 1; (*Stores lead resistances of the ith array element above*)
```

```
RDmeas = RDRV[[i]][[1]];
```

```
R23 = RDRV[[i]][[2]];
```

```
R56 = RDRV[[i]][[3]];
```

```
R52 = RDRV[[i]][[4]];
```

```
R63 = RDRV[[i]][[5]];
```

```
R53 = RDRV[[i]][[6]];
```

```
(*Calculates lead resistances of the ith array element above. Stores them as RDL2,
RDL3, RDL5, & RDL6.*)
```

```
RD1 = RDL5 + RDL3 + RDmeas == R53 ;
```

```
RD2 = RDL3 + RDL6 == R63;
```

```
RD3 = RDL2 + RDL3 + RDmeas == R23;
```

```
RD4 = RDL5 + RDL6 + RDmeas == R56;
```

```
RD5 = RDL2 + RDL5 == R52;
```

```
R = Solve[RD1 && RD2 && RD3 && RD4, {RDL2, RDL3, RDL5, RDL6}][[1]];
```



```

In[770]:= i = 1; (*Calculates lead resistances of the ith array element above*)

(**)
Rmeas = RDRV[[i]][[1]];

RL2 = Round[RDL2 /. R];
RL3 = Round[RDL3 /. R];
RL6 = Round[RDL5 /. R];
RL5 = Round[RDL6 /. R];
RDmeas = RDRV[[i]][[1]];

RB = 9930; (*Input adjustable resistor value in Ohms*)

(*Kirchoff's circuit equations e1-4.*)
e1 = (RB2 + RD + RB1) I1 - RB2 * I2 - RD * I3 - RB1 * I4 == VDC;
e2 = -RB2 * I1 + (RB2 + RB + RL3) * I2 - RL3 * I3 == 0;
e3 = -RD * I1 - RL3 * I2 + (RL3 + Rx + RG1 + RD) I3 - RG1 * I4 == 0;
e4 = -RB1 * I1 - RG1 * I3 + (RG1 + RB + RB1) I4 == 0;

(*Solves Kirchoff's equations. The only parameter to edit is lock-
in oscillator voltage VDC in units of Volts.*)
sol = Solve[e1 && e2 && e3 && e4, {I1, I2, I3, I4}][[1]] /.
  {VDC -> 5, RG1 -> 10 000 000 + RL2, RB1 -> RB + RL6 - 90, RB2 -> RB + RL5, RD -> Rmeas};
VLI = 10 000 000 * (I4 - I3) /. sol; (* 10000000 ohm impedance of lock-in*)
VLI = VLI /. {RD -> Rmeas}; (*Lock-in voltage as a function of RD*)
Rx = Rx /. Solve[VLI == 0, Rx][[1]] // N
(*Calculated variable resistance to balance bridge*)

100 (1 - Rx / RDRV[[i]][[7]]) ;

(*If the output give a "/.False" error, rerun this part of the notebook *)
(*Check that the % deviation between
true Rvar and measured Rvar are within 1.5%*)

```

In[784]= Rx;

```

e1 = (RB2 + RD + RB1) I1 - RB2 * I2 - RD * I3 - RB1 * I4 == VDC;
e2 = -RB2 * I1 + (RB2 + RB + RL3) * I2 - RL3 * I3 == 0;
e3 = -RD * I1 - RL3 * I2 + (RL3 + Rx + RG1 + RD) I3 - RG1 * I4 == 0;
e4 = -RB1 * I1 - RG1 * I3 + (RG1 + RB + RB1) I4 == 0;
sol = Solve[e1 && e2 && e3 && e4, {I1, I2, I3, I4}][[1]] /.
  {VDC -> 5, RG1 -> 10 000 000 + RL2, RB1 -> RB + RL6 - 90, RB2 -> RB + RL5};
VLI = 10 000 000 * (I4 - I3) /. sol;
(**)
Rdevice = RD /. Solve[VLI == 0, RD][[2]] // N; (*Solves for device resistance RD *)
R1 = RD /. Solve[VLI == -5 * 10^-5, RD][[2]] // N;
(*solve for RD for arbitrary lock-in reading*)
R2 = RD /. Solve[VLI == -10 * 10^-5, RD][[2]] // N;
(*solve for RD for arbitrary lock-in reading*)
c = (R2 - R1) / (-10 * 10^-5 + 5 * 10^-5)
(*c value is the multiplicative coefficient desired*)

```